Diffraction-limited spectropolarimetry of quiet-Sun magnetic fields

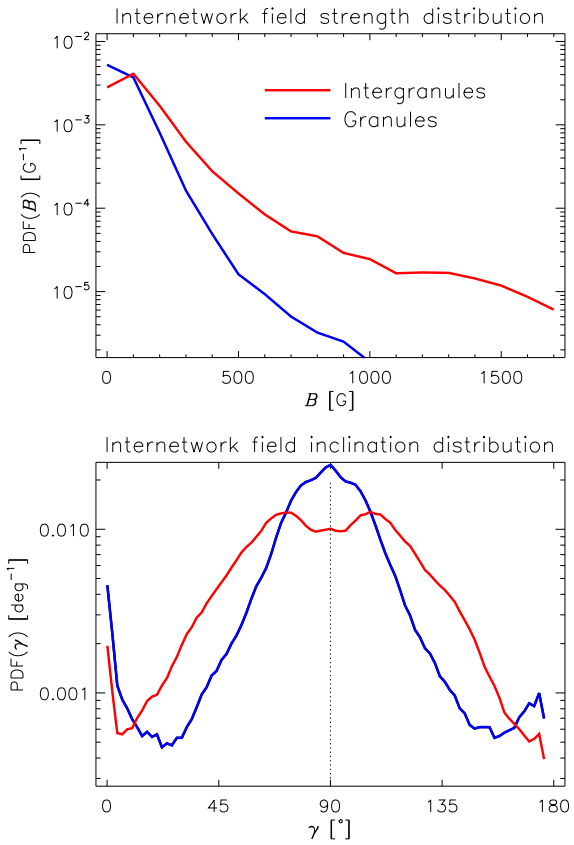

David Orozco Suárez

INSTITUTO Đ ASTROFÍSICA Đ ANDALUCÍA

Consejo Superior de Investigaciones Científicas

DEPARTAMENTO DE FÍSICA APLICADA

Universidad de Granada

Diffraction-limited spectropolarimetry of quiet-Sun magnetic fields

Memoria que presenta
D. David Orozco Suárez
para optar al grado de
Doctor en Astrofísica.

Dr. D. Jose Carlos del Toro Iniesta Dr. D. Luis R. Bellot Rubio

INSTITUTO Đ ASTROFÍSICA Đ ANDALUCÍA

Consejo Superior de Investigaciones Científicas
16 de Septiembre de 2008

Defensa	:	16 de Septiembre de 2008
Directores de la tesis	:	Drs. D. Jose Carlos del Toro Iniesta and D. Luis Ramón Bellot Rubio

ISBN: 978-84-691-5694-0
Depósito Legal: GR.1867-2008
Some of the figures included in this document have been previously published in *The Astrophysical Journal*, *Astronomy & Astrophysics* and *Publications of the Astronomical Society of Japan*

A mi familia

Resumen

Esta tesis presenta en primer lugar la deducción analítica y estudio detallado de las llamadas funciones de respuesta (FR) de las líneas espectrales que se forman en la fotosfera solar con la aproximación Milne-Eddington (ME) a la ecuación de transporte radiativo (ETR). Éstas nos permiten estudiar los cambios que ocurren en las líneas espectrales cuando perturbamos algunos de los parámetros del modelo ME. También nos permiten seleccionar, de forma efectiva, tanto el número de longitudes de onda como sus respectivas posiciones para ser observadas con magnetógrafos vectoriales. A partir de las FR encontramos una estimación de los límites de detectabilidad de los distintos parámetros de la atmósfera modelo.

A continuación, desarrollamos un código de inversión de la ETR en su aproximación ME. El código permite analizar los perfiles de Stokes que emergen de la fotosfera solar, obteniendose así las propiedades magnéticas y dinámicas del plasma fotosférico.

Los parámetros físicos de las atmósferas que dan lugar a los perfiles reales varían con la altura, por lo que que los perfiles observados contienen información sobre la estructura vertical de la atmósfera. La aproximación ME se caracteriza por tratar los diferentes parámetros del modelo como constantes a lo largo de la fotosfera solar. Por esta razón, presentamos un estudio detallado de las capacidades y limitaciones del código ME para el análisis de perfiles reales. Para ello disponemos de simulaciones magnetohidrodinámicas de la fotosfera solar que nos proporcionan los modelos de atmósfera necesarios para generar los perfiles. Éstos son después utilizados para realizar un análisis en profundidad de los errores asociados a la aproximación ME en el análisis.

También hacemos uso de las simulaciones magnetohidrodinámicas para simular datos observacionales del espectropolarímetro del satélite *Hinode*. Realizamos un análisis detallado de los efectos que tienen sobre los perfiles simulados, la difracción del telescopio, el pixelado de la CCD y el ruido fotónico. También analizamos en detalle si somos capaces de obtener los parámetros atmosféricos del modelo mediante inversiones ME. Encontramos que el código ME produce resultados satisfactorios siempre y cuando tengamos en cuenta una contaminación por luz difusa local. Ésta nos permite corregir los efectos de la difracción del telescopio sobre los perfiles de polarización.

También analizamos observaciones de primera luz del satélite japonés *Hinode*. En particular, presentamos los resultados de la inversión ME de perfiles de Stokes pertenecientes a una región del Sol en calma tomados con el espec-

tropolarímetro de *Hinode*. La región observada contiene dos líneas de hierro neutro a 630.15 y 630.25 nm. A partir de estas inversiones determinamos las funciones de densidad de probabilidad de la intensidad y de la inclinación del campo magnético, así como la del factor de luz difusa. Éstas indican que el Sol en calma está mayormente poblado por campos magnéticos del orden de cientos de gauss y preferentemente horizontales. Este análisis nos ha permitido contribuir a resolver el magnetismo del Sol en calma. En el análisis hemos hecho especial hincapié en la unicidad de los modelos proporcionados por la inversión.

También mostramos y describimos una nueva forma de emergencia de flujo magnético a través de celdas convectivas en el Sol en calma. Para ello disponemos de series temporales de datos espectropolarimétricos tomadas por el satélite japonés *Hinode*. Haciendo uso de las propiedades intrínsecas de los parámetros de Stokes estudiamos la evolución temporal de estructuras de campo magnético. En el análisis preliminar de los datos encontramos señales magnéticas unipolares que emergen en los gránulos. No hallamos indicios de señales de polarización lineal, lo que sugiere que las líneas de campo emergentes tienen orientación vertical. Finalmente discutimos posibles mecanismos físicos que podrían dar lugar a este tipo de fenómeno.

Para terminar, hemos simulado datos observacionales del instrumento IMaX (siglas inglesas de Imaging Magnetograph eXperiment) que volará a bordo del globo estratosférico *Sunrise*. Uno de los objetivos es analizar la idoneidad de las líneas candidatas a ser observadas por IMaX para obtener el campo magnético y la velocidad a partir de sus perfiles de Stokes. También analizamos el efecto que produce la difracción del telescopio y el pixelado de la CCD. Prestamos especial interés en como afecta el interferómetro Fabry Pérot de IMaX a los perfiles de Stokes. IMaX tomará un máximo de cinco muestras de longitudes de onda a lo largo de una línea espectral fotosférica, por lo que uno de los objetivos es analizar la precisión con la que somos capaces de determinar el campo magnético y la velocidad a partir de inversiones ME de perfiles muestreados en cinco puntos a lo largo de la línea.

Summary

This thesis firstly introduces the concept of the so-called Response Functions (RFs) of photospheric spectral lines that form in Milne-Eddington (ME) model atmospheres and presents their analytical formulation and main properties. RFs allow the study of the sensitivities of Stokes profiles to perturbations of any of the ME model parameters. They also allow us to select the number and position of wavelength samples to be observed by vector magnetographs and to estimate the minimum variations of the atmosphere model parameters that can be discriminated from noise.

Next, we develop an inversion code of the Radiative Transfer Equation (RTE) in ME atmospheres. The code allows the analysis of Stokes profiles emerging from the solar photosphere, thus obtaining the magnetic and dynamic properties of the photospheric plasma.

The physical quantities describing the solar photosphere that lead to the observed Stokes profiles vary with atmospheric height, therefore the observed profiles contain information about the vertical stratification of the atmosphere. The ME approach is characterized by treating the different model parameters as constant throughout the solar photosphere. For this reason, we present a detailed study of the capabilities and limitations of ME inversions to analyze real observations. To this end, we use magnetohydrodynamic simulations of the solar photosphere. The simulations provide realistic model atmospheres that can be used to synthesize Stokes profiles. The generated spectra are then used to perform a thorough analysis of the errors associated with the ME approach.

We also make use of magnetohydrodynamic simulations to simulate observational data taken with the spectropolarimeter aboard the *Hinode* satellite. We perform a detailed analysis of the impact that telescope diffraction, CCD pixilation, and photon noise have on the simulated profiles. We also carry out a detailed analysis of whether ME inversions are able to retrieve the original model parameters encoded on the polarized spectra. We find that ME inversions produce satisfactory results provided that a contamination by local stray light is taken into account. The use of a local stray-light contamination allows us to correct the effects of telescope diffraction on the polarization signals.

We analyze first-light observations of the *Hinode* satellite. In particular, we present first results from the ME inversion of Stokes profiles from a quiet-Sun region taken by the *Hinode* spectropolarimeter. The observed spectral region contains two neutral iron lines at 630.15 and 630.25 nm. Using the inversion results we determine the probability density function of the magnetic

field strength, field inclination, and the stray-light filling factor. The results show that the quiet Sun is mostly covered by magnetic fields with strengths of the order of hundreds of gauss that tend to be horizontally oriented. These results have contributed to the understanding of the quiet-Sun magnetism. In the analysis we make special emphasis on the uniqueness of the models provided by the inversion.

We also show and describe a new form of magnetic flux emergence in quiet-Sun convective cells. To this end, we use time series data taken by the spectropolarimeter of the *Hinode* satellite. Intrinsic properties of the observed Stokes profiles are utilized to study the temporal evolution of these quiet-Sun magnetic features. In the analysis of the data we detected polarization signals showing a single polarity that appear in granular cells and subsequently vanish. We did not find evidence of linear polarization signals associated to the events, which suggests that the emerging field lines have a preferred vertical orientation. Finally we discuss the possible physical mechanisms that may explain such phenomenon.

Finally, we simulate observational data taken with the Imaging Magnetograph eXperiment (IMaX) that will be aboard the stratospheric balloon Sunrise. One of the goals is to analyze the adequacy of the two candidate spectral lines to be observed by IMAX to derive the photospheric magnetic field vector and plasma velocity from their polarization signals. We also analyze the effects produced by telescope diffraction and CCD pixilation on the simulated profiles. Particular attention is put on the effects of the IMaX Fabry-Pérot interferometer on the spectra. To finish, IMaX will observe a limited number of wavelength samples across the spectral line in addition that it has a limited spectral resolving power, so that we aim at analyzing whether we can infer the physical quantities describing the solar atmosphere from the Stokes profiles in such circumstances and at characterizing the uncertainties of the vector magnetic fields and plasma velocities obtained from IMaX observations.

Agradecimientos

En primer lugar quiero dar las gracias a Jose Carlos y a Luis por todo el esfuerzo que han realizado para llevar a cabo la consecución de este proyecto de tesis, y sobre todo por darme la oportunidad de realizar la tesis en el Instituto de Astrofísica de Granada y trabajar junto a dos grandes científicos. Los resultados de este trabajo no habrían sido los mismos sin la gran aportación de mis directores de tesis. Los cuatro años durante los cuales ésta ha sido desarrollada han sido excepcionales, tanto a nivel profesional como personal.

Quiero darle las gracias a mis profesores de la Universidad de La Laguna: Basilio, Inés, Manolo, Ramón, entre otros, por convertir los estudios de astrofísica en una experiencia inolvidable. En especial le doy las gracias a Basilio, por sus lecciones sobre el transporte de radiación en la fotosfera solar y por ser tan entrañable. Mis estudios en la Universidad no hubieran sido posible sin el apoyo de mis amigos. Desde aquí muchas gracias a: Marian, Rebecca, Nacho, Merche, Asier, Carlos, Fernando, Raquel, Juanma, Ita ... También quiero agradecer a mis compañeros en el Instituto de Astrofísica de Andalucía, especialmente a: Geli, Omaira, Begoña, Yoli, Rene, Maya, Martin, Toni, su apoyo en todo momento. Gracias por ser tan excepcionales.

Le doy las gracias a los miembros de equipo de IMaX con los que he podido colaborar y en especial a Valentín, el invertigador principal de este gran proyecto. Agradezco también al Observatorio Astronómico Nacional de Japón, en particular al Prof. Saku Tsuneta, la oportunidad que me dieron allá por Febrero de 2007, de analizar datos de primera luz del satélite japonés *Hinode*, sobre los cuales se substentan gran parte de los resultados de esta tesis.

Finalmente, quiero añadir que mi padre Carmelo y mi madre Ana son los culpables de que haya terminado haciendo una tesis en Fśica Solar. Ellos me dieron la oportunidad de ir a la Universidad de La Laguna a terminar mis estudios junto a mi compañera de aventuras de siempre, Susi. Allí empezó todo. No quiero olvidarme de mis hermanos, Carmelo y Ana, con los que siempre puedo contar.

Contents

1

Introduction

The concept *quiet Sun* has been employed for long to label regions of the solar photosphere devoid of magnetic signals, in opposition to the so-called *active* regions. Broadly speaking, the Sun was considered quiet (i.e., non-magnetic) everywhere outside sunspots and plages (also called faculae) until the 1970's. From there on, a panoply of magnetic structures at different spatial scales and with different flux values have been discovered in quiet-Sun areas, changing the paradigm of an essentially non-magnetic Sun. The quiet-Sun magnetic structures are somewhat arbitrarily grouped in two families: the *network* and the *internetwork*. As its name suggests, the former is a reticulum of structures mostly located at the boundaries of supergranules. It is made up of individual (or bunches of individual) flux tubes with strengths of 1.4–1.5 kG. The internetwork is that part of the quiet-Sun surface located within the network. Its nature and properties are largely unknown because of the weak and/or very diluted (in area) character of its magnetic fields. The last two decades have witnessed a controversial (thus fruitful) debate about the nature and strength of internetwork magnetic fields, based on observations in visible and infrared spectral lines. No consensus has been reached yet due to the modest spatial resolutions of the data employed by the different authors.

The advent of a new generation of high-spatial resolution spectropolarimeters, capable of delivering observations near the diffraction-limit of the telescope, opens the door to a new era of discoveries. This thesis intends to contribute to the understanding of internetwork magnetic fields through the analysis of spectropolarimetric observations near the diffraction limit. To this purpose we investigate the reliability of diagnostic tools utilized to determine

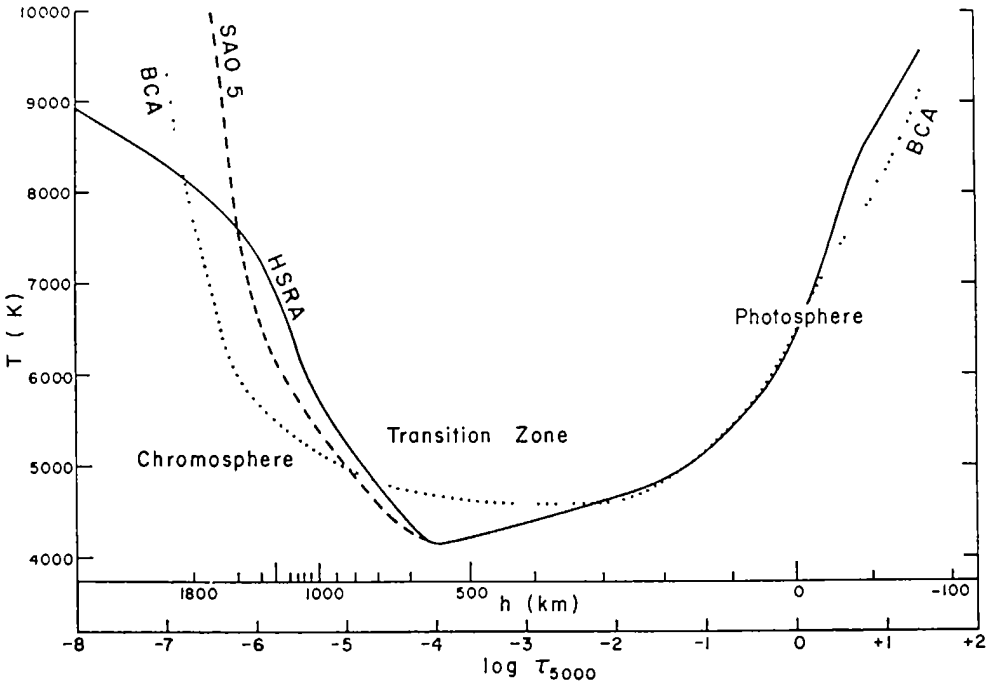

FIGURE 1.1:— Variation of temperature with continuum optical depth at 5000 Å for three solar model atmospheres: the Harvard-Smithsonian Reference Atmosphere (HSRA; Gingerich et al. 1971), the Bilderberg Continuum Atmosphere (BCA; Gingerich & de Jager, 1968), and a revision of the BCA model (SAO 5). The geometrical depth scale h (km) is the height above $\tau_{5000} = 1$ for the HSRA model. Notice that a temperature minimum is reached at $\tau_{5000} = 10^{-4}$. The illustration has been taken from Gingerich et al. (1971).

the vector magnetic field from high-spatial resolution measurements. We also take advantage of transfer theory and numerical experiments to optimize the design of upcoming solar magnetographs.

1.1 Quiet-Sun magnetic fields

To first order, the Sun can be considered as a black body that emits radiation in all directions. This radiation comes from an atmosphere which is divided in three main regions, namely, the photosphere, the chromosphere, and the corona. More than 90% of the visible radiation emerges from the photosphere. We shall not describe the properties of solar plasmas in detail and rather refer the reader to textbooks like those by Foukal (1990) and Stix (2004).

Figure 1.1 shows the thermal structure of the lower solar atmosphere for

different models. The photosphere can be defined as the region extending from $z = -100$ km ($\log \tau_{5000} \simeq -2$) to $z \simeq 500$ km ($\log \tau_{5000} \simeq -4$), i.e., the height at which the temperature reaches a minimum. Its effective temperature is ~ 5700 K and can be modeled sufficiently well assuming local thermodynamic equilibrium[1] conditions.

Early observations of the solar photosphere soon revealed the existence of granules, sunspots, and faculae. After George E. Hale's (1908) discovery of magnetic fields in sunspots, observations progressively suggested an association of the most dynamical (often violent) evolutionary phenomena seen over the Sun with sunspots and their surrounding regions including faculae. These findings led to discriminate between active and non-active regions, based on whether they possess magnetic fields or not. Since then, non-active regions are referred to as the quiet Sun.

Sunspots are concentrations of very strong magnetic fields that emerge from the convection zone with typical strengths of about 1.5–4 kG. For a long time, they were regarded as the main contributors to the total magnetic flux of the solar surface. In the 1970's, however, the community realized that a significant fraction of the solar magnetic flux is organized in small-scale structures outside sunspots. Howard and Stenflo (1972) found that more than 90% of the total magnetic flux of the solar surface is concentrated in network areas. After the detection of weak magnetic signals outside the network, the term internetwork (IN) was coined. The IN corresponds to the interior of supergranular cells. The network outlines the regions where magnetic field lines are advected by the supergranular[2] flow, and is made up of intense flux tubes with diameters of a few hundred km (e.g., Grossmann-Doerth 1994; see Solanki 1993 for a review).

Figure 1.2 displays the quiet solar surface at disk center. The top panel represents the intensity at 430 nm (G band) and the bottom panel shows a filtergram taken in the core of a chromospheric spectral line (Ca II H). In the continuum map, the granulation is seen everywhere. Granulation is nothing but convection: the brighter granules correspond to the upper parts of cells with hot, hence less dense, upwelling plasma; the darker interstices of granulation correspond to downwelling, densers and colder plasmas. The granulation covers the entire photosphere, except those regions where the magnetic flux suffices to inhibit convection (e.g., sunspots and pores). In the granulation we find tiny bright structures that are associated with flux tubes in the network. These

[1] See Mihalas (1978) and Gray (1992) for a comprehensive account of stellar radiative transfer.

[2] The length scales of supergranulation are 20-40 Mm (25″-55″), according to Leighton et al. (1962).

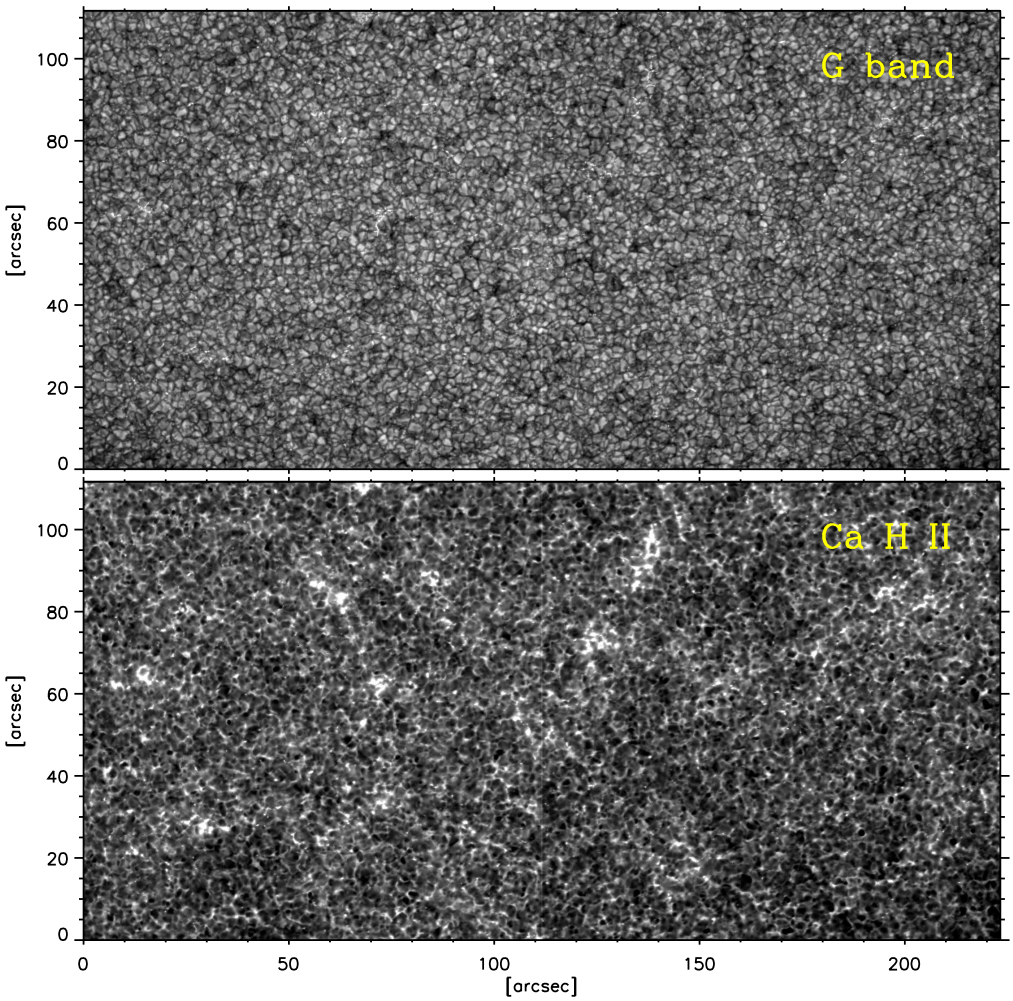

FIGURE 1.2:— Filtergrams taken with the Broadband Filter Imager of the *Hinode* satellite (Tsuneta et al. 2008). The top image shows the photosphere in the G-band near 430 nm. The bottom map corresponds to a filtergram in the Ca II H line core, which represents the low chromosphere. White patches in the chromosphere indicate the presence of magnetic fields. The images corresponds to disk center.

magnetic structures show up as the brightest features in the chromosphere. They can be brighter than the surroundings because the magnetic field evacuates the plasma within the flux tubes, leading to a drop in gas pressure and a reduction of plasma opacity (at this wavelength). However, they can also be related to energy transfer from the photosphere through magnetic fields. The network fields outline the boundaries of supergranular cells.

The first observational evidence of magnetic fields in the IN was reported by Livingston & Harvey (1971). Four years later, the same authors confirmed their findings (Livingston & Harvey 1975; see also Smithson 1975 and Martin 1984). They obtained mean flux densities of 2–3 Mx cm^{-2} at spatial resolutions of $5''$. Contrary to the network fields, which tend to be spatially organized, the IN fields looked highly disorganized.

Little progress in the analysis of IN regions was made during the next twenty years because of the limited sensitivity of the instruments and the modest spatial resolution of the observations. Keller et al. (1994) were the first to obtain circularly polarized spectra of the visible Fe I lines at 524.7 and 525.02 nm in IN regions at $5''$ spatial resolution, using a prototype version of the Zürich Imaging Stokes Polarimeter (Keller et al. 1992). They set an upper limit for the field strengths of 500 G, with a 68% probability.

Many other studies of IN magnetic fields have been carried out during the last decade (see Khomenko 2006 for a review). These studies have attempted to determine the distribution of field strengths in the internetwork by using polarimetric measurements in the spectral regions around 630 nm and 1565 nm. These regions contain spectral lines sensitive to the Zeeman effect. However, the results obtained from the two wavelength regions are contradictory. The visible Fe I lines at 630.2 nm indicate a predominance of kG fields (Sánchez Almeida & Lites 2000; Domínguez Cerdeña et al. 2003; Socas-Navarro & Lites 2004), whereas the infrared lines at 1565 nm suggest hG fields (Lin 1995; Lin & Rimele 1999; Khomenko et al. 2003; Martínez González et al. 2008; Domínguez Cerdeña, Sánchez Almeida, & Kneer 2006). Also, there are strong discrepancies in the filling factors of the magnetic field structures, which range from 1% to 30%, and in the unsigned magnetic flux densities, with reported values from a few Gauss (Lin & Rimmele 1999; Wang et al. 1995) to tens of Gauss (Domínguez Cerdeña, Kneer, & Sánchez Almeida 2003; Sánchez Almeida 2003).

The IN magnetism has also been analyzed using the Hanle effect. The results suggest that, in addition to the weak (or strong) component of magnetic field, there is an unknown amount of "turbulent" flux in the IN with field strengths of few tens of Gauss (e.g., Stenflo 1982, 1993; Faurobert-Scholl 1993; Shchukina & Trujillo Bueno 2003). The latest studies indicate a mean field strength of $\langle B \rangle \sim 100$ G (Trujillo Bueno et al. 2004).

The refinement of magnetohydrodynamic (MHD) simulations has contributed to the understanding of IN regions in recent years. Modern MHD codes can be used to describe the physics of magnetoconvection in the photosphere with reasonable accuracy (e.g., Vögler 2003; Schaffenberger et al. 2006; Stein & Nordlund 2006; Abbett 2007). Simulations of local dynamo action have also been performed to study the IN magnetism. The results suggest that turbulent

convective flows are able to concentrate and hence intensify magnetic fields in granular convection (Cattaneo 1999; Emonet & Cattaneo 2001; Cattaneo, Emonet, & Weiss 2003; Vögler & Schüssler 2007). The turbulent fields in IN areas do not seem to be part of the remnant flux of decaying active regions (cf. Spruit, Title, Van Ballegooijen 1987) since the area covered by IN regions does not vary with the solar cycle.

1.2 Observations and diagnostic techniques

It is not possible to measure *in situ* the physical properties of the photospheric plasma. Therefore, the plasma properties have to be inferred from remote measurements of the polarized radiation emitted by the Sun in selected spectral lines. Such measurements are influenced by the Earth's atmosphere and the instrument. All these conditioning factors introduce difficulties in the interpretation of the observations. Several diagnostic methods based on the solution of the radiative transfer equation have been devised with different degrees of sophistication. Most of them are inversion techniques that fit the observed polarized spectrum through non-linear, least-square minimization algorithms.

There are several ways to explore the IN magnetism. Most of them use observations of magnetically sensitive lines. Both the Hanle and the Zeeman effects imprint their signatures in spectral lines, providing information on magnetic fields. In the last decade, the analysis of Zeeman-sensitive lines has greatly benefited from advances in solar instrumentation and from increases in the spatial resolution. However, the weak signals of IN flux concentrations and the effects of instrumental noise make it difficult to accurately determine field strengths and filling factors within the resolution element. Also, the possible existence of opposite magnetic polarities in the same resolution element represents a strong disadvantage for the Zeeman effect. Opposite-polarity fields would lead to cancellation of the circular polarization signal (at least partially) when they are not spatially resolved. Therefore, diagnostic methods based on the Zeeman effect only provide upper limits to the field strength and magnetic flux values (see e.g., Sánchez Almeida & Lites 2000). Nevertheless, Zeeman measurements have been essential in the discovery of transient, small-scale horizontal IN fields (Lites et al. 1996).

The availability of high-precision measurements in the near infrared (IR) has open new diagnostic capabilities because the magnetic sensitivity increases quadratically with wavelength. However, the results of inversions of visible and IR lines show apparently contradictory results. The visible Fe I lines at 630 nm indicate a predominance of kG fields (Sánchez Almeida & Lites 2000;

Domínguez Cerdeña, Kneer, & Sánchez Almeida 2003; Socas-Navarro & Lites 2004), whereas the IR Fe I lines at 1565 nm suggest hG fields (Lin 1995; Lin & Rimmele 1999; Khomenko et al. 2003; Domínguez Cerdeña, Sánchez Almeida, & Kneer 2006). Several attempts to reconcile these results have been made without much success. Some authors propose that visible and IR lines sample different magnetic structures in the resolution element (Sánchez Almeida & Lites 2000; Socas-Navarro & Sánchez Almeida 2003); others suggest that noise affects the visible lines more dramatically than the IR lines (Bellot Rubio & Collados 2003). On the other hand, Martínez González, Collados, & Ruiz Cobo (2006) reported on the inability of inversion methods (under particular model assumptions) to constrain the thermodynamic and magnetic properties of the plasma using the Fe I lines at 630 nm. In view of the difficulties to obtain reliable field strengths and fluxes, some authors have explored new ways to characterize the fields of IN regions. For instance, the analysis of spectral lines showing strong sensitivity to hyperfine-structure effects (López Ariste, Tomczyk, & Casini 2002, 2006; Asensio Ramos et al. 2007b) support the IR view of an internetwork filled by hG fields.

If the IN had a significant contribution of turbulent fields they could be undetectable via the Zeeman effect because the different components of opposite sign would cancel out (Zirin 1985). In this context, diagnostics methods based on the Hanle effect have been proposed to measure the turbulent component of the field, taking advantage of the fact that the underlying physical mechanism do not suffer from cancellation effects (Trujillo Bueno, Shchukina, & Asensio Ramos 2004).

Another strategy for getting insight on the IN magnetism is through numerical simulations of magnetoconvection (Schüssler 2001, 2003). It allows an *a-priory* test of diagnostics techniques with a simulated (well known) Sun. By modeling observations of given instruments using magnetohydrodynamic (MHD) simulations and then applying diagnostic techniques to the simulated observations we can understand the meaning of the inferred physical parameters and assess the reliability of the diagnostics. Khomenko & Collados (2007a) were the first to use this approach to examine the validity of the line-ratio technique (Stenflo 1973) as a diagnostics of magnetic field strengths in the IN. Unfortunately, line ratios did not perform well in the tests.

In summary, although in recent years our knowledge of the quiet-Sun magnetism has improved dramatically, the nature of the magnetic fields in the interior of supergranular cells still remains unknown to a large degree. The "activity" of these regions represents a challenging problem for both current instrumentation (discrepancies between wavelength ranges, insufficient spatial and temporal resolution, etc) and theoretical understanding (very small scales,

very small magnetic fluxes and filling factors [$\sim 1\%$], and very high magnetic Reynolds numbers[3]).

Further progress in the analysis of IN regions requires diffraction-limited observations at high temporal cadences and large polarimetric sensitivities, efficient analysis techniques that decode the solar information from the spectropolarimetric signal, and realistic MHD simulations.

Higher spatial resolutions will allow the amplitudes of measured Zeeman polarization signals to become larger because cancellation effects will be less frequent and filling factors will be larger, provided the magnetic fields are not structured on scales much smaller than the size of the resolution element. MHD simulations can first be used as a benchmark for the analysis techniques, but in the end, cross-checking real observations and simulations will hopefully improve out theoretical understanding of the physical phenomena taking place in the quiet Sun.

1.3 Motivation of this work

As mentioned before, our comprehension of the nature of quiet-Sun magnetic fields, in particular IN fields, is still limited because of the modest spatial and temporal resolutions achievable with present-day instrumentation. At $1''$ the polarization signals are weak and contaminated by noise. An improvement in the spatial resolution is likely to result in larger polarization signals making them less vulnerable to the effects of noise. The consequent increase in the filling factor will also help discriminate the strength of the fields. The long-term goal is to reach the scale of the mean free path of photons, which is about 100 km in the solar photosphere. Many of the physical phenomena taking place in the photosphere occur at this scale.

The spectropolarimeter (SP) of the *Hinode* satellite (Kosugi et al. 2007; Tsuneta el al. 2008) offers nearly diffraction-limited spectropolarimetric observations of the Fe I lines at 630 nm. These data are leading to new insights into the magnetism of the quiet-Sun (e.g., Centeno Elliot et al. 2007; Lites et al. 2007a,2008a; Orozco Suárez et al. 2007a,b). With a spatial resolution of $0\farcs32$, we have the possibility to analyze whether the increased resolution brings about better conditions to interpret the weak signals of the IN. Note that tangled fields of mixed polarities on very small scales would not be visible to the Zeeman effect even at the resolution of *Hinode*, though. This thesis is devoted to the study of internetwork magnetic fields. We determine and characterize

[3]The magnetic Reynolds number is dimensionless and represents the ratio of convection (advection) to diffusion of the magnetic field.

the distribution of field strengths and inclinations, and also investigate how the magnetic flux appears, evolves and disappears in the IN. We aim to provide new information to settle the controversy between the results from the visible and IR lines and to answer the question on whether the IN fields are organized into flux-tube-like structures or are turbulent in nature.

The internetwork spectropolarimetric measurements have to be interpreted in terms of solar atmospheric parameters using suitable diagnostics. In particular we employ inversion methods based on the Milne-Eddington solution of the radiative transfer equation. In view of the concerns raised about the reliability of results derived from the Fe I lines at 630 nm, we simulate *Hinode*/SP observations and evaluate the performance of Milne-Eddington inversion codes applied to high-spatial resolution observations. To this end we use realistic magnetoconvection models to compute synthetic profiles that are degraded to match the resolution of the *Hinode*/SP.

A promising instrument under development that will reach spatial resolutions of the order of 80 km is the Imaging Magnetograph eXperiment (IMaX; Martínez Pillet et al. 2004). IMaX is a magnetograph with full polarization and imaging capabilities which is designed to fly as a post-focus instrument of the one-meter telescope aboard the *Sunrise* balloon mission (Gandorfer et al. 2006). Being stratospheric (the balloon will reach 40 km of altitude), *Sunrise* will be able to get rid of most of the atmosphere, hence improving the image quality. An image stabilization system will maintain the spatial resolution for long periods of time, thus allowing to explore the evolution of photospheric features. The spatial resolution will be close to the diffraction limit of the telescope. The Solar Physics Group of the Instituto de Astrofísica de Andalucía (CSIC) participates in the design, development, and construction of IMaX. The present thesis is also intended to contribute, at least partially, to the instrument. Among other things, we perform calculations that can help select the spectral line to be observed with IMaX. We test the diagnostic potential of IMaX measurements for vector magnetic field inferences by means of inversions. Our calculations can be easily extended to the design of the Polarimetric and Helioseismic Imager (PHI; Marsch et al. 2005), a magnetograph proposed to fly aboard the ESA/NASA *Solar Orbiter* mission. Again, near diffraction-limited polarization images of the Sun will be used to explore the solar magnetism at a vantage point out of the ecliptic ($\sim 35^\circ$) and a distance of 0.2 AU, with a telescope of ~ 20 cm. Our group is also involved in the design, development, and construction of PHI.

1.4 Overview of the thesis

In what follows, we briefly outline the contents of this thesis. The work is structured in ten Chapters. Chapters 2 and 3 summarize the basics of radiative transfer of polarized light and inversion methods, respectively. Chapter 4 deals with the theory of Milne-Eddington response functions. Chapter 5 to 8 constitute the main body of this thesis. We examine the reliability of Milne-Eddington inversion methods applied to high-spatial resolution data, simulate *Hinode*/SP observations using MHD models, analyze measurements of the quiet-Sun internetwork taken with *Hinode*/SP, and study the evolution of internetwork magnetic features using long time series of *Hinode* observations. IMaX and PHI are the subject of Chapter 9. Finally, Chapter 10 summarizes our main results. More specifically:

- Chapter 2 is an introduction to polarized radiative transfer and the measurement of light. We include a brief description of IMaX. We place emphasis on the polarimetric analysis and spectral modulation carried out by this instrument. At the end of the Chapter, the Milne-Eddington solution to the radiative transfer equation is presented.

- Chapter 3 introduces the concept of Response Functions (RFs) in ME atmospheres. The analysis of these response functions allows to understand the physics of Stokes profile formation under ME conditions. RFs can be used to investigate the sensitivity of spectral lines to model parameters. They also provide us with a means to optimize the selection of wavelength points and number of samples observed by vector magnetographs. We employ the RFs to evaluate the minimum variations of the model parameters that can be seen above the noise, which is of interest for the design of vector magnetographs. Part of this Chapter has been published in *Astronomy & Astrophysics* (Orozco Suárez and del Toro Iniesta 2007).

- In Chapter 4 we review in some detail available methods for the inversion of the radiative transfer equation. We introduce the MILne-Eddington inversion of pOlarized Spectra (MILOS) code. MILOS is used in Chapters 5,6,7, and 9, to analyze simulated and real data. We describe the basic operation of the code and perform several tests to check its performance.

- Chapter 5 we study the relation between the physical quantities describing the photosphere, the measurements, and the atmospheric parameters obtained from Milne-Eddington inversions of the measurements. Are ME inversions adequate to analyze high-spatial resolution observations?

What are the errors associated with the magnetic field components and velocities inferred from the profiles? To answer these questions we generate realistic Stokes profiles from magnetohydrodynamic simulations of the solar photosphere. We analyze basic properties of the MHD models and the synthetic profiles. We then invert the spectra using ME inversions and compare the inferences with the real model stratifications to obtain the uncertainties of the model parameters.

- In Chapter 6 we simulate high-spatial resolution observations taken with the spectropolarimeter attached to the Solar Optical Telescope aboard the *Hinode* satellite. To this end we employ MHD models to synthesize Stokes profiles and degrade the "observations" to match the *Hinode*/SP resolution. We present a detailed description of the effects of diffraction on the simulated profiles. The profiles are analyzed using ME inversions. A comparison with the actual physical parameters in the MHD simulations allows us to assess the performance of ME inversions of *Hinode*/SP data at $0\farcs32$. The results indicate that ME inversions deliver satisfactory results provided the dilution of the polarization signals due to diffraction is corrected for. We propose the use of a local stray-light contamination to do it. Parts of this Chapter have been published in *The Astrophysical Journal Letters* (Orozco Suárez, Bellot Rubio & del Toro Iniesta 2007).

- Quiet-Sun internetwork observations taken with the *Hinode* spectropolarimeter are analyzed in Chapter 7. The analysis of the profiles is carried out using the inversion strategy presented and tested in Chapter 6. In particular, we apply a one-component Milne-Eddington inversion with local stray-light contamination. We determine the distribution of IN magnetic field strengths and demonstrate that the IN consists mainly of hG fields. We analyze the orientation of such fields and conclude that most of them show large inclinations to the vertical. In fact, the amount of nearly horizontal fields is much larger than that of vertical fields in our observations. Both granules and intergranular lanes harbor fields in the IN. We compute the flux values (corrected for diffraction), finding a mean flux density of $\sim$ 7–25 Mx cm^{-2}. The transverse flux amounts to $\sim$ 23–85 Mx cm^{-2}. In this Chapter we perform additional tests to check the dependence of the ME results on the initialization. In particular, we demonstrate that strong and weak-field initializations lead to the same solution. Results from this chapter have been published in *The Astrophysical Journal Letters* and the *Publications of the Astronomical Society of Japan* (Orozco Suárez, Bellot Rubio, del Toro Iniesta, et al. 2007a,b).

- In Chapter 8 we make use of the ability of the *Hinode* spectropolarimeter to continuously raster a small area of the QS in order to obtain maps with high temporal cadence. This allows a study of the evolution of small-scale magnetic features to be performed. We detect the emergence of loops in the quiet photosphere, confirming the results of Centeno et al. (2007). We also find what we believe is a new form of flux emergence in the IN: small patches of magnetic flux appear in granular cells, being visible only in circular polarization, and soon disappear. During the evolution there is no evidence of linear polarization. This finding points to the emergence of apparently *vertical* magnetic flux concentrations in granular convection cells. We analyze five typical examples in an attempt to uncover the physical mechanisms behind them. We base our study on the analysis of the polarization signals rather than on inversion techniques. Results from this Chapter have been published in *Astronomy & Astrophysics* (Orozco Suárez, et al. 2008).

- The capabilities of future ground-based and space-borne solar instrumentation are analyzed in Chapter 9. The focus is on IMaX. We resort again to MHD simulations to simulate IMaX observations. This instrument has to fulfill technical constrains that limit its spectral resolving power and the number of wavelength samples to be observed. We consider the Fe I lines at 525.02 and 525.06 nm, since these are the two candidate lines to be observed by IMaX. Then, using ME inversions we study how the limited spectral resolving power and wavelength sampling of such instruments influence the determination of physical parameters from the Stokes profiles. We also characterize the uncertainties of the vector magnetic fields and plasma velocities obtained from IMaX observations. The results show that IMaX will benefit from the observation of the Fe I line at 525.02 nm for vector magnetic field inferences. They also show that it is possible to infer field strengths and velocities from Stokes profiles when they are sampled at only four wavelength positions across the line profile.

2

Radiative transfer and the measurement of light

Introductions to the measurement of light, to vector, filter-based magnetographs, and to radiative transfer are presented in this Chapter. We will also introduce one of the approximations for solving the radiative transfer equation: the *Milne-Eddington* approximation, which will be widely used in this thesis.

2.1 The measurement of light

A light beam that propagates through an isotropic medium can be interpreted as the superposition of plane electromagnetic waves, each described by its associated electric field vector, which is contained in the plane perpendicular to the direction of propagation of the beam.

If the light beam propagates along the Z-axis, then

$$E_x(t) = A_x(t)\,\mathrm{e}^{-i[\omega t - \delta_x(t)]}, \tag{2.1}$$

$$E_y(t) = A_y(t)\,\mathrm{e}^{-i[\omega t - \delta_y(t)]}, \tag{2.2}$$

where $\delta_x(t)$ and $\delta_y(t)$ represent the phase shift of each of the x and y components, $A_x(t)$ and $A_y(t)$ their amplitudes, and ω the frequency.

Giving values to these four parameters, we can describe any electromagnetic wave. The most convenient form, however, to describe the polarization properties of any electromagnetic wave is by a set of four parameters, called

the Stokes parameters. The Stokes parameters that represent an arbitrarily polarized beam are:

$$\begin{aligned} I = & \quad k(\langle |E_x(t)|^2 \rangle + \langle |E_y(t)|^2 \rangle) & = & \quad k\langle A_x^2 + A_y^2 \rangle, \\ Q = & \quad k(\langle |E_x(t)|^2 \rangle - \langle |E_y(t)|^2 \rangle) & = & \quad k\langle A_x^2 - A_y^2 \rangle, \\ U = & \quad k(\langle E_x(t)^* E_y(t) \rangle + \langle E_y(t) E_x(t)^* \rangle) & = & \quad 2k\langle A_x A_y \cos\delta \rangle, \\ V = & \quad ik(\langle E_x(t)^* E_y(t) \rangle - \langle E_y(t) E_x(t)^* \rangle) & = & \quad 2k\langle A_x A_y \sin\delta \rangle, \end{aligned} \tag{2.3}$$

where * means complex conjugate, k is a dimensional constant, $\delta(t) = \delta_x(t) - \delta_y(t)$ is the phase difference between the x and y components of the electric field and $\langle\,\rangle$ stands for time average. $\mathbf{I} = (I, Q, U, V)^\dagger$ is called the Stokes vector, where $\dagger$ means transposition. The quantities defined above are real and *measurable* and must follow the relationship: $I^2 \geq Q^2 + U^2 + V^2$. When equality occurs, the light beam is said to be totally polarized. When $Q = U = V = 0$, light is called natural or totally unpolarized. In any other case, light is said to be partially polarized. Since no confusion is possible, we hereafter omit the argument (t) on the amplitudes and phase shifts as in the right-most terms of Eq. (2.3).

To analyze the polarization of a light beam we need some optical devices. Among them, linear polarizers and retarders are the most common ones. A linear retarder is an optical device capable of introducing a phase difference, the so-called retardance, between the two perpendicular components of the electric field associated to the beam. Therefore, the linear retarder does not alter the total intensity, I. The device is characterized by two fundamental optical axes, namely the fast and the slow axes. The retardance depends on different optical and geometrical properties of the medium light is travelling through. As an example, let us consider a retarder whose fast axis is aligned with the X-axis of the reference coordinate system. If E_x and E_y represent the input light beam and E'_x and E'_y the output beam, a retardance plate will introduce a phase difference δ in one of the components, say y, as follows:

$$E'_x = E_x \quad ; \quad E'_y = E_y \mathrm{e}^{i\delta}. \tag{2.4}$$

A linear polarizer is an optical device from which the emergent light is completely linearly polarized at an angle θ, regardless of the state of polarization of the incident light. This angle characterizes its fundamental, or transmission, axis along which the transmission of light is maximum. The electric field aligned to the axis propagates naturally through it; the orthogonal component of the field is completely absorbed though. The only non-null component of

the output beam electric field is along the θ axis and given by

$$E_\theta = E_x \cos\theta + E_y \sin\theta. \tag{2.5}$$

An example of a double linear polarizer is the so-called *beam splitter*. It is capable of separating any input light beam into two independent beams with orthogonal polarization states.

As an example, let us suppose a retarder wave plate whose fast axis is oriented along the X-axis followed by a linear polarizer whose fundamental axis form an angle θ with the X-axis. The first optical device introduces a retardance on the phase of the y component of the electric field, δ. Then, the light beam crosses the linear polarizer, which allows only the θ component of the electric field to be transmitted. Thus, the output beam is given by:

$$E_\theta = E_x \cos\theta + E_y \mathrm{e}^{i\delta} \sin\theta. \tag{2.6}$$

In the detector, only the time-averaged square modulus of the beam electric field is measured:

$$I_{\mathrm{meas}} = \langle E_\theta^* E_\theta \rangle. \tag{2.7}$$

Now, according to Eq. (2.3), and assuming $k = 1$ (which is in practice irrelevant), we have

$$\begin{aligned} \langle E_x(t) E_x^*(t) \rangle &= \tfrac{1}{2}(I + Q), \\ \langle E_y(t) E_y^*(t) \rangle &= \tfrac{1}{2}(I - Q), \\ \langle E_x(t) E_y^*(t) \rangle &= \tfrac{1}{2}(U + \mathrm{i}V), \\ \langle E_x^*(t) E_y(t) \rangle &= \tfrac{1}{2}(U - \mathrm{i}V). \end{aligned} \tag{2.8}$$

From these equations, the measured light beam intensity can be cast in terms of the various Stokes parameters as

$$I_{\mathrm{meas}}(\theta, \delta) = \frac{1}{2}(I + Q\cos 2\theta + U \sin 2\theta \cos\delta + V \sin 2\theta \sin\delta)\,. \tag{2.9}$$

This equation provides the possibility of measuring the polarization of light by means of different optical devices and setups, just by giving specific values to θ and δ. Specifically,

$$\begin{aligned} I &= I_{\mathrm{meas}}(0,0) + I_{\mathrm{meas}}(\pi/2, 0), \\ Q &= I_{\mathrm{meas}}(0,0) - I_{\mathrm{meas}}(\pi/2, 0), \\ U &= I_{\mathrm{meas}}(\pi/4, 0) - I_{\mathrm{meas}}(3\pi/4, 0), \\ V &= I_{\mathrm{meas}}(\pi/4, \pi/2) - I_{\mathrm{meas}}(3\pi/4, \pi/2). \end{aligned} \tag{2.10}$$

Hence, I is the total intensity, Q is the difference between the intensities of linear components at 0°and 90°, U is the difference between the intensities of linear components at 45°and 135°, and V is the difference between clockwise and counterclockwise circulary polarized light. In what follows we are introducing a particular optical configuration, namely, that adopted for the IMaX instrument.

2.2 Brief introduction to IMaX

The most suitable instruments to analyze the rapid changes that occur on the magnetic and dynamic properties of solar plasmas in two dimensions are the filter-based magnetographs (Zirin 1995). We shall exemplify the previous section by means of a particular vector magnetograph: the Imaging Magnetograph eXperiment (IMaX; Martínez Pillet et al. 2004) is a vector polarimeter capable of observing a photospheric spectral line in five wavelength samples in less than one minute. It has been designed in order to obtain maps of the magnetic field vector and the flow velocity of a given zone of the solar surface. It is one of the post-focus instruments of the SUNRISE balloon mission (Gandorfer et al. 2006) and will provide invaluable information about the magnetism and the dynamics of the solar photospheric plasmas. It will achieve unprecedented spatial and temporal resolution with high polarimetric sensitivity. To this end, IMaX is made up of two fundamental optical parts: one for the polarimetric modulation of light and another for the spectral analysis. The latter is done by means of a Fabry-Pérot interferometer (étalon) based on $LiNbO_3$ in an incoming collimated system. The étalon is a narrow-band, tunable filter which allows the selection of the different wavelength samples. The system has a narrow-band pre-filter of 10 Å, as well. The polarimetric modulation is carried out by using two liquid crystal variable retarders (ROCLIs)[1] and the final linear polarization analysis is made with a beam splitter. This optical configuration allows us to measure the Stokes vector, $\mathbf{I} = (I, Q, U, V)^\dagger$, at five wavelength samples in less than one minute. In the following subsections we analyze the optical parts of the instrument.

2.2.1 Polarimetric analysis

Equipped with two ROCLIs and a linear polarizer, this instrument (as any other with equivalent optical configuration) will allow to measure the full Stokes

[1]We shall use the Spanish abreviation (Retardadores Ópticos de Cristal Líquido) rather than the English LCVRs.

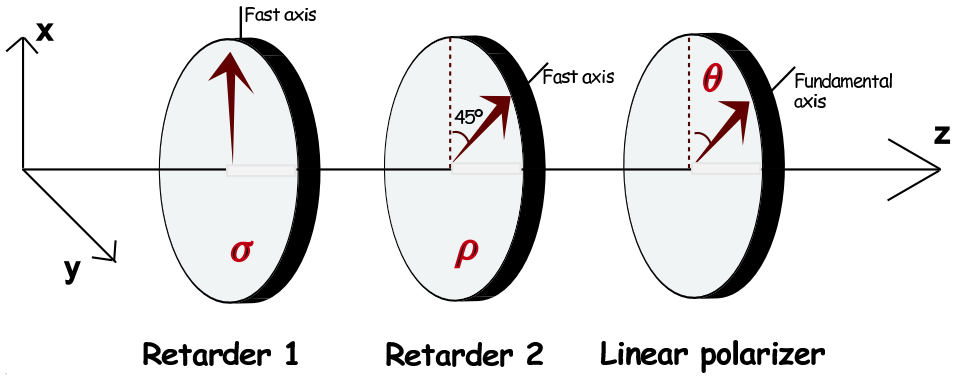

FIGURE 2.1:— Optical scheme for the IMaX polarization analysis.

vector. Figure 2.1 sketches an optical bench with these three devices. The fast axis of the first retarder is vertical while that for the second retarder forms an angle of 45º with the vertical direction. They introduce retardances of σ and ρ, respectively. At the exit of the two retarders there is a linear polarizer whose fundamental axis forms an angle θ with the vertical direction.

Following the same reasoning as in the previous section, we find that at the exit of the optical system the measured intensity is:

$$\begin{aligned} I_{\rm meas} &= \frac{1}{2}[I + Q\cos 2\theta\cos\sigma + U(\cos 2\theta\sin\sigma\sin\rho + \sin 2\theta\cos\rho) + \\ &\quad + V(\sin 2\theta\sin\rho - \cos 2\theta\sin\sigma\cos\rho)]\,. \end{aligned} \tag{2.11}$$

If the linear polarizer is a beam splitter, then at the exit we have two perpendicular light beams with orthogonal polarizations. Moreover, if the fundamental axis of the beam splitter is aligned with the vertical direction, hence parallel to the fast axis of the first retarder, then θ is 0º and 90º, respectively, for the two output beams. Finally, these output beams are measured by two different detectors. The measured intensities are nothing but linear combinations of the four Stokes parameters:

$$\begin{aligned} I_{\rm meas,1} &= \frac{1}{2}(I + Q\cos\sigma + U\sin\sigma\sin\rho - V\sin\sigma\cos\rho)\,, \\ I_{\rm meas,2} &= \frac{1}{2}(I - Q\cos\sigma - U\sin\sigma\sin\rho + V\sin\sigma\cos\rho)\,. \end{aligned} \tag{2.12}$$

To measure the four Stokes vector at least four different intensity modulations, I_i, are needed. This is achieved through changing the σ and ρ values by

simply modifying the applied voltages to the ROCLIs. Thus, assume that the following modulated measurements are recorded by the detectors:

$$\begin{aligned} I_1 &= I + \frac{1}{\sqrt{3}}Q + \frac{1}{\sqrt{3}}U + \frac{1}{\sqrt{3}}V, \\ I_2 &= I + \frac{1}{\sqrt{3}}Q - \frac{1}{\sqrt{3}}U - \frac{1}{\sqrt{3}}V, \\ I_3 &= I - \frac{1}{\sqrt{3}}Q - \frac{1}{\sqrt{3}}U + \frac{1}{\sqrt{3}}V, \\ I_4 &= I - \frac{1}{\sqrt{3}}Q + \frac{1}{\sqrt{3}}U - \frac{1}{\sqrt{3}}V. \end{aligned} \tag{2.13}$$

The four Stokes parameters are then derived from the four modulation states as

$$\begin{aligned} I &= \frac{1}{4}I_1 + \frac{1}{4}I_2 + \frac{1}{4}I_3 + \frac{1}{4}I_4, \\ Q &= \frac{\sqrt{3}}{4}I_1 + \frac{\sqrt{3}}{4}I_2 - \frac{\sqrt{3}}{4}I_3 - \frac{\sqrt{3}}{4}I_4, \\ U &= \frac{\sqrt{3}}{4}I_1 - \frac{\sqrt{3}}{4}I_2 - \frac{\sqrt{3}}{4}I_3 + \frac{\sqrt{3}}{4}I_4, \\ V &= \frac{\sqrt{3}}{4}I_1 - \frac{\sqrt{3}}{4}I_2 + \frac{\sqrt{3}}{4}I_3 - \frac{\sqrt{3}}{4}I_4. \end{aligned} \tag{2.14}$$

The σ and ρ parameters are suitably determined in order to maximize the efficiencies of the polarimeter (see del Toro Iniesta & Collados 2000). In fact, two independent determinations of $\mathbf{I}$ according to Eq. (2.13) are carried out, one with each of the two cameras of the instrument. This double determination helps increase the final signal to the noise (S/N) ratios of the observations.

2.2.2 Spectral modulation: Fabry-Pérot interferometers

In order to obtain 2D maps of the solar photosphere and at different wavelengths we need an optical device capable of sampling different wavelength points through a given spectral line. The chosen device for IMaX is a Fabry-Pérot interferometer. Such an interferometer is an optical instrument which uses multiple-beam interference. It is made up of two plane-parallel plates with a medium in between of a given refractive index. The light beam suffers multiple reflections within the two plates. As a consequence, the optical system has maximum transmission at some wavelengths. The distance between the two plane-parallel plates (and even the angle of attack) can be modified at will, thus changing the wavelength at which the transmission is maximum. As

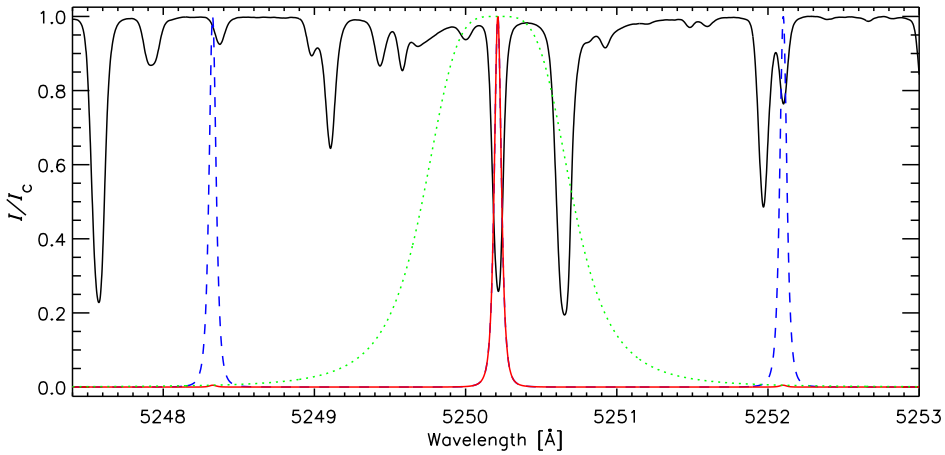

FIGURE 2.2:— FTS spectral atlas (black) around the 525.0 nm spectral region. Over-plotted is the IMaX transmission filter: the blue, dashed line represents the secondary transmission peaks of the Fabry-Pérot (not to scale) while the red, solid one shows the mean transmission peak. The green dotted line stands for the spectral shape of the pre-filter.

a result, this optical device allows the selection of different wavelength samples in a straightforward way, so a spectral line can be scanned. For further reading on how these optical systems work see e.g. Kentischer et al. (1998) and references therein. Fabry-Pérot interferometry is the most suitable way for simultaneous high-resolution imaging and spectroscopy.

The main transmission profile of a Fabry-Pérot is approximately given by a Lorentzian function. The full-width-at-half-maximum (FWHM) of this function characterizes the spectral resolution of the Fabry-Pérot. When more than a Fabry-Pérot is employed, the FWHM can be decreased, therefore increasing the spectral resolution of the instrument. The IMaX solution is a double passage through the same étalon. It is also important to reduce the amplitude of the secondary transmission peaks (Lorentzians as well) of the étalon. To this end, the system is also equipped with an interference pre-filter which opens a narrow spectral window. In Fig. 2.2 we represent the transmission function of the Fabry-Pérot over-plotted with a spectral region of ~ 6 Å from the NSO Fourier Transform Spectrometer atlas (Kurucz et al. 1984) centered at 525.0 nm. The dashed line represents the secondary peaks of the transmission filter while the dotted line the pre-filter. The amplitude of the secondary peaks is strongly reduced by the interference filter, thus minimizing their effect. Note that these secondary peaks should lie on continuum windows whereby minimizing (if not avoiding) spurious polarization signals since the continuum polarization level

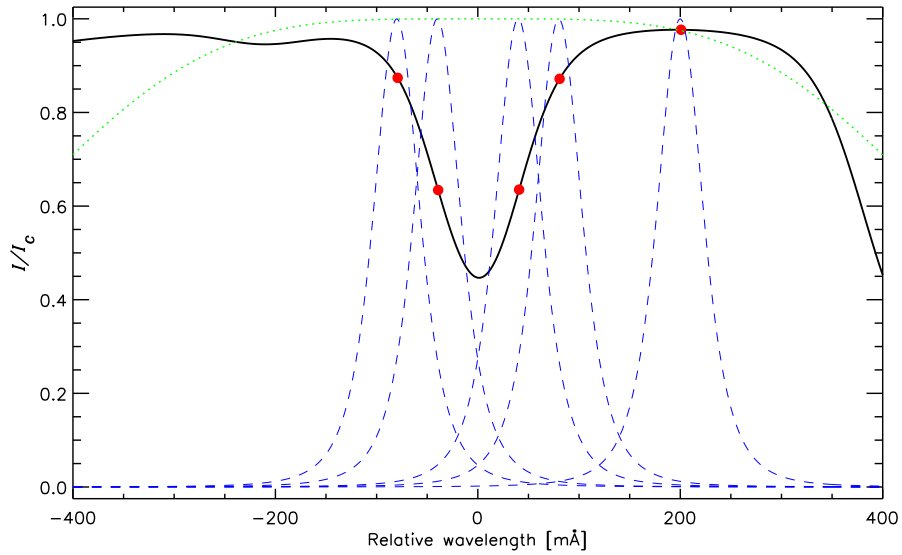

FIGURE 2.3:— Possible observed wavelength samples for the IMaX magnetograph. Wavelength samples are at [±80, ±40, 200] mÅ from the reference wavelength of the Fe I 525.02 nm spectral line. The green, dotted line stands for the pre-filter and the dashed ones for the Fabry-Pérot profile at the various sample wavelengths.

is smaller than the noise level of $10^{-3}I_c$. In the case illustrated in Fig. 2.2, the secondary peak locations coincide with various spectral lines. This should be avoided whenever possible.

Typical setups for Fabry-Pérot interferometers are collimated or telecentric mountings. For a number of reasons, the selected configuration for IMaX is collimated. This setup generates a wavelength blueshift across the field of view (FOV), but it provides a better spectral resolution and image quality than the telecentric configuration (Kentischer et al. 1998).

The polarimetric modulation analysis and the spectral analysis have to be performed in such a way that the whole process takes the shorter duration possible. Measurements should be carried out in a time shorter than the characteristic variation of solar structures. This is the main reason for limiting the number of wavelength samples that are measured. IMaX will observe five wavelength samples (four within the line plus one in the nearby continuum). To reach a S/N= $10^{-3}I_c$ in the continuum, a given set of measurements (e.g. five wavelengths times four polarization states) should be repeated a number of times, and the resulting images accumulated. Figure 2.3 illustrates how the Fabry-Pérot interferometer will scan the Fe I 525.02 nm spectral line. The

green, dotted line illustrates the pre-filter transmission. The blue, dashed lines show the Fabry-Pérot transmission curve tuned to the various wavelength samples. The final transmission is given by the product of the two functions. In this example we have taken the wavelength samples at [±80, ±40, 200] mÅ from the reference wavelength of the line. One of the questions we will be tackling in this thesis (Chapter 9) is whether it is possible (and to which extent) to infer the magnetic field vector and the flow velocity from a spectral line that has been scanned at only a few wavelength points.

2.3 Radiative transfer

In this section we discuss the basic concepts for the radiative transfer through magnetized atmospheres and introduce one of its multiple representations: the Milne-Eddington approximation.

The radiative transfer equation (hereafter referred to as RTE) for polarized light in a plane-parallel atmosphere reads

$$\frac{d\mathbf{I}}{d\tau} = \mathbf{K}(\mathbf{I} - \mathbf{S}), \tag{2.15}$$

where $\mathbf{I} = (I, Q, U, V)^\dagger$ stands for the Stokes vector which gives a full description of the polarization state of light, τ for the continuum optical depth at a reference wavelength, $\mathbf{K}$ for the 4x4 propagation matrix, $\mathbf{S}$ for the source function vector, and † means the transpose. All the medium properties relevant to line formation are contained in $\mathbf{K}$ and $\mathbf{S}$. In local thermodynamic equilibrium conditions (LTE) conditions, $\mathbf{S} = (B_\lambda(T), 0, 0, 0)^\dagger$, where $B_\lambda(T)$ is the Planck function at the local temperature T.

The propagation matrix $\mathbf{K}$ of the RTE can be cast in the form (e.g. del Toro Iniesta, 2003):

$$\mathbf{K} = \begin{pmatrix} \eta_I & \eta_Q & \eta_U & \eta_V \\ \eta_Q & \eta_I & \rho_V & -\rho_U \\ \eta_U & -\rho_V & \eta_I & \rho_Q \\ \eta_V & \rho_U & -\rho_Q & \eta_I \end{pmatrix}, \tag{2.16}$$

where

$$
\begin{aligned}
\eta_I &= 1 + \frac{\eta_0}{2}\left[\phi_p \sin^2\gamma + \frac{\phi_b+\phi_r}{2}(1+\cos^2\gamma)\right], \\
\eta_Q &= \frac{\eta_0}{2}\left[\phi_p - \frac{\phi_b+\phi_r}{2}\right]\sin^2\gamma\cos 2\chi, \\
\eta_U &= \frac{\eta_0}{2}\left[\phi_p - \frac{\phi_b+\phi_r}{2}\right]\sin^2\gamma\sin 2\chi, \\
\eta_V &= \frac{\eta_0}{2}\left[\phi_r - \phi_b\right]\cos\gamma, \\
\rho_Q &= \frac{\eta_0}{2}\left[\psi_p - \frac{\psi_b+\psi_r}{2}\right]\sin^2\gamma\cos 2\chi, \\
\rho_U &= \frac{\eta_0}{2}\left[\psi_p - \frac{\psi_b+\psi_r}{2}\right]\sin^2\gamma\sin 2\chi, \\
\rho_V &= \frac{\eta_0}{2}\left[\psi_r - \psi_b\right]\cos\gamma,
\end{aligned}
\tag{2.17}
$$

and $\phi_{p,b,r}$ and $\psi_{p,b,r}$ are the absorption and dispersion profiles, the p, b, r indices stand for the π and σ components of a Zeeman multiplet, and η_0 is the ratio between the line and continuum absorption coefficients.

$\phi_{p,b,r}$ and $\psi_{p,b,r}$ can be written as a sum of as many absorption and dispersion profiles as the number of p, b, r components as follows:

$$
\begin{aligned}
\phi_j &= \frac{1}{\sqrt{\pi}} \sum_{M_l - M_u = j} S_{M_l M_u, j} H(a, \upsilon), \\
\psi_j &= \frac{2}{\sqrt{\pi}} \sum_{M_l - M_u = j} S_{M_l M_u, j} F(a, \upsilon),
\end{aligned}
\tag{2.18}
$$

$S_{M_l M_u, j}$ being the strength of each component with $j = -1, 0, 1$ corresponding to b, p and r. υ stands for the wavelength shift in Doppler units:

$$
\upsilon = \frac{\lambda - \lambda_0}{\Delta\lambda_{\rm D}} + \frac{\Delta\lambda_{\rm B}}{\Delta\lambda_{\rm D}} - \frac{\lambda_0 \upsilon_{\rm LOS}}{c\Delta\lambda_{\rm D}}. \tag{2.19}
$$

$H(a, \upsilon)$ and $F(a, \upsilon)$ are the Voigt and Faraday-Voigt functions:

$$
H(a, \upsilon) = \frac{a}{\pi} \int_{-\infty}^{\infty} e^{-y^2} \frac{1}{(\upsilon - y)^2 + a^2} dy, \tag{2.20}
$$

$$
F(a, \upsilon) = \frac{1}{\pi} \int_{-\infty}^{\infty} e^{-y^2} \frac{\upsilon - y}{(\upsilon - y)^2 + a^2} dy. \tag{2.21}
$$

The wavelength shift of the different Zeeman components with respect to the original position is given by

$$\Delta\lambda_{\rm B} = \frac{e\lambda_0^2 B}{4\pi mc^2}(g_l M_l - g_u M_u), \tag{2.22}$$

where l and u stand for the lower and upper levels of the line transition, g for the level Landé factor, and M for the magnetic level quantum number; e and m are the electron charge and mass, and c is the speed of light. $v_{\rm LOS}$ is the plasma bulk velocity along the line of sight.

2.3.1 The Milne-Eddington approximation

In a Milne-Eddington (ME) model atmosphere, an analytical solution is found for the RTE (see, e.g. Unno 1956; Rachkovsky 1962, 1967; Landolfi & Landi Degl'Innocenti 1982). In such an atmosphere, all the atmospheric quantities are constant with depth except for the source function that varies linearly:

$$\mathbf{S} = \mathbf{S}_0 + \mathbf{S}_1\tau = (S_0 + S_1\tau)(1,0,0,0)^\dagger. \tag{2.23}$$

The propagation matrix is also constant with depth. Following, for instance, the notation in del Toro Iniesta (2003), such an analytical solution reads

$$\begin{aligned} I &= S_0 + \Delta^{-1}[\eta_I(\eta_I^2 + \rho_Q^2 + \rho_U^2 + \rho_V^2)]\, S_1, \\ Q &= -\Delta^{-1}[\eta_I^2\eta_Q + \eta_I(\eta_V\rho_U - \eta_U\rho_V) + \rho_Q\Pi]\, S_1, \\ U &= -\Delta^{-1}[\eta_I^2\eta_U + \eta_I(\eta_Q\rho_V - \eta_V\rho_Q) + \rho_U\Pi]\, S_1, \\ V &= -\Delta^{-1}[\eta_I^2\eta_V + \eta_I(\eta_U\rho_Q - \eta_Q\rho_U) + \rho_V\Pi]\, S_1, \end{aligned} \tag{2.24}$$

with

$$\Delta = \eta_I^2(\eta_I^2 - \eta_Q^2 - \eta_U^2 - \eta_V^2 + \rho_Q^2 + \rho_U^2 + \rho_V^2) - \Pi^2, \tag{2.25}$$

where

$$\Pi = \eta_Q\rho_Q + \eta_U\rho_U + \eta_V\rho_V. \tag{2.26}$$

It can easily be seen that η_I, η_Q, η_U, η_V, ρ_Q, ρ_U, and ρ_V, and hence the solution depend on just nine parameters, namely, on (B, γ, χ), the three components of the vector magnetic field, on S_0, S_1, the two parameters describing the source function, on η_0, the line-to-continuum absorption coefficient ratio, on $\Delta\lambda_{\rm D}$, the Doppler width of the line, on the damping parameter a, and on the line-of-sight velocity, $v_{\rm LOS}$.

3

ME response functions and their practical applications

In this chapter we introduce analytical response functions and their main properties as an important diagnostic tool that help understand Stokes profile formation physics and the meaning of well-known behaviors of Stokes inversion codes. We also show that response functions can be used to optimize the wavelength sampling of a line for better parameter diagnostics and to estimate the minimum variations of the model parameters that can be discriminated from noise.

3.1 Introduction

The adventure of diagnosing the solar atmosphere from spectropolarimetric observations is one of the most challenging subjects of modern solar physics. Both the theoretical understanding of the processes taking place in the photosphere and the design of new instrumentation can benefit from a thorough study of the radiative transfer equation (RTE) which is, in fact, the only tool we have to describe the problem mathematically. Approximations have been devised so far to tackle the tasks depending on both the observational and the *post-facto* computational capabilities. The Milne-Eddington (ME) approximation has provided for long a good means for gaining insight into the processes of line formation and for inferring the physical parameters of the solar atmosphere. Its analytical character implies a remarkable practical usefulness.

An analysis of the sensitivities of spectral lines in terms of analytic functions is still missing in the literature. It certainly would provide insights into how the solar parameters influence the shape of the polarization line profiles. It would also explain several (if not all) trade-offs and other well-known behaviors of inversion codes currently used to infer of such solar atmospheric parameters. Here we introduce the *analytic* response functions (RFs) of Stokes profiles as formed in ME model atmospheres and thoroughly discuss their main properties.

Weighting functions for unpolarized light (Mein 1971) were the precursors of RFs, extended to polarized light by Landi Degl'Innocenti & Landi Degl'Innocenti (1977). As explained by Ruiz Cobo & del Toro Iniesta (1994), RFs provide the sensitivities of Stokes profiles to the various atmospheric quantities playing a role in line formation. Since all these quantities are constant with depth in a ME atmosphere, ME RFs are simply partial derivatives of the analytic solution of the RTE with respect to the model parameters. This feature enables us to deduce analytic formulae for the sensitivities and to study their characteristics and properties. Such properties turn out to be useful for understanding the behavior of spectral lines as well as for helping in line and sample selection when designing new instruments.

In this Chapter we firstly introduce the concept of response functions in a Milne-Eddington atmosphere and present their analytical formulation. We then use a simple ME model atmosphere to discuss the main qualitative properties of the RFs through a prototypical spectral line (Sect. 3.2). The usefulness of the RFs for selecting the number and position of wavelength samples to be observed by vector magnetographs are discussed in Sect. 3.3. Their ability to estimate minimum detectable values of various model parameters is discussed in Sect. 3.4. Finally, we summarize our main conclusions in Sect. 3.5.

3.2 Response functions in a Milne Eddington atmosphere

3.2.1 Milne-Eddington response functions

According to Ruiz Cobo & del Toro Iniesta (1994) (see also del Toro Iniesta & Ruiz Cobo 1996; del Toro Iniesta 2003), the sensitivity of the Stokes profiles to perturbations of the atmospheric quantities is given by the response functions (RFs). These response functions can be written as:

$$\mathbf{R}_i(\tau_c) \equiv \mathbf{O}(0,\tau_c)\left[\mathbf{K}(\tau_c)\frac{\partial \mathbf{S}}{\partial x_i} - \frac{\partial \mathbf{K}}{\partial x_i}[\mathbf{I}(\tau_c) - \mathbf{S}(\tau_c)]\right], \tag{3.1}$$

with $\mathbf{O}(0,\tau_c)$ being the evolution operator from τ_c to the surface, $\mathbf{K}$ the propagation matrix and $\mathbf{S}$ the source function vector.

In the specific case of constant quantities with depth, as is the case of a ME atmosphere, such RFs are the partial derivatives of the Stokes vector with respect to the corresponding model parameter:

$$\mathbf{R}_x(\lambda) = \frac{\partial \mathbf{I}(\lambda)}{\partial x}, \tag{3.2}$$

where x represents any of the model parameters.

Therefore, by simply taking derivatives of the analytical solution (2.24), the sensitivities of the Stokes profiles to perturbations of the ME model parameters can be found (see Appendix A for explicit formulae). Note that these sensitivities are the only tools we have to evaluate our ability for determining the various quantities: should the Stokes vector not vary after a perturbation of a parameter, we would be unable to infer it from the observations.

3.2.2 Line sensitivities: the shape of RFs

Equations (2.24) and (3.2) provide all the necessary means for studying the behavior of the ME Stokes profiles. Fortunately, the shapes of RFs do not vary dramatically either from model to model or from line to line. In fact, the RFs look homologous to each other. This property allows us to choose a single line to illustrate the practical usefulness of our functions. Let us take the Fe I line at 525.064 nm as an example. We select this line because it is one of the candidate lines to be used by IMaX and some of the results may have implications either for the design or for the analysis of the data to be obtained with this magnetograph. The line has an effective Landé factor of 1.5 and is often considered to be quite insensitive to temperature perturbations (e.g., Stenflo et al. 1984). A single model is also enough to our purposes. To construct it we have inverted the intensity profile of the line in the quiet Sun, as given by the Fourier Transform Spectrometer atlas. The inversion yielded errors smaller than 2% (see Chapter 4 for further details about the inversion procedure). The resulting ME parameters are: $S_0 = 0.02$, $S_1 = 1$, $\eta_0 = 7.2$, $a = 0.3$, $\Delta\lambda_D = 30$ mÅ, and a macroturbulent velocity $v_{mac} = 0.37$ km/s. Unless otherwise stated, all the numerical examples that follow in this Chapter refer to this line and this model. Several magnetic field strengths (200, 800, 1400, and 2000 G) have been used to synthesize the Stokes profiles and their RFs, assuming a constant field inclination and azimuth of 45°.

Figure 3.1 shows the synthesized Stokes profiles. It can be seen how, as the magnetic field increases, the Stokes V lobes grow in amplitude but their peaks

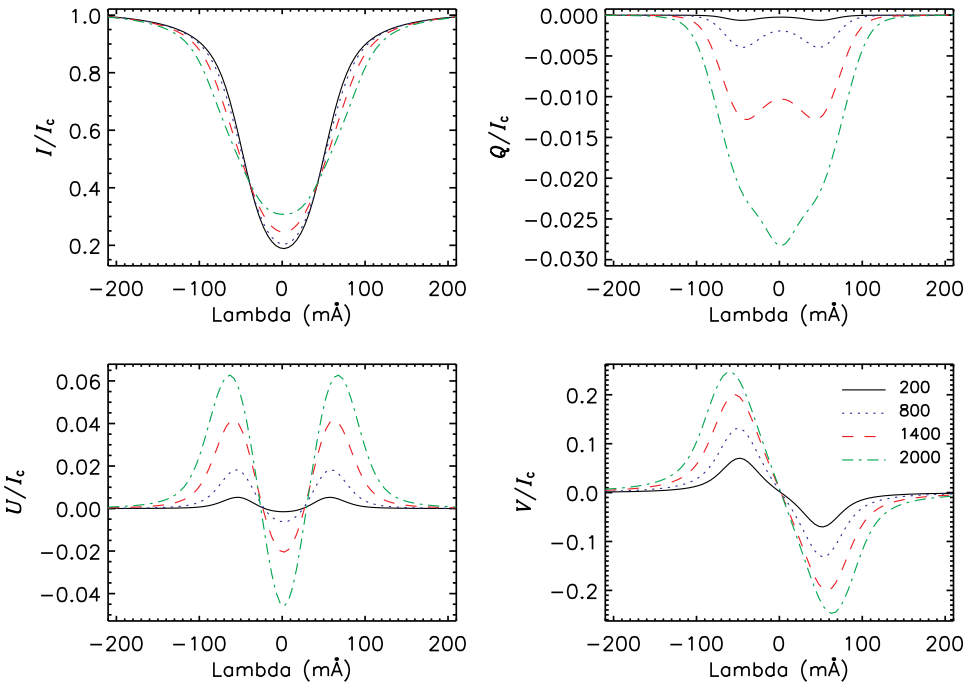

FIGURE 3.1:— Stokes I, Q, U and V profiles of the Fe I line at 525.06 nm, with a magnetic inclination and azimuth of 45°. Different lines stand for different magnetic field strength values. The Stokes parameters are normalized to the local continuum.

do not separate much because the strong field regime has not yet been reached with these strengths. In Figs. 3.2 and 3.3, we present the analytical RFs of the four Stokes parameters to magnetic field strength and velocity perturbations. By simply looking at these RFs, different properties can be drawn. Note that both the Stokes profiles and the RFs present wavelength symmetry properties, as expected from a ME model atmosphere. The RFs to the magnetic field strength preserve the Stokes profile symmetries whilst velocity RFs display opposite parity.

As can be seen in Fig. 3.2, the most evident property is that the response of the line is wavelength dependent. Different wavelength positions have different sensitivities. Within a single Stokes profile, different wavelength samples react differently to the same perturbation. Some of the samples, in fact, show little or no sensitivity to the atmospheric parameters. For instance, in this numerical example the Stokes V zero-crossing point remains the same independently of B and, hence, the response of V to B is zero at this wavelength. All the RFs

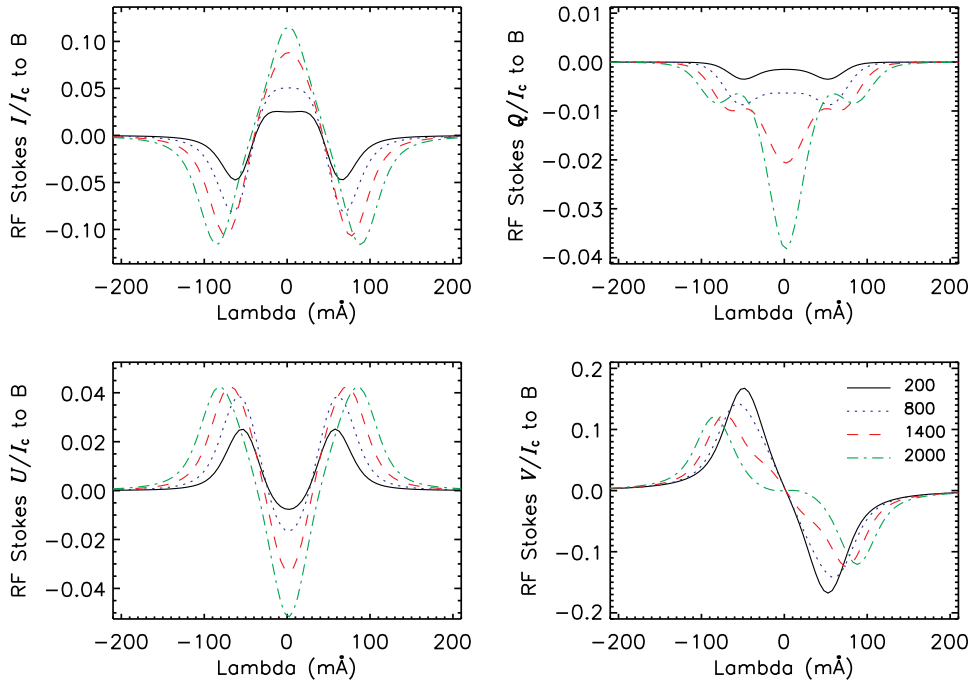

FIGURE 3.2:— Analytical ME RFs of Stokes I, Q, U and V to magnetic field strength for the Fe I line at 525.06 nm, with a magnetic inclination and azimuth of 45°. Different lines stand for different magnetic field strength values. Units are 10^{-3} G^{-1}.

show peaks corresponding to different maxima and minima. Note that these extrema pinpoint where the Stokes profiles are more sensitive to perturbations of the physical quantity: the bigger the peak, the larger the sensitivity.

Remarkably, although Stokes I, Q and U are more sensitive to B perturbations when the field is stronger, the Stokes V profile sensitivity to field strength perturbations is maximum for the weak fields and decreases while increasing the field strength. This effect can easily be understood: in the weak field regime, Stokes V is proportional to B and any change of B translates directly to an increase (or a decrease) of the V signal; when the field increases, however, a competition between increasing the profile and peak separation becomes important; finally, at a given B the peaks of V will no longer increase but will just separate from each other. This behavior is known for long but the Stokes V panel of Fig. 3.2 illustrates it in a very clear way. Moreover, the significant sensitivity of Stokes V in the weak field regime provides an argument to understand the reasonably accurate inversion results obtained in numerical

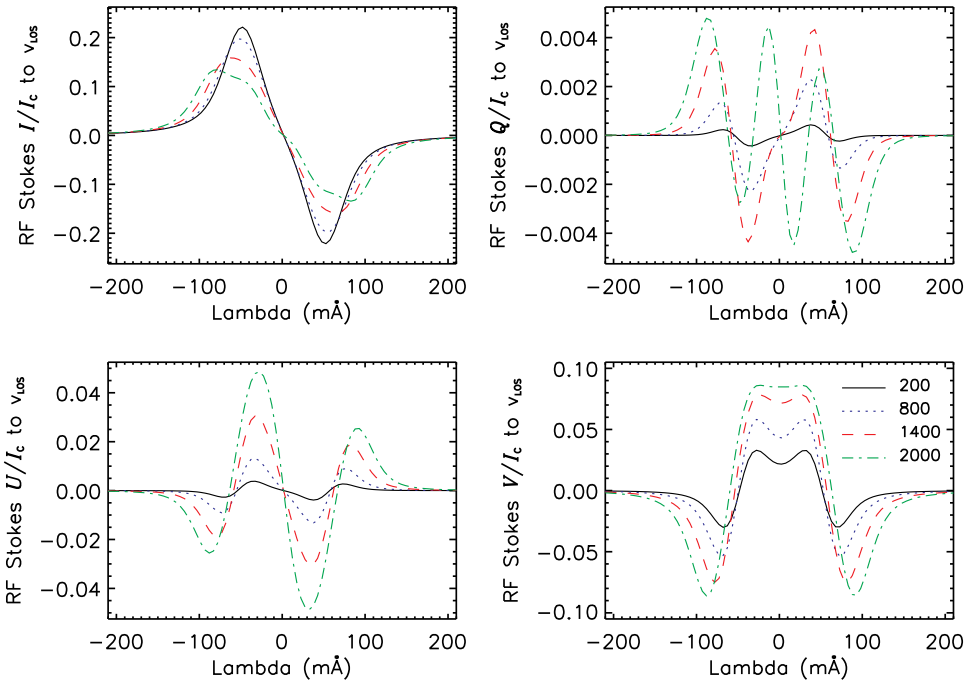

FIGURE 3.3:— Analytical ME RFs of Stokes I, Q, U and V to LOS velocity for the Fe I line at 525.06 nm, with a magnetic inclination and azimuth of 45°. Different lines stand for different magnetic field strength values. Units are $[\mathrm{km/s}]^{-1}$.

experiments by Westendorp Plaza et al. (1998).

Figure 3.3 shows the Stokes RFs to LOS velocity. The first clear feature in this figure is that neither the sizes nor the shapes depend on the velocity. The latter only shifts the RFs as it does with the profiles. The RF amplitude is larger for Stokes I and V than for Stokes Q and U, simply because of the corresponding profile amplitudes. Since Stokes I and V are larger than Stokes Q and U in this example, the velocity information is carried mainly by I and V. The LOS velocity can always be well determined because the loss of sensitivity to v_{LOS} of the Stokes I profile when the field strength increases is compensated by that of the V profile.

The Stokes I RF to LOS velocity decreases with B while the Stokes Q, U, and V RFs increase. This result is mostly due to the different shape ratios of the various profiles. According to Cabrera Solana, Bellot Rubio, and del Toro Iniesta (2005), the spectral line sensitivity to the LOS velocity is mostly determined by the ratio between the width and the depth of the line. It is

clear that the larger the field strength, the wider and shallower the Stokes I profile. Therefore, its sensitivity to $v_{\rm LOS}$ decreases with increasing B. Each lobe of Stokes V, however, first becomes bigger and then narrower and steeper at the central wavelength as B increases. Hence its larger sensitivity to $v_{\rm LOS}$ for stronger fields.

The relative maxima of the RFs to LOS velocity perturbations correspond to wavelength positions where the inflection points of the Stokes profiles are located, independently of the model atmosphere and spectral line. For instance, the minimum of Stokes I and the peaks of Stokes V correspond to zeros in the corresponding RFs to LOS velocity, and therefore they are regions where the Stokes profiles do not change even if LOS velocity does.

The extrema of the RFs to B and $v_{\rm LOS}$ do not coincide with those of the corresponding profiles. This fact can be clearly seen in, e.g., the bottom right panels of Figs. 3.2 and 3.3. Therefore, the extrema of the Stokes profiles are not carrying, in principle, more information on given parameters than other wavelength samples. Another very interesting feature is that, for a given spectral line, the RFs differ from each other: RFs to magnetic field strength perturbations do not resemble those to LOS velocity perturbations (compare Figs. 3.2 and 3.3). For instance, their maximum sensitivities (RF peaks) are placed at different wavelengths. These differences among RFs help disentangle the influences on spectral line formation of the various atmospheric parameters and, allow inversion algorithms based on RFs to get accurate results: if a given Stokes profile is useless at a particular wavelength sample, other profile or wavelength sample provides the required information. Differences between RFs can also be seen for the other ME parameters except for $\Delta\lambda_{\rm D}$, η_0 and a. The RFs to these thermodynamic parameters are very similar to each other as can be seen in Fig. 3.4. A small perturbation of any of these three parameters produces a modification in the Stokes profiles that is very similar to the changes produced by small perturbations of the other two. These similarities between the $\Delta\lambda_{\rm D}$, η_0 and a RFs explain the trade-offs often observed in ME inversions among them. Fortunately, their RFs are different enough from those of the other model parameters as for them to be accurately retrieved (see, e.g., Westendorp Plaza et al. 1998). In other words, we can say that the ME model atmosphere, although providing a probably too simplistic scenario for the line formation which may not give full account of thermodynamic properties, allows fairly accurate inferences of the constant magnetic field vector $\mathbf{B}$ and line-of-sight velocity.

The RFs to magnetic field inclination and azimuth perturbations do not depend on the derivatives of the absorption and dispersion profiles; thus, the shapes of the RFs are very similar to the corresponding Stokes profiles (see

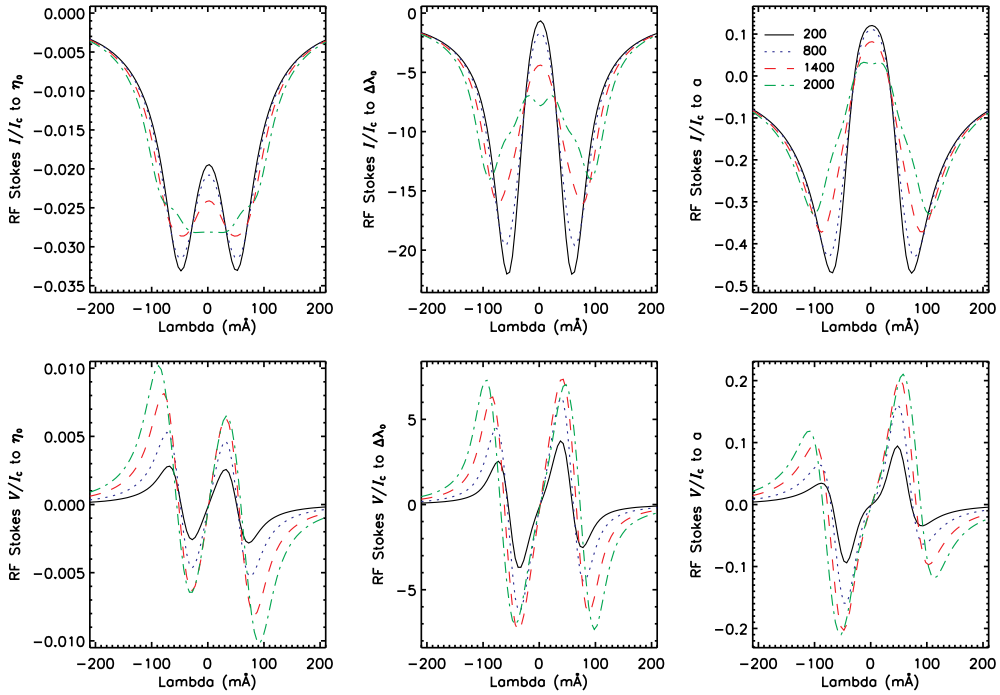

FIGURE 3.4:— Analytical ME RFs of Stokes I (upper panels) and V (bottom panels) to η_0, to $\Delta\lambda_D$ and to a (left, middle and right panels respectively), for the Fe I line at 525.06 nm, with a magnetic inclination and azimuth of 45°. Different lines stand for different magnetic field strengths. Units are none for the left and right panels since η_0 and a are dimensionless. Units for the middle panels are Å^{-1}. Note the similarities among the different RFs.

Fig. 3.5). Of course, only Stokes Q and U respond to azimuth perturbations. The stronger the field, the larger the sensitivity of the Stokes profiles to γ and χ perturbations. This again reflects a well known fact: we measure γ and χ better when B is strong.

3.2.3 Relative response functions

So far we have only discussed "absolute" RFs, i.e., functions with dimensions; for example, the RF to B is measured in G^{-1}, that to v_{LOS} is measured in $(\text{km s}^{-1})^{-1}$, and so on: RFs give modifications of the profile per unit perturbation of the parameter. To compare them to one another, relative RFs should be used (Ruiz Cobo & del Toro Iniesta 1994; del Toro Iniesta & Ruiz Cobo 1996). These ME relative responses are obtained by multiplying the standard RFs by the corresponding model parameter. Relative RFs tell us how much sensitive

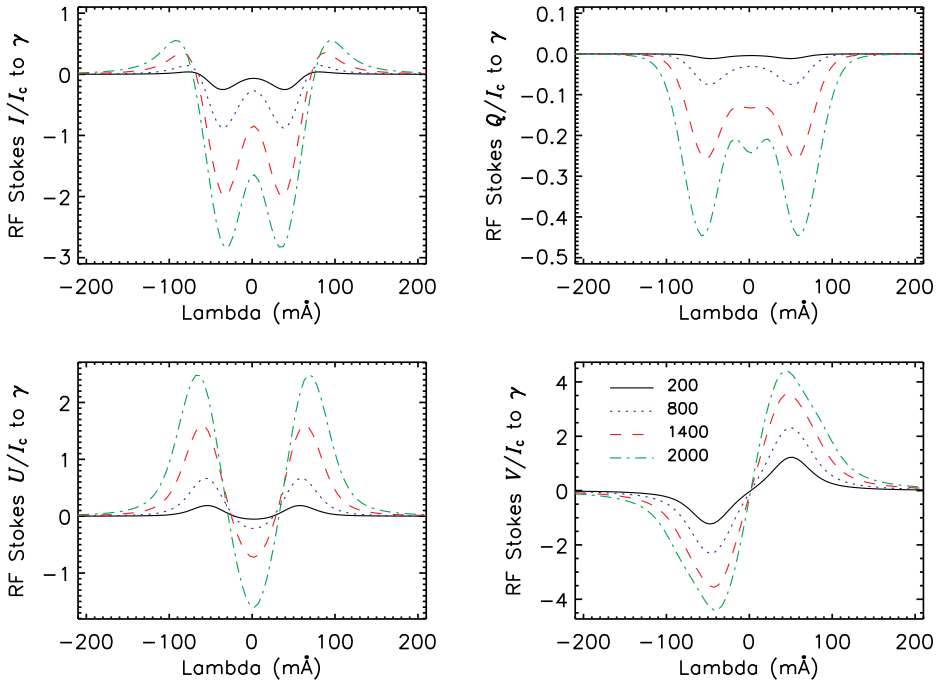

FIGURE 3.5:— Analytical ME RFs of Stokes I, Q, U and V to magnetic field inclination, γ, for the Fe I line at 525.06 nm, with a magnetic inclination and azimuth of 45°. Different lines stand for different magnetic field strengths. Units are 10^{-3} [degree]$^{-1}$.

one model parameter is compared with the others. For instance, the relative RF to $\Delta\lambda_D$ is much larger than that to η_0 and that to a (in particular three times as large as the RFs to η_0 and twenty times larger than those to a for Stokes I, in our sample ME atmosphere). This means that a small relative perturbation of $\Delta\lambda_D$ changes the Stokes profiles much more efficiently than the same relative perturbation of η_0 or a. Consequently, $\Delta\lambda_D$ should be better determined by ME inversion codes.

3.2.4 Two-component model atmospheres

Model atmospheres with two or more components are commonly used in the analysis of observations. Any two-component model atmosphere is based on the assumption that within the resolution element two different atmospheres coexist, namely, one magnetic atmosphere filling a surface fraction f, and one non-magnetic atmosphere in the remaining $(1 - f)$ fraction. f is called the

magnetic filling factor. If $\mathbf{I}_{\rm m}$ stands for the Stokes profile vector emerging from the magnetic region and $\mathbf{I}_{\rm nm}$ for that of the non-magnetized atmosphere, the observed Stokes vector can be written as $\mathbf{I} = (1-f)\mathbf{I}_{\rm nm} + f\mathbf{I}_{\rm m}$.

Thus, according to Eq. (3.2), the RFs to f perturbations are given by $\mathbf{I}_{\rm m} - \mathbf{I}_{\rm nm}$. Hence, the larger the difference between the magnetic and the non-magnetic atmospheres, the bigger the sensitivity to f. But this is once more a known fact: since most of the differences is the polarization signal itself, $Q_{\rm m}$, $U_{\rm m}$, $V_{\rm m}$, when this signal is strong we can easily discern it from the non-magnetic signal.

3.2.5 The influence of spectral smearing

Spectral smearing by macroturbulence is a well known effect that needs to be taken into account in the analysis of most observations except, perhaps, in those with very high spatial resolution (Asplund et al. 2000). Besides macroturbulence, instruments have finite-width profiles that produce smearing of the observed Stokes spectra which become wider and weaker. This smearing reduces the information on physical parameters carried by the spectral line through convolution: $\mathbf{I}_{\rm obs} = \mathbf{I} * F(\lambda)$, where the scalar smearing profile, $F(\lambda)$, is convolved with all the four Stokes parameters.

This loss of information through smearing also translates into a loss of sensitivity to the atmospheric quantities. In fact, since the derivative of a convolution is equal to the convolution of the derivative of one of the functions with the second, response functions become smeared as well:

$$\mathbf{R}_{{\rm obs},x} = \mathbf{R}_x * F(\lambda). \tag{3.3}$$

Figure 3.6 shows the effect of RF smearing. The convolved RFs are smoother and some information is lost.

3.3 The usefulness of the RFs for designing instruments

Modern vector magnetographs are not restricted to one or two wavelength samples as the classical ones. Instruments like IMaX are devised to measure five or more wavelengths: one in the continuum and four across the line profile. The choices of spectral line, number of samples and their precise wavelengths are important issues that arise during the design phase of the instrument. This section illustrates how RFs can help make such decisions.

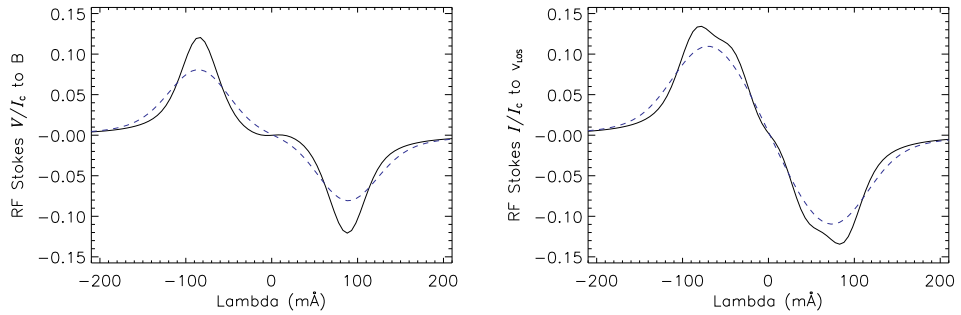

FIGURE 3.6:— Analytical ME RFs of Stokes V to the magnetic field strength (left panel) and of Stokes I to the LOS velocity (right panel) for the Fe I line at 525.06 nm, with a magnetic field strength of 2000 G and field inclination and azimuth of 45°. The dashed lines correspond to the RFs convolved with a Gaussian smearing profile of 60 mÅ of full width at half maximum. Solid lines correspond to the original RFs. Units are in 10^{-3} G^{-1} (left) and $[km/s]^{-1}$ (right).

Finding a suitable spectral line is crucial and can be achieved through RFs using the simple phenomenological model by Cabrera Solana et al. (2005) that allows establishing a ranking of sensitivities to the different atmospheric parameters among the various lines considered. The IMaX Fe I 525.064 nm[1] line can be seen in Figs. 3.7 and 3.8. Data for this line have been included in the original figure by Cabrera Solana et al. (2005), where it is identified as one of the most sensitive of the set to velocity perturbations. It has a medium sensitivity to magnetic field strength perturbations in both the strong and the weak field regimes. However, it is not very sensitive to temperature (not shown) and, therefore, a good candidate for inferences in different solar structures avoiding thermodynamical trade-offs. The Helioseismic and Magnetic Imager (HMI; Scherrer & SDO/HMI Team 2002) and the Polarimetric and Helioseismic Imager (PHI, a proposal for the Visible-light Imager and Magnetograph; Marsch et al. 2005), planned instruments for the NASA *Solar Dynamics Observatory*, and the ESA/NASA *Solar Orbiter*, missions respectively, will use the Fe I line at 617.334 nm. This spectral line is very well ranked in Figs. 3.7 and 3.8 for inferences of magnetic field strengths and LOS velocities.

A minimum number of wavelength samples is obtained by roughly doubling the free parameters of the model: since a ME model is made up with just ten parameters, a minimum of twenty observables (five wavelength times the four

[1]This line was the principal candidate to be observed with the IMaX instrument. By the time of this thesis, the line has been changed to its neighbor Fe I line at 525.02 nm. The analysis in this section is straightforwardly applicable to other lines.

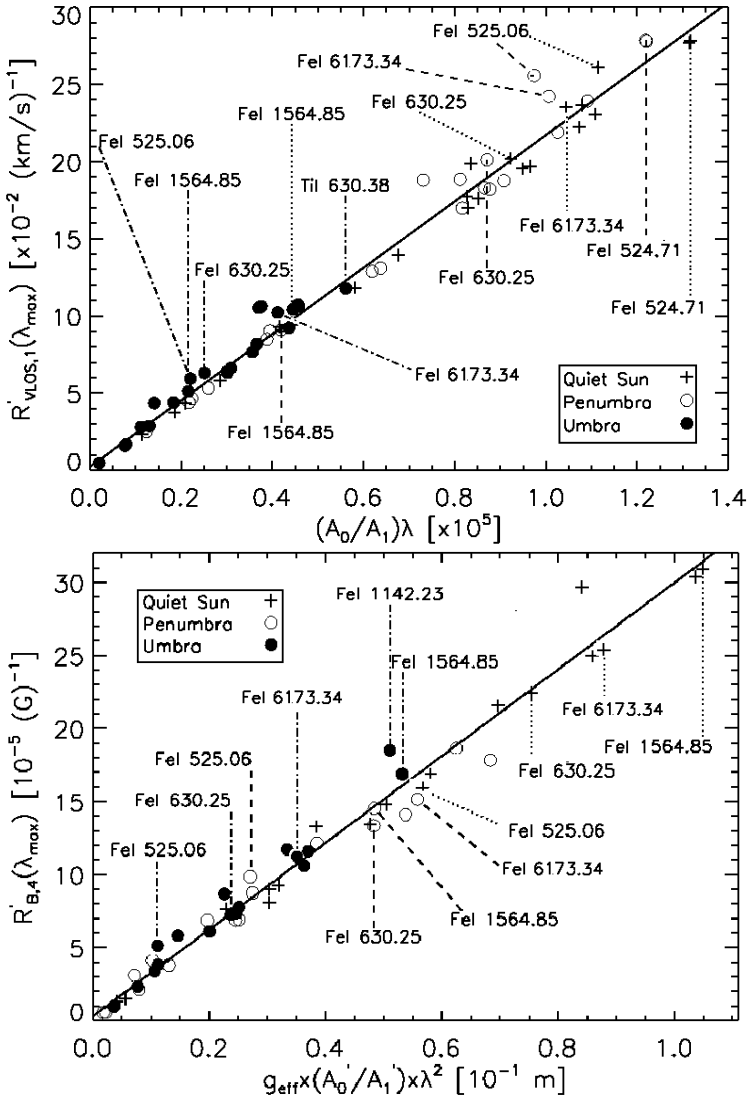

FIGURE 3.7:— Top: Maximum value of the integrated RF to $v_{\rm LOS}$ for different lines as a function of the shape ratio multiplied by the central wavelength of the transition. Bottom: Maximum values of the integrated RF to B for the same set of lines with $g_{\rm eff} \neq 0$, as a function of the shape ratio multiplied by the squared central wavelength (strong field regime). The sensitivities have been evaluated in the quiet Sun (crosses), penumbral (circles) and hot umbral (filled circles) model atmospheres. Dotted, dashed, and dash-dotted lines mark specific transitions in the quiet sun, penumbral, and umbral models, respectively. Adapted from Cabrera Solana et al. (2005).

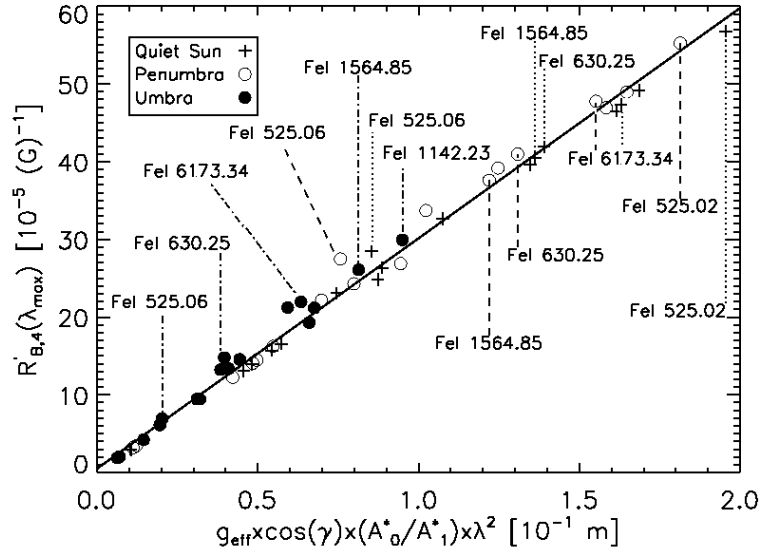

FIGURE 3.8:— Same as Fig. 3.7 but for the maximum values of the integrated RF to B (weak field regime).

Stokes parameters) is needed. This is the choice for all the three instruments mentioned above. Unfortunately, no purely objective means exist to select the wavelengths for the samples. Nevertheless, RFs are a powerful tool to select wavelengths that better suit our purposes. If one is interested, for instance, in just the magnetic field strength and neglect the other physical quantities, choosing those wavelengths where the RFs to B reach local maxima would be advisable. If the interest lies in several physical quantities at the same time (e.g. the three components of the magnetic field and the LOS velocity) we suggest the use of a linear combination of regular RFs weighted according to the specific interests. In fact, since RFs can be positive or negative, we propose the use of absolute-valued RFs. Hence, we suggest to consider

$$\mathcal{R}_j = \sum_i \beta_i \, |R_{j,i}|, \tag{3.4}$$

where j runs from 1 through 4, corresponding to the four Stokes parameters, and index i accounts for the physical parameters. Since the set of weights β_i can be tailored at will, there is no single choice for samples but an examination of $\mathcal{R}$ provides important hints for the selection. As an example, Fig. 3.9 shows different such linear combinations for the IMaX line case. If index i runs from 1 through 4 standing for B, γ, χ, and $v_{\rm LOS}$, respectively, the plotted curves correspond to $\beta_{1,2,3,4} = 1, 1, 1, 1$ (black lines), $\beta_{1,2,3,4} = 2, 2, 2, 0.5$ (blue lines),

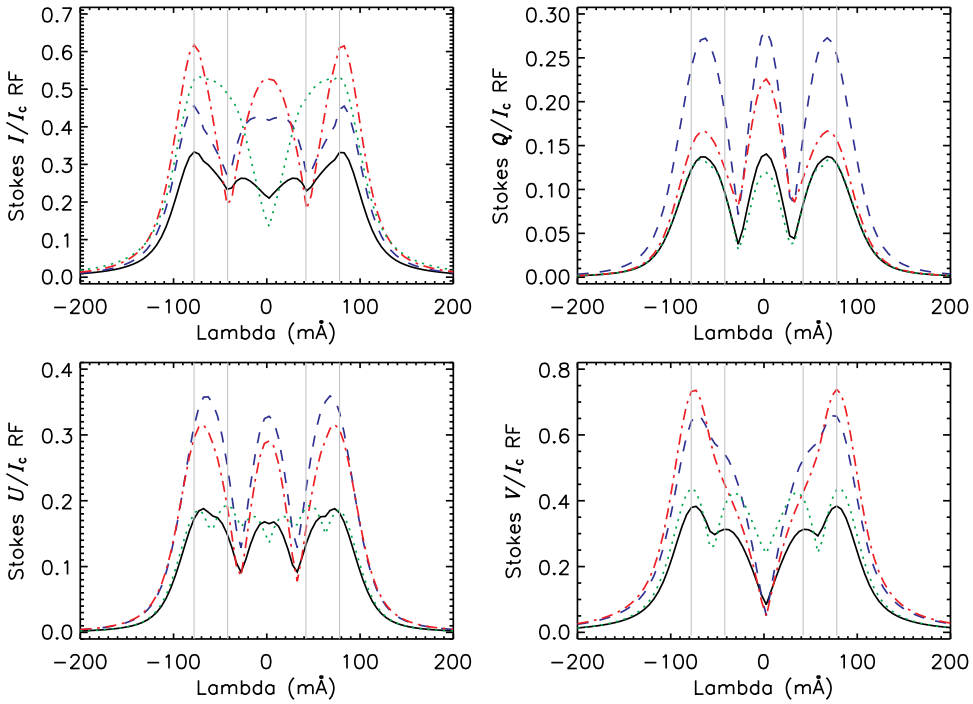

FIGURE 3.9:— Four different linear combinations of the Stokes vector RFs for the IMaX line. The plotted curves correspond to $\beta_{1,2,3,4} = 1, 1, 1, 1$ (solid, black lines), $\beta_{1,2,3,4} = 2, 2, 2, 0.5$ (dashed, blue lines), $\beta_{1,2,3,4} = 3, 1, 1, 0.5$ (dashed-dotted, red lines), and $\beta_{1,2,3,4} = 0.5, 1, 1, 3$ (dotted, green lines). The light-grey, vertical lines indicate a possible choice for wavelength sampling ($\pm 42, 78$ mÅ).

$\beta_{1,2,3,4} = 3, 1, 1, 0.5$ (red lines), and $\beta_{1,2,3,4} = 0.5, 1, 1, 3$ (green lines). The vertical lines indicate a possible choice for wavelength sampling ($\pm 42, 78$ mÅ), selected mostly from the properties of the Stokes I and V RFs since these two parameters usually exhibit the largest signals in solar atmospheres. While the most external samples seem to be quite optimum, some other good choices for the inner wavelengths are possible and up to the user.

3.3.1 Noise and inference accuracy

Stokes profiles are affected by the intrinsic noise of the observational process. Should the polarization signal be buried in the noise, any algorithm one could devise to determine atmospheric quantities would dramatically fail. Therefore, our abilities to infer accurate solar parameters depend significantly on the signal-to-noise ratio of the observations.

Response functions can help quantify this effect. In fact, since RFs simply provide the modification of the Stokes profiles after a perturbation of the physical quantities, if that modification is smaller than the noise level it will be effectively undetectable. In other words, the size of RFs to perturbations of a given quantity sets a threshold for the detection of a unit of such a quantity. For instance, according to Fig. 3.2, 1 G will only be detectable by a single wavelength sample if noise is below 1.5×10^{-4} (continuum intensity is at 1); within the linear approximation[2], 10 G will be detectable with a noise below 1.5×10^{-3} and so on.

In any case, what matters is the whole profile (or the whole set of samples). Single sample determinations will certainly be less accurate. In what follows we provide an estimate on how noise influences the accuracy in parameter determination.

Assume that all inaccuracies in the m physical parameters contribute in a similar amount to the final noise. (In reality, our assumption is that noise imparts equally distributed inaccuracies to the m parameters that are sought). In such a case, the variance of the j wavelength sample in the i-th Stokes parameter[3] can be written as

$$\sigma_{i,j}^2 = mf^2(R_{i,j}^x)^2\sigma_x^2, \tag{3.5}$$

where f stands for the magnetic filling factor, $R_{i,j}^x$ is the RF of Stokes i at wavelength j to perturbations of the x model parameter, and σ_x^2 is the variance of that parameter. Summing up for all Stokes parameters and wavelengths, Eq. (3.5) becomes

$$\sum_{i=1}^{4}\sum_{j=1}^{n_\lambda}\sigma_{i,j}^2 = mf^2\sigma_x^2\sum_{i=1}^{4}\sum_{j=1}^{n_\lambda}(R_{i,j}^x)^2, \tag{3.6}$$

where n_λ is the number of wavelength samples.

According to del Toro Iniesta & Collados (2000), if all the modulated measurements (n_p) needed to derive the Stokes parameters have the same variance, σ^2, due, for instance, to photon noise, then

$$\sigma_{i,j}^2 = \frac{1}{n_p}\frac{\sigma^2}{\epsilon_i^2}, \forall j = 1,\ldots,n_\lambda, \tag{3.7}$$

where ϵ_i is the polarimetric efficiency of the i-th Stokes parameter.

[2]RFs come in fact from a linear perturbation analysis of the radiative transfer equation

[3]Index i runs from 1 through 4, corresponding to Stokes I, Q, U, and V, respectively.

Using Eq. (3.7), the inaccuracy of the x parameter can finally be written as

$$\sigma_x = \frac{\sqrt{n_\lambda \sum_{i=1}^{4} (1/\epsilon_i^2)}\,\sigma}{f\sqrt{n_p m}\sqrt{\sum_{i=1}^{4}\sum_{j=1}^{n_\lambda} (R^x_{i,j})^2}}. \tag{3.8}$$

The above formula gives an estimate for the noise-induced, i.e. random, effects and no systematic errors are included. It illustrates very well how the noise on the polarization measurement influences directly the accuracy of any inferred parameter. Obviously, the better the polarimetric efficiencies of the instrument, the smaller the inaccuracies. That is also the case for RFs: the larger the RFs, the smaller the value of σ_x.

Finally, notice that this representation holds when dealing with Stokes profiles that can be satisfactorily represented with ME models. In any other case, it simply represents *minimum* errors.

3.3.2 Practical examples

As a practical example, let us consider the wavelengths proposed in Sect. 3.3 for IMaX, i.e., four wavelength samples across the line plus one in the continuum [±78, ±42, 300] mÅ. Let us assume an instrumental smearing of FWHM 60 mÅ described by a Gaussian function and a noise level $\sigma = 10^{-3} I_c$. By appropriately substituting the values of the RFs in Eq. (3.8), and assuming $m = 9$ and $f = 1$, we can evaluate the minimum detectable values for the model parameters. Figure 3.10 illustrates the results of such a numerical experiment for the magnetic field strength, inclination and azimuth, and for the LOS velocity, as a function of the magnetic field strength. Different colors stand for three different configurations of the magnetic field vector. The solid and dashed lines stand for the two Fe I lines of the 525.0 nm spectral region. For both lines, the ME model parameter characterizing them have been obtained by fitting the FTS quiet-Sun line profiles.

The figure indicates that spectropolarimetic observations in these lines would yield errors that are of the order of 4 to 10 G for the magnetic field strength and 5.5 to 10 m s^{-1} for the LOS velocity, depending on the spectral line and on the magnetic field configuration.

Also, the results show the dissimilar sensitivities of the two lines to magnetic fields and velocity perturbations. For instance, the 525.02 nm spectral line has larger sensitivity to the magnetic field vector than the 525.06 nm line and provides more accurate magnetic field strength, inclination and azimuth values.

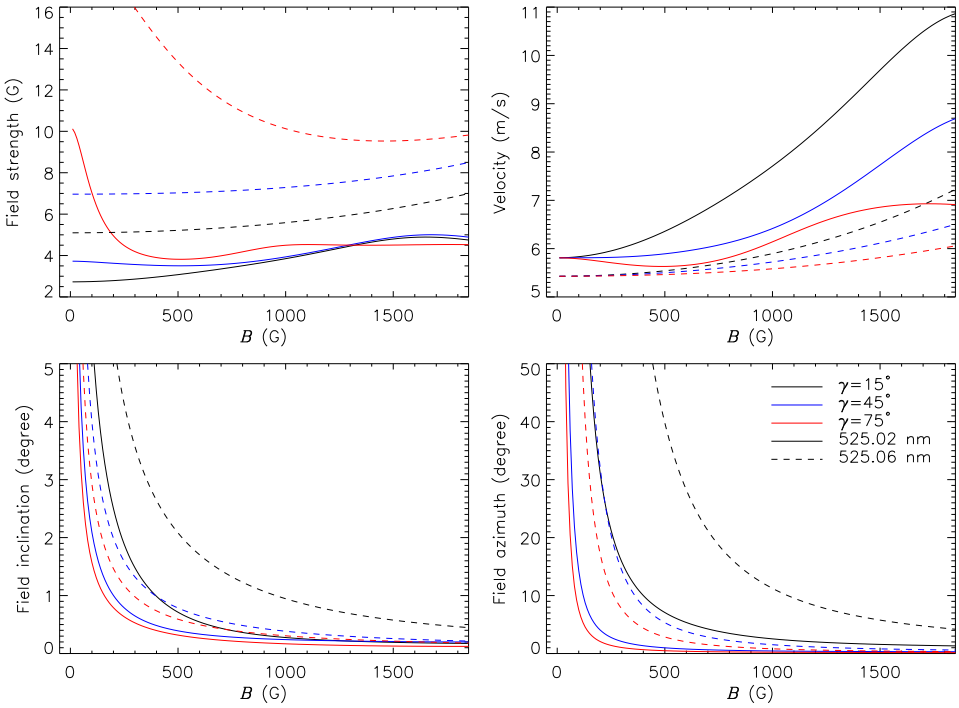

FIGURE 3.10:— Minimum detectable magnetic field strength, field inclination and azimuth, and LOS velocity as a function of the magnetic field strength. Different line shapes stand for two different spectral lines.

In both lines, the uncertainties in the field strength increase for weaker fields. This increase is larger for Fe I 525.06 nm. The same holds for the magnetic field inclination and azimuth. Contrary to that, the 525.06 nm spectral line has larger sensitivity to velocity perturbations. The uncertainties for the LOS velocity increase for larger field strengths.

The overall increase in the $v_{\rm LOS}$ uncertainty with field strength takes place because spectral lines become broader as the strength grows. It is not so easy to understand the slight but appreciable increase of σ_B with B. The behavior of the inclination and filling factors are supposed to be more natural: determinations are better when B is strong. Nevertheless, as we advanced in the previous section, it is the effect of all the four Stokes profiles that is relevant to the final inference; arguments based on just one Stokes parameter may fail.

In the test, f has been set to unity. Therefore these calculations apply to very high spatial resolution observations, where the magnetic field occupies the whole resolution element. It is noteworthy how the accuracy in each parameter

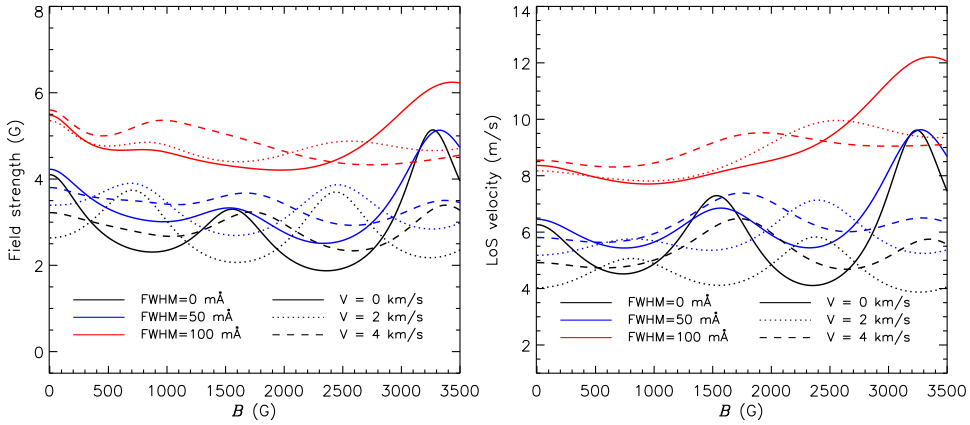

FIGURE 3.11:— Minimum detectable magnetic field strength and LOS velocity as a function of the magnetic field strength for the PHI instrument. Different line shapes stand for three different velocity shifts of the plasma and colors stand for different smearing filter widths.

is inversely proportional to the magnetic filling factor, according to Eq. (3.8). Hence, the ordinate scale of the figure should be multiplied by 10 if $f = 0.1$. In such a case, and even in the eventual assumption that our estimates are wrong by 100%, the expected uncertainties support the fact that strong and weak fields can be distinguished when observed with modern instruments and interpreted with modern inversion techniques. We also caution that this analysis is valid as long as statistical errors are concerned. We have not included any systhematic error, apart from those associated with the limited wavelength sampling and spectral purity.

In any case, Eq. (3.8) allows us to test the sensitivities of spectral lines to various physical parameters and to evaluate how these sensitivities vary with the instrumental approach. For instance, it helps in determining the effects of the instrumental filter width in the inferences. To illustrate this we resort to the HMI and PHI instruments. Both will observe the 617.3 nm spectral line at 6 wavelength positions across the line, say at -78, -42, 0, 42, 78 and 300 mÅ from line center. We can solve Eq. (3.8) for this spectral line and check the dependencies of the inferences on the instrument configuration. Let us take three different instrumental filter widths and bulk velocities. f is set to unity. Then, Eq. (3.8) provides us with the minimum detectable magnetic field strengths and LOS velocities as a function of the magnetic field strength (Fig. 3.11).

It is noticeable that the various curves show significant periodic variations. These are explained by the fact that we are sampling the spectral line at only

few wavelength positions. The maximum sensitivities of the different model parameters pinpoint wavelengths (see e.g., Fig. 3.9) whose location change with the magnetic field strength and velocity. Notice that the curves representing different bulk velocities have essentially the same shape. Notice as well that the broader the filter the smoother the different curves. As we mentioned in Sect. 3.2.5, the instrumental smearing affects the RFs through convolution; therefore we expect RFs smaller in amplitude and broader.

3.4 Conclusions

Many interesting features of analytic response functions have been discussed in this Chapter by considering the specific case of a ME model atmosphere. Since an analytic solution for the radiative transfer equation is available for this atmosphere, the sensitivities of spectral lines, as described by RFs, can also be expressed in analytical form by simply taking partial derivatives of such a solution with respect to the model parameters. The analytic ME solution has been thoroughly used in the past to gain insight into the physics of radiative transfer and as a purely practical diagnostic tool for ME inversion codes. Likewise, we have shown that the analytic ME RFs are useful to better understand spectral line formation and the behavior of Stokes profiles in different conditions and also to get practical recipes that can help in selecting spectral lines for given purposes, in selecting wavelength samples, etc.

A summary of the various results obtained follows:

1. Response functions look homologous to each other, enabling qualitative general discussions by considering a single spectral line in a specific model atmosphere. Here, we have targeted the Fe I line at 525.06 nm in a ME model representative of the quiet Sun thermodynamics (as observed with the FTS) and with various vector magnetic fields and LOS velocities.

2. The sensitivities of spectral lines to the various parameters depend on wavelength: some samples are better suited to diagnose one given parameter or another; some wavelengths are even insensitive to given parameters. The RF extrema show trivially those wavelengths were sensitivity is maximum.

3. As expected in ME conditions where no gradient of LOS velocity is present, RFs display wavelength symmetry properties. The RFs to magnetic field strength perturbations show similar parity as the Stokes profiles while the RFs to LOS velocity perturbations are of opposite parity.

4. Stokes V sensitivities to B perturbations are significant for very weak fields. This fact explains the reasonably accurate results of ME inversions in this regime.

5. The shape of the RFs to LOS velocity perturbations does not depend on $v_{\rm LOS}$ except for the Doppler shift. Variations of sensitivity of the Stokes I and V profiles due to the magnetic field strength are compensated: when the velocity information decreases in Stokes I for increasing field strengths, it increases in Stokes V, so that $v_{\rm LOS}$ remains well inferred in any circumstance.

6. We understand the trade-offs often found among ME thermodynamic parameters in the inversion results: their corresponding RFs are very similar to each other. Fortunately, these RFs are neatly different from the other RFs, which make it possible to accurately infer vector magnetic fields and LOS velocities. Among the thermodynamic parameters, the relative sensitivity to $\Delta\lambda_D$ perturbations is larger than that to η_0 and a, thus enabling better inferences.

7. Response functions can be used to select spectral lines for given purposes or for given measurements. Moreover, a suitable combination of RFs provide quantitative arguments for wavelength sample choice.

8. It is possible to analytically evaluate the minimum detectable values for each of the model parameters by suitably re-writing the variances. The results provided us with *a-priory* estimations of affordable errors for different model parameters and with useful hints to select a suitable spectral line, given the design of the instrument.

4

The inference of physical quantities: inversion methods

This Chapter aims at introducing a family of available techniques to extract the atmospheric parameters encoded in polarized spectra: the inversion methods of the RTE. In particular, we discuss the capabilities and disadvantages of inversion codes based on the Levenberg-Marquardt algorithm, with especial interest on those based on the Milne-Eddington solution to the RTE.

4.1 Introduction

The fundamental goal in solar physics is the derivation of the physical variables that characterize the processes taking place in the solar atmosphere. Extracting the information about the magnetic, dynamic and thermal properties of the media from the observed Stokes profiles is not a straightforward task, though. The data do not only contain information about the plasma properties, but are also affected by the way we measure them. Therefore, in the selection of specific diagnostics to infer the desired information, we have to make sure that the observables are able to disentangle the searched-for physical variables from all the effects that degrade the data.

Fortunately, the Stokes profiles that emerge from the solar atmosphere and that we measure are well described by the RTE for polarized light. This equation shows us how the Stokes profiles depend on the physical conditions of the atmosphere, i.e., on the prevailing thermodynamic equilibrium, on the temper-

ature, on the electronic pressure, on the plasma velocity, on the magnetic field strength, inclination and azimuth, and on the abundance and other atomic parameters of the various chemical species. They depend on the line-of-sight stratification of these physical parameters as well.

To infer the different physical quantities, with special interest on the magnetic field vector and plasma velocity, a variety of techniques have been developed in the past, most of them based on different approximations to the RTE and exploiting the various properties exhibited by the spectral lines sensitive to the magnetic field. Among them, the line ratio technique of the Stokes V profiles, developed by Stenflo (1973), the center-of-gravity technique (Semel 1967; del Toro Iniesta et al. 1990), or the weak-field approximation (Jefferies & Mickey 1991). These techniques have been reviewed by, e.g., Solanki (1993).

Besides these techniques, the most widely used methods for the analysis of spectropolarimetric observations are based on the inversion of the Stokes profiles. All inversion algorithms obey the same principle, namely, the attempt to retrieve the different model parameters through comparison of the observed Stokes profiles with synthesized ones.

We can classify them in two groups: those that use iterative mathematical (fitting) algorithms and the rest. The first ones are usually based on the minimization of a merit function. This quantity gives information about the goodness of the fit and can be used by any iterative algorithm to find the best profiles that fit the observations. For instance, iterative methods based on the minimization of a merit function are the genetic algorithms (Charbonneau 1995). These have been successfully applied to observations of the He I triplet line at 1083.0 nm (Lagg et al. 2004). Well known are those based on non-linear, least-square algorithms. Starting from an initial model atmosphere, i.e., from an initial set of the physical parameters, they are able to modify the model until the observations are reproduced. All is done by means of analytical or numerical solutions of the RTE. The first inversion method based on this approach was proposed by Auer et al. (1977). Since then, many inversion codes have been developed. Among them, SIR (Stokes Inversion based on Response functions; Ruiz Cobo & del Toro Iniesta 1992), SPINOR (Frutiger 2000), and those based on the ME approximation for the RTE (e.g. Skumanich and Lites 1987; Lites and Skumanich 1990; Orozco Suárez & del Toro Iniesta 2007 [see Sect. 4.4.2]).

Among the techniques that do not use iterative methods we shall highlight those based on look-up tables. For instance, the principal components analysis (PCA) method described by Rees et al. (2000), see also López Ariste & Casini (2002), or the techniques based on Artificial Neural Networks (ANNs, Carroll and Staude 2001; Socas Navarro 2003,2005; Carroll and Kopf 2008). These

techniques are less accurate but faster. This feature is of special interest for ongoing (and planned) instruments which are delivering (and are expected to deliver) huge amounts of data and hence require large amounts of computing time. Finally, Bayesian techniques have also been successfully applied to the inversion of Stokes profiles (Asensio Ramos et al. 2007a). The reader is referred to Bellot Rubio (2006) for a recent review.

In the next sections we will be discussing the non-linear, least-square inversion problem and in particular the Levenberg-Marquardt algorithm. We will also introduce the two codes that will be employed throughout this thesis and perform some numerical tests. Finally we will summarize the main conclusions.

4.2 The inversion problem

By contrast to the so-called direct method problem in which model parameters are modified manually until synthetic profiles match the observations, we usually understand by the inversion problem that of obtaining the relevant model parameters through automatic minimization of the squared differences between synthetic and observed Stokes profiles. Hence, all inversion codes are based on the minimization of a merit function $\chi^2(\mathbf{x})$, given by

$$\chi^2(\mathbf{x}) = \frac{1}{\nu}\sum_{i=1}^{4}\sum_{j=1}^{M}\frac{\left[I_i^{\rm obs}(\lambda_j) - I_i^{\rm syn}(\mathbf{x},\lambda_j)\right]^2}{\sigma_i^2}w_i^2, \tag{4.1}$$

where i refers to the four Stokes parameters, $j = 1 \ldots M$ represents the wavelength samples, σ_i the uncertainties of the observations, w_i is an arbitrary weight that can be assigned to the different Stokes profiles, $\mathbf{x}$ is a vector containing the N model parameters, and $\nu = 4M - N$ is the number of degrees of freedom. $I_i^{\rm obs}(\lambda_j)$ and $I_i^{\rm syn}(\mathbf{x},\lambda_j)$ stand for the observed and synthetic Stokes profiles respectively.

To obtain the model parameters $\mathbf{x}$, we have to find the absolute minimum of the $\chi^2(\mathbf{x})$ function. This is not a trivial task since the $\chi^2(\mathbf{x})$ is a non-linear function in a N-dimensional space. In the case of a ME atmosphere N is, at least, nine. In addition, the $\chi^2(\mathbf{x})$ function may have several local minima; this increases dramatically the complexity of the problem. In the next section we briefly introduce one of the most efficient methods to minimize a merit function.

4.2.1 The Levenberg-Marquardt algorithm

The Levenberg-Marquardt (LM) algorithm is an iterative technique aimed at finding out the absolute minimum of a given merit function. It was first pro-

posed by Levenberg (1944) and later modified by Marquardt (1963). The method is a combination of the Gauss-Newton method and the steepest descent method. When the solution if far from the local minimum the algorithm behaves like the steepest descent method, more robust but poor in the final convergence. When the solution is close to the local minimum then the Gauss-Newton method is favored. The last is based on the Taylor expansion of the merit function and has quadratic final convergence. Therefore it possesses the advantages of the two methods, improving the general convergence. For the sake of completeness, we briefly describe the basics of the LM algorithm. The detailed analysis of the algorithm and its practical applications is beyond the scope of this section. For a more comprehensive treatment, refer to Press et al. (1992).

Suposse that a merit function $\chi^2(\mathbf{x}) : \mathbb{R}^n \to \mathbb{R}$ is being minimized, i.e., that we are looking for a vector $\mathbf{x} \in \mathbb{R}^n$ that minimizes $\chi^2(\mathbf{x})$. Then, the algorithm is based on the solution of

$$\nabla\chi^2(\mathbf{x}) + \mathbf{H}'\delta\mathbf{x} = 0, \tag{4.2}$$

where the $\delta\mathbf{x}$ stand for the direction on the N-dimansional space. $\nabla\chi^2(\mathbf{x})$ stands for the Jacobian of the merit function, i.e., the gradient. $\mathbf{H}' = \mathbf{H}(\mathbb{1} + \lambda)$ is referred to as the modified Hessian matrix $\mathbf{H}$. Here, $\mathbb{1}$ is the identity matrix and λ is the so called Marquardt damping parameter. Notice that λ affects only the diagonal elements of $\mathbf{H}$. This improves the numerical computational properties and the stability of the algorithm. The elements of $\mathbf{H}$ contain the second partial derivatives of the merit function with respect to $\mathbf{x}$ approximated by the product of first derivatives:

$$H_{kl} = \frac{\partial\chi^2(\mathbf{x})}{\partial x_k}\frac{\partial\chi^2(\mathbf{x})}{\partial x_l}. \tag{4.3}$$

The iterative LM algorithm can be described as follows

1- Set the initial guess model, $\mathbf{x} = \mathbf{x}_0$, and damping parameter $\lambda = \lambda_0$,

2- solve Eq. (4.2) for $\delta\mathbf{x}$,

3- set $\mathbf{x} = \mathbf{x} + \delta\mathbf{x}$,

4- update λ according to the new χ^2,

5- repeat from 2 through 4 until one of the stopping criteria have been reached (Eqs. 4.8 and 4.9).

Of interest is the evaluation of the inverse of the modified Hessian matrix $\mathbf{H}'$. It is symmetric and positive semidefinite. Then, $\mathbf{H}' = \mathbf{u}\Sigma\mathbf{v}^\dagger$ is its singular value decomposition, where Σ is diagonal with non-zero elements μ_k, the columns $\mathbf{u}_k$ and $\mathbf{v}_k$ are called the left and right eigenvectors. † indicates transposition. Then the solution of Eq. (4.2) can be cast as

$$\delta\mathbf{x} = -\mathbf{H}'^{-1}\nabla\chi^2(\mathbf{x}) = -\sum_{k=1}^{N}\frac{\mathbf{u}_k^\dagger\nabla\chi^2(\mathbf{x})}{\mu_k}\mathbf{v}_k, \tag{4.4}$$

where n is the number of free parameters.

A critical step on the LM algorithm is the updating of the λ parameter. Marquardt proposed that given λ_0, when in an iteration step $\chi^2(\mathbf{x}+\delta\mathbf{x}) < \chi^2(\mathbf{x})$ then $\lambda = \lambda/10$, the Gauss-Newton method is favored, or else $\lambda = \lambda \times 10$, so the steepest descent method is favored, meaning that we are far from the solution. Therefore, the damping term ensures the convergence of the algorithm when the parameter space is highly non-linear, avoiding singularities on the $\mathbf{H}'$ matrix.

4.2.2 The MILne-Eddington inversion of pOlarized Spectra: MILOS

The MILOS inversion code has been developed during this thesis. It is capable of fitting a given set of Stokes profiles under the Milne-Eddington (Sect. 2.3.1) approximation. The inversion code uses the LM iterative scheme that has been described in the previous section. The code defines the merit function as in Eq. (4.1). Thus, the derivatives of the merit function can be cast as

$$\frac{\partial\chi^2(\mathbf{x})}{\partial x_k} = -\frac{2}{\nu}\sum_{i=1}^{4}\sum_{j=1}^{M}\frac{\left[I_i^{\rm obs}(\lambda_j) - I_i^{\rm syn}(\mathbf{x},\lambda_j)\right]}{\sigma_i^2}w_i^2 R_i^{x_k}(\lambda_j), \tag{4.5}$$

where $R_i^{x_k}(\lambda_j)$ is the corresponding RF with respect to x_k, j stands for the wavelength samples and i for the Stokes parameter. The elements of the Hessian matrix can be written as

$$H_{kl} \simeq -\frac{2}{\nu}\sum_{i=1}^{4}\sum_{j=1}^{M} R_i^{x_k}(\lambda_j)R_i^{x_l}(\lambda_j)\frac{w_i^2}{\sigma_i^2}. \tag{4.6}$$

Equations (4.5) and (4.6) show that the Jacobian and the Hessian depend on RFs, implying that the LM iterative algorithm uses the properties of RFs (see Chap. 3) to find the direction $\delta\mathbf{x}$. In a ME model atmosphere, these RFs can be evaluated analytically; this improves the computational times.

The nine free parameters are: the thermodynamic parameters, S_0, S_1, η_0, $\Delta\lambda_{\rm D}$ and a, the magnetic field vector, B, γ, χ, and the plasma velocity, $v_{\rm LOS}$.

Fundamentals of operation

Running the inversion code is straightforward: one has to provide a set of observed Stokes profiles and an initial guess model atmosphere. Then, the code solves the RTE within the ME approximation, computes the corresponding RFs and iteratively updates the model until it finds the best fit. The user has also to provide the initial λ_0 parameter and the intrinsic noise σ of the observations.

The user can account for the finite spectral resolution of the instrument by giving the full width at half maximum of an assumed Gaussian function with which the synthesized Stokes profiles are then convoluted.

It also accounts for the effects of scattered/stray light by the instrument. One should model the appropriate Stokes I profile to account for stray light and then give it to the inversion code. As a stray-light profile, an averaged Stokes I coming from the surrounding, non-magnetized regions is typically used. The code then fits the stray-light factor α, and the final emergent Stokes spectrum is given by $\mathbf{I} = \alpha\mathbf{I}_{\rm stray} + (1-\alpha)\mathbf{I}_{\rm m}$, where $\mathbf{I}_{\rm m}$ stands for the magnetic component and $\mathbf{I}_{\rm stray}$ for the stray-light component. When stray light is accounted for the number of free parameters increases to ten ($N = 9 + 1$). Notice that the stray light may be interpreted as a non-magnetized component. In this case, the fill fraction of the magentic component is given by $f = (1 - \alpha)$.

An extra broadening of the spectral lines by macroturbulent velocity, $v_{\rm mac}$, can be included as well. In this case, each Stokes parameter is convolved with a Gaussian function

$$f_{\rm mac}(\lambda) = \frac{1}{\sqrt{2\pi}\sigma}\exp^{-\frac{1}{2}\left(\frac{\lambda-\lambda_{\rm lc}}{\sigma}\right)^2}, \tag{4.7}$$

where $\sigma = \dfrac{\lambda_0 v_{\rm mac}}{c}$, $\lambda_{\rm lc}$ being the central wavelength of the transition and c the speed of light. This increases the free parameters by one as well.

As shown in Eq. (4.1) one can also set the different weights for the different Stokes profiles and wavelength samples, for instance, in order to give more importance to the linear polarizations signals in detriment of the circular polarization signal.

The code stops once any of the two criteria hold

$$\chi^2(\mathbf{x}) < \epsilon_1, \tag{4.8}$$

$$k \geq k_{\rm max}, \tag{4.9}$$

where k stands for the number of iterations and ϵ_1 is a constant.

Evaluating Eq. (4.4) by means of the SVD algorithm, allows additional control over each iteration step. This helps as well to tackle singularities of the

Hessian matrix. For instance, by simply truncating the number of eigenvalues μ_k used to evaluate Eq. (4.4), we can control the effect of noise on $\delta\mathbf{x}$. This is known as the Tikhonov SVD (Press et al. 1992).

Initialization and convergence tests

To initialize the LM algorithm, one has to provide an initial guess model and λ_0. There exist no specific rule to assign values to these parameters. In practice, depending on the initial guess model we have to set the λ_0 parameter: should the guess model be close to the final solution, the λ_0 would be smaller than unity, therefore favoring the Gauss-Newton method. In case the guess model is far from the best solution, λ_0 should be grater than unity to favor the steepest descent method. In addition to this, the final solution has to be found in, at least, a nine-dimensional parameter space. This increases the possibility of the code being settled in a secondary minimum instead on an absolute one.

This behavior of the LM algorithm settling in local minima (in the ME fitting scenario) have been reported before (e.g. Socas-Navarro et al. 2001) and have led to adopt different criteria in order to circumvent the limitations of the inversion. For instance, one can generate a set of n random initial model atmospheres an then run the corresponding n inversions, the solution will be that which gives better convergence (smaller $\chi^2(\mathbf{x})$). This way of tackling the problem is however extremely slow.

Other strategy may be based by adopting the solution from the fit of a neighbor pixel as the initial guess model. Although, being much faster than the previous, it may also fail, introduce non-desired dependences on the final solution, and errors can propagate easily. This can happen as well when using approximate solutions to the RTE to initialize the inversion.

There are codes that use genetic algorithms to fit the Stokes profiles. Then, the retrieved model is used to initialize an LM iterative scheme for a more robust final convergence (hybrid codes, e.g. ASP code, Skumanich and Lites 1987). The results indicate great final convergence, although at the expense of a big computational time. Other hybrid codes exists, for instance, based on efficient numerical methods for global optimization as the DIRECT method (Jones et al. 1993) used to initialize an inversion code for the He I 1083 nm spectral line (Asensio Ramos, Trujillo Bueno, & Landi Degl'Innocenti 2008).

But, why does the LM occasionally fail? There are only two reasons, namely, that the merit function has no well-defined global minimum or that the updating strategy for the model atmosphere or for the damping parameter is not well suited to the problem. Let us discuss both reasons separately.

If two or more model atmospheres produce equally good fits (i.e., equally

low values of χ^2), then either the observational noise is such that hides the true minimum or the underlying model assumptions are ambiguous, or both. That the noise hampers the measurements is out of the question. However, the physical constraints behind the model can be such that, for instance, the number of free parameters are too high for the information available from the observables. For example, Martínez González et al. (2006) have shown that the Fe I pair of lines at 630 nm is not able to provide a single solution for a scenario in which two atmospheres variable with depth, one magnetic and another non-magnetic, fill each spatial resolution element. On the other hand, the well-known trade-off between the η_0, $\Delta\lambda_D$, and a parameters of ME inversions (see Westendorp Plaza et al. 1998; Orozco Suárez, Bellot Rubio & del Toro Iniesta 2007; Chapter 2 of this thesis) produces that several sets of such three parameters may give fits with the same quality without changing the magnetic and velocity parameters. In other words, the navigation of the algorithm through the parameter space is difficult and ambiguous.

Let us suppose that the model fully explain the observations, i.e., that a clear global minimum exists. To reach it the usual strategy is to increase or decrease the λ parameter by a factor ten, depending on the divergence or not of the algorithm. If the code settles in a local minimum, the damping parameter has to be large enough in order to favor bigger $\delta\mathbf{x}$ steps and overcome that local minimum. Sometimes however, the updating strategy is such that the "damping" is unable to get rid of the local minimum.

To illustrate the problem, in Fig. 4.1 (left panel) we represent the evolution of λ and χ^2 for a particular inversion, started with a $\lambda_0 = 1$ and not too close, neither too far from the final solution. We can see how χ^2 decreases very fast at the beginning, and then stabilizes. We also see how, while the fit improves (smaller χ^2), the λ parameter decreases until a certain value at which it starts oscillating. *The inversion code has been trapped in a local minimum.* The example fit is shown in the right panel from Fig. 4.1. In this case the final solution is very close to the absolute minimum. We notice that this can happen at any iteration, depending on the shape of the N-parameter space.

Therefore, to overcome this convergence limitations an efficient updating strategy for the damping parameter is needed, as well as a proper initial λ_0 value. Different damping strategies can enormously improve LM convergence speeds. Our experience using the MILOS code tells that a small percent ($\sim$3%) of the inversions with real data fail to converge (using the Marquardt damping strategy). The general convergence of the algorithm improves when allowing only $\delta\mathbf{x}$ relative variations smaller than a fixed percentage, but this strategy has slower final convergence. An example for a different updating strategy of the damping parameter can be found in (Borrero et al. 2008).

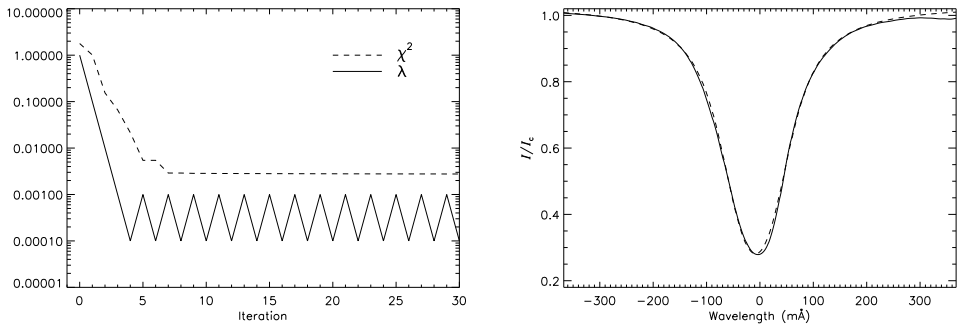

FIGURE 4.1:— Left: evolution of the damping parameter, λ, and the best χ^2 with the iteration steps. Units are dimensionless. Right: example fit (dashed) to the Fe I line at 525.06 nm (solid), and used to calculate the evolution of the merit function and the damping parameter.

Hereafter and unless otherwise stated, we set $\lambda_0 = 10$, regardless of the initial guess model. In cases where we detect that the inversion has failed to converge, we just remove this result from the analysis.

4.2.3 SIR

Developed by Ruiz Cobo and del Toro Iniesta (1992), SIR (Stokes Inversion based on Response Functions) represents one of the most robust inversion techniques that have ever been successfully applied to Stokes spectra. It is based on the solution of the RTE under local thermodynamic equilibrium (LTE) and in plane-parallel atmospheres. It takes into account the depth dependence of all important physical parameters for the formation of spectral lines. The code uses the LM algorithm to modify the initial model atmosphere which is dependent on the optical depth. Unlike the ME case, RFs are evaluated numerically since the evolution operator has not an analytical expression in general (see, e.g., del Toro Iniesta 2003). We will not analyze in detail the guts of the SIR inversion code (see the original paper or del Toro Iniesta 2003, for details) but we shall pay attention to one of its peculiarities.

SIR deals with the full stratification of the various model parameters. If the atmosphere is sampled at m different optical depths, the number of free parameters would increase by a factor m. In practice it is useless to modify the whole stratification as it would lead the code to fail. Therefore, SIR evaluates the perturbations to the different model quantities at selected optical depths, called nodes, in such a way that the whole stratification is taken into account. For instance, if one assumes a single node for a given physical quantity, the

whole atmosphere will be modified by a constant in that quantity; if two nodes are selected instead, the atmosphere will be perturbed linearly throughout; the perturbation will be parabolic if the number of nodes is three, and so on. This approach reduces the dimensionality of the problem, and strengthen its abilities to disentangle model parameters from one another.

4.3 Reliability of the inversion code

In this section we test the robustness of the inversion code. To this end we have generated a reference basis of Milne-Eddington Stokes profiles for the Fe I 525.06 nm line by using the MELANIE code developed by Héctor Socas Navarro at the High Altitude Observatory (HAO)[1]. This code has been widely used for the analysis of solar observations and is based on the ASP code (Skumanich & Lites 1987; Lites & Skumanich 1990). Then we have inverted the full profiles with the MILOS code. The inversion results allow us to check the reliability of the code and provide the uncertainties on the model parameters due to the intrinsic noise (statistical errors of the ME inversion).

The reference basis consists of a set of synthesized Stokes profiles emerging from 10 000 ME model atmospheres with a *uniform random distribution* of vector magnetic fields (B from 0 to 2500 G, inclination and azimuth from 0 to 180°) and LOS velocities (between -4 and 4 km s^{-1}). The remaining model parameters have been determined by fitting the FTS atlas (Kurucz et al. 1984). The fits of the lines have yielded errors smaller than 2%. Importantly, we have added noise to all profiles at the level of 10^{-3}. The wavelength sampling has been 0.1 pm, with a total of 100 samples across the spectral line.

The inversion of the profiles has been carried out under the following initial conditions: the initial damping parameter have been set to $\lambda_0 = 10$, the maximum number of iterations $k = 300$, the ϵ_1 parameter, which controls when the inversion has converged has been set small enough to allow the inversion code to perform the 300 iterations. Finally, the initial model parameters were: $S_0 = 0.2$, $S_1 = 0.8$, $\eta_0 = 6.5$, $B = 200$ G, $\gamma = 20°$, $\chi = 20°$, $\Delta\lambda_D = 30$ mÅ, $v_{LOS} = 0.25$ km s^{-1} and $a = 0.03$. In the inversion we determine all the 9 free parameters. The weights on the χ^2 have been set to unity, and $\sigma = 10^{-3}$ to account for the noise introduced on the simulated profiles.

Figure 4.2 shows the rms values of the relative errors on the magnetic field strength, field inclination and LOS velocity (left, right and middle panels, respectively).

[1]MELANIE is is part of the Community Inversion Codes project of the HAO

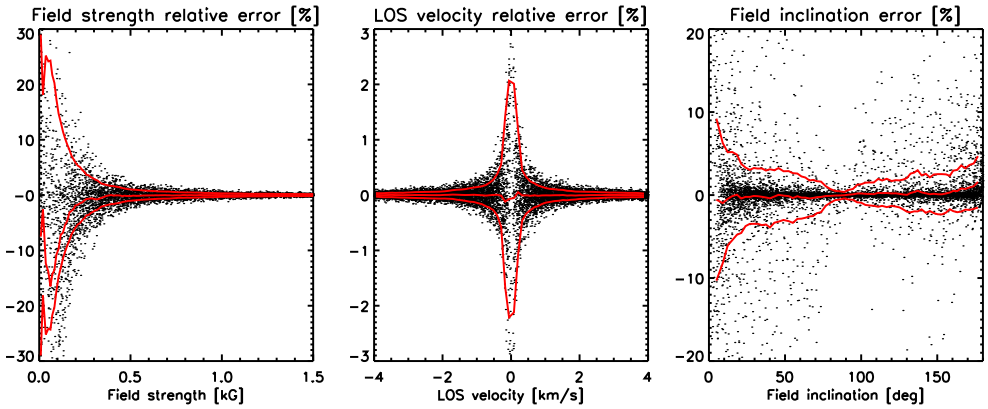

FIGURE 4.2:— Relative errors for the magnetic field strength, field inclination and LOS velocity from the full profile inversion with noise added at the level of 10^{-3}. The solid lines stand for the mean and rms values.

Note that the retrieved errors are very small, being for the magnetic field strength, smaller than 2% for fields larger than ∼500 G, or smaller than 0.1% for the LOS velocity. This errors are solely due to photon noise. The results for the inclination are noisier. Also, the rest of model parameters are determined with high accuracy (not shown). Additional test results from the inversion of the full Stokes profiles in the absence of noise retrieve negligible errors. All results together demonstrate the reliability of the inversion code, as long as the inverted profiles are generated from ME atmospheres.

5

ME inferences of solar magnetic fields: a performance analysis based on MHD simulations

The solar atmosphere is complex and features rapid changes in its physical conditions both horizontally and vertically. Such a complexity may pose a serious obstacle to the accurate determination of solar magnetic fields. In this Chapter we examine the applicability of ME inversions to high spatial resolution observations of the quiet Sun. Our aim is to understand the connection between the ME parameters inferred from the inversion and the real stratifications of the atmospheric parameters. To this end, we use magnetoconvection simulations of the solar surface to synthesize Stokes profiles such as those observed in the Sun. We then invert the profiles with the ME approximation. We perform an empirical analysis of the heights of formation of ME measurements and analyze quantitatively the errors due to the ME approximation. We also investigate the quality of the best-fit ME profiles and their relationship with the particular model stratifications.

5.1 Introduction

Stokes profiles contain information about the physical properties of the solar atmosphere. In general, the information encoded on the shape of the lines is not confined to single atmospheric layers, but to a broad range of heights. The

extraction of such information directly from the observables is difficult. The measurement of the Stokes profiles in combination with the method of analysis introduce uncertainties in the physical quantities retrieved from the observations. The former includes errors due to detector photon noise and instrumental effects, e.g., the limited spectral resolution and wavelength sampling, the finite angular resolution, etc. The latter contains uncertainties due to the simplifications and approximations of the physical model used to explain the observed profiles.

In this Chapter, we want to analyze real Stokes profiles with the ME approximation. This approximation do not account for vertical stratifications of the atmospheric quantities (see Chapter 2), making it unfruitful to reproduce the physical conditions of the solar atmosphere as long as its physical properties (temperature, density, magnetic field, etc.) change through the photosphere. When the "observations" are synthetic ME Stokes profiles, the ME model is fully compatible and lead to uncertainties that are solely due to the intrinsic noise and, to a smaller extent, to the convergence of the algorithm, provided the spectral resolution and wavelength sampling is appropriate. Uncertainties caused by noise are known as statistical errors. They can be evaluated by means of numerical tests or, more efficiently, by using ME Response Functions (see Chapter 3). What does it happen when we analyze realistic Stokes profiles (with no noise) with the ME approximation? What are the intrinsic errors of such an analysis? This is, in all purposes, the aim of the present Chapter.

A pioneering study of the capabilities and limitations of ME inversion codes was carried out by Westendorp Plaza et al. (1998) using the Fe I spectral lines at 630.15 and 630.25 nm. They made a quantitative comparison between results obtained with SIR and the ASP ME code, all using synthetic Stokes profiles describing different solar scenarios. The conclusion of their work was that the ME inversion provides accurate average values for the "real" stratifications of the physical quantities.

More recently, Khomenko & Collados (2007b) have analyzed whether it is possible to determine the magnetic field stratification from SIR inversions of Stokes profiles synthesized from MHD simulations. They have shown that the inversion is able to recover the magnetic stratifications for fields as weak as 50 G, using the Stokes profiles of the Fe I at 630 nm in the absence of noise. This work complements the results of Westendorp Plaza et al. (1998). Also with the help of MHD simulations, Khomenko & Collados (2007a) have evaluated the diagnostic potential of different spectral lines for magnetic field measurements based on the line ratio technique. The results were not very satisfactory for the pair of Fe I lines at 630 nm. They have shown that errors are large, making the line ratio technique useless. They also pointed out the

importance of accounting for atmospheric gradients to infer the field strength from these two lines accurately. Note that the information about atmospheric gradients is contained in the line asymmetries: *the ME model cannot reproduce Stokes profile asymmetries*.

In this Chapter we carry out a complete analysis of the capabilities and limitations of ME inversion codes for the analysis of real observations: first, we take a set of state-of-the-art magnetohydrodynamic simulations to describe the solar photosphere as realistically as possible (Sect. 5.2). Then, the Stokes I, Q, U and V profiles are synthesized from the model atmospheres provided by the simulations (Sect. 5.3). The SIR code is used for these calculations. We then apply the ME inversion to the profiles in the absence of noise and instrumental effects. For the inversions, we use the MILOS code. A direct comparison of the retrieved atmospheric parameters and real ones allows us to determine the uncertainties due to the ME approximation (Sect. 5.4). The lines used for the analysis are Fe I 630.15 and Fe I 630.25 nm. As mentioned before, in this study we neglect any source of errors due to the use of solar instrumentation (including photon noise). In Chapters 6 and 9 we fully simulate measurements made by real instruments.

5.2 Magnetohydrodynamic simulations

To describe the Sun's photosphere we use the radiative MHD simulations of Vögler et al. 2005 and Vögler 2003. They were performed with the MURaM[1] code which solves the 3D time-dependent MHD equations for a compressible and partially ionized plasma, taking into account non-grey radiative energy transport and opacity binning.

The code has been used to evaluate the diagnostic potential of different spectral lines and to compare them with real observations (Khomenko & Collados 2007a,b; Khomenko et al. 2005a,b; Shelyag et al. 2007), to study facular brightenings (Keller et al. 2004) and to investigate the relationship between G-band bright points and magnetic flux concentrations (Schüssler et al. 2003; Shelyag et al. 2004). More recently the simulations have been used to simulate high-spatial resolution spectropolarimetric observations of space-borne instruments and to analyze the diagnostic potential of visible lines for internetwork field determinations (Orozco Suárez, Bellot Rubio, & del Toro Iniesta 2007). It has also been used to simulate small solar pores (Cameron et al. 2007), umbral dots (Schüssler & Vögler 2006), the emergence of magnetic flux tubes from the upper convection zone to the photosphere (Cheung 2006; Cheung et al.

[1] MPS/University of Chicago RAdiative MHD

TABLE 5.1:— Physical parameters provided by the simulation runs

VARIABLE	UNITS	DESCRIPTION
ρ	g cm^{-3}	Density
$\rho_{m_{x,y,z}}$	g cm^{-2} s^{-1}	Momentum density components
e_{tot}	g cm^{-1} s^{-2}	Total energy density
$B_{x,y,z}$	G/$\sqrt{4\pi}$	Magnetic field components
T	K	Temperature
P_g	g cm^{-2} s^{-2}	Gas pressure

2007), and to study the origin of the strong horizontal internetwork magnetic fields in the quiet solar photosphere revealed by the *Hinode* spectropolarimeter, to which the near-surface local dynamo action seems to contribute signicantly (Schüssler & Vögler 2008). Finally, the code has been used to analyze the image contrast of the solar granulation as seen by the *Hinode* spectropolarimeter (Danilovich et al. 2008).

To develop our work we employ two snapshots from simulation runs representing a very quiet, unipolar internetwork region and a weak plage region with an average magnetic field, $\langle B \rangle$, of 10 and 50 G, respectively. We also use a sequence of 5 minutes with a cadence of 10 seconds (which makes a total of 30 snapshots) of a mixed-polarity simulation run representing a strong network region of $\langle B \rangle = 140$ G. To generate the snapshots the simulation was initialized with a homogeneous vertical magnetic field of 200 G and continued until $\langle B \rangle$ at $\tau = 1$[2] had decayed to a level of about 50 and 10 G. For the strong network region, the simulations were started with a bipolar distribution of vertical fields with average strength of 200 G. The 5-minute sequence was taken relatively early after the beginning of the simulation.

Each of the simulation runs consists of single precision cubes of dimension $288 \times 100 \times 288$ pixels. The horizontal and vertical extent are respectively 6000 and 1400 kilometers, thus the horizontal mesh-width is about 20.8 km and the vertical step size is 4.86 km, extending from $z = -800$ to $z = 600$ km. $z = 0$ km is the height where $\tau = 1$. The equivalent grid resolution is $0\farcs0287$, implying a spatial resolution of $0\farcs057$ (41.6 km) on the solar surface. The physical parameters provided by the MHD models are summarized in Table 5.1.

In the simulation runs, the time-averaged radiation flux density which leaves the box at the top has the solar value $F_\odot = 6.3410^{10}$ erg s^{-1} cm^{-2}. One has to keep in mind that the behavior of the models resulting from the simulations are strongly influenced by the limited box extensions. As a consequence, although

[2]All continuum optical depths refer to the opacity at 500 nm

acoustic oscillations emerge naturally in the simulations, they populate a rather small wavenumber space and their amplitudes are unrealistically large, implying that the simulations cannot be used to predict the magnitude of oscillation-induced line-shifts in the real Sun (as those caused by the 5-min oscillations)[3].

5.3 Spectral synthesis

In order to synthesize the Stokes profiles that emerge from the MHD simulations we have to solve the RTE for polarized light. This process has been carried out using SIR. The spectral synthesis is accomplished in two steps: first, the input model atmospheres needed by SIR are built from the MHD simulations; and secondly the RTE is solved.

5.3.1 Extracting the atmospheric parameters

The atmospheric parameters needed to synthesize the Stokes profiles are the temperature (T), electron pressure (P_e), line of sight velocity ($v_{\rm LOS}$), magnetic field strength, inclination and azimuth (B, γ and χ) as well as the optical depth (τ). To derive them from the MHD model we have to carry out the following computations. Firstly, B, γ and χ are calculated as follows:

$$B = \sqrt{4\pi}\sqrt{B_x^2 + B_y^2 + B_z^2}, \tag{5.1}$$

$$\gamma = \arccos \frac{\sqrt{\pi} B_y}{B}, \tag{5.2}$$

$$\chi = \arctan \frac{B_z}{B_x}, \tag{5.3}$$

where γ and χ range from 0 to 180°, and from 0 to 360° respectively, and the magnetic field B in G. The LOS velocity is extracted from the y-component of the momentum density

$$v_{\rm LOS} = \frac{\rho_{m_y}}{\rho}. \tag{5.4}$$

The electron pressure and optical depth are inferred from the temperature, gas pressure (P_g), and density (ρ). To this end we solve the Saha and Boltzmann equations every 14 km in the vertical direction. The electron pressures and optical depths are different for each pixel. The calculations have been

[3]Solar oscillations shift the Stokes profiles back and forth, therefore they have a direct impact on the design of solar instrumentation, especially on filter-based magnetographs which scan a spectral line at limited, fixed wavelength positions.

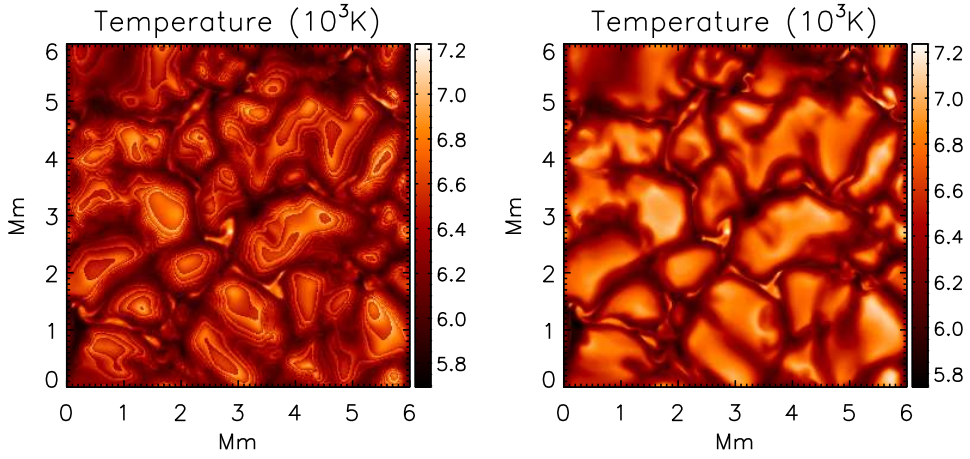

FIGURE 5.1:— Maps of temperature at the nearest value of the level $\tau = 1$ for one data cube without vertical interpolation (left) and with the models properly interpolated (right). The effect of the non-evenly spaced $\log \tau$ scale is clearly seen in the left map. The data correspond to the $\langle B \rangle = 140$ G simulation run.

carried out assuming $\log \tau = -4.9$ as a boundary condition at the top of the computational domain ($z = 600$ km). This value has been taken from the Harward-Smithsonian Reference Atmosphere (Gingerich et al. 1971).

5.3.2 Interpolating the atmospheres

Figure 5.1 (left) shows a map of the temperature values at the optical depths closest to the $\tau = 1$ level in each pixel, corresponding to the first snapshot of the simulations run with $\langle B \rangle = 140$ G. The effects of the non-evenly spaced $\log \tau$ scale are clearly seen as a non-continuous spatial distribution, exhibiting very strong differences from pixel to pixel, like a contour lines pattern. In order to correct this effect the various atmospheric model parameters are interpolated through the whole atmosphere. We have used a second order polynomial interpolation for all atmospheric quantities. Also, we have let the depth grid vary from $\log \tau = -4$ to 2, with a step size of $\Delta \log \tau = 0.05$. This depth range encompasses the atmospheric heights to which the most commonly used photospheric lines are sensitive to the magnetic field vector and to the flow velocity.

Figure 5.2 shows an example of vertical stratifications for several of the model parameters (black). Overplotted are the results from the interpolation (red). Similar results are obtained for other pixels. The right panel of Fig. 5.1 shows the temperature map from the interpolated atmospheres. Obviously, the

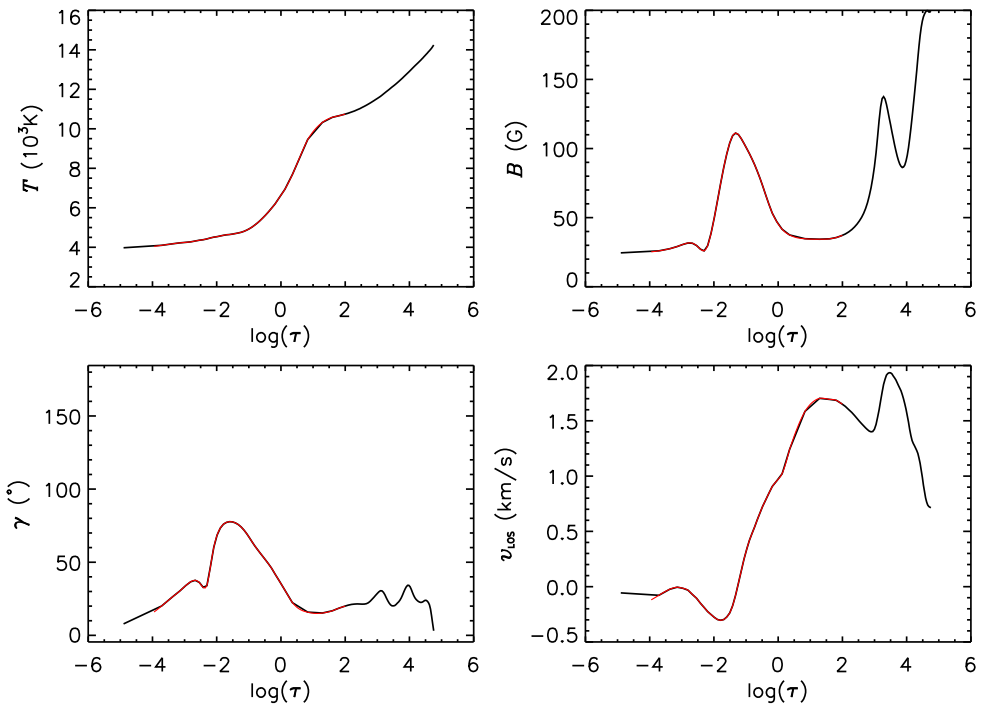

FIGURE 5.2:— Example of stratifications resulting from the simulations. This pixel correspond to a granule. The interpolated atmosphere (red) coincides almost exactly with the non-interpolated one (black). The interpolated model extends from $\log\tau = 2$ to $\log\tau = -4$.

effect of the non-evenly spaced grid has disappeared.

Figure 5.3 displays maps of the field strengths, inclinations, azimuths and velocities found in the simulation run with $\langle B \rangle = 140$ G at $\tau = 1$. In the LOS velocity map the granulation pattern can be clearly seen. The granules exhibit negative velocities while the intergranules show positive velocities. In the intergranular lanes there are small scale structures as well. Some of these structures exhibit velocities of up to 6 $\mathrm{km\,s^{-1}}$.

The magnetic field strength map shows that the field tends to concentrate within the intergranular lanes, reaching values of 2500 G in some locations. The granules harbor weak fields that occasionally reach 300 G. The inclination map indicates that the fields are mostly vertical in intergranular regions, and tend to be horizontal in granules. The azimuth map presents granular-sized structures (1″-2″).

For a more quantitative description of the fields present in the simulations, Fig 5.4 illustrates the field strength and inclination Probability Density Func-

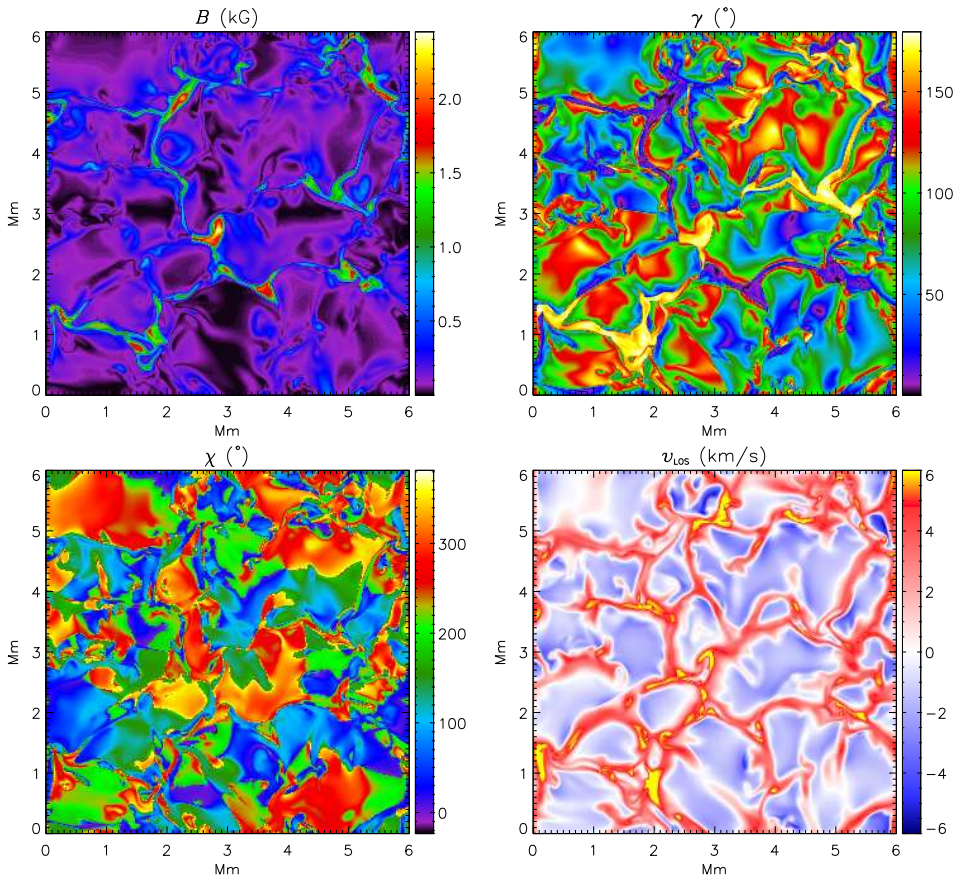

FIGURE 5.3:— Magnetic field strength, inclination and azimuth, and LOS velocity at $\tau = 1$ from the simulation run corresponding to $\langle B \rangle = 140$ G.

tions (PDFs)[4] for the three simulation runs at optical depth $\log \tau = -1$. The PDFs indicate that most of pixels have magnetic field strengths of the order of hectoGauss (hG). The PDFs are stepper as the initial flux density of the simulation decreases.

The PDFs of the field strength increases rapidly toward weaker fields. For the $\langle B \rangle = 140$ G case the distribution peaks at about 20 G. The inclination PDFs show few vertically oriented fields while there is a larger occurrence of horizontal fields. The $\langle B \rangle = 140$ G run was seeded with mixed-polarity vertical fields, therefore the distribution is rather symmetric about $\gamma = 90°$.

[4]The PDF is defined in such a way that $P(B)dB$ is the probability of finding a magnetic field B in interval $[B, B + dB]$. The integral of the PDF is unity, i.e., $\int_0^\infty P(B)dB = 1$.

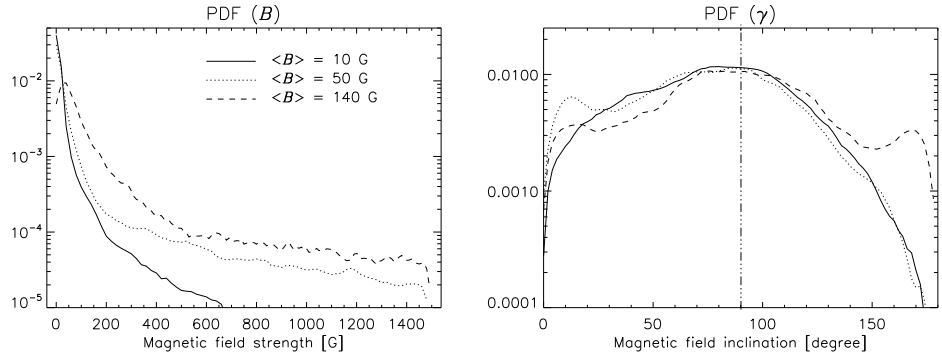

FIGURE 5.4:— Magnetic field strength (left), and field inclination (right) probability density functions from the magneto-convection simulations for $\langle B \rangle = 10$ (solid), 50 (dotted) and 140 G (dashed), taken at optical depth $\log \tau = -1$

The $\langle B \rangle = 10$ and 50 G simulations were initialized with unipolar vertical fields, resulting in asymmetric distributions.

5.3.3 Spectral lines and synthesis

Once we have built up the model atmospheres for each of the 288×288 pixels and for all the snapshots we use them as input models for SIR. The spectral synthesis has been carried out for several lines[5] located in the 525.0, 630.2 and 617.3 nm regions (see Table 5.2).

The wavelength sampling has been set to 1 pm except for the 630.2 nm spectral region, which has been sampled at 113 wavelength positions in steps of 2.15 pm. This region contains the two Fe I lines at 630.15 and 630.25 nm. They are the lines observed by the spectropolarimeter aboard *Hinode* (for details, see Tsuneta et al. 2008). The atomic parameters used for the synthesis are given in Table 5.2. The $\log(gf)$ values have been taken from the VALD database (Piskunov et al. 1995) except for Fe I 630.25 nm. The collisional broadening coefficients α and σ due to neutral hydrogen atoms have been evaluated following the procedure proposed by Anstee & O'Mara (1995) and Barklem et al. (1998, 2000). The abundances have been taken from Thevenin (1989). The computation of the Stokes profiles of a single spectral line from a snapshot takes about 12 hours in a 3 GHz single-processor workstation.

In the synthesis process we have not included broadening due to macro- or microturbulent velocity fields. Turbulent fields have been extensively used in

[5]The 525.0 nm spectral region includes a large number of transitions in order to evaluate the effects of the secondary transmission peaks of the IMaX étalon (see Chapter 9).

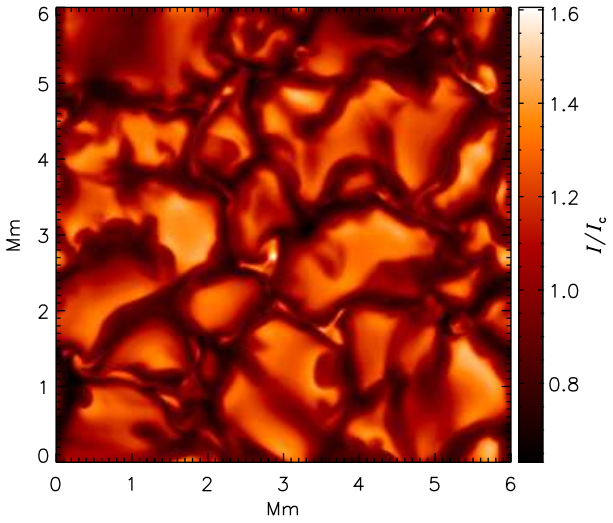

FIGURE 5.5:— Continuum intensity image at 525.0 nm.

the past to artificially broaden the spectral lines with the only purpose of fitting the observed line widths. The simulations are of sufficiently high resolution to describe the smallest scale plasma motions. They also reproduce larger scale motions, such as the convective velocity fields. This broad range of plasma motions makes the use of macro- or microturbulent velocity fields unnecessary in a 3D analysis. Asplund et al. (2000) showed that in the case of seeing-free observations the convective flow velocities, in addition to other well-known processes like the thermal or collisional line broadening, are sufficient to explain the observed widths of photospheric spectral lines.

5.3.4 Synthesis results

In this section we examine basic properties of the simulated region and make a comparison of the synthetic profiles with real observations. This provides us with information about the realism of the MHD simulations.

Continuum contrast

Figure 5.5 shows the continuum intensity map at 525.0 nm for a single snapshot of the $\langle B \rangle = 140$ G run. Not surprisingly, it is rather similar to the temperature map shown in Fig. 5.1. In the continuum map the granular and

TABLE 5.2:— Atomic parameters for the synthesized lines. λ stands for the central (laboratory) wavelength of the transition, χ_{low} is the excitation potential of the lower level of the line in eV, $\log_{10}(gf)$ stands for the multiplicity of the lower level of the transition times the oscillator strength of the line, α and σ (in units of Bohr's radius, a_o)are the collisional broadening parameters from the quantum theory of Anstee, Barklem and O'Mara, and $g_{\rm eff}$ the effective Landé factor of selected lines.

ION	λ (nm)	χ_{low}	$\log_{10}(gf)$	TRANSITION	α	σ	$g_{\rm eff}$
Ti I	524.65500	0.836	-2.695	$5F_4 - 5D_3$	-	-	-
Cr II	524.67680	3.714	-2.466	$4P_{0.5} - 4P_{1.5}$	-	-	-
Fe I	524.70504	0.087	-4.946	$5D_2 - 7D_3$	-	-	-
Ti I	524.72890	2.103	-0.727	$5F_3 - 5F_2$	-	-	-
Cr I	524.75660	0.961	-1.640	$5D_0 - 5P_1$	-	-	-
Co I	524.79110	1.785	-2.070	$4P_{0.5} - 4D_{0.5}$	-	-	-
Ni I	524.83720	3.941	-2.426	$3G_3 - 3F_2$	-	-	-
Ti I	524.83830	1.879	-1.818	$3G_4 - 3F_4$	-	-	-
V I	524.90730	2.365	-2.067	$2F_{3.5} - 2H_{4.5}$	-	-	-
Fe I	524.91054	4.473	-1.480	$3G_3 - 3F_3$	-	-	-
Cr II	524.94370	3.758	-2.489	$4P_{1.5} - 6D_{2.5}$	-	-	-
Nd II	524.95760	0.976	0.094	$4F_{8.5} - 6D_{7.5}$	-	-	-
Co I	525.00000	4.175	0.320	$4G_{2.5} - 4H_{3.5}$	-	-	-
Fe I	525.02080	0.121	-4.938	$5D_0 - 7D_1$	0.253	207.070	3.0
Fe I	525.06450	2.198	-2.047	$5P_2 - 5P_3$	0.268	343.720	1.5
Ti I	525.09210	0.826	-2.363	$5F_3 - 5D_2$	-	-	-
Ti I	525.14780	0.818	-2.541	$5F_2 - 5D_1$	-	-	-
Fe I	525.19659	3.573	-1.990	$1H_5 - 1H_6$	-	-	-
Ti I	525.21000	0.048	-2.448	$3F_4 - 3F_3$	-	-	-
Fe I	525.30300	2.279	-3.940	$3P_2 - 5P_1$	-	-	-
Fe I	525.32400	3.635	-3.179	$3D_1 - 5F_1$	-	-	-
Fe I	525.34617	3.283	-1.573	$5D_1 - 5D_1$	-	-	-
Fe I	525.33100	4.320	-3.896	$5G_6 - 5H_5$	-	-	-
Co I	525.46470	3.971	-1.249	$4D_{3.5} - 4D_{3.5}$	-	-	-
Fe I	525.49554	0.110	-4.764	$5D_1 - 7D_2$	-	-	-
Cr I	525.51330	3.464	-0.386	$7P_4 - 7D_5$	-	-	-
Mn I	525.53260	3.133	-0.763	$4G_{5.5} - 4F_{4.5}$	-	-	-
Nd II	525.55060	0.205	-0.697	$4F_{4.5} - 6D_{4.5}$	-	-	-
Fe I	630.15012	3.654	-0.75	$5P_2 - 5D_2$	0.243	840.477	1.667
Fe I	630.24936	3.686	-1.236	$5P_1 - 5D_0$	0.240	856.772	2.5
Fe I	617.33356	2.223	-2.879	$5P_1 - 5D_0$	0.266	281.000	2.5

intergranular regions can be clearly seen. The rms intensity contrast[6] is 17.9 %. It is greater than typical values obtained from ground-based observations. The contrast measured from speckle reconstructed G-band images does not surpass 15% (Uitenbroek, Tritschler, & Rimmele 2007). The only difference between the synthetic images and real observations is that the latter are affected by atmospheric distortions and optical degradations, while the former are not.

Results for the different spectral lines

In order to check whether the synthesized Stokes profiles reproduce real solar observations, we have compared the (temporally and spatially averaged) quiet Sun Stokes I profile observed with the Fourier Transform Spectrograph (FTS) atlas by Brault & Neckel (1987) and Neckel (1999), which has minor instrumental broadening effects.

Figure 5.6 shows the comparison between the FTS atlas and the average Stokes I for each of the synthesized spectral regions. The mean profiles correspond to the $\langle B \rangle = 140$ G simulation run, since it allows for temporal averages (30 snapshots representing 5 minutes of evolution). The average profiles have been shifted in wavelength to correct for the solar gravitational redshift (611 $\mathrm{m\,s^{-1}}$). An additional minor correction to the wavelength shift has been allowed to improve the fits. The spectral resolution of the FTS ($\lambda/\Delta\lambda \sim 500\,000$) has also been taken into account. The figure shows that the widths of the average profiles are very similar to those recorded by the FTS. The intensity differences (represented at the bottom of each panel from Fig. 5.6) do not exceed 3%. These differences are not symmetric around the line core position, indicating the presence of line asymmetries in the FTS profile, the average I profile, or both.

To carry out the comparison, the FTS and the mean profiles have been normalized to the local continuum. However, the continuum intensities of the average profiles turn out to be 2.15, 2.93 and 4.02% higher than those of the FTS for the 630.1, 617.3 and 525.0 nm spectral regions, respectively. These differences may partly be due to the finite temporal and spatial dimensions of the simulation box which prevent, for instance, the generation of realistic 5-min solar oscillations (Khomenko et al. 2005).

A brighter continuum indicates that the mean effective temperature[7] of the simulations is larger than the real one (Holweger 1970). Note that uncertainties

[6]The intensity contrast is evaluated as the standard deviation of the image divided by its mean value

[7]The mean effective temperature is defined as the mean temperature of the solar photosphere at the Rosseland optical depth, $\tau_R = 2/3$.

in the atomic parameters used to synthesize the spectral lines can modify the shape of the lines, but not the continuum level.

Figure 5.7 represents the temperature profile averaged over all pixels in the 140 G snapshot. In the same plot we have drawn the temperature stratification of the HSRA model atmosphere. The temperature excess of $\Delta T = 90$ K exhibited by the simulations at $\log \tau = 0$ is the cause of the brighter continuum intensities of the synthetic profiles mentioned above.

Khomenko et al. (2005) and Sheylag et al. (2007) found that the averaged intensity profiles from the simulations fit the continuum of the FTS. Contrary to our results, however, they found differences of 10% in the core of the Fe I lines at 630 nm.

In summary, despite slight differences between the FTS and the averaged intensity profiles, the simulations resemble quite satisfactorily the observations, yielding intensity differences smaller than 3%. Therefore, the MHD models seem appropriate to simulate realistic Stokes profiles.

5.4 ME inversion of the Stokes profiles

To determine the vector magnetic field and the LOS velocity, we perform a ME inversion of the two Fe I spectral lines at 630 nm simultaneously[8] using the MILOS code (see Chapter 4). The Stokes profiles are taken from a single snapshot of the 140 G simulation run. No noise is added to the Stokes profiles. Hereafter all results will refer to these specific spectral lines and this simulation run.

We assume a single one-component model atmosphere. Given the very high spatial resolution of the simulations we do not consider broadening of the spectra by macroturbulent velocities, although it is implicitly contained in the thermodynamic parameters of the ME atmosphere. A total of 9 free parameters are determined: the thermodynamic parameters, S_0, S_1, η_0, $\Delta\lambda_D$ and a; the magnetic field strength, inclination and azimuth B, γ and χ; and the line-of-sight velocity, v_{LOS}. The filling factor is unity, i.e., the whole pixel is occupied by the magnetic atmosphere.

The inversion process is started using the same guess model, and is stopped when convergence is achieved or 200 iterations have been performed. The

[8] The Fe I pair of lines at 630 nm can be inverted simultaneously because they belong to the same multiplet. This implies that no more parameters are needed for the ME model (Lites et al. 1988), besides the ratio of oscillator strengths of the two lines that is indeed well known from atomic physics. Note that this shortening only applies to ME inversion. Codes whose assumptions are less restrictive (e.g., SIR) can simultaneously invert several lines.

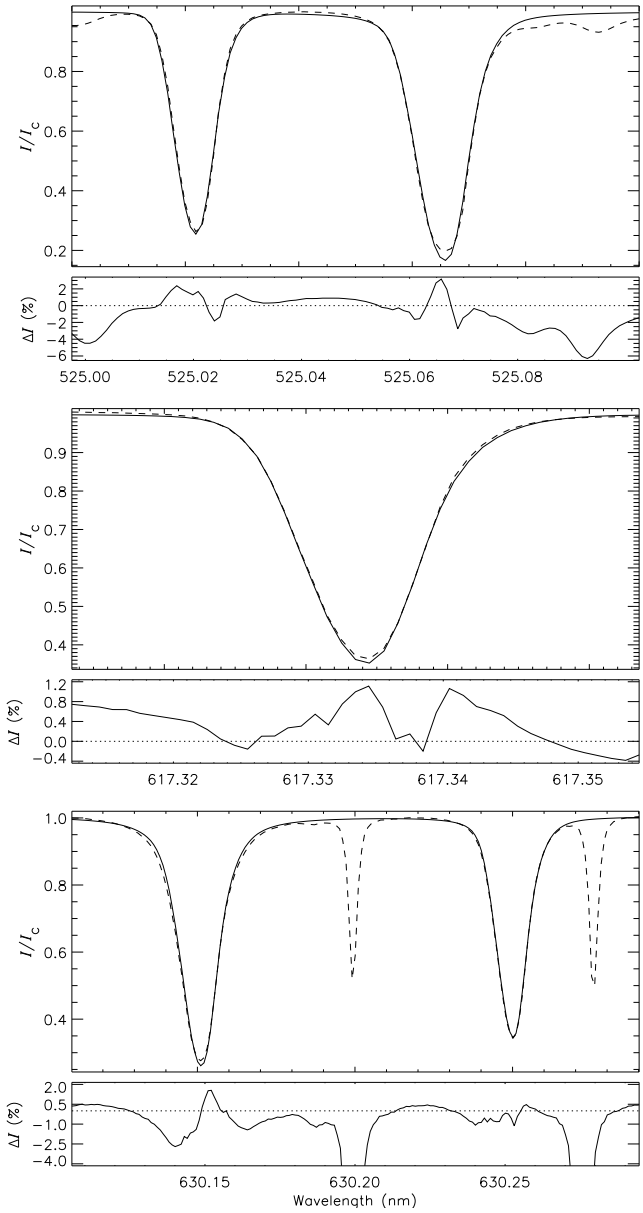

FIGURE 5.6:— From top to bottom: FTS intensity profile (dashed) compared with the mean profiles from the simulation run with $\langle B \rangle = 140$ G (solid), for the Fe I lines at 525.0, 617.3 and 630.15 nm, respectively. At the bottom of each panel we represent the intensity differences (FTS - simulation) in percent.

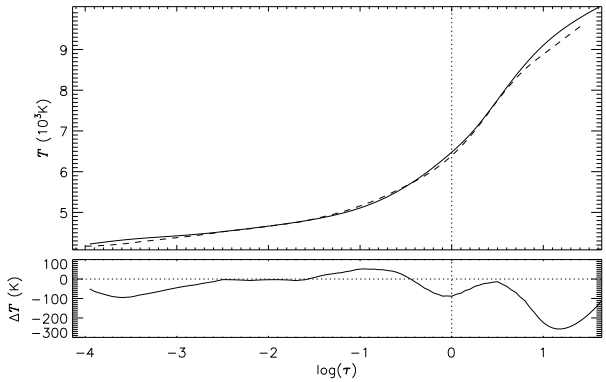

FIGURE 5.7— Mean temperature profile over all pixels (dashed) and temperature profile from the HSRA model atmosphere (solid). At the bottom we represent the temperature differences (HSRA - simulation) in K.

initial model was $S_0 = 0.2$, $S_1 = 0.8$, $\eta_0 = 6.5$, $B = 200$ G, $\gamma = 20°$, $\chi = 20°$, $\Delta\lambda_D = 30$ mÅ, $v_{LOS} = 0.25$ km s^{-1} and $a = 0.03$.

5.5 Understanding ME inferences

ME inversions provide a single value for the LOS velocity and for the magnetic field strength, inclination and azimuth. However, the analyzed spectral lines are sensitive to a broad range of optical depths. The variations of the physical properties of the atmosphere with height are encoded in the shape of spectral lines. For instance, the wings of the lines carry information from relatively deeper layers while the core tells us about the physical properties of higher layers. Thus, the asymmetries in the profile shapes give information about vertical gradients. However, a ME model is unable to produce asymmetric profiles. Under these conditions the success of ME inversions may be questionable. Are ME inversions appropriate for analyzing real observations?

Figure 5.8 represents the magnetic field strength, inclination, azimuth and LOS velocity stratifications of three pixels, (a), (b) and (c). In the same figure we represent the corresponding Stokes I, Q, U, and V profiles. The result of the ME fit is overplotted in red. Case (a) shows symmetric polarization profiles, in (b) the profiles are rather asymmetric and (c) shows three-lobed V profiles and anomalous linear polarization profiles. (a) represents a strong field case and (b) and (c) weak fields. In the three cases the atmospheric quantities show large variations with optical depth.

The ME fit is good in (a) and worse in (b) and (c). Clearly, as the asymmetry level increases, the ME model has more difficulties in reproducing the profiles. The misfit are clearly visible in Stokes Q, U and V and less dramatic in Stokes I.

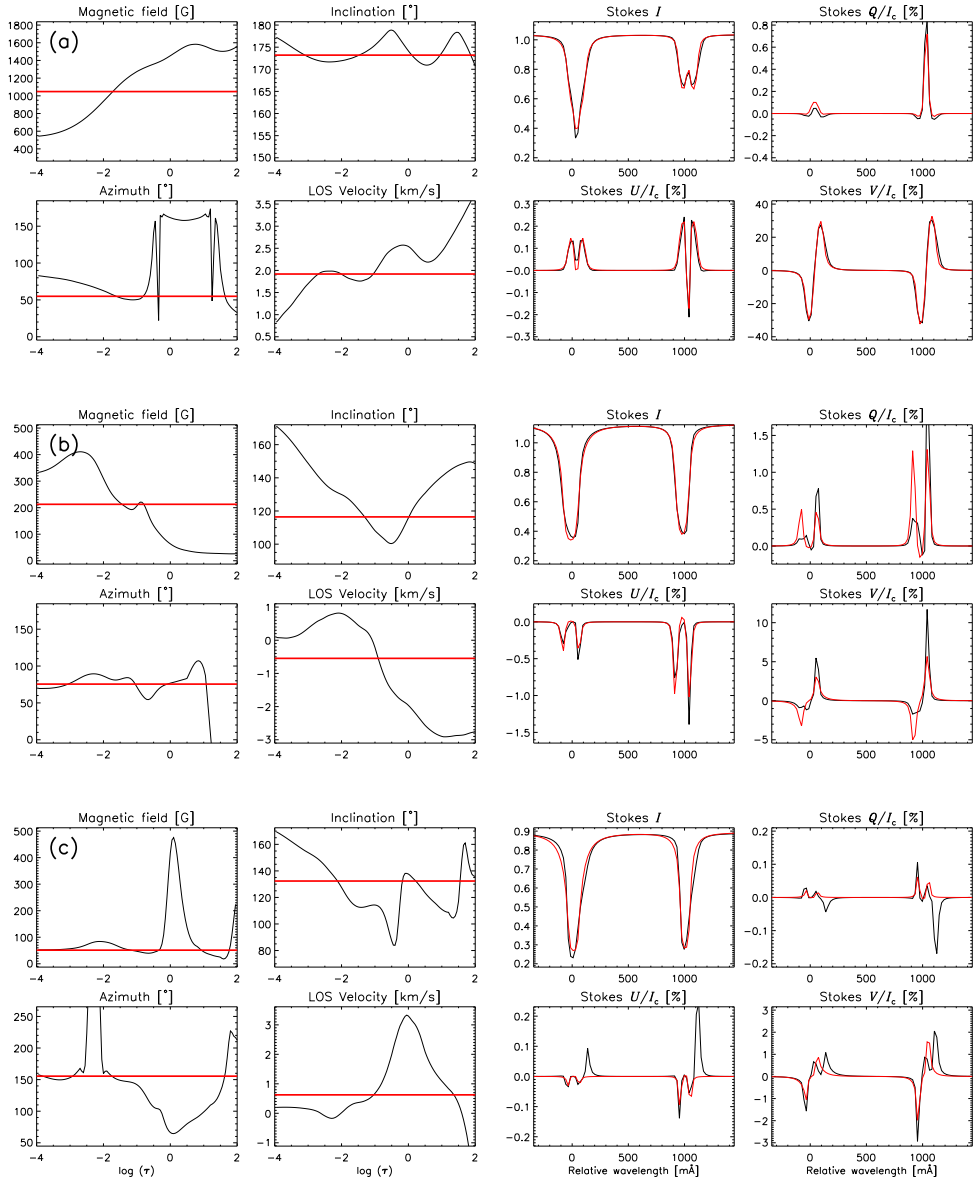

FIGURE 5.8:— Examples of MHD atmospheres and simulated profiles (black) and ME fits (red) for three different pixels. Left panels: stratifications of the magnetic field strength, inclination and azimuth, and LOS velocity. The red horizontal lines indicate the ME inversion result. Right panels: Stokes I, Q, U and V profiles synthesized from the MHD simulations with no noise (black) and ME fit to the profiles (red). Cases (a), (b) and (c) correspond to pixel locations (x,y)=(84,52), (139,124), and (80,83), respectively.

The ME models retrieved from the inversion are presented in the left panels of Fig. 5.8 (red lines). The figure demonstrates that ME inversions result in height-independent parameters which can be interpreted as RF-weighted averages of the real stratifications (Westendorp Plaza et al. 1998). However, it is difficult to confirm this fact by simply looking at the parameter stratifications. To get an insight into the aforementioned issue, let us make a detailed analysis of case (c) from Fig. 5.8. This case represents a pixel whose ME fit is not satisfactory. The analysis of the stratifications shows that the profile arises from an atmosphere that has a sharp discontinuity in field strength and in LOS velocity. A visual inspection of the Stokes V profiles signatures readily provides information from the different atmospheric layers (see Khomenko et al. 2005; Ploner at al. 2001). Surprisingly, the ME model resulting from the inversion seems to account only for the weaker "component" of the atmosphere. How is this possible?

The ME inversion algorithm uses all wavelength samples along the line to determine the best-fit ME parameters. As mentioned before, different wavelength positions across the line sample different atmospheric layers. Thus, the ME inversion is forced to return average parameters along the LOS in order to fit the whole line profile reasonably well without any bias toward better fits in the line core or in the line wings.

Figure 5.8 demonstrates that the ME model parameters coincide with the real stratifications at specific optical depths. Sometimes this occurs at various depths. We can determine the optical depths at which the inferred ME parameter coincide with, or is closer to, the stratifications. This allows us to determine the effective "height of formation" of the ME parameters.

Formation-height maps have been calculated taking the depth location of the stratification value closer to the inferred ME parameter. The computation of the optical depths has been limited to the range $\log\tau = 0$ to -2.5. This range of optical depths includes most of the layers to which the Fe I lines are sensitive. When more than one value of the MHD stratification coincides with the corresponding ME parameter, we take the one located deeper in the atmosphere. The optical depth location of the minimum (or maximum) of the MHD stratification is taken if the ME parameter is smaller (or larger) than all stratification values.

Figure 5.9 shows the results for the magnetic field strength and the LOS velocity. For convenience, the figure also displays a map of the continuum intensity and the field strength as retrieved from the inversion. Different colors indicate different atmospheric layers. There are clear differences between the two formation-height maps: in the granular centers the predominant color in the LOS velocity map is green ($\log\tau \in [-0.7, -1.2]$), with the size of the

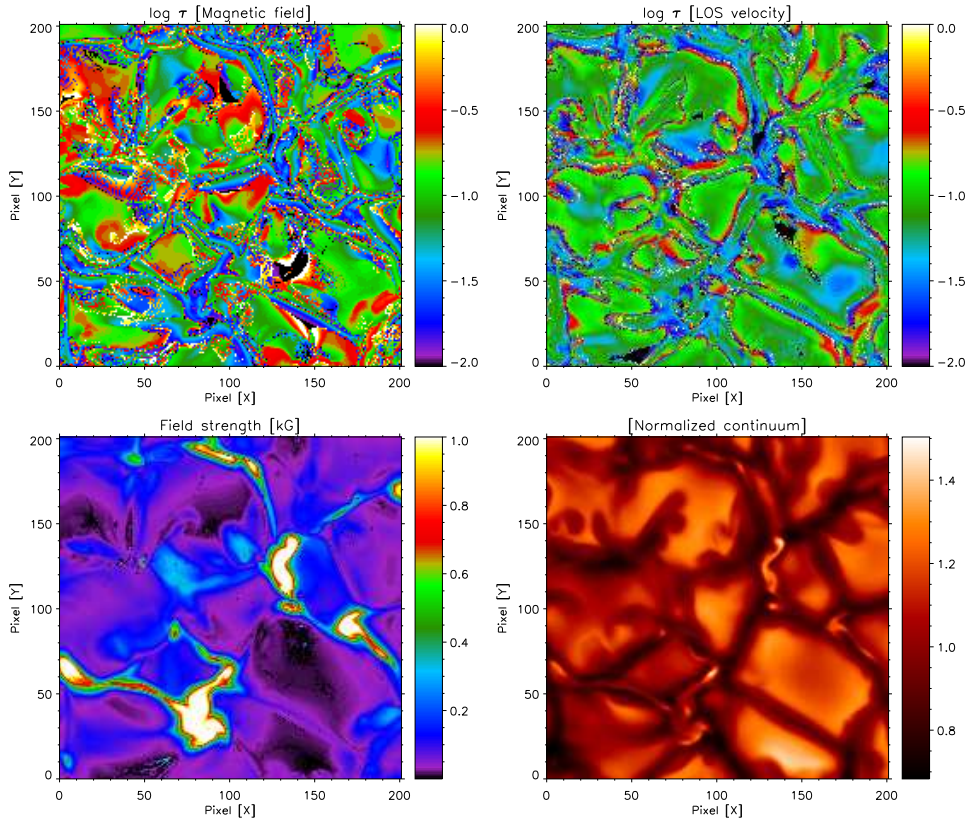

FIGURE 5.9:— Upper panels: Maps showing the optical depths at which the inferred ME parameter coincides with the real stratifications for the magnetic field strength and LOS velocity (top left and right, respectively). Bottom panels: Magnetic field strengths retrieved from the ME inversion and normalized continuum intensities (left and right, respectively).

patches being comparable to the granules; in the field strength map, smaller patches (green and red, i.e., $\log\tau \in [-0.3, -0.7]$) are seen above granules. The intergranular lanes show small-scale structures (blue, $\log\tau \in [-1.3, -1.7]$) in both maps. Note that the stronger the field, the higher the optical depth at which the ME parameter coincides with the real stratification. As we go from the granule centers towards the intergranular lane in the formation height map for the LOS velocity, the ME results correspond to deeper layers (green turns into red). Nevertheless, sharp discontinuities are seen since the intergranular lanes tend to be blue. Note that the heights at which these spectral lines are sensitive to the magnetic field and the LOS velocity go from $\log\tau \sim 0$ to -2.5, approximately.

Both maps exhibit differences from pixel to pixel, which are more noticeable for the field strength. Remarkably, the formation height for a single ME parameter may vary up to $1 - 1.5$ dex in the same area. The noise in the two panels is due to MHD stratifications with many jumps in the vertical direction.

In conclusion, as expected, ME inversions provide results that cannot be assigned to a constant optical depth layer, as shown by the large differences across the FOV. Also, as follows from the comparison of the two optical depth maps, the heights to which the ME parameters refer change depending on the physical parameter (as predicted by del Toro Iniesta & Ruiz Cobo 1996; Sánchez Almeida, Ruiz Cobo, & del Toro Iniesta 1996; and Westendorp Plaza at al. 1998). For the Fe I 630.2 nm lines, we find a mean optical depth $\log \tau = -1$ and -1.1 for the LOS velocity and the field strength, respectively. This includes granular and intergranular regions. If only intergranular regions are considered, the mean optical depths shift ~ 0.2 dex toward higher layers. The rms is about 0.4 and 0.5, respectively.

From theoretical point of view, it is possible to determine the "height of formation of a ME measurement". This concept was introduced by Sánchez Almeida et al. (1996) and is based on generalized response functions (Ruiz Cobo and del Toro Iniesta 1994). However, in practical applications, the concept of generalized RFs is of little use, since the physical conditions of the solar atmosphere are not known (in fact, the goal of any inversion is to determine them). Note also that the stratifications resulting from the MHD simulations are highly non-linear, which lead to inaccurate theoretical predictions.

5.6 Inversion results

In this section we make a qualitative and a quantitative comparison between the ME inversion results and the real stratifications of the atmospheric parameters. The comparison is done with the MHD simulations at $\log \tau = -1$, hereafter referred to as the "reference model". We have selected this layer as the best choice for all the physical parameters since ME inferences cannot be ascribed to a single optical depth for all the pixels.

Figure 5.10 shows maps of the magnetic field strength, inclination and azimuth, and the LOS velocity. The left panels correspond to the reference model while the right panels depict the parameters retrieved from the ME inversion. To better visualize the details we only show a small area of about 9 Mm^2.

At first glance, one notices the strong resemblance between the reference parameters and the results of the inversion. If we look in greater detail, we see that the shape of the different structures are better reproduced in the

magnetic field strength and inclination maps than in the LOS velocity and azimuth maps. There are places where the inversion yields bad results for the inclination and azimuth. These areas show weak polarization signals. In general one can say that the ME inversion is able to determine the magnetic field vector satisfactorily. Even magnetic structures showing field strengths as low as 100 G are recovered.

Figure 5.11 shows the atmospheric parameters at $\log\tau = -1$ in the MHD simulations vs the ME parameters inferred from the fit. These scatter plots include all the pixels (as mentioned in Sect. 5.4 noise has not been added to the profiles) and allow us to estimate the uncertainties that can be expected from the use of the ME approximation.

As can be seen, the scatter is larger for the magnetic field inclination than for the field strength or LOS velocity. For the azimuth the scatter is high. The mean values[9] (blue dots) show that the magnetic field strength is really close to that in the reference model from 0 to 500 G. For larger fields the retrieved values are slightly underestimated, although the deviation is always smaller than ∼200 G. The rms fluctuations of the field strength (red) show deviations smaller than ∼150 G for the whole range of strengths. The inclination rms is smaller than 10° for vertical fields, and reaches 25° for inclined fields.

The LOS velocity panel shows that the retrieved velocity is some 200-300 $\mathrm{m\,s^{-1}}$ smaller than the reference velocities for receding flows (intergranular lanes). The rms values are smaller than 500 $\mathrm{m\,s^{-1}}$ in the full velocity range.

The scatter shown by the different panels of Fig. 5.11 originates from a combination of the use of a ME model atmosphere to fit asymmetric Stokes profiles and the pixel-to-pixel variations of the height of formation of the ME parameters, as explained in the previous section. The deviation of the ME field strengths from a one-to-one correspondence with the MHD field strengths can easily be understood by looking at the top panel of Fig. 5.9. We have choosen the atmospheric layer at $\log\tau = -1$ as a reference. For those spatial locations at which the optical depth value assigned to the inferred ME parameter is smaller that the optical depth of the reference layer, the resulting field strength will "apparently" be underestimated. These spatial locations are associated with strong field concentrations. In the MHD models the field lines spread out with height; therefore we retrieve weaker fields.

The previous discussion explain the deviations of the ME inferences from the one-to-one correspondence. These deviations are caused by the pixel-to-pixel variations of the formation height. Therefore, the important quantity to keep in

[9]The average values have been calculated by taking bins along the X-axis of size 28 G, 3°, and 115 $\mathrm{m\,s^{-1}}$, depending on the physical quantity.

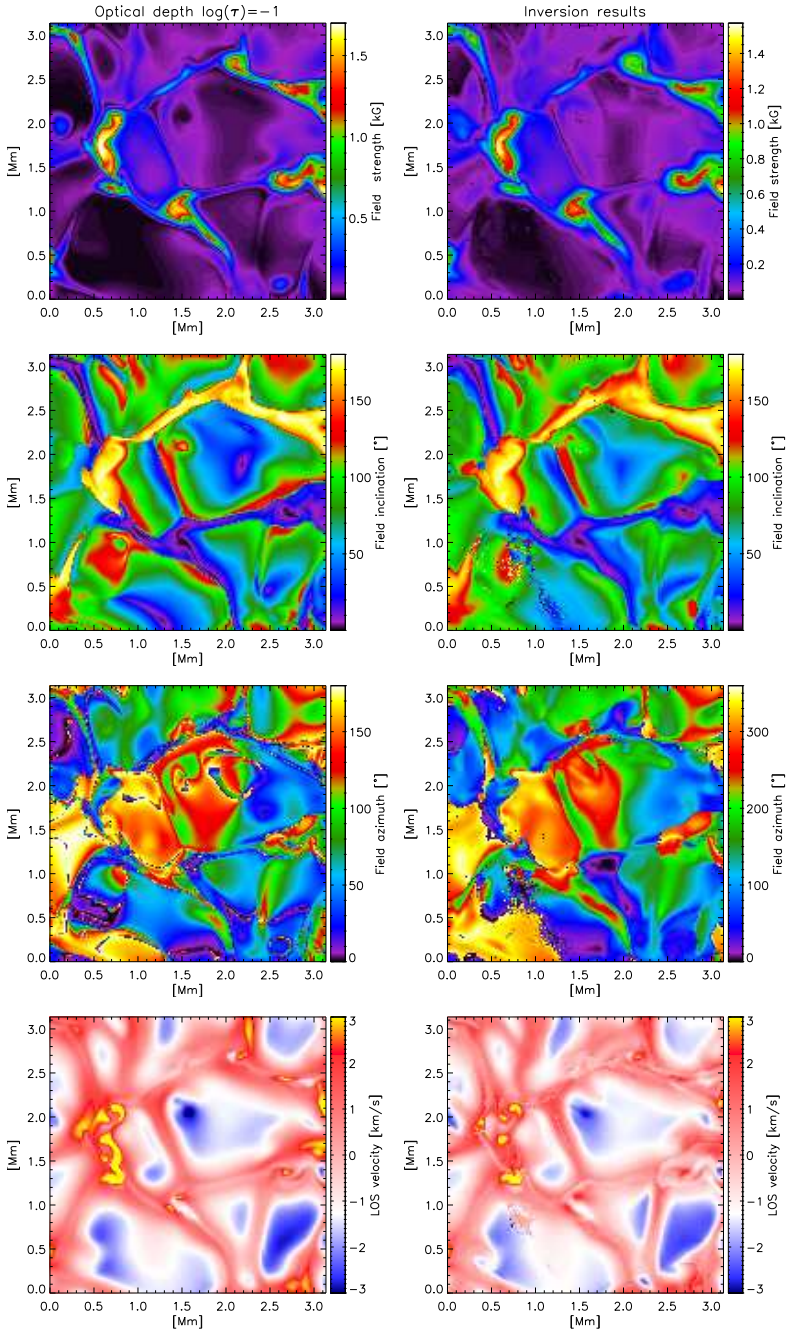

FIGURE 5.10:— From top to bottom: magnetic field strength, inclination and azimuth, and LOS velocity. Left represents the layer from the $\langle B \rangle = 140$ G simulation run at $\log \tau = -1$. Right shows the result of the ME inversion of the Fe I lines at 630.2 nm.

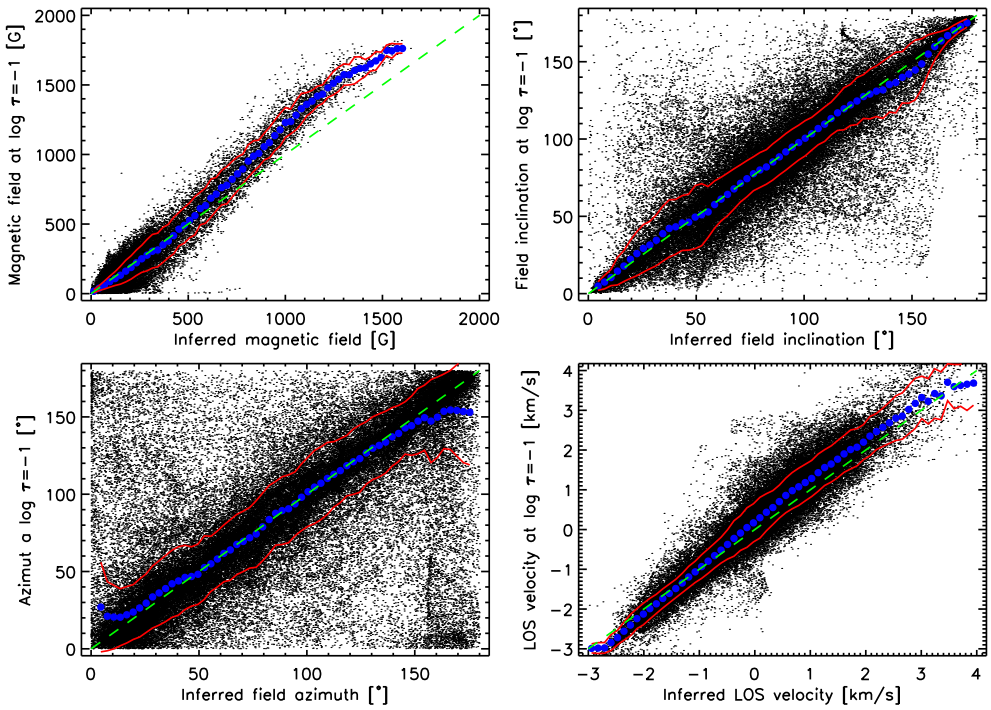

FIGURE 5.11:— Scatter plot of the magnetic field strength, inclination, azimuth and LOS velocity from the simulations at $\log\tau = -1$ vs the ME model parameters inferred from the inversion. The green dashed lines represent one-to-one correspondences. The blue dots represents the average mean values over very small, evenly-spaced intervals along the X-axis. The red line represents the rms fluctuations of the ME parameters.

mind is the rms fluctuation of the differences between the ME parameters and the reference model. This quantity inform us about the statistical deviations of the ME inferences from the real stratifications.

Depending on the optical depth assigned to the reference model the mean and rms in the various physical quantities change. To illustrate this, Fig. 5.12 represents histograms of the differences between the inferred parameters and the reference model taken at different optical depths ($\log\tau = -0.5, -1, -1.5$, coded in black, red and blue, respectively).

For the magnetic field strength, the histogram corresponding to $\log\tau = -1$ peaks at around zero. It shifts towards negative values when the inversion results are compared with deeper layers (fields are underestimated on average) and towards positive values when the comparison is made with higher layers (over-estimating the strength). The full width at half maximum (FWHM) is

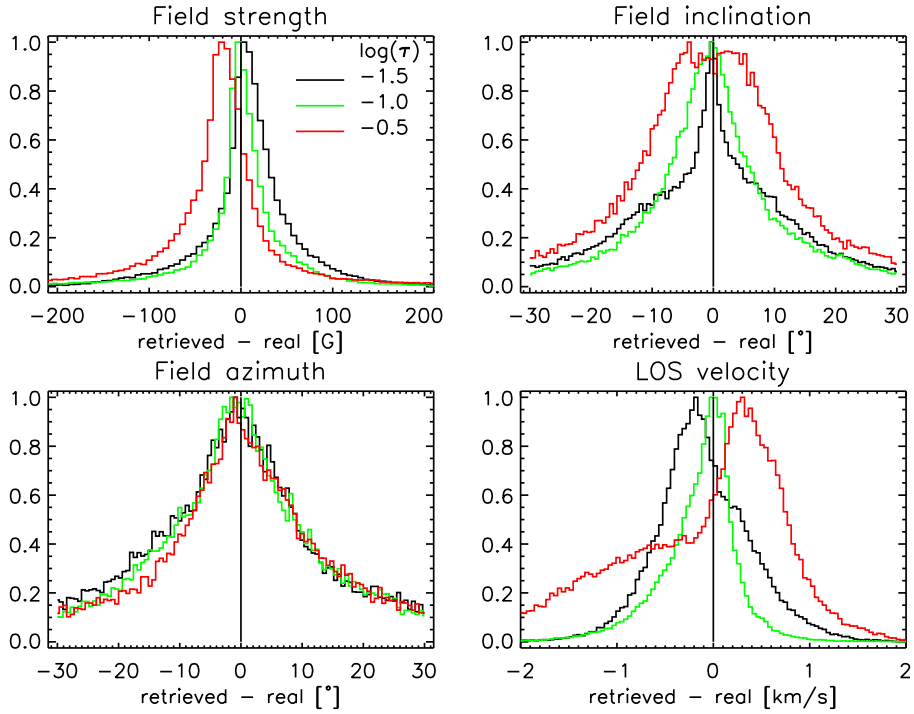

FIGURE 5.12:— Normalized histograms of the differences between the inferred ME model parameters and the real ones taken at different optical depths.

about 30 G for $\log\tau = -1$, and increases up to ∼45 and ∼50 G for $\log\tau = -1.5$ and -0.5, respectively. These effects are less pronounced for the field inclination. In this case the peaks of the histograms are located at zero and the FWHM varies from 6° ($\log\tau = -1.5$) to ∼13° and ∼23° ($\log\tau = -1$ and -0.5, respectively). The larger FWHM originate from the extended wings of the distribution. The azimuth histogram does not vary when the comparison is made with different optical depths. In this case, the FWHM is about 20°.

The histograms of the LOS velocity differences show larger variations. The one corresponding to $\log\tau = -1$ has the smaller FWHM ($\sim$ 500 $\mathrm{m\,s^{-1}}$). It also shows a long tail towards negative values which corresponds to pixels located in intergranular lanes. The asymmetry of the histograms around the location of the peaks changes dramatically when we compare the results of the inversion with different atmospheric layers. For instance, if the reference layer is taken at $\log\tau = -0.5$, the histogram is a clear combination of two different distributions, one representing granular centers (higher and narrower) and the other one representing intergranular lanes (smaller in amplitude and broader).

5.6.1 Summary and conclusions

In this Chapter we have described basic properties of MHD simulations of the quiet Sun. We have used the simulations to synthesize the Stokes profiles emerging from three different spectral regions (525.0, 630.2, and 617.3 nm). The comparison of the synthetic profiles with real observations of the quiet Sun (as represented by the FTS atlas) has proved that the simulations describe quite satisfactorily the physical conditions of the solar surface, although the MHD models are slightly hotter that the solar photosphere.

After synthesizing the Stokes profiles, the applicability of ME inversions to high spatial resolution observation has been examined. We have considered the case of the Fe I pair of lines at 630.2 nm. The analysis of the profiles by means of ME inversions has allowed us to characterize the uncertainties that can be expected from the ME approximation. For this reason, the synthetic profiles have not been degraded by noise, instrumental effects, or spatial resolution.

The main limitation of ME inversions is that they provide atmospheric quantities that are constant with height, whereas the MHD atmospheres feature physical properties that change with height. This limitation means that ME models are unable to reproduce spectral line asymmetries. Also, the ME inferences cannot be assigned to single atmospheric layers. Depending on the physical conditions of the atmosphere, the inferred ME parameters sample different ranges of optical depth. This makes the interpretation of ME inferences difficult.

However, from a statistical point of view we can conclude that ME inversions provide fair estimates of the physical quantities present at $\log\tau = -1$. The rms error is smaller than 30 G for the magnetic field strength, 6° and 20° for the field inclination and azimuth, and 500 $\mathrm{m\,s^{-1}}$ for the LOS velocity. These values correspond to the FWHM of the histograms of the differences between the inferred ME parameters and the real ones. We caution that the errors may be rather large for individual pixels, even when the best-fit ME profiles satisfactorily reproduce the observed ones (cf. field strength in case (a) from Fig. 5.8).

It is important to remark that the errors associated with the ME approximation dominate against those due to the intrinsic noise of the observations (photon noise), as demonstrated by the analysis of photon noise errors (see Chapter 3 and 4). Note, however, that noise also prevents polarimetric signals from being detectable, something that we have not considered in our study.

Thus, the analysis presented in this Chapter is not complete because we have ignored important instrumental effects such as photon noise and image degradation by telescope diffraction or atmospheric seeing. These effects intro-

duce additional uncertainties in the determination of solar magnetic fields.

In the next Chapter we go one step further and simulate real observations with all the instrumental effects involved. We consider the case of the spectropolarimeter aboard *Hinode*, since it provides the highest spatial resolution currently achievable.

6

Simulation and analysis of *Hinode* spectropolarimetric observations

In the previous Chapter we have demonstrated that ME inversions are able to determine the magnetic field vector and the LOS velocity from simulated Stokes profiles that are unaffected by the measurement process. In this Chapter we study a more realistic scenario in which the profiles are degraded by the instrument: we simulate high-spatial resolution observations of the spectropolarimeter aboard the *Hinode* satellite using model atmospheres from MHD calculations. Subsequently, the "observations" are analyzed with the help of the MILOS code. This allows us to assess the performance of ME inversions of high-spatial resolution observations of the quiet Sun. Such an analysis is essential to validate the results obtained from ME inversions of *Hinode* spectropolarimetric measurements. We find that the ME inversion results are satisfactory as soon as we correct for the dilution of the polarization signals due to the effects of telescope diffraction.

6.1 Introduction

The spectropolarimeter (SP; Lites et al. 2001) of the Solar Optical Telescope (SOT; Tsuneta et al. 2008; Suematsu et al. 2008; Shimizu et al. 2008; Ichimoto et al. 2008) aboard *Hinode* (Kosugi et al. 2007) provides nearly diffraction-limited observations of the solar photosphere, with a spatial resolution of $0\farcs32$. The instrument measures the Stokes profiles of the photospheric Fe I lines at

630 nm with high spectral resolution and polarimetric sensitivity (S/N = 1000).

Here we investigate whether reliable magnetic field strengths and field inclinations can be derived from *Hinode*/SP observations of the quiet-Sun. To this aim we again make use of MHD simulations to synthesize the Stokes profiles of the Fe I 630 nm lines. The profiles are degraded to the nearly diffraction-limited resolution of $0\farcs32$ achieved by *Hinode*/SP. Then, we add noise to the Stokes profiles and infer the various atmospheric parameters by means of ME inversions. The comparison of the inferred values with the real ones will provide us with an estimation of the uncertainties in field strength, field inclination, and magnetic flux to be expected from the analysis of *Hinode* measurements.

To date, only Khomenko et al. (2007a,b) have examined the diagnostic potential of high spatial resolution observations in the absence of atmospheric seeing. Among other topics, they investigated the capabilities of the Fe I 630 nm lines for quiet Sun internetwork (IN) studies.

A complete analysis of the capabilities of these two lines for IN field determination is of interest in view of the results of Martínez González et al. (2006). These authors argued that the Fe I 630.2 nm lines do not carry enough information to uniquely determine the magnetic field strength at $1''$. Moreover, they suggested that inversions of IN Stokes profiles seem to be biased toward strong fields. Therefore, there are clear needs to examine whether or not it is possible to derive the field strength distribution of IN regions from very high spatial resolution polarimetric observations in the visible, as those carried out by the *Hinode*/SP.

The Chapter is structured as follows: first, we describe the MHD simulations and how we have degraded them to match the spatial resolution and pixel size of *Hinode*/SP. The effects of the degradation of the Stokes vector is discussed in some detail. Then, we explain the strategy used to invert the simulated profiles, introducing the concept of local stray light to account for the effects of telescope diffraction. At the end of the Chapter we discuss the inversion results and carry out a comparison with the real model quantities.

6.2 MHD simulations and spectral synthesis

We use three snapshots from the radiative MHD simulations of Vögler et al. (2005) to describe the solar photosphere in the more realistic way possible. They correspond to simulation runs with mean flux $\langle B \rangle = 10$, 50 and 140 G. Figure 6.1 shows the corresponding PDFs for the magnetic field strength and inclination, taken at optical depth $\log \tau = -2$. As can be seen, most of the magnetic fields have strengths of the order of hG. Note also that horizontal fields

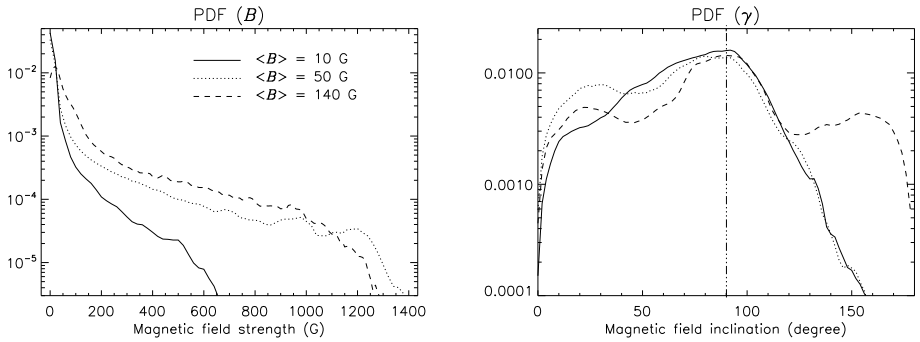

FIGURE 6.1:— Magnetic field strength (left), and field inclination (right) probability density functions in the magneto-convection simulations with $\langle B \rangle = 10$ (solid), 50 (dotted) and 140 Gauss (dashed), taken at optical depth $\log \tau = -2$.

are very common. We synthesize the Stokes spectra of the two Fe I lines using SIR. The lines are sampled at 113 wavelength positions in steps of 2.15 pm, following the *Hinode*/SP normal map mode (for details, see Shimizu 2004). For details of the MHD simulations and the synthesis of the Stokes profiles the reader is referred to Chapter 5.

The sampling interval in the simulations is 0.″0287, which implies a spatial resolution of 0.″057 (41.6 km). Thus, the synthetic Stokes profiles derived from the MHD snapshots have to be degraded to match the *Hinode*/SP resolution.

6.3 Instrumental degradation of the simulated data

In this section we describe the alterations that the instrument introduces in the "observed" Stokes profiles. The effects of the optical system, i.e, the telescope, the spectrograph, and the detector are included. All of them modify the observations to a larger or smaller extent, degrading their original resolution and image contrast. We do not consider the influence of the Earth's atmosphere since we concentrate on high spatial resolution data taken from space. Simulating a solar observation is critical because the optical system employed to observe the Sun prevents it from being recorded at optimum quality.

6.3.1 Spatial degradation: basics

Let be $I_o(x, y)$ the true intensity distribution coming from the solar surface. This distribution is distorted by the optical system according to

$$I(x, y) = I_o(x, y) * \mathrm{PSF}(x, y) + n(x, y), \tag{6.1}$$

where $I(x, y)$ is the observed image, $\mathrm{PSF}(x, y)$ denotes the Point Spread Function of the optical system, and $n(x, y)$ stands for the noise (photon noise due to the detector). The symbol $*$ indicates convolution. We can write this equation in the Fourier domain as

$$\hat{I}(x, y) = \hat{I}_o(x, y) \cdot \mathrm{OTF}(s_x, s_y) + \hat{n}(x, y), \tag{6.2}$$

where the Optical Transfer Function (OTF) is the Fourier transform of the PSF and describes the spatial frequency response of the optical system. The Modulation Transfer Function (MTF) is the modulus of the OTF. The symbol $\hat{}$ represents the Fourier transform. The MTF includes all the effects of the optical system, i.e., the possible aberrations associated with the telescope (polishing errors, defocus, etc), the transfer optics, the spectrograph or filtergraph (e.g. the amplitude and phase shifts of an étalon or the limited resolving power of a spectrograph), and finally the detector.

The effective spatial resolution of the telescope corresponds to the cut-off frequency of the first term of the MTF (diffraction limit). To first order, the PSF can be considered rotationally symmetric in the X-Y plane. If only telescope diffraction contributes to the PSF, it can be shown that

$$\mathrm{PSF}(r) = \frac{1}{\pi}\left[J_1(\frac{D\pi}{\lambda r})/r\right]^2 \tag{6.3}$$

(Born and Wolf 1980), where J_1 is the order 1 Bessel function of the first kind (Airy diffraction pattern), r the angular distance from the center of the PSF in the image plane, λ the working wavelength, and D the telescope's aperture. The first zero of Eq. (6.3) occurs at $r_{\mathrm{min}} = 1.22\lambda/\mathrm{D}$. This expression is known as the Rayleigh criterion. Thus, the resolving power of the telescope is given by the diameter of the telescope and the working wavelength. In practice, it is preferable to define the diffraction limit as $r_{\mathrm{cut}} = \lambda/\mathrm{D}$, i.e., the highest detectable angular frequency in arcsec (first minimum of the MTF). It is 1.02 times the FWHM of the central component of the Airy diffraction pattern.

6.3.2 Modeling the *Hinode*/SOT+SP MTF

To model the combined MTF of the *Hinode* Solar Optical Telescope and the spectropolarimeter we need a set of parameters describing the optical system. They are summarized in Table 6.1. In particular, we include the following effects in the MTF:

- the limited spatial resolution of the telescope which cuts off high frequencies while allowing low and mid frequencies to be transmitted,

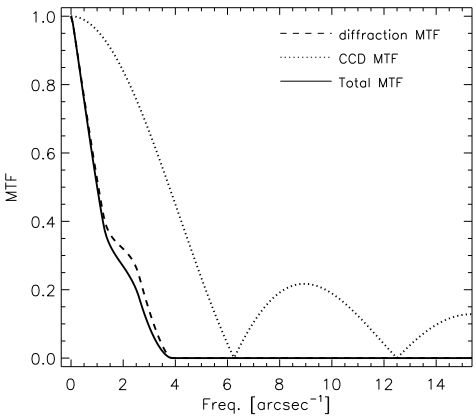

FIGURE 6.2— MTF of the *Hinode*/SP detector (dotted line), diffraction limited MTF (dashed line), and combination of both (solid line).

- the central obscuration of the entrance pupil (caused by the secondary mirror), which affects the intermediate frequencies, and
- the pixilation of the detector (detector footprint MTF)[1] and spatial sampling, which introduce an extra lost of contrast.

The diffraction-limited spatial resolution of *Hinode* SOT is $\sim 0\farcs26$ (cut-off frequency of the first term of the MTF), but the final spatial resolution of $\sim 0\farcs32$ provided by the SP is determined by the detector pixel size ($0\farcs16 \times 0\farcs16$). When the detector sampling is larger than the spatial resolution of the telescope, the highest spatial frequencies transmitted by the optics are lost. This effect is known as aliasing.

Figure 6.2 shows the MTFs describing the filtering of spectral components induced by telescope diffraction and pixilation effects in the CCD. Note the modification of the effective MTF caused by the central obscuration of the entrance pupil. The cut-off frequency ($f_{\rm cut} = {\rm D}/\lambda$) determines the spatial resolution of the image while the shape of the MTF affects the overall image contrast. The plot also shows that the shape of the MTF is only slightly modified by the detector MTF.

6.3.3 Spectral smearing

The finite spectral resolving power of the *Hinode*/SP affects the Stokes profiles through convolution:

$$\mathbf{I}_{\rm obs} = \mathbf{I} * F(\lambda), \tag{6.4}$$

[1] It represents the loss of contrast of the image due to the integration of signal in each of the pixels of the CCD camera

TABLE 6.1:— Basic optical parameters of *Hinode*/SOT and SP.

APERTURE	0.5 m	
WORKING WAVELENGTH	630 nm	
SPATIAL RESOLUTION	$\sim 0\farcs26$	$\sim$ 190 km
CENTRAL OBSCURATION	34.4%	
CCD PIXEL SIZE	$0\farcs16 \times 0\farcs16$	

where $F(\lambda)$ stands for a scalar smearing profile and $\mathbf{I}_{\rm obs}$ is the observed Stokes vector[2]. This spectral smearing produces well known effects in the Stokes spectra: it broadens the polarization profiles and reduces their amplitudes. In general, the smearing reduces the quality of the observations and diminishes the sensitivity of spectral lines to the atmospheric quantities (see Chapter 2).

The effect of the finite resolving power of the spectrograph has to be included in the image degradation process. In our case, we use a Gaussian function of a given FWHM to represent the smearing profile. Note that, in this case, the limited resolution of the spectrograph produces the same effects as a macroturbulent velocity field.

6.3.4 Degradation of the data

Santiago Vargas and José Antonio Bonet, from the Instituto de Astrofísica de Canarias, have developed a code that is able to simulate the degradation of an image (real object) caused by an instrument. To this end the code needs several input parameters: the aperture of the telescope, the working wavelength, the size of the primary mirror, the central obscuration of the telescope and the CCD pixel size (spatial sampling). Finally, the user has to specify the dimensions of the real object, in pixels, as well as the sampling interval, in arcsec.

The spatial degradation we perform with this code includes the most important terms, but is not complete because other effects are difficult to model. For instance, we do not consider the polishing quality of the primary mirror (which affects the MTF at high frequencies), the spider legs supporting the secondary mirror, or stray light by scattering in the optical path. A more detailed theoretical calculation of the *Hinode*/SOT+SP MTF has been carried out by Danilovic et al. (2008). They included the effects of the spider legs and SP defocus. Both contributions reduce the contrast of the continuum images by $\sim$1% at most, depending on the defocus of the SP. The spatial resolution remains unaltered, though. For an empirical determination of the PSF of *Hinode*

[2]We understand that convolution with a vector is a convolution with all its components.

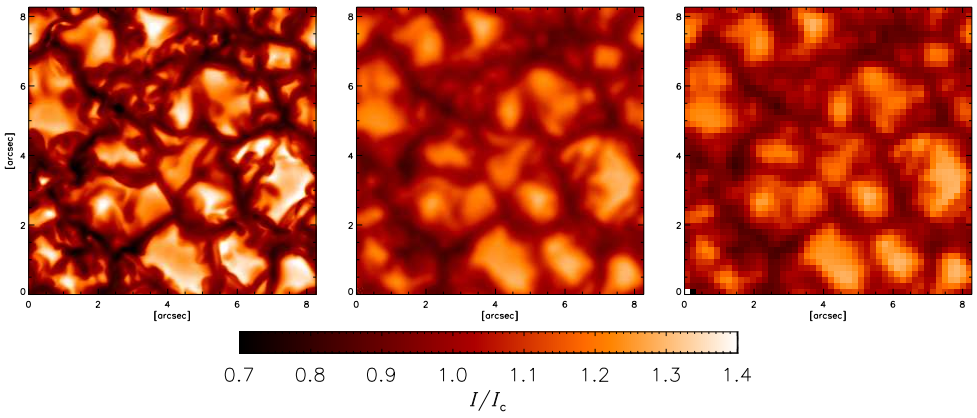

FIGURE 6.3:— Left: Continuum intensity maps from the simulation snapshot with average unsigned flux of 10 Mx cm^{-2}. Middle: same, but for the data spatially degraded considering telescope diffraction. Right: same after further degradation by CCD pixel size. Color scales are the same in the three maps. The contrast varies from 13.7% in the original image to ∼8.5% in the spatially degraded ones.

Broadband Filter Imager, see Wedemeyer-Böhm (2008).

The spatial degradation is applied to monocromatic images, i.e., for each snapshot we have spatially degraded a total of 113×4 images, corresponding to the number of wavelength samples times the number of Stokes parameters. Once the images have been degraded by telescope diffraction[3], we take into account the sampling of the detector, i.e., the 113×4 images are rebined to match the *Hinode*/SP CCD pixel size of 0.″16. Actually, the spatial sampling of the rebined images corresponds to 0.″172. The reason is the following: the step size of the MHD simulations is 0.″0287. A pixel size of 0.″16 corresponds to 5.6 pixels in the original data. To avoid interpolations between pixels, we assume a final spatial sampling of 0.″172, i.e., 6 pixels from the original resolution, which leaves us with monochromatic images of 48×48 pixels.

Once the spatial degradation has been applied to the data, we account for the spectral smearing of the *Hinode* spectrograph. To this end all four Stokes profiles from the 48×48 pixels of the FOV are convolved with a Gaussian of 25 mÅ FWHM. Finally, noise at the level of $10^{-3}\,I_c$ is added to the profiles to simulate the detector photon noise.

[3]Since no confusion is possible, we hereafter refer to telescope diffraction and CCD pixel size effects as spatial degradation.

6.3.5 Effects of telescope diffraction and spectral smearing

Figure 6.3 shows continuum intensity maps for the original data, and for the degraded data with and without CCD pixilation, corresponding to the 10 G snapshot. The instrument causes two main effects: a reduction of the rms contrast from 13.7% to 8.5%, and a worse spatial resolution, as can be seen from the pixilation due to the CCD in the degraded image. Intergranular fine-scale structures are apparently lost after degrading the image. The rms intensity contrast of the granulation in real *Hinode*/SP observations is about 7.5%, slightly lower than in our spatially degraded data. As shown by Danilovic et al. (2008), the spider legs of the secondary mirror reduce the rms contrast an additional ∼0.2%. The difference between the contrast in real images and the spatially degraded simulations can be ascribed to second-order optical aberrations, including SP defocus (which may reduce the contrast by 1%). The focal plane package of SOT is not achromatic, and therefore some amount of defocus occurs in the SP when the BFI or the NFI are focused.

The top panel of Fig. 6.4 compares the average Stokes I profiles from the spatially degraded data (10 G) and the NSO Fourier Transform Spectrometer Atlas of the quiet Sun. Both spectra are very similar, with only small differences in the line core and wings of Fe I 630.1 nm. The lack of a temporal average excludes, for instance, the effect of the 5-min oscillation in the simulated profile. This might explain part of the observed differences.

The bottom panels of Fig. 6.4 show the distribution of the Stokes V and $L = \sqrt{Q^2 + U^2}$ amplitudes of the spatially and spectrally degraded profiles for the three simulation snapshots used in this Chapter. Clearly, the amplitude of the polarization signals increases as the mean flux density of the snapshot increases.

Telescope diffraction modifies the shape of the Stokes profiles. Figure 6.5 shows an example from an intergranular lane, before and after the spatial degradation of the image. The profile shapes change dramatically after the degradation: Stokes I is broader and shifted towards the blue; Stokes Q, U, and V are smaller in amplitude and smoother; finally, the spectra show less asymmetries. The comparison of the profiles has been done before binning the images to the final pixel size of $0\farcs172$ and without considering the finite resolving power of the spectrograph.

Diffraction affects each pixel differently depending on its neighboring pixels. This makes it difficult to characterize how telescope changes the Stokes profiles. To get some insight we analyze the total circular polarization and total linear polarization signals, defined as TCP $= \int |V(\lambda)|/I_{\rm c} d\lambda$ and TLP $= \int (Q^2(\lambda) + U^2(\lambda))^{1/2}/I_{\rm c} d\lambda$, respectively. Figure 6.6 shows the TCP and the

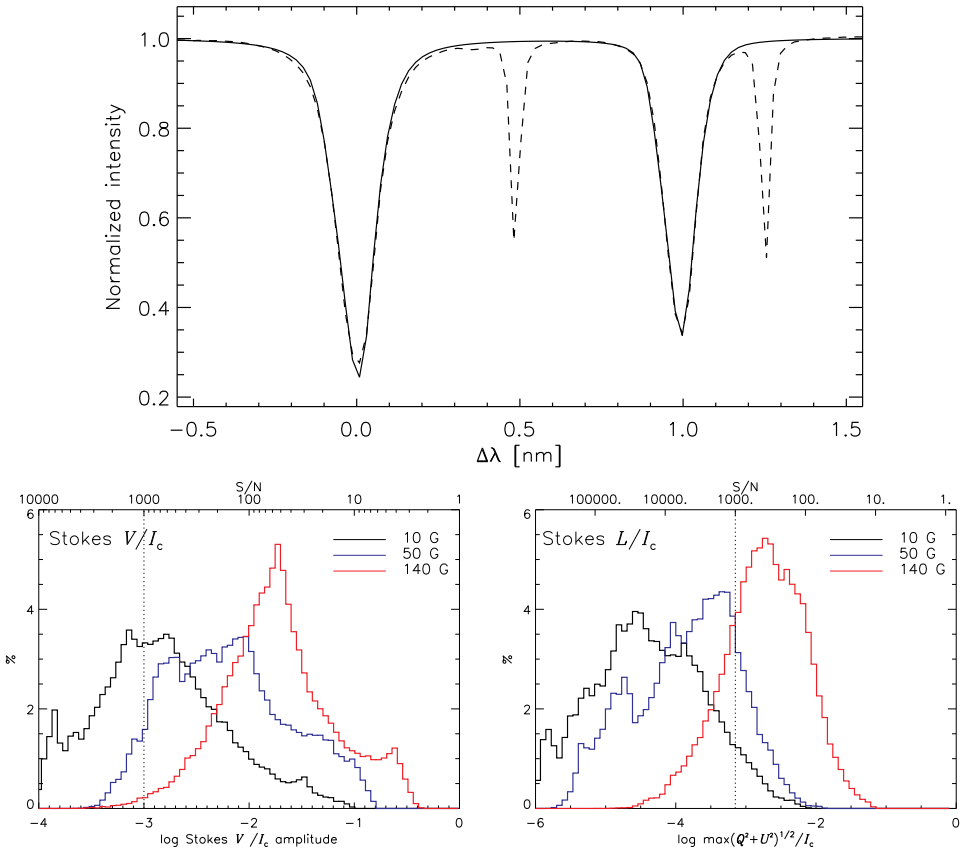

FIGURE 6.4:— Top: Comparison between the average Stokes I profiles from the spatially degraded data (solid) and the FTS spectral atlas (dashed). Their continua are both normalized to unity. Bottom: Distribution of the Stokes V and $L = \sqrt{Q^2 + U^2}$ amplitude in the spatially and spectrally degraded images corresponding to the simulation runs with $\langle B \rangle = 10$, 50, and 140 G. Vertical lines indicate S/N = 1000 for each Stokes parameter.

TLP maps for the original and degraded data both of them rebinned to the *Hinode*/SP CCD pixel size. The pixilation is clearly visible in the four panels of the figure. The color scales are the same in the various panels to emphasize the differences in contrast that occur. The top panels show the images as we would record them with an ideal telescope of 50 cm allowing all spatial frequencies to be identically transmitted, while the bottom panels show the real effects of telescope diffraction.

Diffraction makes polarization signals to appear "blurred" in the degraded image. It also substantially diminishes the contrast due to the weakening of the

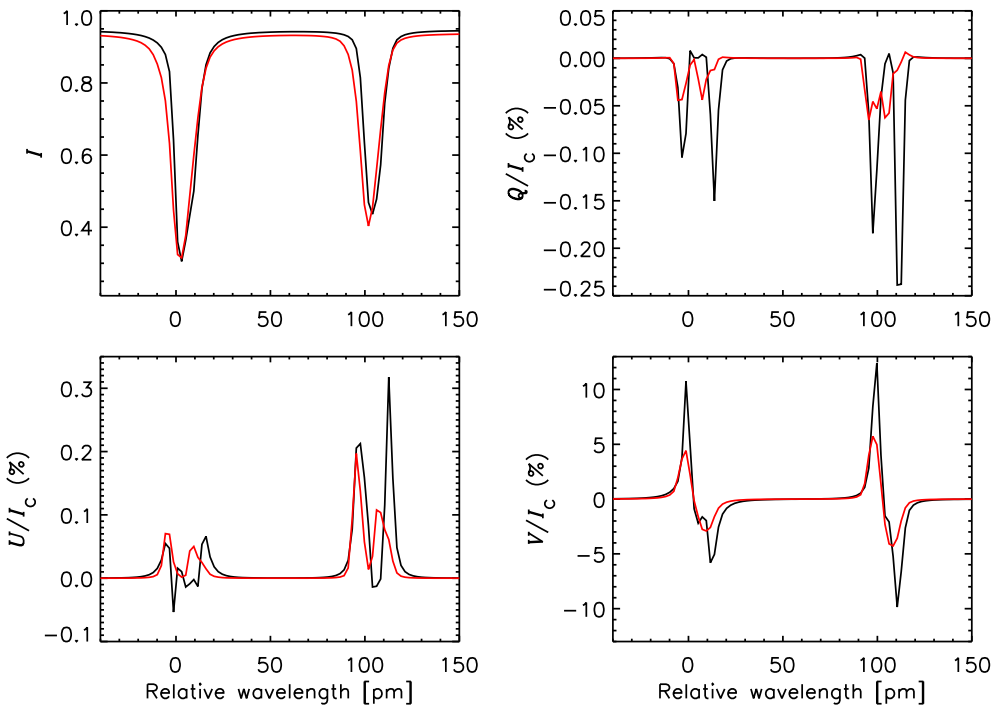

FIGURE 6.5:— Stokes I, Q, U and V profiles corresponding to the pixel x=87 y=170 of the simulation run with $\langle B \rangle = 10$ G before and after image degradation (black and red lines, respectively). The image has not been rebinned to the pixel size of $0\farcs16$, in order to make a direct comparison.

polarization signals. The spatial degradation acts in the same direction for both the TCP and TLP signals. It is also clear that small-scale structures (higher spatial frequencies) seen on the TCP and TLP original maps disappear after the image object has passed through the telescope: the MTF of the telescope behaves as a *low-pass* filter. Finally, notice that *the effect of diffraction on the polarization is the same as that of a magnetic filling factor*: in both cases the polarization signals are smaller in amplitude.

The distributions of Stokes V and L amplitudes in the original and degraded maps provide more quantitative information about the effects of telescope diffraction and CCD pixel size. In Fig. 6.7 we show histograms corresponding to the simulation run with $\langle B \rangle = 10$ G. Noise has not been considered in this analysis. The histograms of V and L are asymmetric, with a steep tail toward large and small amplitude values, respectively. They have a clear maximum, which in the case of Stokes V is located at about -2.6 and -3 dex for

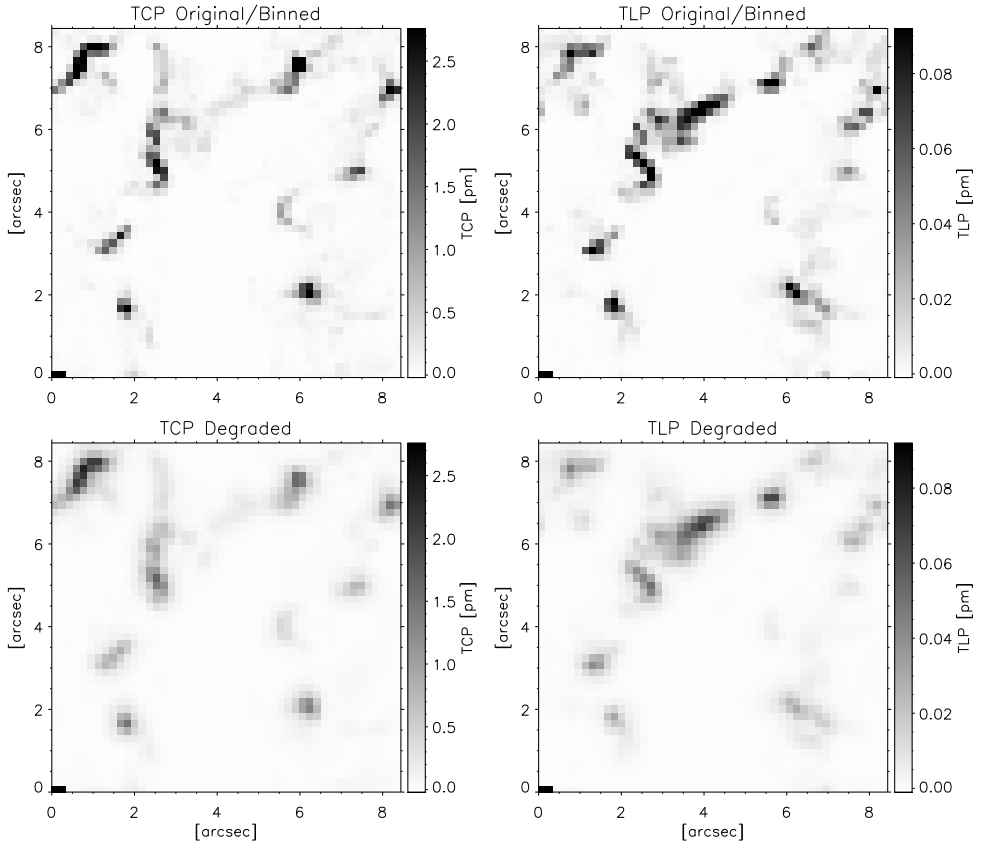

FIGURE 6.6:— Total circular polarization signal (TCP) and total linear polarization signal (TLP), as we would record it on the *Hinode*/SP CCD without the effects of telescope diffraction, i.e., the binned original image, and with the changes due to telescope diffraction (bottom panels).

the original and degraded images, respectively.

The distribution of Stokes V amplitudes reflects the effects of diffraction: first, its shape is modified, i.e., the large Stokes V amplitude region is less populated while the weaker amplitudes are more numerous, and secondly the histogram shifts as a whole towards smaller amplitude values. The effects on L are slightly different. The distribution of Stokes L after diffraction is narrower. The largest/weakest Stokes L amplitudes are less populated while the frequency of intermediate amplitudes increases. The position of the histogram peak does not change significantly.

The PSF of the telescope distributes part of the polarization signal of a pixel

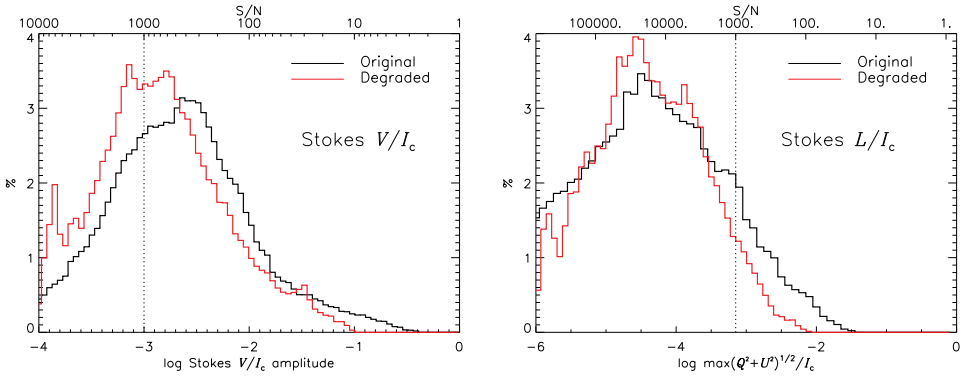

FIGURE 6.7:— Distribution of the Stokes V and $L = \sqrt{Q^2 + U^2}$ amplitudes in the original (black) and degraded (red) images. The Stokes profiles have been taken from the simulation run having $\langle B \rangle = 10$ G.

to nearby ones. For point sources the effect of diffraction is easily visualized as a "bloom" of the polarization signals (Lites et al. 1999): the pixel spreads out its signal to the immediate non-magnetic vicinity, generating a bigger structure. In general, polarization signals are not isolated and therefore all pixels will spread their signal out. However, pixels with strong polarization signals will tend to loose strength and those with weaker signals will take that from their surroundings.

Overplotted in Figs. 6.4 and 6.7 are vertical lines indicating S/N=1000, i.e., the typical noise level of *Hinode*/SP. Stokes V (or L) signals with amplitudes below these thresholds would be hard to detect. The position of the maximum of the non-degraded Stokes V histogram lies close to the S/N=1000 boundary, while the maximum of Stokes L is always below it. This implies that a non-negligible amount of pixels exhibit circular and linear polarization signals that are below the detection limit already in the original MHD simulations. The fraction of such pixels increases when the image is spatially degraded. The number of Stokes V signals above the noise level decreases to ∼12%. In this analysis we have included the contribution of the limited resolving power of *Hinode*/SP, which shifts the histograms as a whole toward smaller amplitude values. For a FWHM of 25 mÅ, however, the shifts are small.

6.4 Inversion

As we have shown, diffraction alters the shapes of the Stokes profiles, mixing information from nearby pixels. Is it possible to infer the magnetic field vector

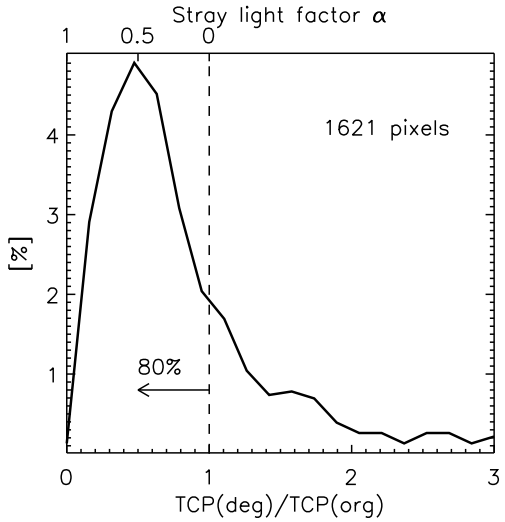

FIGURE 6.8— Histogram representing the ratio of total circular polarization signal in the degraded image with respect to that in the original image, for the simulation run with $\langle B \rangle = 10$ G. The upper X-axis indicates the equivalent stray-light contamination factor.

under these conditions? In this section we aim at understanding how telescope diffraction hampers the inversion of *Hinode*/SP measurements. In other words, we want to examine how the degradation of the data by the telescope affects the inference of the various physical quantities.

We derive the magnetic field vector from the simulated profiles using the MILOS code. As we have discussed in Chapter 5, inversion techniques based on ME atmospheres represent the best option to interpret the measurements if one is not interested in vertical gradients of the physical quantities. They are simple and often provide reasonable averages of the atmospheric parameters over the line formation region (e.g. Westendorp Plaza et al. 1998; Bellot Rubio 2006).

6.4.1 Modeling telescope diffraction

In this section we explain a possible way to take into account the effects of telescope diffraction. Figure 6.8 displays the ratio of total circular polarization signal in the degraded snapshot with respect to that in the original snapshot, for the simulation run with $\langle B \rangle = 10$ G. Only pixels whose Stokes Q, U, or V amplitudes remain above $4.5 \times 10^{-3}\, I_c$ after degradation are considered here, since the others are below the noise level. This leaves us with 1621 pixels. In line with the results of Sect. 6.3.5, the histogram indicates that the circular polarization signal is smaller in the degraded image: 80% of the pixels show weaker signals. The decrease in polarization signal is not due to cancellation of opposite polarity fluxes (since mixed polarities are not present in the snapshot

at very small spatial scales), but is truly the result of diffraction.

If one does not account for the reduction in polarization signals caused by telescope diffraction, the inversion would systematically fail. In pixels where the magnetic field is intrinsically weak, the field strength is determined mainly from the Stokes V amplitude. In this case, not correcting for the effects of diffraction would lead to inferred field strength that are too weak.

For this reason we use a stray/scattered-light contamination factor in the inversion of the Stokes profiles even if there is no atmospheric seeing affecting the SP observations. A reduction in polarization signals also occurs when only a fraction of the pixel is occupied by the magnetic field. In this case, the stray-light contamination factor we use would act as the filling factor of a non-magnetic component (the one generating the stray-light profile) which occupies the rest of the resolution element. There is no way to distinguish between the two cases, i.e., between the effects of diffraction and those of a real magnetic filling factor.

Since telescope diffraction mixes light from nearby pixels, not from pixels far away, a local stray-light profile must be considered. This differs from typical strategies for the stray-light evaluation. In our case, the stray light profile is computed individually for each pixel by averaging the Stokes I profiles within a box $1''$-wide centered on the pixel. Notice that the FWHM of the *Hinode*/SP MTF (Fig. 6.2) is about 1 arcsec.

This treatment of telescope diffraction is simplistic because we use an *unpolarized*[4] stray-light contamination, while it is clear that diffraction also mixes the polarization signals. In Fig. 6.8 it can be seen that 20% of the pixels show larger polarization signals after degradation. For those pixels the adopted strategy of a stray/scattered-light for the inversion is not appropriate because a stray-light factor can only reduce the polarization signals. However, as we will see below, this new strategy represents a significant improvement over conventional treatments in which a single global stray-light profile is employed to invert the observed spectra.

The differences between simulated *Hinode*/SP observations analyzed with a global and a local stray-light profile are illustrated in Fig. 6.9 for a single pixel. The best fit using a global stray-light contamination cannot simultaneously explain the intensity and polarization spectra because the stray-light profile has a different shape than that needed to account for the observed Stokes I profile. The problem disappears when a local stray-light profile is used, improving the

[4]By unpolarized stray light we mean that the Stokes Q, U and V parameters are identically zero. Note that when averaging the Stokes I profiles in the neighborhood of a pixel we are including the polarization signatures present in Stokes I as, for example, the Zeeman splitting.

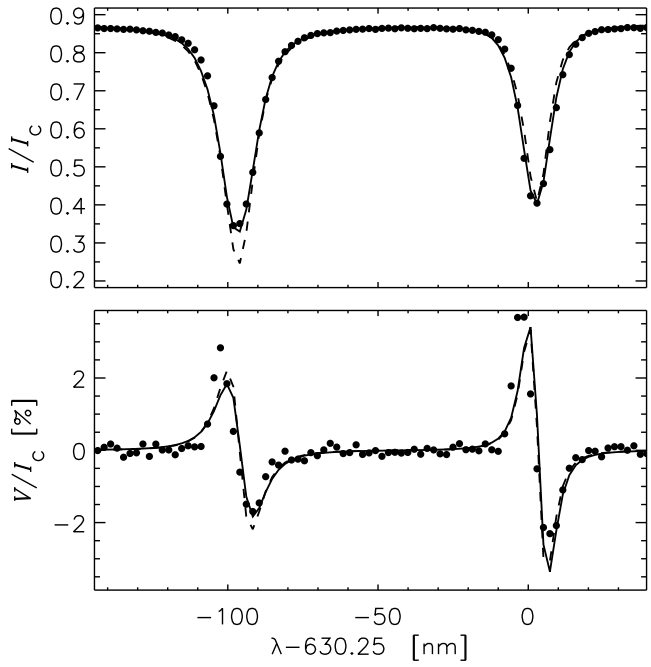

FIGURE 6.9:— Observed (dots) and best-fit Stokes I and V profiles from simulated *Hinode*/SP observations using a global (dashed) and a local (solid) stray-light profile in the inversion. The stray-light factors are 15% and 55%, respectively. The local stray-light inversion results in a significantly better fit to the intensity profile.

determination of the intrinsic field strength.

6.4.2 Inversion strategy

To determine the atmospheric parameters from the simulated *Hinode*/SP observations we apply the ME inversion to the Fe I 630.15 nm and Fe I 630.25 nm lines simultaneously. A total of 10 free parameters are retrieved (S_0, S_1, η_0, $\Delta\lambda_D$, a, B, γ, χ, v_{LOS}, and α). We do not allow for additional broadening of the profiles by macroturbulence. In all inversions we use the same initial guess model, allowing a maximum of 300 iterations. The initial guess model given by S_0=0.02, S_1=1, η_0=4.9, $\Delta\lambda_D$=29 mÅ, a=0.45, B=100 G, γ=45°, χ=45°, v_{LOS}=0.1 km s^{-1}, and $\alpha = 10\%$.

Three different inversions are performed to derive the atmospheric parameters. All of them use a simple one-component model, i.e., *a laterally homogeneous magnetic atmosphere occupying the whole resolution element*. We first

invert the profiles in the absence of noise, and then with noise added at the level of $10^{-3}\,I_c$. In the third inversion, the noisy profiles are fitted considering non-zero stray-light contaminations factors. The last two inversions allow us to study the improvement brought about by the use of a stray light profile to account for telescope diffraction. The inversion is applied to the three snapshots with $\langle B \rangle = 10$, 50 and 140 G (see Sect. 6.2).

6.5 Results

Figure 6.10 shows the vector magnetic field (strength, inclination, and azimuth) retrieved from the inversions of the Stokes profiles. The first row displays a cut at optical depth $\log \tau = -2$ of the simulation snapshot with average flux density of 10 Mx cm^{-2}. The second and third rows contain the results of the ME inversions of the degraded profiles in the absence of noise and the specific case of a S/N of 1000, respectively. Finally, the fourth row shows the atmospheric parameters derived from the noisy profiles accounting for telescope diffraction. White regions represent pixels which have not been inverted because of their small polarization signals (we only consider pixels whose Stokes Q, U or V amplitudes exceed three times the noise level).

Over the granules, the magnetic field is very weak and the polarization signals are buried in the noise for the most part. These pixels represent $\sim$55% of the total area (white regions in Fig. 6.10). The stronger fields concentrate in intergranular regions. In those regions, the magnetic structures inferred from the inversion have bigger sizes than the real ones, i.e., they appear "blurred". This is caused by the degradation of the images due to telescope diffraction and CCD pixel size as explained in Sect. 6.3.5. The field inclination and azimuth structures resulting from the inversion are blurred as well. The azimuth values are rather uncertain because of the tiny linear polarization signals produced by the weak fields of the simulations.

Figure 6.11 is a close up of small features observed in intergranular lanes. When we consider that the polarization signal is produced by a single magnetic component within the resolution element and the telescope diffraction is not corrected, the inferred field strengths are smaller than those in the model, so the field is underestimated (middle panels of Fig. 6.11). If one accounts for the effects of telescope diffraction via a stray-light factor, the inferred fields become stronger, i.e., closer to the actual ones (right panels), but also noisier due to the increased number of free parameters. Note that each *Hinode*/SP pixel of $0\farcs16 \times 0\farcs16$ corresponds to 36 pixels in the simulation, hence they usually contain a broad distribution of magnetic field strengths.

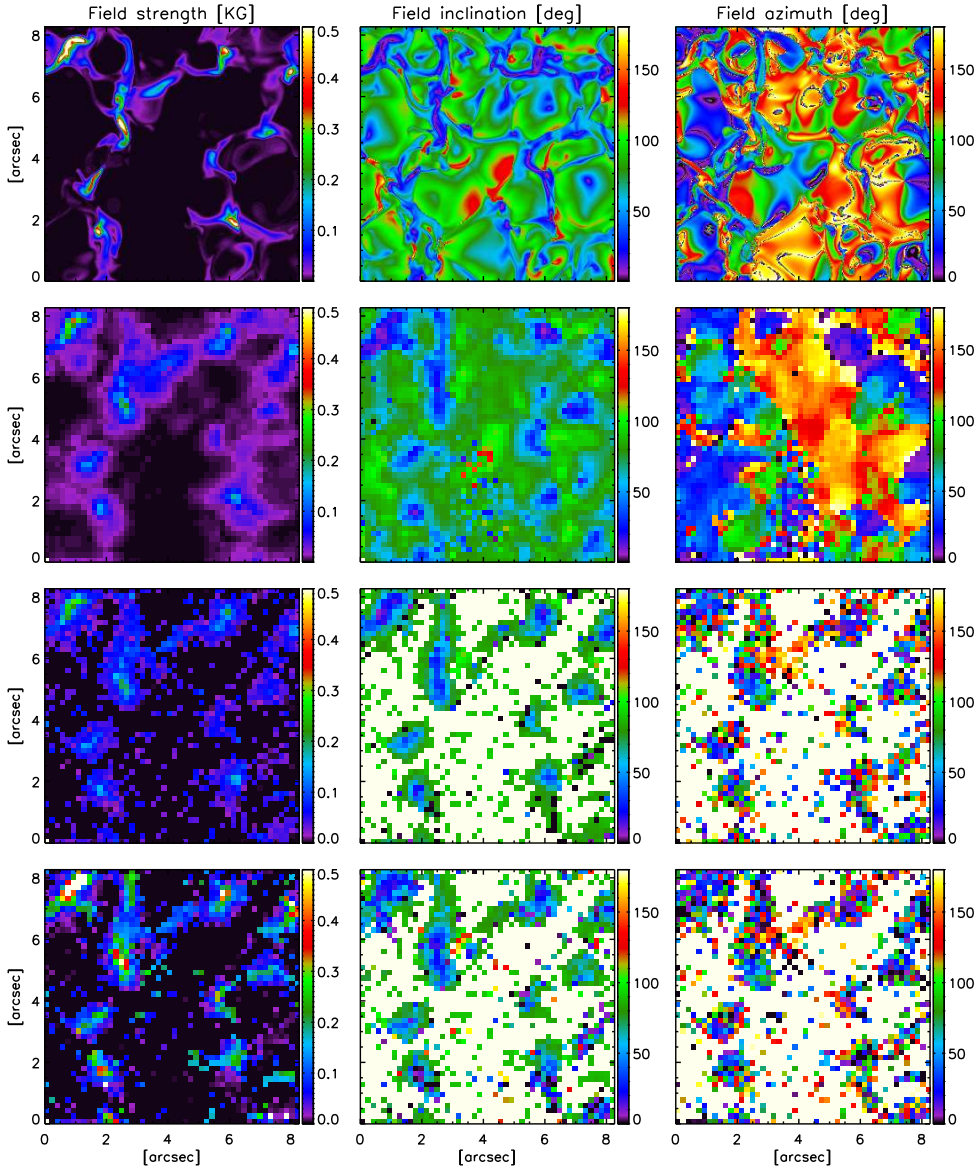

FIGURE 6.10:— First row: Cuts at optical depth $\log\tau = -2$ of the model atmospheres provided by the MHD simulation with average unsigned flux of 10 Mx cm^{-2}. Second row: Maps of the physical quantities retrieved from the ME inversion of the simulated SP profiles with no noise. Third row: Maps retrieved from the ME inversion of the profiles with S/N of 1000 and no correction for telescope diffraction. Fourth row: Same as before, but accounting for diffraction (through stray-light contamination). From left to right: magnetic field strength, inclination, and azimuth. White pixels represent non-inverted pixels.

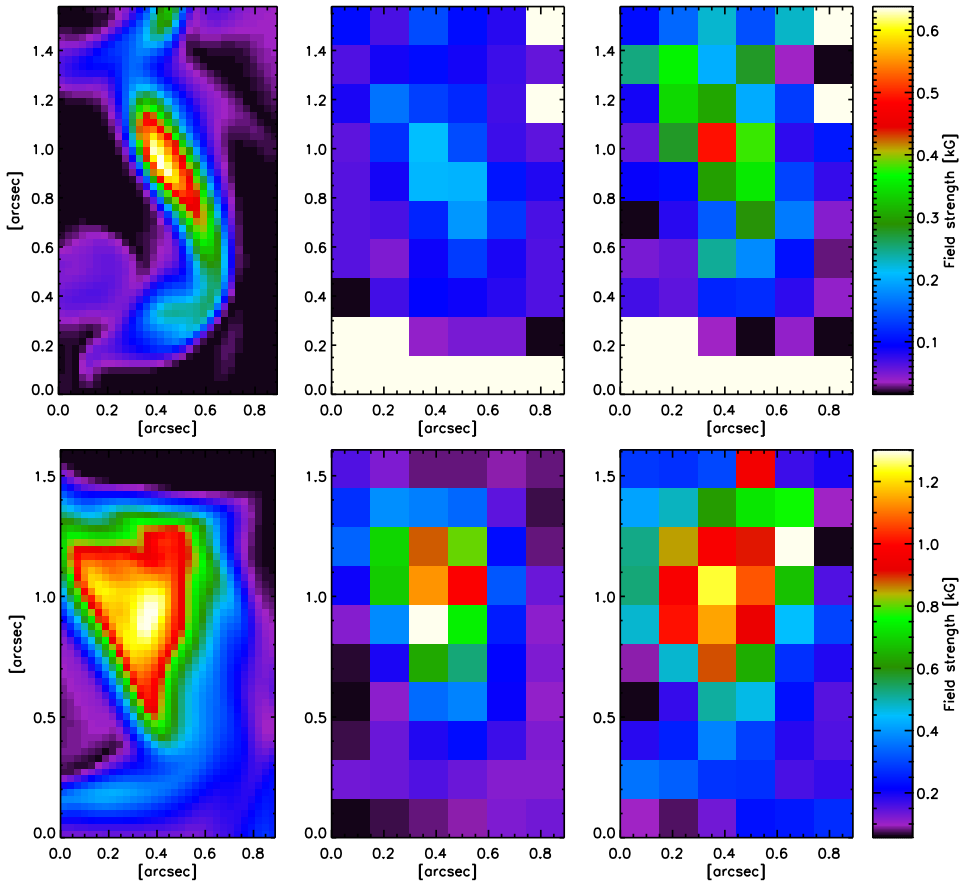

FIGURE 6.11:— Left: Field strengths at $\log\tau = -2$ in the MHD simulations with 10 Mx cm^{-2} (top) and 50 Mx cm^{-2} (bottom). Middle: Field strengths derived from the ME inversion of the spatially degraded Stokes profiles with S/N=1000 and no stray light contamination. Right: Field strengths from the ME inversion correcting for telescope diffraction.

To analyze these results in a more quantitative way we calculate the mean and rms values of the errors. We define the error as the difference between the inferred and the real parameters at optical depth $\log\tau = -2$. This optical depth has been chosen after the comparison of the inversion results with the real stratifications at different optical depths. It is indeed the one yielding smaller rms errors for the inferred model quantities. Since one pixel of the degraded contains 36 pixels in the simulations, we compare each inverted pixel with the mean of the corresponding 36 pixels in the original map. By comparing the retrieved atmospheric quantities with the real ones at a fixed optical depth we

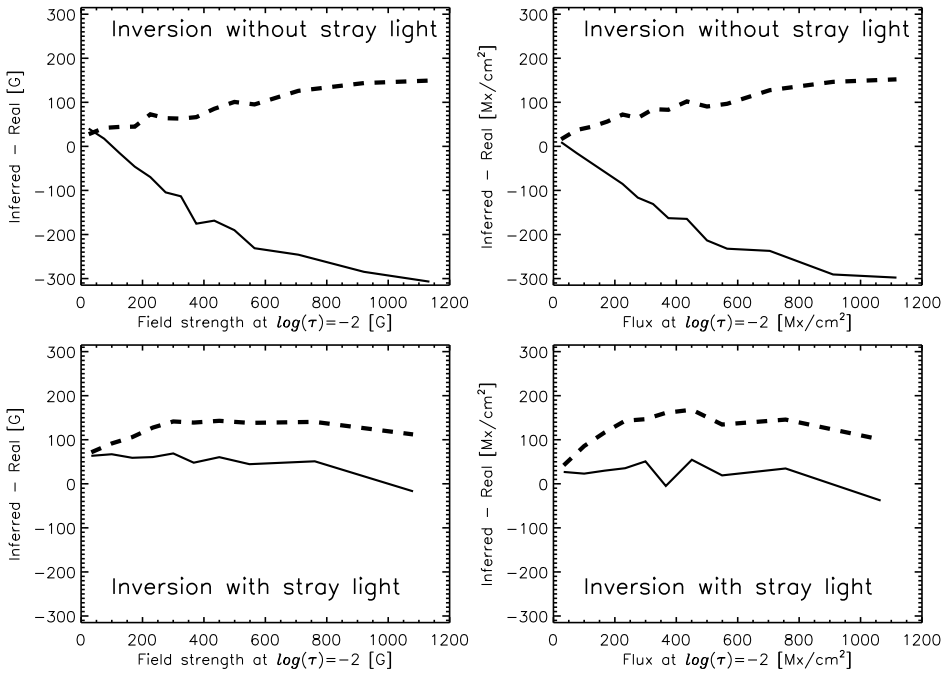

FIGURE 6.12:— Top: Mean (solid) and rms (dashed) errors of the field strength (left) and flux density (right) derived from the inversion of the profiles with S/N=1000 assuming a single magnetic atmosphere and no stray-light contamination. Bottom: Same as on top but accounting for stray-light contamination.

are including all possible sources of error in the analysis, i.e., the inability of the ME solution to fit asymmetric profiles, the degradation of the images, and photon noise.

Figure 6.12 shows the mean and rms errors of the field strength resulting from the inversion without accounting for telescope diffraction (top left panel). It is clear that fields above ∼100 G are underestimated. The results are similar for the magnetic flux density (top right panel). The inversion considering stray-light contamination as a means to correct for telescope diffraction yields much better inferences, as can be seen in the bottom panels of Fig. 6.12. The field strength and flux are slightly overestimated for weak fields, but the rms errors do not exceed 150 G in any case.

Figure 6.13 shows the mean and rms errors for the field inclination resulting from the inversion with and without stray-light contamination (right and left panels, respectively). Interestingly, the mean and rms values are larger when we correct for the effects of telescope diffraction. The rms errors remain well

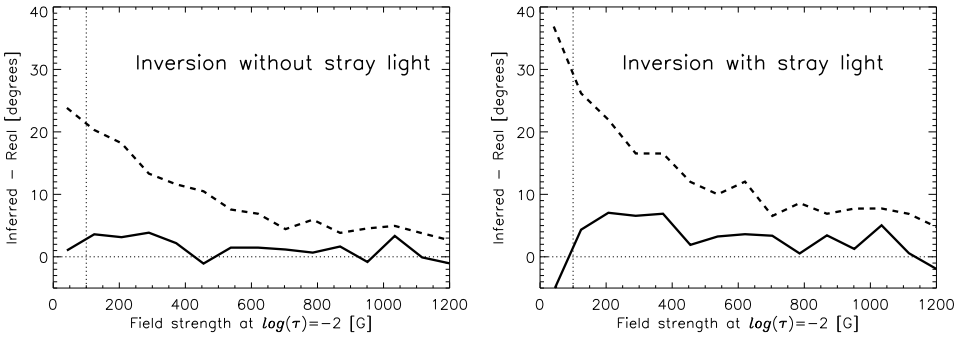

FIGURE 6.13:— Left: Mean (solid) and rms (dashed) errors of the field inclination derived from the inversion of the profiles with S/N=1000 assuming a single magnetic atmosphere and no stray-light contamination. Right: Same as before but accounting for stray-light contamination.

below $\sim 20^\circ$ for fields stronger than 200 G, increasing linearly for weaker fields. The mean values are of about $\sim 5^\circ$, at most.

Figure 6.14 shows the distribution of stray-light factors derived from the inversion of the simulated profiles with noise at the level of S/N=1000. The histogram is rather symmetric and has a clear maximum at $\alpha = 0.55$. Overplotted is the ratio of total circular polarization signal in the degraded image with respect to that in the original image (dashed line). The strong resemblance between the two distributions indicates that *the stray-light factors derived from the inversion actually model the effects of telescope diffraction and CCD pixel size*. In other words: the inferred α's do not represent a real magnetic filling factor, but just the degradation of the image caused by the instrument. This is valid under the following conditions:

- a simple one-component model is used in the inversion
- the data have a spatial resolution of $0\farcs32$
- the data are not contaminated by atmospheric seeing.

6.6 Discussion

ME inversions of the Fe I 630 nm lines at spatial resolutions of about $0\farcs3$ (the case of *Hinode*/SP) underestimate the magnetic field strength by some hundred G if no correction for telescope diffraction is made. When a stray-light factor

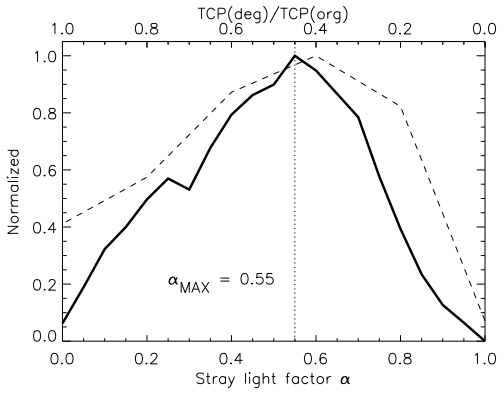

FIGURE 6.14— Normalized histogram of the stray light factor derived from the inversion of the profiles with S/N=1000 (solid line). Overplotted is the histogram representing the ratio of TCP in the degraded image with respect to that in the original image (dashed line). Equivalent units are in the upper X-axis. The dotted vertical line indicates the peak of the stray light factor distribution.

is used, ME inversions are able to recover the magnetic field strength and inclination with reasonable accuracy.

A very important result of our analysis is that we always derive weak fields from the simulated *Hinode*/SP observations where the field in the MHD model is weak. Likewise, strong fields retrieved by the ME inversion actually correspond to strong fields in the MHD model. This is in sharp contrast with the results of Martínez González et al. (2006), whose inversions of IN profiles observed at $\sim$1″-1.″5 resolution yield strong or weak fields depending on the initialization. The difference between our results and those of Martínez González et al. is probably due to:

1- Our significantly higher spatial resolution, which makes the polarization signals larger by a factor of $\sim$10 and also narrows the range of field strengths present in the pixel. In fact, higher resolutions can be expected to imply larger filling factors. Stronger polarization signals should reduce the effects of noise on the observed Stokes profiles. Another advantage of the increased spatial resolution is that signals which were buried in the noise now become visible.

2- Our model atmosphere is much simpler than those considered by Martínez González et al. (one component vs two-component models) and we do not employ micro- or macroturbulent velocities. This reduces the degrees of freedom of the solution and the possibility of crosstalk between different atmospheric quantities.

3- The simple description of the thermodynamics provided by the ME model, which does not allow the temperature and micro-turbulence to compensate for incorrect magnetic parameters, contrary to the atmospheres used by Martínez González et al.

To determine the magnetic field strength and magnetic flux we need to account for telescope diffraction. We do it by including a stray-light profile in the inversion. Our results show that the inferences of the field strength and magnetic flux improve when a local stray-light contribution is used. Due to the larger number of free parameters, the field inclinations retrieved from the inversions are more uncertain. In any case, the variation is not dramatic: on average, the inclination error is smaller that $\sim 5^\circ$ and the rms remains below 20° for fields stronger that 200 G. This means that the ME inversion is able to distinguish purely vertical fields from purely horizontal ones, even when Q and U, or V, are below the noise level. The reason is that Stokes I also carries information about the inclination of the magnetic field vector.

We caution that these results may only be valid as long as the MHD simulations provide a realistic description of the Sun. The performance of ME inversions could be different if the magnetic field is structured on scales much smaller than $\sim 0\farcs3$. For the moment, however, there is no compelling observational evidence of extremely tiny magnetic elements in the quiet solar photosphere.

Finally, it is important to remind that ME inversions are not able to reproduce the asymmetries exhibited by the Stokes profiles used in this analysis. Interestingly, image degradation "helps" the ME inversion algorithm fit the profiles because *degradation smooths out profile asymmetries*. An analysis of the χ^2 values of the fits to the profiles before and after the degradation shows that the inversion of the degraded profiles yields better χ^2 values. This, however, does not mean smaller uncertainties for the inferred atmospheric parameter. Independently of the fit quality, the ME model is not always able to explain the shapes of the Stokes profiles, especially those exhibiting strong asymmetries. As we have shown in Chapter 5 ME inversions do not account for vertical stratifications, they just provide averaged values of the atmospheric quantities over the line forming region.

6.7 Conclusions

We have used the best magnetoconvection simulations of the quiet-Sun surface currently available to examine the diagnostic potential of the pair of Fe I lines at 630 nm in the case of very high spatial resolution, seeing-free observations as those provided by the *Hinode*/SP instrument. To this end we have applied a degradation to the original Stokes profiles to simulate the SP and then we have used MILOS code to infer the magnetic field vector.

Telescope diffraction and CCD spatial sampling lead to:

- Reduced image contrast and blurred polarization signals
- Disappearance of the smallest structures
- A mixing of light from nearby pixels: 80% of the pixels show weaker polarization signals
- A smoothing of the asymmetries exhibited by the Stokes profiles
- A reduction of the amount of polarization signals detectable above the noise level. As a consequence, the number of pixels showing weak fields decreases against those harboring stronger fields, whose abundance does not change.

The ME inversion results show that the visible lines at 630 nm can be used to study the magnetism of the quiet Sun when the spatial resolution is high. At $0\farcs3$ we obtain for the magnetic field strength uncertainties smaller than 150 G in the whole range of strengths from ∼0.1 to 1 kG. The magnetic field inclination is nearly determined (uncertainties smaller that 20°) for field as weak as 200 G. The azimuth values, however, are rather uncertain because of the very weak linear polarization signals present in the IN. Overall, these results justify the use of the Fe I 630.2 nm line pair by space-borne instruments.

Previous analyses of visible (630.2 nm) and near-infrared (1565 nm) iron lines do not agree on the distribution of field strengths in IN regions, as observed at $\sim1''$. In particular, the visible lines systematically deliver kG field strengths and small filling factors, while the near-infrared lines favor a predominance of hG fields (see Khomenko 2006, for a recent review). Our analysis suggests that *Hinode*/SP observations should make it possible to determine the real distribution of field strengths in quiet Sun internetwork regions using one-component Milne-Eddington inversions, provided the effects of telescope diffraction are modeled by means of a local, stray-light contamination factor.

In the next Chapter, we undertake an analysis of real *Hinode*/SP observations of the quiet-Sun, in an attempt to characterize the magnetic fields of IN regions. Hopefully, this will help bring to an agreement the results from the spectral ranges mentioned above.

7

Quiet Sun internetwork magnetic fields from the inversion of *Hinode* measurements

In this Chapter we analyze Fe I 630 nm observations of the quiet Sun taken with the spectropolarimeter of the Solar Optical Telescope aboard the *Hinode* satellite. The analysis of the polarization profiles is based on the strategy presented in Chapter 6, i.e., a Milne-Eddington inversion that includes a *local* stray-light contamination to account for the effects of telescope diffraction. We derive the distribution of field strengths, inclinations, and stray-light factors, and compare them with earlier results. We also analyze the magnetic flux and other polarimetric quantities derived from the Stokes profiles. The influence of noise and initial guess models in the inversion results is investigated thoroughly. We find that the internetwork consists of very inclined, hG fields, while network areas exhibit a predominance of kG field concentrations, as expected. Accordingly to our results, the longitudinal and transverse flux density of the internetwork are 25 and 85 Mx cm^{-2} , respectively. The *Hinode*'s spectropolarimetric measurements bring to an agreement the results obtained from the analysis of visible and near-infrared lines.

7.1 Introduction

Since its launch in September 2006, the *Hinode*/SP has been taking high-precision, high-angular resolution measurements of the Fe I lines at 630.2 nm. The SP angular resolution of about $0\farcs32$ opens exciting possibilities for the analysis of the weak magnetic signals observed in the quiet Sun. It should permit, for instance, a better isolation of the magnetic elements that form the quiet photosphere, provided they are not organized on scales much smaller than $0\farcs1$. The increased spatial resolution may result in significantly larger polarization signals than those recorded on the ground. This would minimize the influence of noise, which has long been recognized as one of the main problems in the study of quiet Sun magnetic fields (Bellot Rubio & Collados 2003; Martínez González et al. 2006; López Ariste et al. 2006).

The availability of very high angular resolution observations, virtually free from seeing effects, is also important for other reasons. Since individual pixels sample a much smaller region of the solar surface, the effect of different atmospheres contributing to the intensity and polarization profiles is decreased. This should facilitate the interpretation of the measurements, as relatively simple one-component atmospheres may be sufficient to explain the observations. Stokes inversions of ground-based data are usually performed in terms of two-component atmospheres because the intensity and polarization profiles are not compatible with the signals emerging from a homogeneous magnetic atmosphere, due to the relatively modest angular resolution attained.

Both the smaller influence of noise and the possibility of using simple model atmospheres make high resolution measurements ideal to study the magnetism of the quiet solar photosphere. In Chapter 6 (see also Orozco Suárez et al. 2006) we investigated the diagnostic potential of the visible Fe I lines at 630 nm using radiative magnetoconvection calculations. The main result was that Milne-Eddington (ME) inversions of high-angular resolution Fe I 630 nm measurements satisfactorily recover the actual field strengths present in the simulations, provided the effects of telescope diffraction are accounted for.

In this Chapter we analyze measurements of the quiet Sun taken with *Hinode*/SP. These data have also been analyzed by Lites et al. (2007a, 2008a) and Orozco Suárez et al. (2007a,b). In Sect. 7.2 we describe the observations and some line parameters derived from the Stokes profiles. Next, the spectra are inverted in Sect. 7.3 using the strategy explained in Chapter 6. The qualitative results of the inversions are presented and discussed in Sect. 7.4. Sections 7.5 to 7.7 contain a quantitative analysis of the ME inversion results. We calculate the distributions of magnetic field strengths, inclinations, and filling factors for the full observed area and for the internetwork regions. We also evaluate the

TABLE 7.1:— Log of the observations. Note that the FOV in data set #2 corresponds to space and time (see text).

	DATA SET #1 (NORMAL MAP)	DATA SET #2 (HIGH S/N MAP)
Date	March 10, 2007	February 27, 2007
Start time (UT)	11:37:37	00:20:00
FOV	$302'' \times 162''$	$302'' \times 0\farcs16$
(Pixels)	1024×2048	1024×727
Exp. time	4.8 s	67.2 s
Stokes V noise	$1.1 \times 10^{-3}\, I_{\rm QS}$	$3 \times 10^{-4}\, I_{\rm QS}$
Stokes Q and U noise	$1.2 \times 10^{-3}\, I_{\rm QS}$	$2.9 \times 10^{-4}\, I_{\rm QS}$

magnetic flux density and compare our results with earlier observations and magnetoconvection simulations. In Sect. 7.10 we perform an in-depth analysis of how the ME solution depends on various inversion conditions, most notably the field strength initialization. This study demonstrates that the fields determined from the *Hinode*/SP measurements are reliable. We discuss the results and summarize the main conclusions in Sects. 7.11 and 7.12, respectively.

7.2 Observations

We use two different data sets taken at disk center. They will be referred to as sets #1 and #2, respectively. Table 7.1 summarizes the main parameters of the observations. To obtain the observation #1, the spectrograph slit (with solar N-S orientation), of width $0.16''$, was moved across the solar surface in steps of $0\farcs1476$ to measure the four Stokes profiles of the Fe I 630 nm lines with a spectral sampling of 2.15 pm pixel^{-1} and a exposure time of 4.8 s. The spatial coverage of data set #2 was smaller. In this case, the slit was kept fixed at the same spatial location and the Stokes spectra were recorded with an exposure time of 9.6 s. The completion of data set #1 took about 3 hours while the time series of data set #2 covers one hour and 51 minutes. The effective exposure time in observation #2 was increased by averaging seven consecutive 9.6 s measurements. This allowed a final exposure time of 67.2 s to be reached, which corresponds to a S/N gain by a factor of 3.74 with respect to data set #1. The *Hinode* correlation tracker makes it possible to perform averages over more than one minute due to the $\sim 0\farcs01$ rms image stabilization it provides (Shimizu et al. 2008). Such long effective exposure times decrease the spatial resolution of the observations to some degree, but the granulation is still perfectly visible

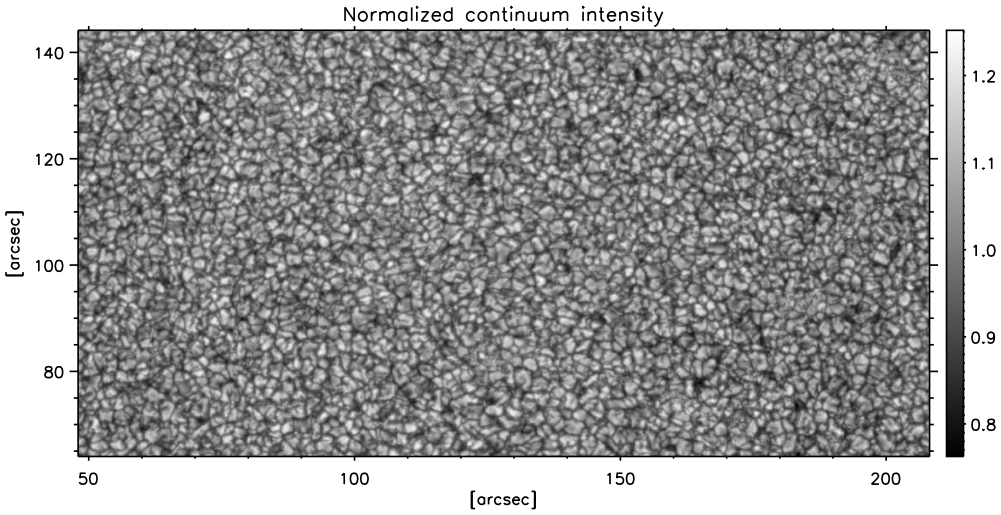

FIGURE 7.1:— Small area of $160'' \times 80''$ showing the continuum intensity of observation #1. The granulation contrast is 7.44%.

due to the much longer lifetime of regular granules (about 5 min, Title et al. 1998).

The polarization noise levels are shown in Table 7.1 for the two data sets. As explained before, the noise is reduced from observation #1 to #2 due to the longer exposure times of the latter. The noise level was obtained by taking the mean value of the standard deviation of the corresponding Stokes profile in continuum wavelengths. Before evaluating the noise, the data were corrected for dark current, flat-field, and instrumental cross-talk as explained by Lites et al. (2008b). The whole process was done using the IDL routine `sp_prep.pro` of the SolarSoft package. The Stokes profiles were normalized to the average quiet Sun continuum intensity, $I_{\rm QS}$, computed using all pixels from each data set. We will refer to the average quiet Sun continuum as either $I_{\rm QS}$ or $I_{\rm c}$.

7.2.1 Qualitative analysis of the polarization signals

Figure 7.1 shows the normalized continuum intensity of data set #1 (hereafter referred to as normal map) for a small subfield of $160'' \times 80''$. The scanned area covers both network and internetwork regions. The high contrast of the granulation, of about 7.5%, testifies to the quality of the observations.

Figure 7.2 shows maps of the (signed) total circular and linear polarization,

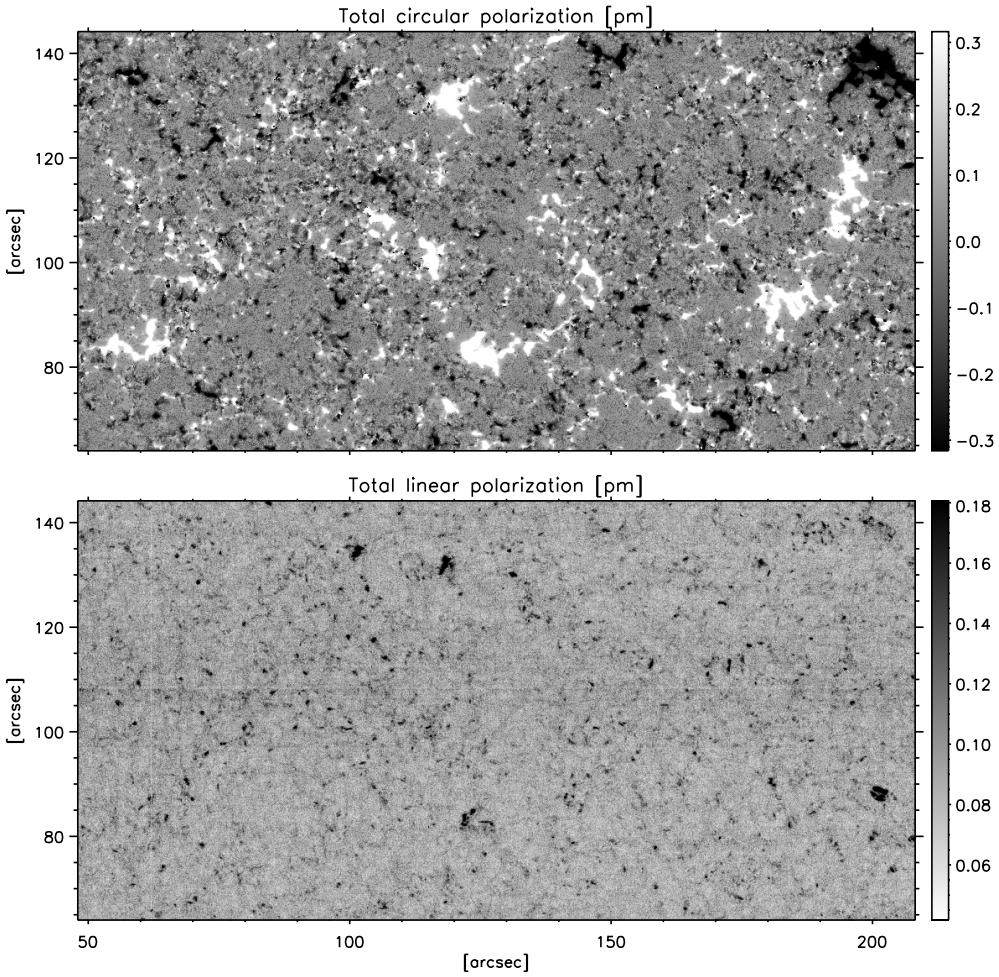

FIGURE 7.2:— Small area of $160'' \times 80''$ showing the total circular polarization, $V_{\rm TOT}$, and total linear polarization, $L_{\rm TOT}$ (top and bottom panels, respectively). Network and internetwork areas can easily be identified. The circular and linear polarization maps have been clipped at ± 0.7 and 0.3 pm, respectively.

defined as

$$\begin{aligned} V_{\rm TOT} &= {\rm sgn}(V_{\rm blue}) \frac{\int |V(\lambda)|\, {\rm d}\lambda}{I_{\rm c}}, \\ L_{\rm TOT} &= \frac{\int (Q(\lambda)^2 + U(\lambda)^2)^{1/2}\, {\rm d}\lambda}{I_{\rm c}}, \end{aligned} \tag{7.1}$$

where the integrals cover 21 wavelength samples centered on the line core position of the 630.25 nm line. For weak fields $V_{\rm TOT}$ is proportional to the longitu-

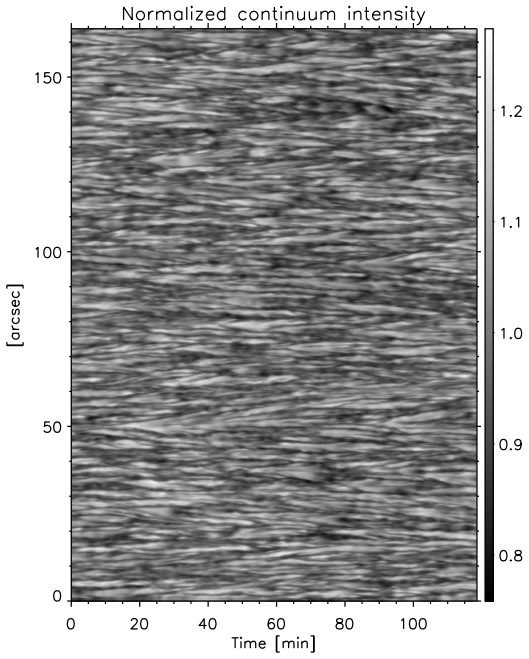

FIGURE 7.3— Normalized continuum intensity of data set #2. The Y-axis represents the slit, while the X-axis is time. The granulation contrast is 7.3%.

dinal magnetic flux density, while $L_{\rm TOT}$ represents the transverse flux density.

These maps contain a wealth of magnetic signals. In the $V_{\rm TOT}$ map one can easily identify several supergranular cells outlined by the network fields (intense white and black flux concentrations). The larger polarization signals correspond to areas where the granulation is distorted. The interior of the supergranular cells, i.e., the internetwork, is not devoid of magnetic signals. A careful look reveals many small patches of weak signal. Note that the gray scale for the total circular polarization map has been clipped at ± 0.7 pm to emphasize the IN. The $L_{\rm TOT}$ map shows a smaller abundance of magnetic features. The different patches, of similar sizes, are scattered across the map. The stronger (and larger) concentrations are located in network areas. The map also contains appreciable signal due to noise in addition to solar features (light-gray background). The nature of these IN fields is a controversial topic (see Khomenko 2006 for a recent review).

The continuum intensity map corresponding to data set #2 (hereafter referred to as the high S/N dataset) is shown in Fig. 7.3, while Fig. 7.4 dis-

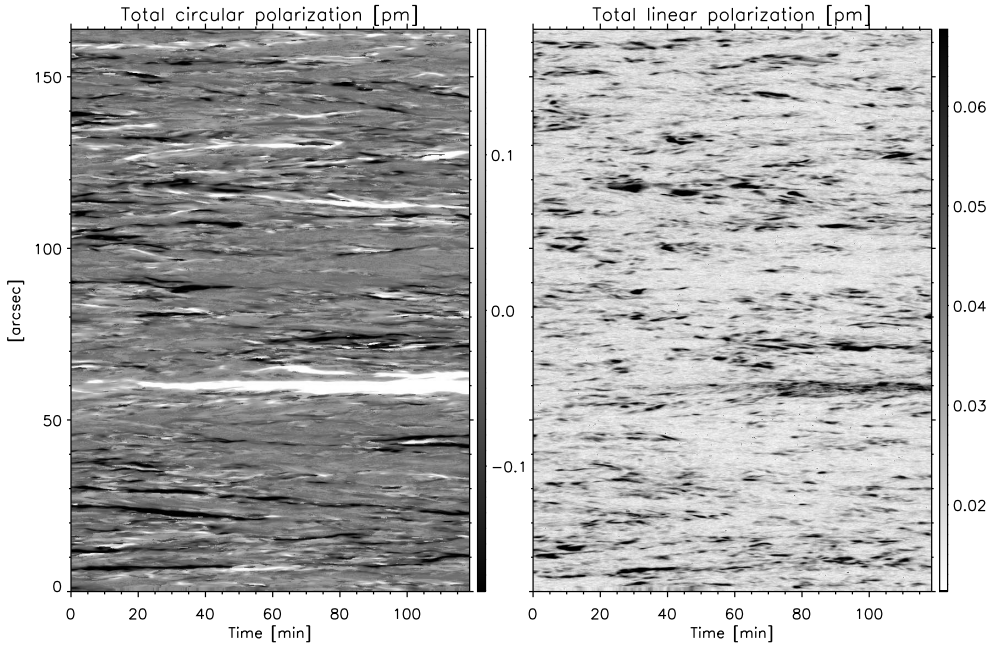

FIGURE 7.4:— Total circular and linear polarization in data set #2 (left and right panels). The signal maps have been clipped at 0.4 and 0.15 pm, respectively.

plays the corresponding maps of total circular and linear polarization. The slit crosses a supergranular cell (as demonstrated by the co-spatial Ca II H filtergrams recorded simultaneously). The intensity image shows, in the X-axis, the evolution of the granulation (granules can be identified as bright streaks, while intergranular lanes are darker). The maps do not represent single snapshots but rather the time evolution of a very narrow area of the quiet-Sun, although we will use them as if they were regular maps (we are not interested in the evolution of the different solar features tracked by the slit). The continuum contrast is slightly lower than in the normal map by about 0.2%. This is a consequence of the longer exposure times.

The linear polarization signals are more abundant for these data than for the normal map. The reason is the higher S/N. The horizontal sizes (lifetimes) of the flux structures are larger in circular polarization than in linear polarization. A network patch (positive polarity) is identified at around 1/3rd of the slit

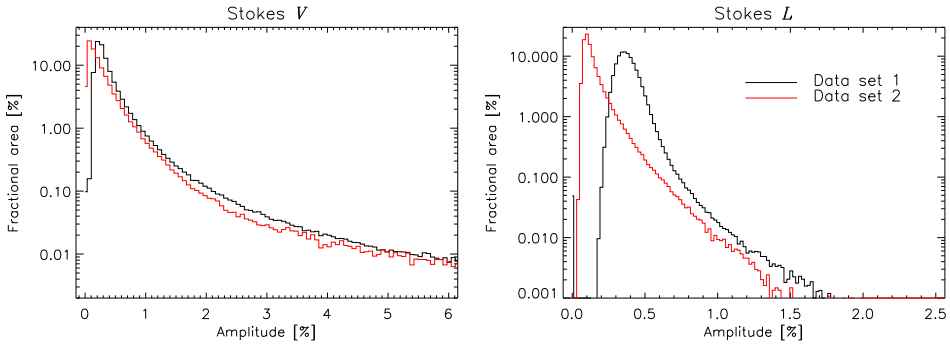

FIGURE 7.5:— Histograms of the Stokes V and Stokes L amplitudes in units of I_c (left and right panels). Black and red stand for the normal and high S/N maps respectively.

($Y \sim 60''$) in the maps.

These two data sets complement each other: the normal map scans a large solar area while the high S/N map pushes the intrinsic noise of the measurements down to the minimum reachable with the *Hinode*/SP. A noise level of $3 \times 10^{-4}\, I_{QS}$ at $0\farcs3$ is comparable to the best noise levels (close to $10^{-5}\, I_{QS}$) achieved by ground-based observations at $1''$ (Martínez González et al. 2008).

7.2.2 Noise analysis and selection of IN areas

Photon noise is present in real observations and prevents polarization signals from being cleanly detectable. It also affects the Stokes profiles, hiding the information encoded on their shapes. The inversion of noisy polarization signals may lead to undesirable results in the final analysis. For this reason only pixels showing polarization signals above a reasonable threshold will be analyzed by means of inversions. This should exclude profiles that cannot be inverted reliably.

Figure 7.5 shows the histograms of the Stokes V and $L = \sqrt{Q^2 + U^2}$ amplitudes of the Fe I line at 630.25 nm (left and right panels, respectively). Both of them demonstrate the large occurrence of weak polarization signals. The distributions for the high S/N and normal maps are similar, although differences exist. The histograms for the normal map have their peak at larger amplitudes than the high S/N map. In both data sets, the peaks are close to the corresponding noise levels. In particular, the Stokes V distributions peak at about 2 and 2.3 times the noise levels of the two maps. For Stokes L, the peaks are at 2.6 and 2.4 times the noise level.

We expect photon noise to contribute to a larger or smaller extent to gen-

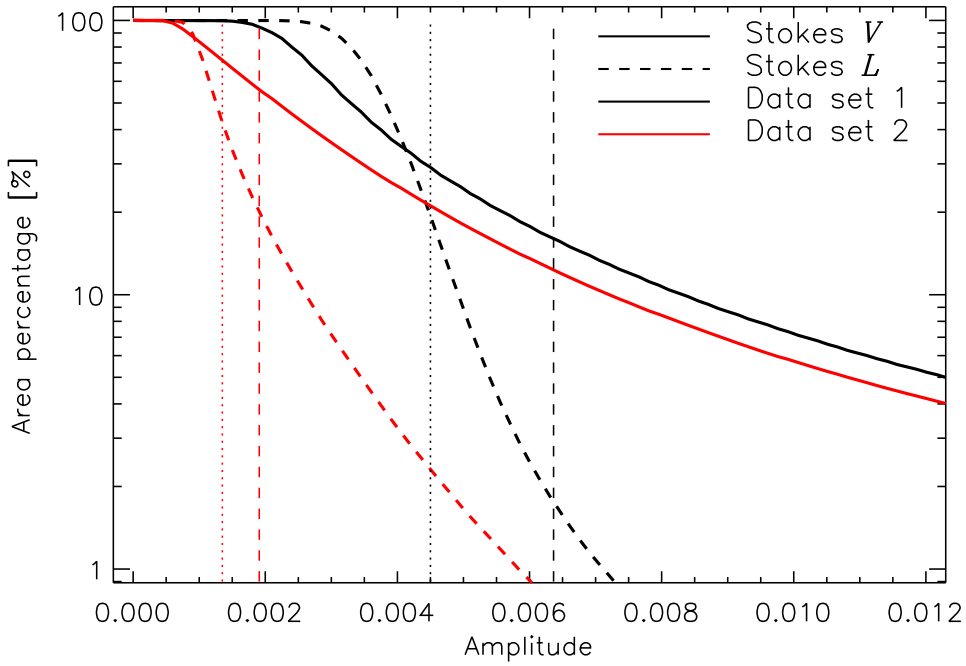

FIGURE 7.6:— Surface area occupied by signals with Stokes V and L amplitudes larger than a given value, for the two data sets analyzed in this Chapter. The vertical lines mark the 4.5 times noise levels in the normal map and in the high S/N map. Dotted and dashed lines refer to Stokes V and L, respectively.

erate the maximum of the histograms. Noise can also contribute to the rapid increase of polarization signals at the low amplitude end. Ground-based observations of the same pair of Fe I lines find that the distribution of Stokes V amplitudes clearly peaks above the noise level (Martínez González et al. 2008). These authors made numerical simulations and proposed that the peaks they observe can be taken as observational evidence of flux cancellations within the resolution element, for data with noise values of $4\times10^{-5}\,I_{\rm QS}$ and spatial resolutions of $1''$. However, at $\sim 0\farcs3$ we do not find the same results. Our histogram peaks are close to the noise levels. Values of $3\times10^{-4}\,I_{\rm QS}$ at $\sim 0\farcs3$ (high S/N map) are comparable to $4\times10^{-5}\,I_{\rm QS}$ at $1''$.

To avoid polarization signals that are highly contaminated by noise, we only analyze pixels with Stokes Q, U or V amplitudes larger than 4.5 times their noise levels. This threshold translates into an apparent flux density[1] of

[1]The term "apparent flux density" refers to the quantity $f\mathbf{B}\cos\gamma$, where f is the fill

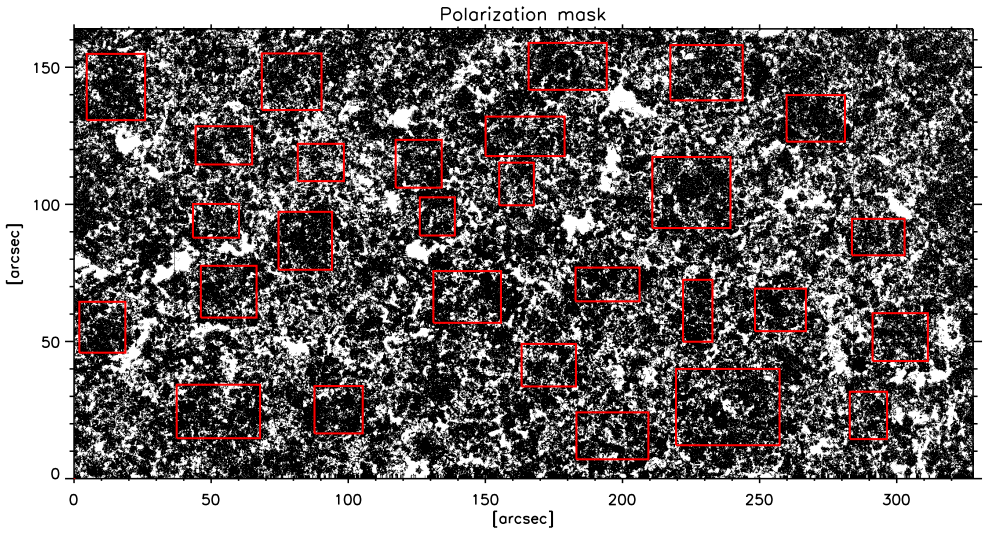

FIGURE 7.7:— Locations of pixels with any of their polarization signals exceeding 4.5 times the noise level (white). Red boxes indicate the selected IN areas. The figure shows the full orbserved area (normal map).

13.4 Mx cm^{-2}. The fraction of pixels fulfilling this condition is 33.1% and 74.4% in the normal and high S/N maps, respectively.

Figure 7.6 show the fraction of the FOV with Stokes V and L signals above a given amplitude. The vertical lines indicate 4.5 times the noise levels of sets #1 and #2, for Stokes V and L (black and red, and dotted and dashed lines, respectively).

Only 31.2% of the normal map area exhibit Stokes V signals above our 4.5 σ noise threshold. This fraction increases to 71.5% in the high S/N map. The area with significant polarization signals increase rapidly as soon as we lower the noise thresholds. The same occurs for the linear polarization signals, with image areas of 1.6% and 19.1%, respectively. We estimate that 58.8% and 87.4% of the FOVs covered by the two sets show Stokes V signals above

fraction of the magnetic field (see Keller et al. 1994; Lites et al. 1999). This quantity is the one measured by solar magnetographs, with sensitivities that depend on the measurement technique, the instrument, and the angular resolution. We have calculated the apparent flux density by determining the magnetic parameters of a ME atmosphere with vertical fields that produces Stokes V signals at the level of the noise, assuming $f = 1$. The thermodynamic parameters of the model have been fixed to the mean values derived from the inversion of the *Hinode* measurements (see next sections).

3 σ (cf. with the 92.6% provided by Martínez González et al. 2008 for visible observations from the ground).

IN areas have been identified manually in the normal map. More specifically, we have selected squared areas in the interior of supergranular cells, avoiding the strong flux concentrations of the network. Figure 7.7 shows in white the pixels where Stokes Q, U, or V exceed 4.5 times the noise level. It also displays the selected IN areas. For the high S/N data set we have just removed the strong magnetic feature visible in the polarization maps (Fig. 7.4).

7.2.3 Wavelength calibration

The wavelength scale of the observations has been determined by comparing the mean quiet-Sun intensity profiles with the Fourier Transform Spectrometer Atlas (Brault & Neckel 1987) which provides a reference spectrum. The calculation has been done separately for the two data sets.

We first average the Stokes I profiles over all pixels exhibiting negligible polarization signals (below five times the noise levels). The line cores of the two Fe I lines were fitted with a Gaussian in order to determine the position of the absolute minimum of the two lines with sub-pixel accuracy. The same was done with the reference profiles. Then, the comparison between the position in pixels of the average profile and the wavelength positions of the reference profile determines the initial wavelength and spectral sampling. The gravitational redshift is removed afterwards. The results are the same for the two data sets. They also coincide with the ones provided by Lites et al. (2007a, 2008a). The initial wavelength is 630.08921 nm and the sampling 2.148 pm pixel^{-1}.

7.3 Inversion of the data

To analyze the observations we follow the approach described in Chapter 6, i.e., a least-squares inversion based on a simple one-component, laterally homogeneous ME atmosphere and a local stray-light contamination factor to correct for the reduction of the polarization signals due to diffraction. The inversion is performed with the MILOS code. As a first approximation, we evaluate the stray-light profile individually for each pixel as the average of the Stokes I profiles observed in a box 1″-wide centered on the pixel. The inversion is performed with only 10 free parameters: the three components of the magnetic field (strength B, inclination γ, and azimuth χ), the line-of-sight velocity ($v_{\rm LOS}$), the two parameters describing the linear dependence of the source function on optical depth (S_0 and S_1), the line strength (η_0), the Doppler width

($\Delta\lambda_D$), the damping parameter (a), and the stray-light factor (α). The number of iterations was 300. No broadening by macroturbulence needs to be considered, while microturbulent velocities should effectively be accounted for by the Doppler width parameter. The inversion is applied to the Fe I 630.15 and 630.25 nm lines simultaneously, using a Gaussian of 2.5 pm FWHM to account for the spectral resolving power of the SP. As mentioned in Sect. 7.2.2, we only analyze pixels with Stokes Q, U or V amplitudes larger than 4.5 times their noise levels.

The local stray-light profile is evaluated differently for the high S/N map. In this case we cannot perform a two-dimensional average. Therefore, we take the stray light as the average Stokes I profile along $1''$ of the SP slit centered on the pixel. With this approximation we avoid using data acquired more than a minute apart, although we introduce uncertainties in the inferences because the stray light may not appropriately account for diffraction.

7.4 Inversion results

The maps of the retrieved field strength, inclination, azimuth, stray-light factor, and LOS velocity are shown in Figs. 7.8, 7.9, and 7.10 for a small portion of the normal map. The inversion results for the high S/N map can be found in Appendix B. Black regions represent pixels which have not been analyzed because of their small signals. Arrows indicate the position of the profile fits discussed in Sect. 7.10.1. Pixels #1 and #2 belong to the network, while #3 and #4 are representative of IN regions.

In the field strength map two different regions can be identified: the network, characterized by strong fields (above 1 kG), and the IN, with much weaker fields. Supergranular cells are clearly outlined by the network fields. The inclination map shows that network flux concentrations exhibit nearly vertical fields in their interiors and more inclined fields toward the edges, suggesting the presence of magnetic canopies. By contrast, IN fields are rather horizontal. The stray-light factor map shows average values of ~ 0.6–0.8. Finally, the velocity map uncover the granulation pattern, with upflows in granules and downdrafts in intergranular lanes. Note the attenuation of the velocity pattern in areas with strong field concentrations.

The results from the inversion of the high S/N data show a large population of magnetic features. Again, we find fields with strengths of the order of hG and nearly horizontal inclinations. The stray-light factor values are of the same order as those from the normal map.

Figure 7.11 represents a zoom over a $7\farcs4 \times 7\farcs4$ IN area (white boxes in

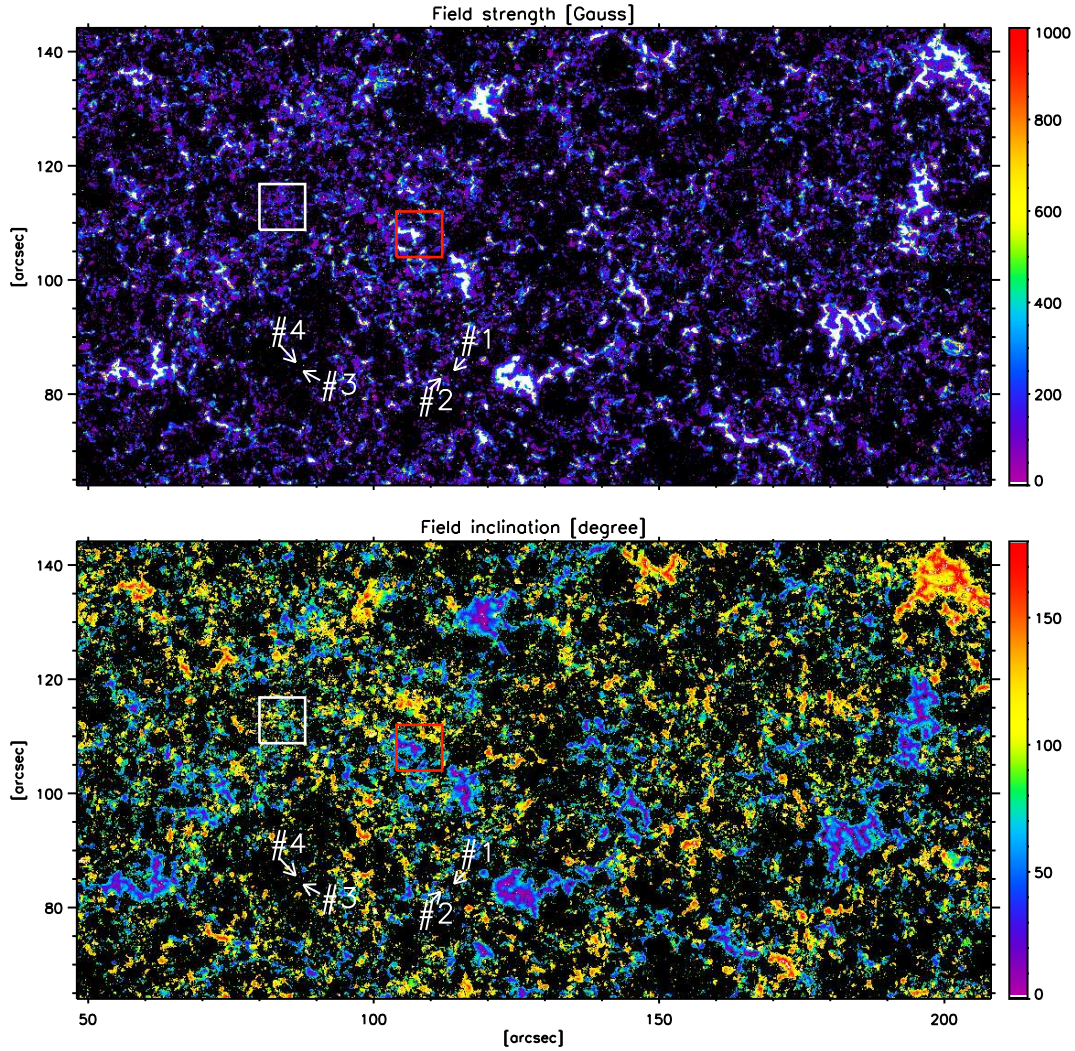

FIGURE 7.8:— Small area of $160'' \times 80''$ showing the magnetic field strengths (top) and inclinations (bottom) inferred from the inversion. Network and internetwork areas can be easily identified. Black areas correspond to non-inverted pixels. The field strength color bar has been clipped at 1000 G (white).

Figs. 7.8, 7.9, and 7.10) and display continuum intensities, magnetic field strengths, field inclinations, azimuths, stray-light factors, and total polarization,

$$P = \frac{\int [Q(\lambda)^2 + U(\lambda)^2 + V(\lambda)^2]^{1/2} \, \mathrm{d}\lambda}{I_\mathrm{c} \int \mathrm{d}\lambda}. \tag{7.2}$$

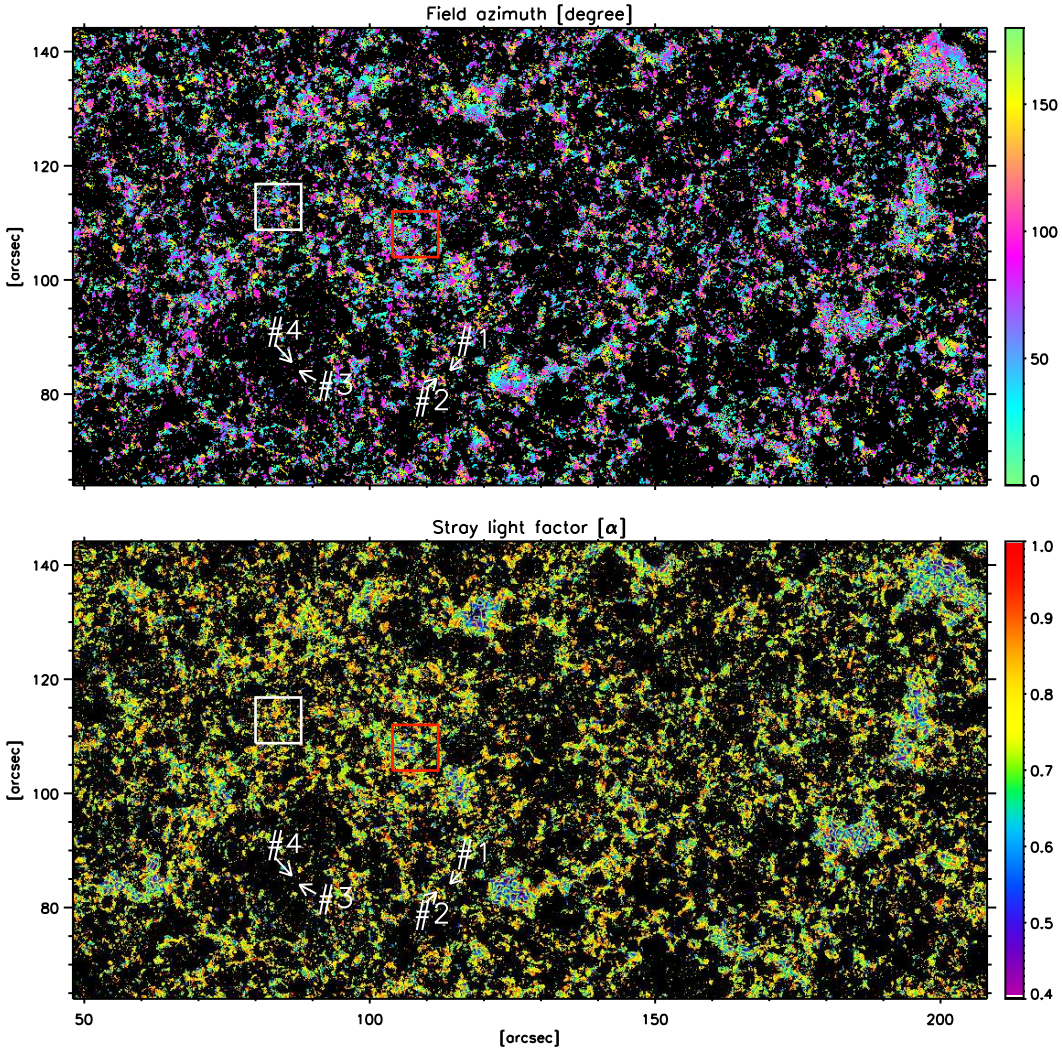

FIGURE 7.9:— Same as Fig. 7.8 but for the magnetic field azimuth and the stray-light factor (top and bottom, respectively).

The field strength map demonstrates that most of the fields are weak. The stronger concentrations are located in intergranular lanes (the contours outline the granulation). Interestingly, we find ubiquitous weak fields over granules. The map showing the total polarization just confirms this finding. Note also that the fields are more horizontal in granular regions than elsewhere. The azimuth map shows small patches with sizes of $\sim 1''$. Finally, the map of stray-light factors shows values between 70% and 90%, and no conspicuous variations

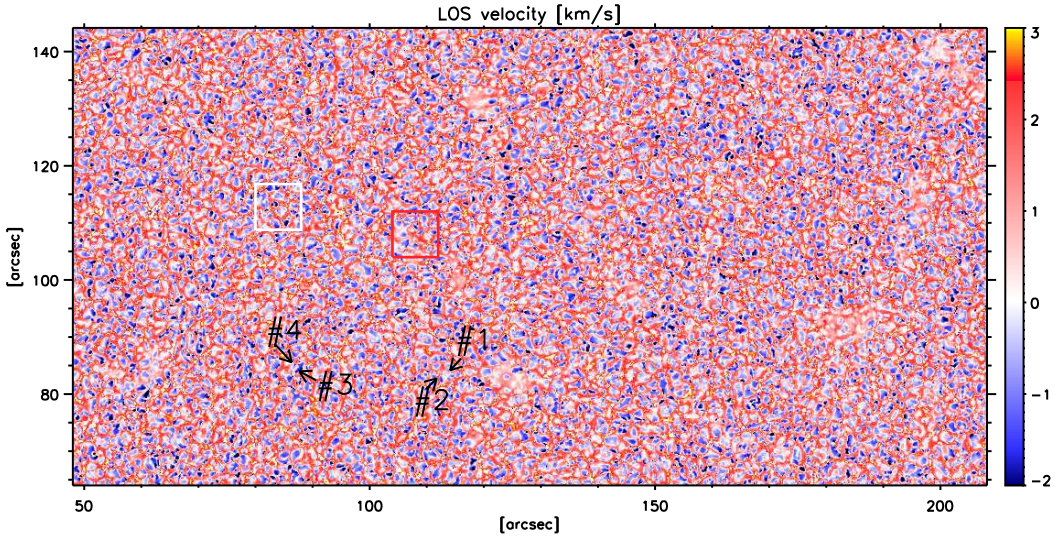

FIGURE 7.10:— Same as Fig. 7.8, but for the LOS velocity.

from granule centers to intergranular regions.

The intrinsic magnetic field of network patches lie between 1200 and 1700 G (see Solanki 1992 for a review) and the field lines tend to be vertically oriented (Sánchez Almeida, & Martínez Pillet 1994; Martínez Pillet, Lites & Skumanich 1997). Figure 7.12 shows the results of the inversion of a network element found in the normal map. The field retrieved for this particular magnetic feature is nearly perpendicular to the solar surface at the center of the network patch and the retrieved magnetic flux (2×10^{18} Mx) is compatible with earlier observational estimates of $\sim 10^{18} - 10^{19}$ Mx (e.g. Schrijver et al. 1997a,1997b). To finish, the recovered stray-light factors are of the order of 60-80%, slightly smaller than for IN areas.

Note from Fig. 7.12 that the total polarization signal is well correlated with the magnetic field strength. The network magnetic element is strongly associated with abnormal granulation. Also, the field inclination increases as we go from the center of the magnetic patch outward, indicating the existence of a canopy[2]. We would like to mention that the blurring of the polarization signals due to diffraction can apparently extent the size of magnetic canopies. The visual appearance of the magnetic canopies and the effects of diffraction are similar in the polarization maps. Both effects can be seen as a "bloom" of the polarization signals (Lites 2002). Note that we correct the effects of

[2]A magnetic canopy is a surface that separates two distinct physical environments along the LOS, one magnetic (upper layers) and one non-magnetic (bottom layers)

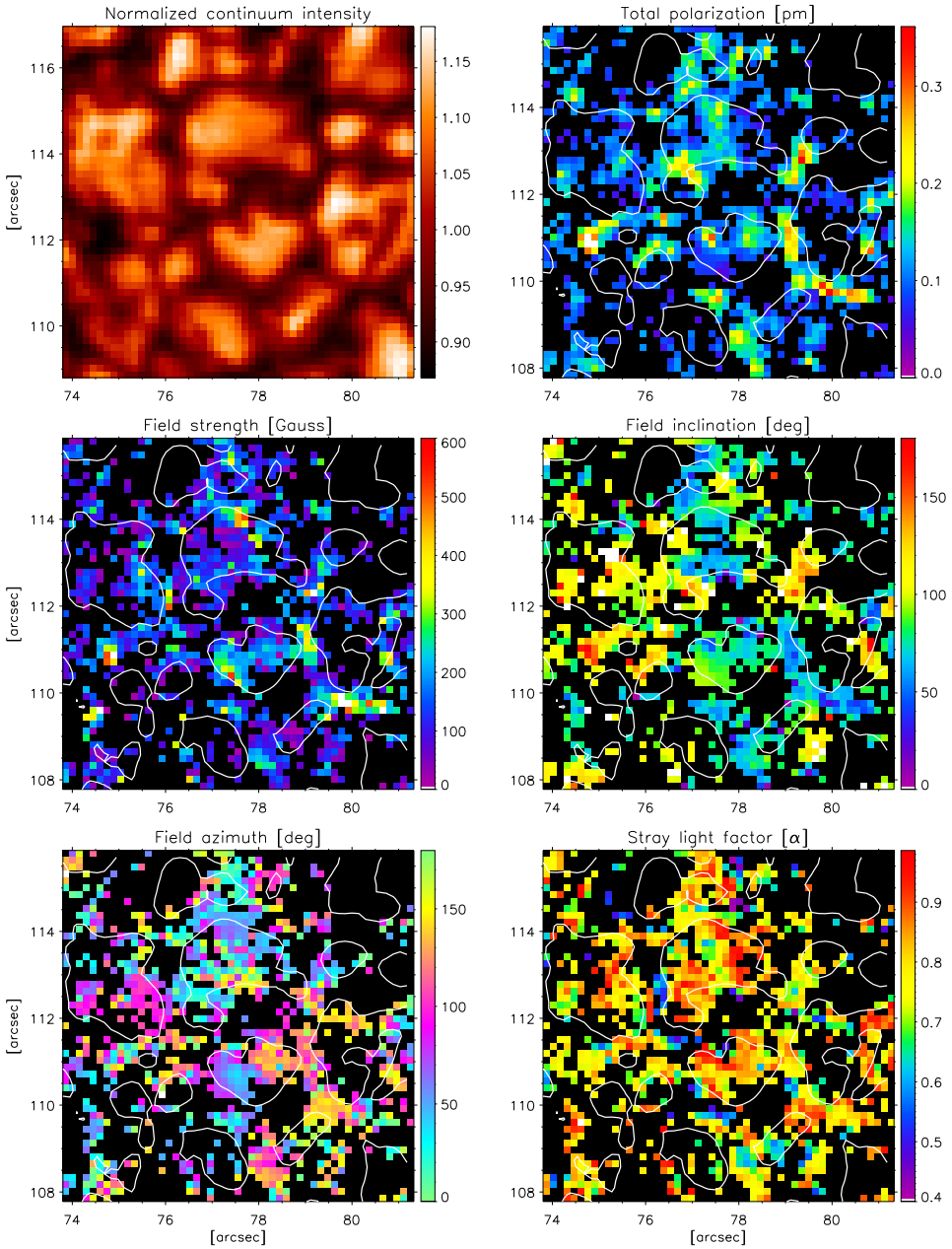

FIGURE 7.11:— Small IN area of $7.4'' \times 7.4''$ (white boxes shown in Figs. 7.8, 7.9, and 7.10). The different panels display continuum intensities, total polarization, magnetic field strengths, field inclinations, field azimuth, and stray-light factors. Contour lines represent regions with continuum intensities $I_c/I_c^{QS} > 1.03$. The field strength color bar has been clipped at 600 G (white).

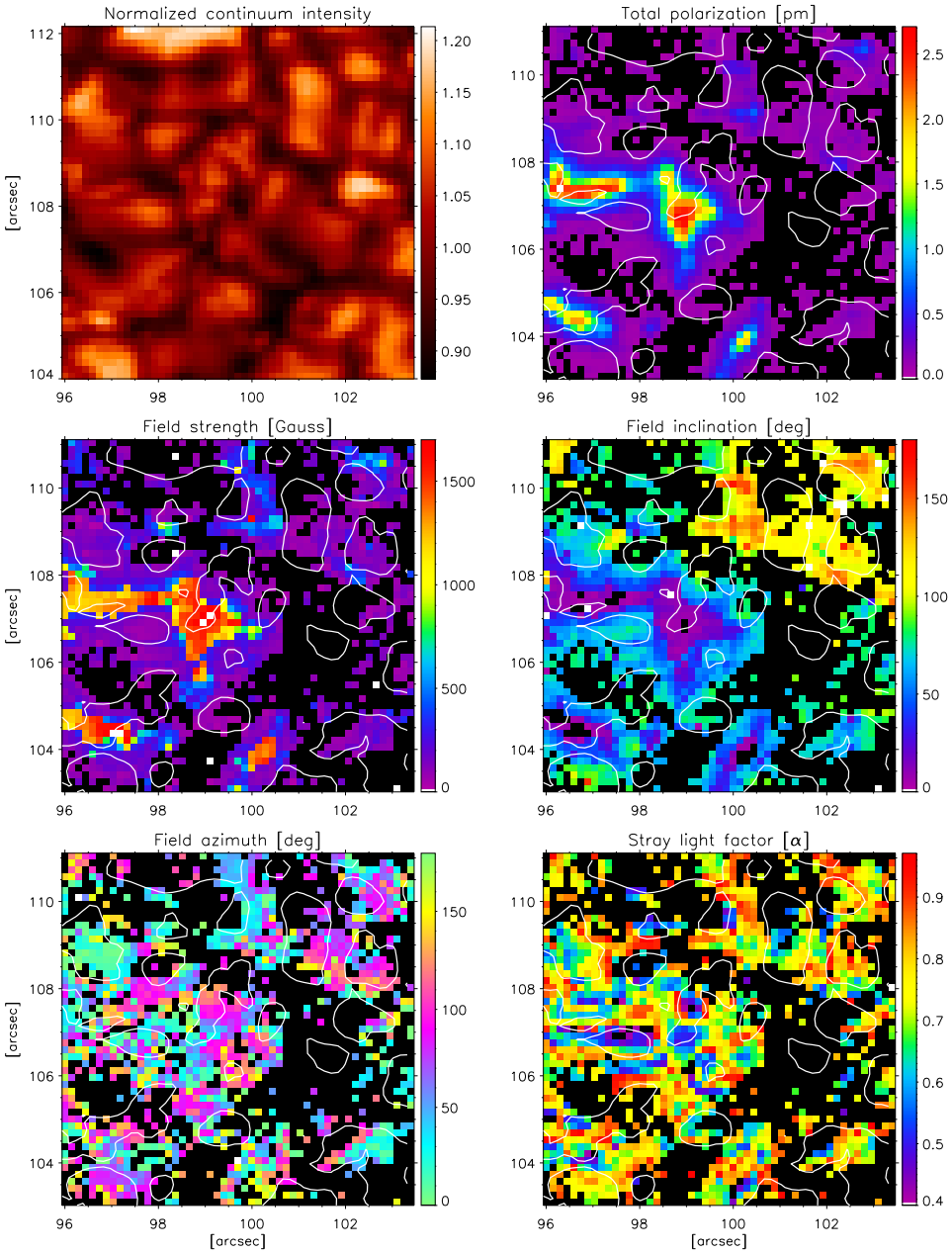

FIGURE 7.12:— Same as Fig.7.11 but for a network area (red boxes shown in Figs. 7.8, 7.9, and 7.10). In this case the field strength color bar has been clipped at 1700 G.

diffraction in the inversion.

7.5 Distribution of field strengths and inclinations

A common way to characterize the distribution of field strengths is through the so-called Probability Density Function (PDF). It represents the probability of finding a magnetic field strength B in the interval $[B, B + dB]$ and its integral is unity, i.e., $\int_0^\infty P(B)dB = 1$. For a detailed account of the properties of the PDF and definitions used in quiet-Sun studies, see Steiner (2003).

Most analyses of IN areas based on the visible lines at 630 nm have resulted in PDFs peaking above 1000 G (Socas Navarro, & Sánchez Almeida 2003, Domínguez Cerdeña et al. 2003; Sánchez Almeida al. 2003; Lites, & Sócas Navarro 2004; Domínguez Cerdeña et al. 2006, and Martínez González 2007). Only few studies have delivered field strengths in the hG range with these spectral lines (see e.g., Rezaei et al. 2007). The distribution of IN field inclinations is very poorly known, and has been studied only by Lites et al. (1996) and Khomenko et al. (2003).

Figure 7.13 shows the distribution of magnetic field strengths (left) and field inclinations (right) in IN regions of the normal map. IN areas have been selected manually in the interior of supergranular cells, avoiding the strong flux concentrations of the network (see Sect. 7.2.2). Contrary to most of the results previously published, the peak of the PDF for the field strength is located near 90 G. The field strength distribution decreases rapidly toward larger fields. This demonstrates that *the IN basically consists of hG flux concentrations*. In addition, *the IN fields tend to be horizontally oriented* as shown by the inclination distribution, in agreement with the finding of Lites et al. (1996).

It is important to emphasize that the PDF is not monotonic. This suggests that the inversions are not biased by noise, and that the peak at 90 G is likely solar in origin. We mention again that we have analyzed only pixels with polarization signals above 4.5 times their noise levels. The peak may also represent cancellation of magnetic flux at spatial scales smaller than $0\farcs32$ (Martínez González et al. 2008). However, we do not favor this interpretation because MHD simulations do not show significant mixing of opposite-polarity fields on scales of $0\farcs3$ or less (see Chapter 5).

The results for the magnetic field strength are in agreement with Keller et al. (1994) who also found weak fields in the internetwork using the Fe I 525.0 nm lines, although at a lower spatial resolution. They also agree with the results derived from infrared lines (Lin 1995: Lin & Rimmele 1999; Khomenko et al. 2003) and from simultaneous inversion of visible and infrared lines (Martínez

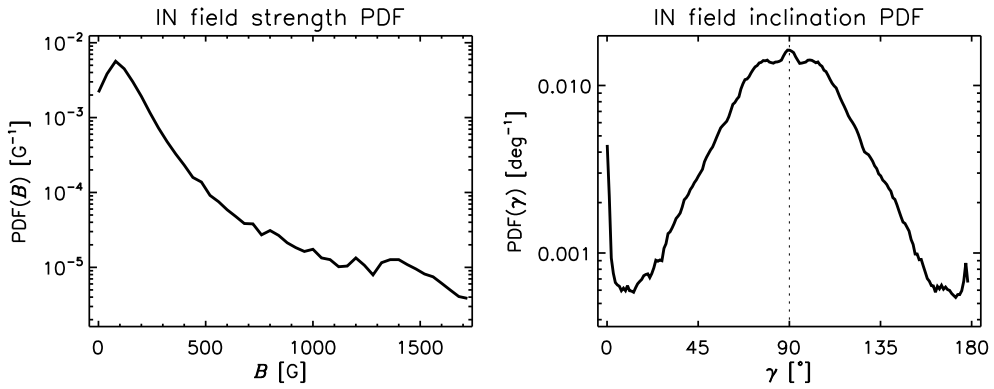

FIGURE 7.13:— Magnetic field strength (left) and inclination (right) probability density functions for internetwork regions.

González et al. 2008).

The inclination PDF peaks at 90° and decreases toward more vertical orientations of the fields. At 0° and 180° the distribution increases again. The shape of the PDF shows that although most of the fields are highly inclined with respect to the line-of-sight, some of them are vertically oriented. The shape of the inclination distribution differs from that reported by Khomenko et al. (2003) using IR lines. They found that most of the magnetic fields are oriented nearly vertically. Only 5% of the pixels showed inclinations larger than 70%.

Figure 7.14 displays the distribution of field strengths (left) and inclinations (right) resulting form the ME inversion of $\sim$ 650 000 pixels belonging to the normal map, given as probability density functions. Hereafter, we will refer to them as the *total* PDF, because they do not distinguish between network and IN regions. The peak of the total PDF for the field strength is located at about 90 G, as in the IN distribution. The curve decreases rapidly toward stronger fields: at around 1 kG it reaches a minimum and then shows a small hump centered at about 1.4 kG. Strong fields (B >1 kG) are found in only 4.5% of the pixels, the majority of which correspond to network areas.

In Fig. 7.14 we have overplotted the PDFs representing the IN. There are clear differences between the PDFs for IN areas and for the full FOV. First, the field strength PDF is steeper for the IN, indicating that the majority of fields contributing to the IN are in the hG range. Secondly, the fraction of pixels showing inclinations near 0° and 180° is larger for the full FOV case. Those fields correspond to network magnetic fields.

Finally, Fig. 7.15 plots the retrieved field strengths against the inclination

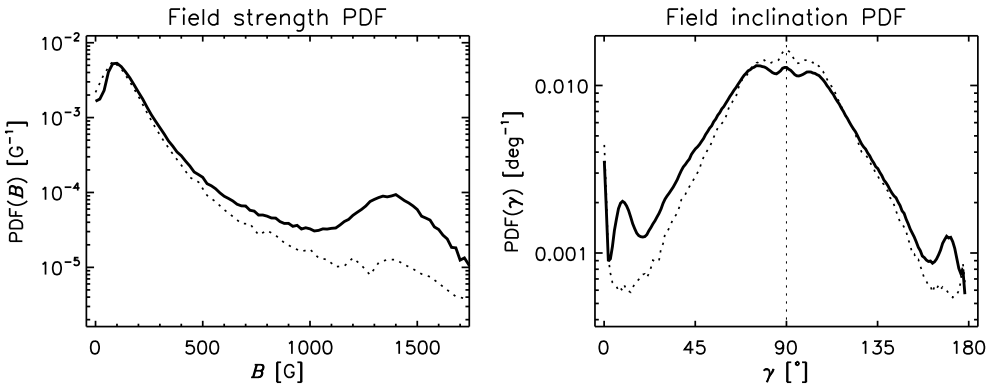

FIGURE 7.14:— Magnetic field strength (left) and inclination (right) probability density functions for the full FOV (solid curves). For comparison, dotted line represents the PDF for the internetwork shown in Fig. 7.13.

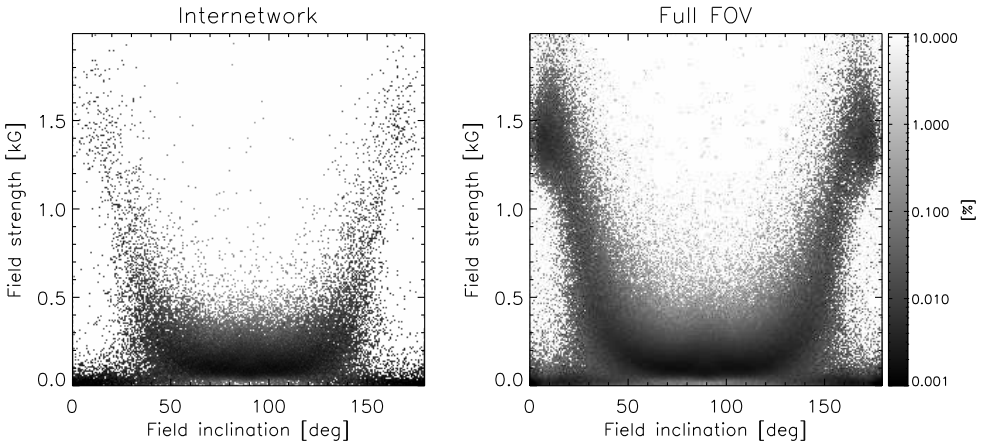

FIGURE 7.15:— Magnetic field strength versus the inclination of the field as inferred form the inversion, for the full FOV and for IN regions (right and left panels, respectively). The color of each point indicates the density of pixels in each data bin.

of the field for the full FOV and only for IN regions (right and left panels, respectively). As pointed out by Martínez González et al. (2008) there is a clear tendency for strong fields to be vertically oriented (network). Magnetic fields weaker than ∼500 G tend to have orientations between 30 and 150°. In the IN, there are fields with strength smaller than 100 G an all posible orientations. Interestingly, no magnetic fields stronger than ∼500 G occur in the range of inclinations from 50° to 130°.

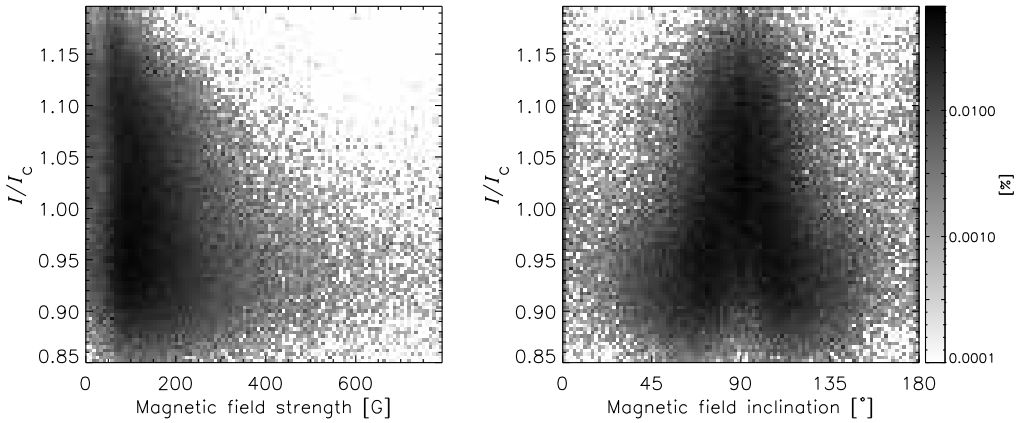

FIGURE 7.16:— Distribution of continuum intensities vs the retrieved magnetic field strengths and inclinations, for IN regions (left and right panels, respectively).

7.5.1 Granular and intergranular fields

One of the most surprising results of our analysis is that a large fraction of granules host magnetic fields. Figure 7.16 displays continuum intensities against the magnetic field strengths and inclinations retrieved in IN areas.

We estimate that 24% of the surface covered by granules in the IN contains magnetic flux detectable above 4.5 σ. Surprisingly, the fraction of total intergranular area that harbors magnetic fields in the IN does not increase significantly, amounting to 28%. The left panel shows that the stronger fields tend to be located in the darker lanes, while the weaker fields are homogeneously distributed across granules and intergranules. The right panel shows that most of the fields found in granules have nearly horizontal orientation. The inclination distribution covers a wider range of values when the fields are located in intergranular lanes. There are also some points with inclinations near 0° and 180° indicating the presence of vertical fields.

It is important to remark that leakage from intergranular lanes due to diffraction cannot be the source of the magnetic signals above granules, given their very large spatial extents (see, e.g., Fig. 7.11).

Figure 7.17 shows the PDFs for granules and intergranular lanes in the internetwork (blue and red lines, respectively). The separation between granular and intergranular regions has been performed using the continuum intensity and the retrieved LOS velocity from the inversion. In particular we define granular (intergranular) regions as those areas whose pixels show larger (lower) continuum intensities than the mean intensity of the full map and also show

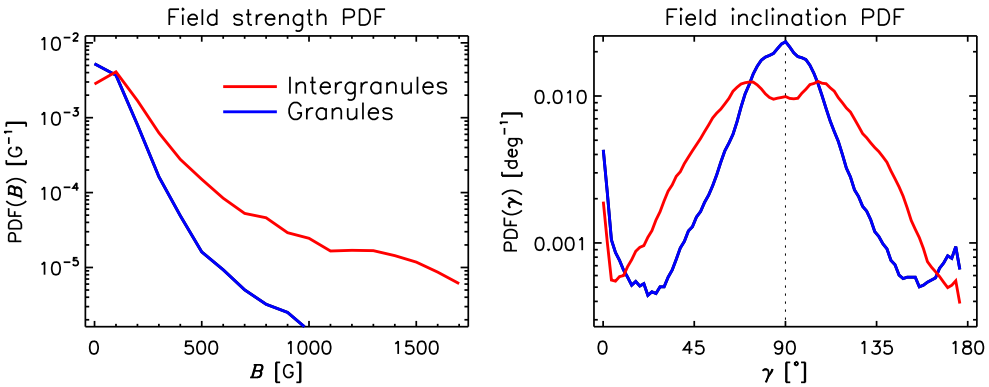

FIGURE 7.17:— Same as Fig 7.13 but the red, and blue lines stand for pixels in the selected internetwork areas corresponding to intergranular lanes and granules, respectively.

blue- (red-) shifted velocities.

The distribution of field strengths is steeper in granules as compared with intergranular lanes, i.e., strong fields are much less abundant in granular regions. Noticeable is the large fraction of very inclined ($\sim 90°$) fields in granules. Although inclined fields are also common in downdrafts, the field lines tend to be more horizontal over convective upflows (right panel of Fig. 7.17). The increase of the PDF near 0° and 180°, however, indicates that vertical fields also exist in granules. The nature of these vertical fields will be studied in Chapter 8.

There are humps in the inclination distributions at $\gamma \sim 10°$ and $\sim 170°$, and at $\gamma \sim 70°$ and $\sim 110°$. The reason may be that it is not possible to determine purely vertical or horizontal fields when the field is weak (Khomenko et al. 2003). For vertical fields, the inversion algorithm tries to fit the noise in Stokes Q and U, while for horizontal ones it tries to fit the noise in Stokes V. In both cases the inversion would yield field inclinations which are biased by several degrees. However, we sometimes find purely vertical and horizontal fields in the IN. How is this possible? The reason is that, in the weak field regime, Stokes I shows greater sensitivity to the field inclination than Stokes V, Q, or U. Therefore, although the polarization profiles can be largely affected by noise, the intensity profile provides additional information that helps determine the correct value of the inclination. Numerical tests have also shown that ME inversion do infer the correct field orientations in the weak field case provided S/N $\geq$ 1000 (Lites 2002).

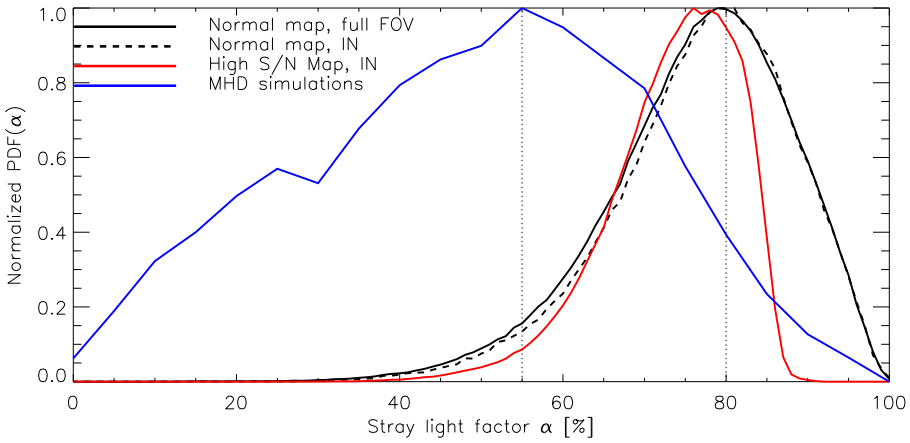

FIGURE 7.18:— PDF of the stray light-factor corresponding to the normal map (black) and to the high S/N map (red). Solid and dashed lines represent the full FOV and IN regions, respectively. Overplotted is the histogram representing the stray-light factors derived from the inversion of simulated Stokes profiles. The dotted vertical lines indicates the peak of the stray-light factor distributions.

7.6 Distribution of stray-light factors

Current ground-based spectropolarimetric observations at 1″-1.″5 do not spatially resolve the magnetic field structures present in IN areas. This relative lack of spatial resolution is largely responsible for the different field strength distributions found from the analysis of visible and infrared lines. The most recent analyses of visible and IR lines by means of inversion techniques have estimated magnetic filling factors of about 1-2% and 0.5-1%, respectively, for both spectral regions (Martínez González et al. 2008).

In Figure 7.18 we show the distribution of the stray-light factor for the full FOV and IN regions of the normal map, and for IN regions of the high S/N map (black and red lines, respectively). The PDFs for the normal map peak at $\alpha \sim 80\%$, while the PDF for the high S/N map peaks at about 75%. There are differences in the width of the PDFs corresponding to the two data sets, but otherwise they are remarkably similar.

We have included a stray-light contamination in the inversion to correct for the effects of diffraction in the polarization signals. According to the numerical experiments carried out in Chapter 6, diffraction alone would produce stray-light factors of about 55%, on average. For comparison, we have overplotted in Fig. 7.18 the PDF of stray-light factors derived from the analysis of Stokes

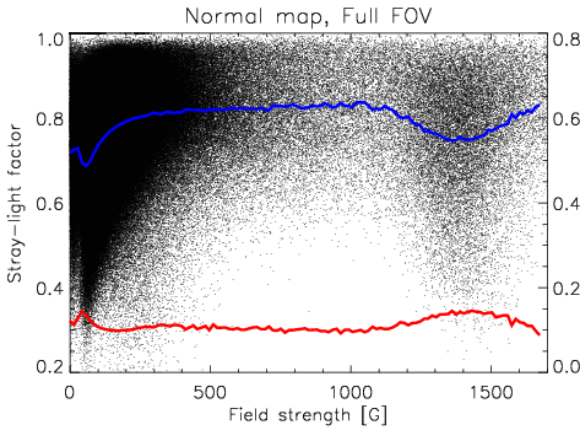

FIGURE 7.19— Stray light-factor resulting from the inversion of the normal map vs the inferred field strength. The blue line represents the average of stray-light factors over evenly-spaced intervals along the X-axis. Red line stands for the rms fluctuation. The rms scale is given in the right Y-axis.

profiles that arise from MHD simulations (blue).

The majority of pixels have stray-light factors above 55%. These stray-light factors represent the combination of two effects: (i) the reduction of the polarization signals due to the action of the telescope (diffraction) and, (ii) a real magnetic filling factor due to insufficient angular resolution. Therefore, the area of the resolution element devoid of magnetic fields is smaller than the stray-light factor inferred in the inversion.

We know that the magnetic signal measured by the instrument is reduced to 45% of its value in the presence of diffraction, which is equivalent to a stray-light factor of 55%. Thus, the real magnetic filling factor (without diffraction effects) is

$$f = \frac{1-\alpha}{0.45}, \tag{7.3}$$

corresponding to $f = 45\%$ in our example, not 20% as $f' = 1-\alpha$ appears to suggest[3] . This value is considerably larger than typical filling factors inferred from ground-based observations in the visible at $1''$.

Figure 7.19 shows a scatter plot of the stray-light factors vs field strength in the full FOV of the normal map. The mean stray-light factors are represented in blue line and the rms fluctuations in red. The mean stray light decreases for weak and strong fields. The rms is almost constant and below 0.2. We would like to mention that the quantity $f' = (1-\alpha) = 20\%$ is similar to the average magnetic filling factor of 23% inferred by Lites et al. (2008a) using the MERLIN[4] code. Thus, the two estimates of the magnetic filling factor in the IN differ only in that we remove the effects of diffraction from the values returned

[3]We utilize the notation f' in order to distinguish it from the real magnetic filling factor.
[4]Milne-Eddington gRid Linear Inversion Network

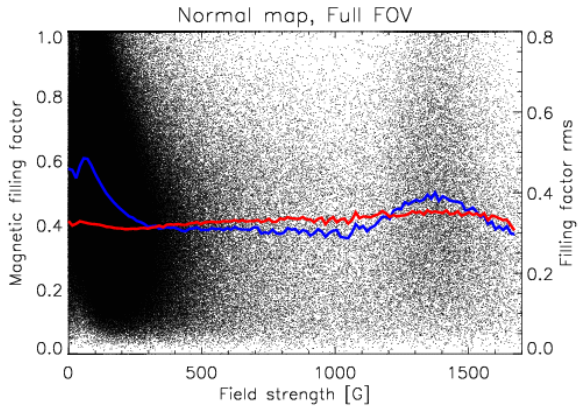

FIGURE 7.20— Magnetic filling factors resulting from the inversion of the normal map vs the inferred field strength. The blue line represents the average of magnetic filling factors over evenly-spaced intervals along the X-axis. Red line stands for the rms fluctuation. The rms scale is given in the right Y-axis.

by the inversion codes. Our final estimates of the magnetic filling factors in the IN are given in Fig. 7.20.

7.7 The magnetic flux density in the IN

The determination of the (unsigned) averaged flux density of quiet Sun IN regions has been pursued by many authors. It ranges from the 6-9 Mx cm^{-2} reported by, e.g., Sánchez Almeida et al. (2003) and Khomenko et al. (2003), to the 21 Mx cm^{-2} found by Domínguez Cerdeña et al. (2003). Other studies using simultaneous observations of visible and infrared lines give 11-15 Mx cm^{-2} (Khomenko et al. 2005a). An upper limit to the flux density seems to be $\sim$ 50 Mx cm^{-2} (e.g., Lin & Rimmele 1999; Faurobert et al. 2001).

There is a large disparity between the average flux densities reported in the literature. One of the reason is that the estimates are biased by the angular resolution of the observations. Also, the different analysis techniques have contributed to such discrepancies.

The *(net) magnetic flux* through a portion of the solar surface is defined as:

$$\Phi = \mathbf{BS}, \tag{7.4}$$

where $\mathbf{B} = B(x, y, z)$ is the magnetic field vector, $\mathbf{S} = \hat{n}S$ is the surface crossed by the magnetic field lines, and $\hat{n}$ the unit vector perpendicular to the solar surface. Averaging over the pixel surface $A_{\rm px}$ we obtain the *magnetic flux density* $\phi = \Phi/A_{\rm px}$, expressed in Mx/cm^2. If the field element occupies a fraction f of the resolution element, $S/A_{\rm px} = f$, then

$$\Phi = f A_{\rm px} B \cos\gamma \tag{7.5}$$

TABLE 7.2:— Estimated flux values of the FOV and IN regions corresponding to the normal map and to the high S/N map. Columns are the *unsigned*, magnetic flux and transversal flux densities, $\overline{\phi}$ and $\overline{\phi}_\perp$, and the net flux $\overline{\phi}_\mathrm{n}$ in units Mx cm^{-2}, and the averaged field strength $\langle B\rangle$ in units of G.

		$\overline{\phi}$	$\overline{\phi}_\perp$	$\overline{\phi}_\mathrm{n}$	$\langle B\rangle$
Normal map	FOV	20.3	35.0	3.62	75.49
	IN	7.23	22.6	-0.22	41.48
High S/N map	FOV	35.19	86.76	6.86	137.47
	IN	24.31	84.6	-5.39	124.2

and

$$\phi = fB\cos\gamma = fB_\mathrm{long} \tag{7.6}$$

where B is the field strength and B_long represents the longitudinal (vertical to the surface) component of the field. γ stands for the zenith angle. ϕ is often referred to as the longitudinal flux density. The mean *net* magnetic flux density is $\overline{\phi}_\mathrm{n} = \sum_{i=1}^{N}\phi_i/N$ and the *unsigned* magnetic flux density $\overline{\phi} = \sum_{i=1}^{N}|\phi_i|/N$ where N is the total number of pixels and ϕ_i the flux density for each pixel i. Some athors also compute the so-called transverse flux density $\overline{\phi}_\perp = \sum_{i=1}^{N} f_i^{1/2}B_i\sin\gamma_i/N$. This quantity has little physical significance, and is provided in the literature as a means to quantify the amount of linear polarization observed. Finally, we also compute the averaged field strength[5] as $\langle B\rangle = \sum_{i=1}^{N} B_i/N$, which has units of G.

Table 7.2 shows the different fluxes obtained for the normal map and the high S/N map[6]. The fluxes are computed assigning zero values to pixels which were not inverted (those with Stokes Q, U or V amplitudes below 4.5 σ). To evaluate the flux we use the "true" magnetic filling factor, $f = (1-\alpha)/0.45$, i.e., we remove the amount of stray-light due to diffraction in all pixels[7], as explained in Sect. 7.6.

The flux values that we have estimated are in agreement with the large occurrence of horizontal field in the IN. For the normal map the flux values are

[5]In Orozco Suárez et al. (2007a) we determined the quantity "mean unsigned apparent flux density" when we really calculated the meaningless quantity $\sum_{i=1}^{N}(1-\alpha_i)B_i/N$.

[6]We also include the transverse flux density for comparison with earlier works.

[7]In practice, it is not possible to separate stray-light from filling factor because both affect the polarization signals in a similar way (diminishing their amplitudes). If we assume that the contribution of diffraction to the stray-light is constant, then the filling factor would be over- or underestimated depending on the pixel. The symmetric shape of the stray-light factors distribution from the numerical experiments in Chapter 6, however, indicate that the correction is appropriate.

below those reported by Lites et al. (2007a, 2008a)[8], who obtained $B^L_{\rm app} \simeq 11.0$ and $B^T_{\rm app} \simeq 55.3$ Mx cm^{-2}. These flux values cannot be compared directly to ours since they are based on a different diagnostic technique. The ratio between the transverse and longitudinal flux is about $r \sim 3$ for the IN, while Lites et al. estimate $r \sim 5$.

The longitudinal and transverse flux values increase substantially with increasing S/N. In fact, the transverse flux we obtain from the inversion of the high S/N data is larger than the 64 Mx cm^{-2} deduced by Lites et al. (2008a) using similar ME inversions. For the high S/N data, the ratio between the longitudinal and transverse flux increases to $r \sim 3.5$, still far to the one found by Lites et al. (2008a).

It is important to remark that part of the quantity α corrects the dilution of the polarimetric signals due to diffraction. In Chapter 6 we found that this approximation works for $\sim 80\%$ of the pixels. The remaining $\sim 20\%$ corresponds to pixels whose polarization signals have increased after diffraction. Our strategy assigns wrong flux values to those pixels, but most of them remain below the noise threshold and are not included in the analysis. We have determined that only 1% of the pixels from the IN show stray-light factors below 55% (1.7% in the full FOV). This amount increases to 7.7% in the S/N map (7.5%). These pixels are assigned $f = 1$. Their contribution to the flux, however, turns out to be negligible.

Note that, if we do not remove the effects of diffraction, the flux density would be underestimated by a factor of ~ 2.2. For the transverse flux, the appropriate factor is $\sim$1.5 because it scales with $\sqrt{f}$. Moreover, the ratio between the longitudinal and transverse flux densities would increase (Steiner et al. 2008).

7.8 Dependence of field distributions on polarization signal strengths

The polarization signals in the internetwork are much smaller than those in active regions. As a result, they are more affected by noise. This may make the determination of vector magnetic fields less reliable. To minimize the influence of noise we have analyzed only Stokes profiles whose polarization signals exceed a given threshold above the noise level σ. The inversions presented in this Chapter correspond to pixels whose Q, U or V signals are larger than 4.5 σ.

[8]The quantities $B^L_{\rm app}(\propto \phi)$, and $B^T_{\rm app}(\propto \phi_\perp)$, are called the apparent longitudinal and transversal flux densities (Lites et al. 1999).

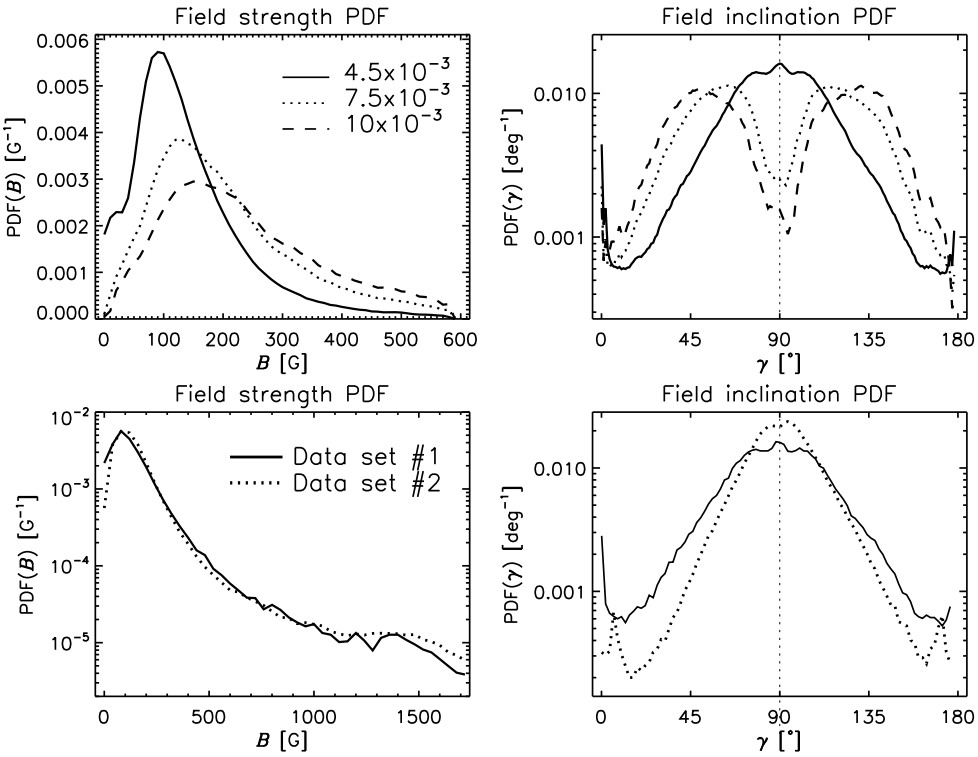

FIGURE 7.21:— Top panels: Magnetic field strength (left) and inclination (right) PDFs for IN regions of data set #1 and for different threshold levels. Pixels whose Stokes Q, U or V amplitudes do not exceed the corresponding level are excluded from the distributions. Bottom panels: The same as before but for internetwork regions resulting from the inversion of data sets #1 and #2 (solid and dotted lines, respectively).

This should increase the robustness of the results because we do not include too noisy profiles in the analysis.

To evaluate the effect of noise in more detail we have calculated the field strength and inclination PDF of IN regions for three different polarization thresholds: 4.5, 7.5, and 10 σ. Figure 7.21 (top panels) displays the results. As the threshold level increases, the peak of the field strength PDF decreases in amplitude, shifts toward stronger fields, and becomes broader. Thus, the larger the threshold, the smaller the percentage of weak fields detected. Since weak fields are usually associated with weak polarization signals, this is exactly what one would expect just because the weak polarization signals are excluded from the analysis. The important result is that, independently of the polarization

threshold used, the amount of strong fields remains unchanged. Even for very high polarization thresholds, the field strength PDFs are dominated by weak fields, so they cannot be the result of noise in the profiles.

The field inclination PDF provides clear evidence that the IN is full of horizontally oriented fields. For large polarization thresholds (10 and 7 σ) the PDFs show two clear humps located between 45 and 65° and the occurrence of horizontal fields is smaller. As we reduce the threshold, the humps disappear and the probability of finding fields at 90° increases.

In the bottom panels of Fig. 7.21 we also represent the PDFs of IN regions from to the inversion of the high S/N map (blue lines). For comparison, the PDFs obtained from the normal map corresponding to a polarization threshold of 4.5 σ is displayed. The S/N of these observations is about 3.7 times larger than that of the normal map. However, the location of the peak of the PDF and the width of the distribution do not change. The inclination PDF changes considerably when increasing the S/N: the amount of nearly horizontal fields increases. This indicates that the weakest polarization signals contribute a substantial amount of horizontal fields to the inclination PDF.

7.9 Comparison with MHD simulations

Figure 7.22 compares the PDFs of IN regions in the normal map (black) with those calculated from the magneto-convection simulations of Vögler et al. (2005), for three snapshots with mean unsigned flux densities of 10, 50 and 140 Mx cm^{-2} (color coded lines).

The simulation run that better matches the slope of the IN field strength distribution is the one corresponding to $\langle B \rangle = 10$ G at optical depth $\log \tau_5 = -2$. However, this distribution of fields does not reproduce the hump observed in the PDF at around 90 G. The distribution from the simulation increases monotonically towards 0 G, while the distribution of strengths in the IN has a clear maximum. As we have discussed in previous sections, this hump is solar in origin. Only the PDF corresponding to the $\langle B \rangle = 140$ G run has a clear hump, but the slope is completely different.

Notice that the mean field strength of IN regions in the normal map is ~ 20 G. This value increases dramatically for the high S/N map to ~ 80 G. The slope of the magnetic field strength distributions is similar, though.

The field inclination distributions in the simulations are much flatter than that obtained from the inversions. The simulations do not show a dominance of horizontal fields as it is the case in the IN. New simulations from Schüssler & Vögler (2008) and Steiner et al. (2008) result in a larger abundance of horizontal

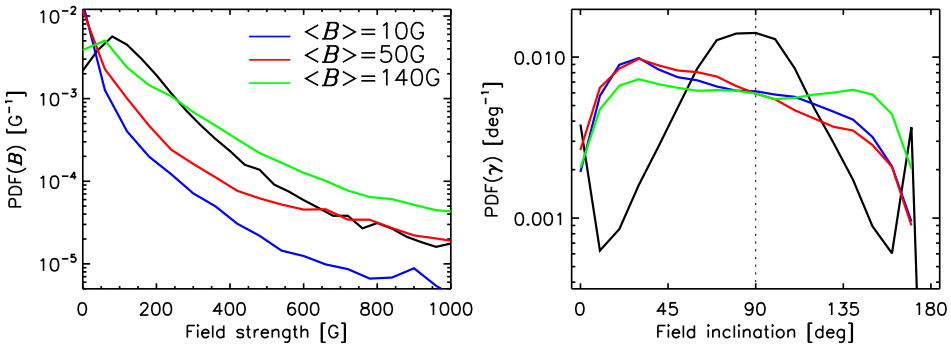

FIGURE 7.22:— Magnetic field strength and inclination probability density functions for IN regions and from the magneto convection simulations with $\langle B \rangle = 10$, 50 and 140 Gauss, taken at optical depth $\log \tau = -2$

fields, but detailed comparison with the PDF derived from *Hinode*/SP remains to be done.

In order to make the IN field strength distribution available for the community we have fitted it in the range 1-8 hG to a lognormal function

$$f(B) = (\pi^{1/2}\sigma B)^{-1} \exp[-(\ln B - \ln B_0)^2/\sigma^2 \tag{7.7}$$

which describes satisfactorily the PDF with $B_0 = 36.7$ G and $\sigma = 1.2$.

7.10 Testing the robustness of the inversion results

In this section we perform several tests to check the validity of the ME parameters provided by the inversion of real *Hinode*/SP data. We undertake such an analysis in view of the results of Martínez González et al. (2006), who concluded that the Fe I 630.2 nm lines may not contain sufficient information to determine the field strength and the stray-light factor unambiguously under particular analysis conditions. We will see that the Stokes I profile plays an essential role in the determination of these quantities.

7.10.1 Profile fits

Figure 7.23 displays sample fits for individual pixels belonging to the network in the normal map. Pixel #1 (top) represents a typical network element at the center of strong flux concentrations, whereas pixel #2 (bottom) comes from the edge of a network patch. The inversion returns a field strength of 1334 G, a field inclination of 19°, and a field azimuth of 136°, with a stray-light factor

of 61%, for pixel #1, and a field strength, inclination, and azimuth of 237 G, 69°, and 160°, with a stray-light factor of 71%, for pixel #2.

Figure 7.24 displays observed and best-fit profiles for two pixels belonging to the internetwork in the normal map. The observed Stokes V amplitudes exceed ∼10 and ∼13 times the noise level, respectively. In contrast to the profiles coming from the network, Fe I 630.15 nm shows significantly smaller Stokes V amplitudes than Fe I 630.25 nm, suggesting weak fields. The inversion indeed confirms this point, retrieving field strengths, inclinations and azimuths of 247 G, 141° and 248° for pixel #3 (top) and 380 G, 115° and 164° for pixel #4 (bottom).[9] The stray-light contamination factor are 88% and 85%, respectively.

Overall, the quality of the fits is remarkably good keeping in mind the limitations of the ME approximation and the fact that only one-component atmospheres are used.

7.10.2 Influence of the initial guess model

Different initial guess models may lead to different results. This has raised concerns about the uniqueness of the model atmospheres derived from quiet Sun inversions of Fe I 630.15 and 630.25 nm (Martínez González et al. 2006). For the inversion of the data sets considered in this Chapter we have employed a weak-field initialization with $B = 100$ G, $\gamma = 30°$, $\chi = 30°$, and $\alpha = 10\%$.

How do the results change when a strong-field rather than a weak-field initialization is used? To investigate this issue we have inverted a small IN area of $32\farcs2 \times 32\farcs2$ adopting different initialization for the magnetic field strength. In particular we have carried out four inversions with initial strengths of 100, 500, 1000, and 1500 G.

Figure 7.25 shows histograms of the differences between the field strengths, inclinations and azimuths resulting from the 100 and 1500 G initializations. This plot demonstrates that the solutions do not depend on the initial magnetic field strength. Even the azimuth shows variations smaller than 1° (the azimuth angle is usually the parameter with the largest uncertainties, just because it derived only from Stokes Q and U only, which are, in general, more affected by the noise). Finally, Figure 7.26 shows the differences between the stray-light factors obtained from the 100 and 1500 G initializations.

Another indication that the results are largely independent of the initial guess is provided by the fact that the percentage of pixels which get substantially better fits is small: only 3.1% for the 500 G initialization, 4.7% for the

[9] The azimuth values are less reliable when the Stokes U and Q signals approach the noise level, as in pixel #2 (Fig. 7.23) or pixel #3 (Fig. 7.24).

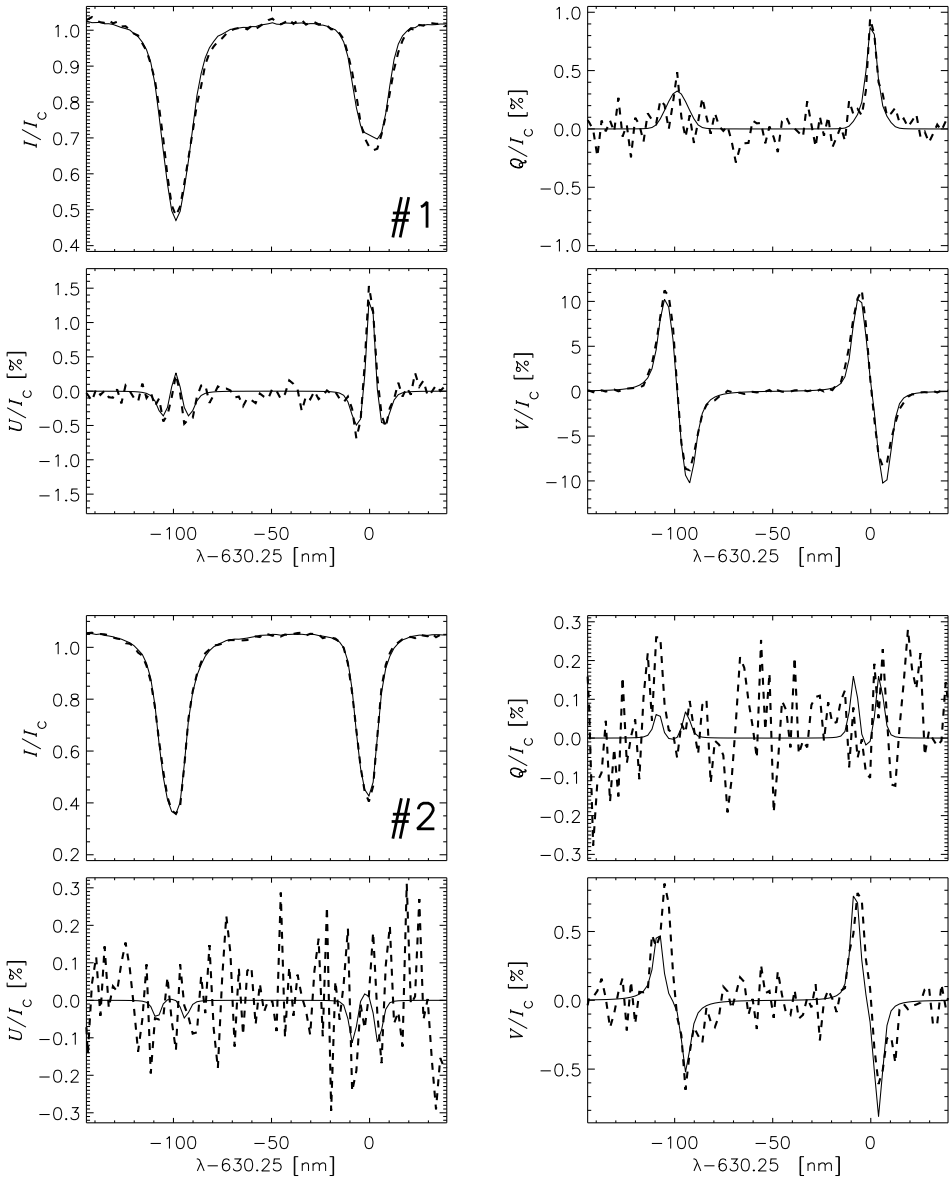

FIGURE 7.23:— Observed (dashed) and best-fit (solid) Stokes profiles emerging from network pixels #1 (top) and #2 (bottom). The field strengths and the stray-light factors retrieved from the inversion are 1334 and 237 G, and 61 and 71%, respectively. The specific locations of the pixels are indicated in the maps discussed in Sect. 7.4.

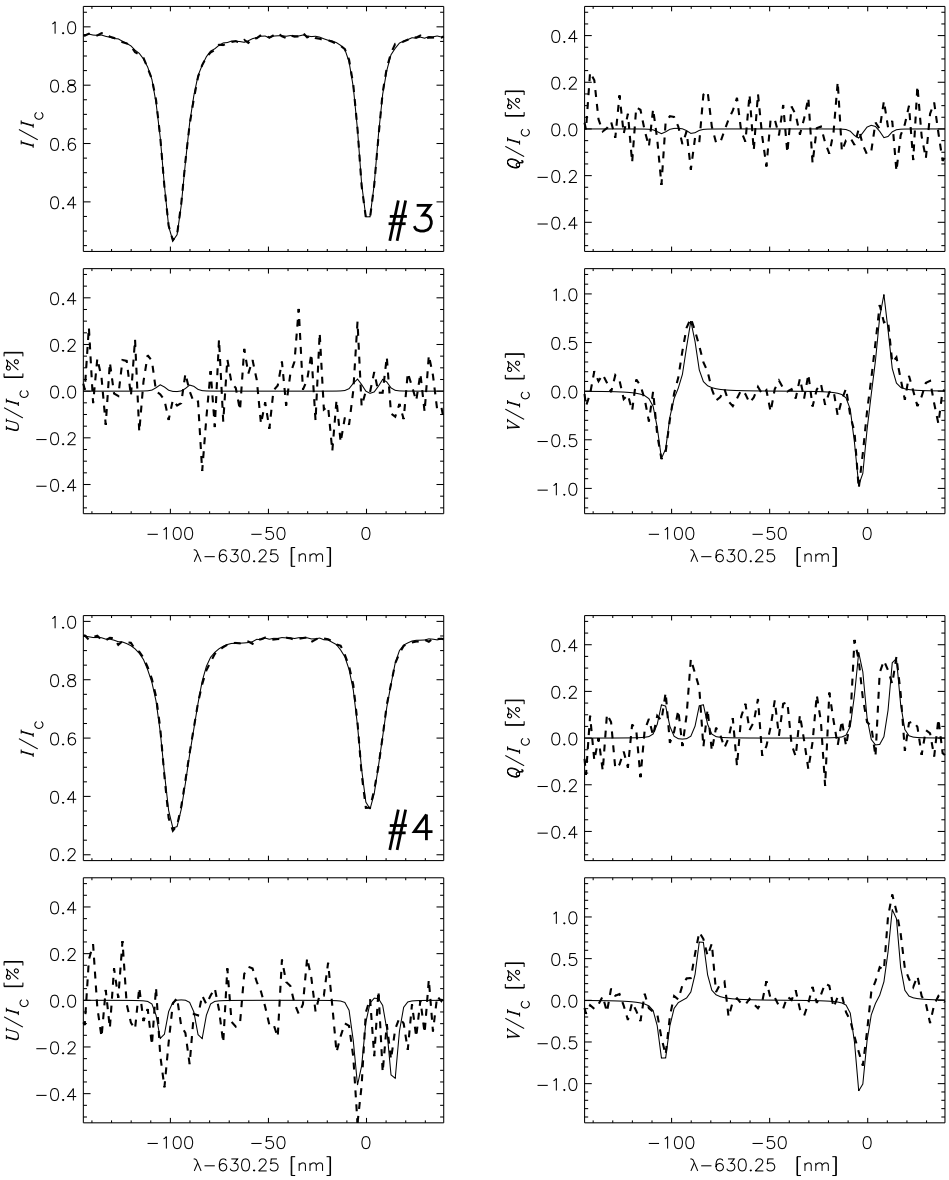

FIGURE 7.24:— Same as Fig. 7.23 but for Stokes profiles emerging from the internetwork. The field strength and the stray-light factor are 247 and 380 G for pixel #3 (top) and 88 and 85% for pixel #4 (bottom), respectively.

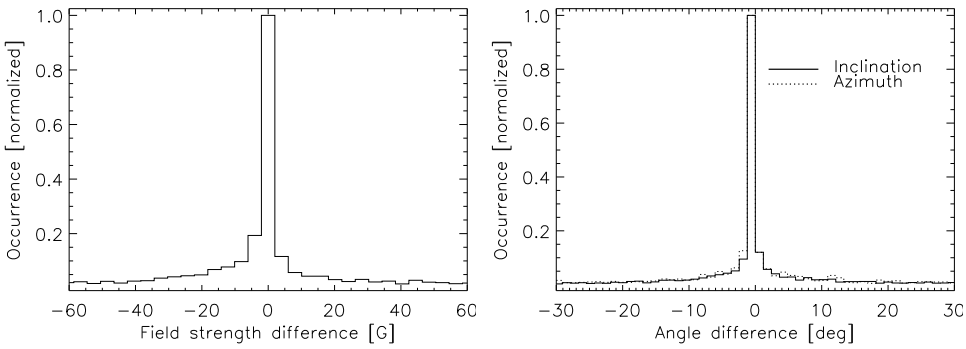

FIGURE 7.25:— Histogram of the differences between the field strengths (left), inclinations and azimuths (right) inferred with two different initializations: 100 and 1500 G.

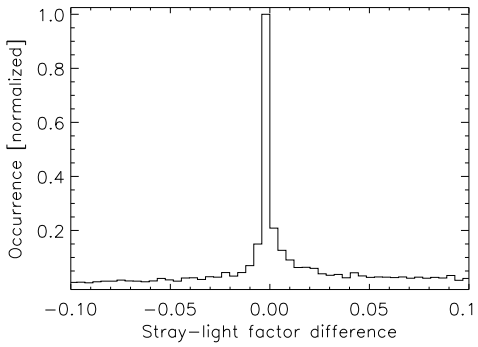

FIGURE 7.26— Histogram of the difference between the stray-light factor values inferred with two different initializations, 100 and 1500 G.

1000 G initialization, and 4.3% for the 1500 G initialization. Here, "substantially" better fits mean that the final χ^2-value is at least 50% smaller than the one obtained with 100 G.

In conclusion, even if there are unavoidable differences between the results of different initializations (mainly because of the noise), their magnitude is so small that the field strength, inclination, azimuth and stray-light factor distributions remain essentially the same. This is in sharp contrast with the inversions of the Fe I 630 nm ground-based measurements described by Martínez González et al. (2006).

7.10.3 ME inferences in the weak field regime

The tests presented in Sect. 7.10.2 demonstrate that the ME inversions are capable of disentangling the effects of the various atmospheric parameters. In

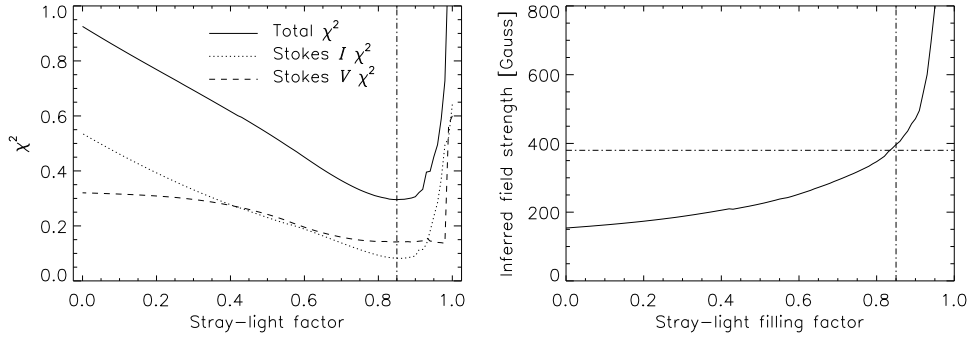

FIGURE 7.27:— Left: χ^2 values of the best-fit profiles resulting from the inversion of pixel #4 (as observed by *Hinode*) with fixed, erroneous stray-light factors. The solid, dotted and dashed lines stand for the total, Stokes I and V χ^2-values, respectively. The vertical line represents the "true" stray-light factor. Right: magnetic field strength retrieved for each fixed value of the stray-light factor. The dash-dotted line indicates the best-fit solution.

particular, they successfully distinguish between the stray-light factor and the magnetic field strength, the inclination, and even the azimuth. How is this achieved in the weak-field regime that applies to most of the IN pixels?

To answer this question, let us assume that the ME models derived from the profiles of Sect. 7.10.1 are the "true" solution. We have repeated the inversion of those profiles fixing the stray-light factor to erroneous values. 101 different stray-light factors, from $\alpha = 0$ to 1, have been considered. The other parameters for the initial guess model are the same as those described in Sect. 7.10.2 (except for the the stray-light factor, which is fixed to a wrong value).

To analyze how the fits are degraded, we evaluate the χ^2 function. This is basically the same as looking to the profiles, but mathematically. To see the "differences" between the synthetic and the observed Stokes I and V profiles, we also evaluate the merit function separately for Stokes I and V.

In Fig. 7.27 (left panel) we represent the χ^2-values of the 101 fits against the corresponding fixed stray-light factors, for the particular case of pixel #4 in Fig. 7.24. The solid line displays the total χ^2, whereas the dotted and dashed lines indicate the χ^2-values for Stokes I and V, respectively. The vertical line represents the "true" solution. Note that χ^2 is dimensionless and that its absolute value is irrelevant to the inversion code.

This analysis has been carried out for 12 different pixels, taken from network and internetwork areas. For simplicity, we show the results only for pixel #4.

Figure 7.27 gives a clear explanation of what is happening. When the stray-light factor is fixed to erroneous values, the fits worsen and the total χ^2

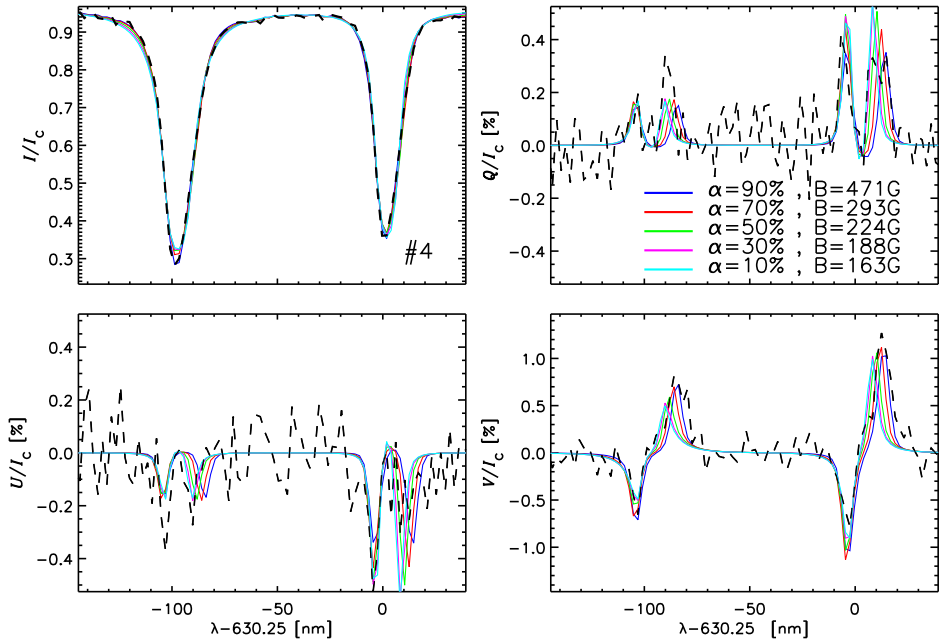

FIGURE 7.28:— Best-fit profiles resulting from the inversion of pixel #4 with fixed, erroneous stray-light factors. Different line colors stand for different values for the stray-light factor. It is difficult to visually determine the best fit which is actually the one represented in blue.

increases. The variation of the total merit function is large enough to be detectable by the inversion algorithm. Remarkably, the Stokes I and V merit functions behave quite differently. The χ^2 curve for Stokes V is rather flat around $\alpha = 0.8$. This implies that different stray-light contaminations produce equally good fits to Stokes V. In other words: many compatible solutions, characterized by different stray-light factors and correspondingly different field strengths, exist for Stokes V. However, *the range of acceptable stray-light contaminations is strongly limited by Stokes I*. This is reflected in the rapid increase of the Stokes I merit function away from the correct stray-light factor. The conclusion is the following: for the most part, the inversion algorithm uses the information encoded in Stokes I to determine the stray-light contamination. Thus, the often-forgotten Stokes I plays an essential role in the process of finding the absolute minimum of the total merit function. Once a good estimate of α is available, the amplitude of V determines the field strength.

In the right panel of the same figure we plot the retrieved magnetic field

strength for each fixed value of the stray-light factor. The vertical and horizontal lines represent the real solution. We see that the field strength varies smoothly from some 100 G when there is no stray-light contamination ($\alpha = 0$) to more that 1 kG when $\alpha = 1$. However, the merit function increases rapidly in the region of large stray-light contaminations ($\alpha \geq 0.9$), which makes it impossible to retrieve kG fields from this particular example.

Figure 7.28 shows the best-fit profiles for 5 fixed stray-light factors. It is difficult to determine which fit is better from a simple visual inspection. However, there are differences in the wings and core of Stokes I. Also, Stokes Q, U and V show differences in the splitting of the lobes.

For this pixel we can conclude that the inversion algorithm does its job properly, just using the information contained in the Stokes profiles. However, this particular case corresponds to a Stokes vector exhibiting some linear polarization signal. This may raise concerns as to the validity of these results because field strength information is also provided by Q and U. A significant fraction of IN Stokes profiles do not exhibit linear polarization signals and therefore, in order to generalize the analysis, we have studied two additional cases (pixels #5 and #6) showing negligible linear polarization signals.

Figures 7.29 and 7.30 show two observations belonging to IN regions with very weak circular polarization signals and no Stokes Q or U. Overplotted are the best-fit profiles. Notice that the best-fit profiles show Stokes Q and U signals below the noise level.

The bottom panels represent the χ^2-values of the 101 fits against the corresponding fixed stray-light factors (as previously explained for pixel #4). The analysis of pixel #5 just confirms the results from #4. The inversion algorithm finds the best solution only with Stokes I and V since there is no linear polarization that could help.

Profile #6 represents an extreme case. The circular polarization signal is 7 times larger than the noise. Interestingly, this profile can not be fully explained with a ME model and local stray light. The reason is that there are "two" different models that could reproduce Stokes I and V separately. Let us explain this in greater detail.

The Stokes I χ^2 has a clear minimum. Also, the Stokes V χ^2 has a clear one. The location of the two minima correspond to different values of the stray-light factor. For instance the Stokes I χ^2 has its minimum located at about ~ 0.7, while for Stokes V it is close to $\alpha = 1$. This indicates that the model is not able to explain Stokes I and V simultaneously (there are two best solutions for the χ^2). The inversion code is then forced to find a compromise between the best fits to Stokes I and V. In practice, $\chi^2_{\rm Total} \sim \chi^2_I/\sigma_I + \chi^2_V\sigma_V$, and so, depending on the weight of Stokes I and V, the inversion will favor the fit to

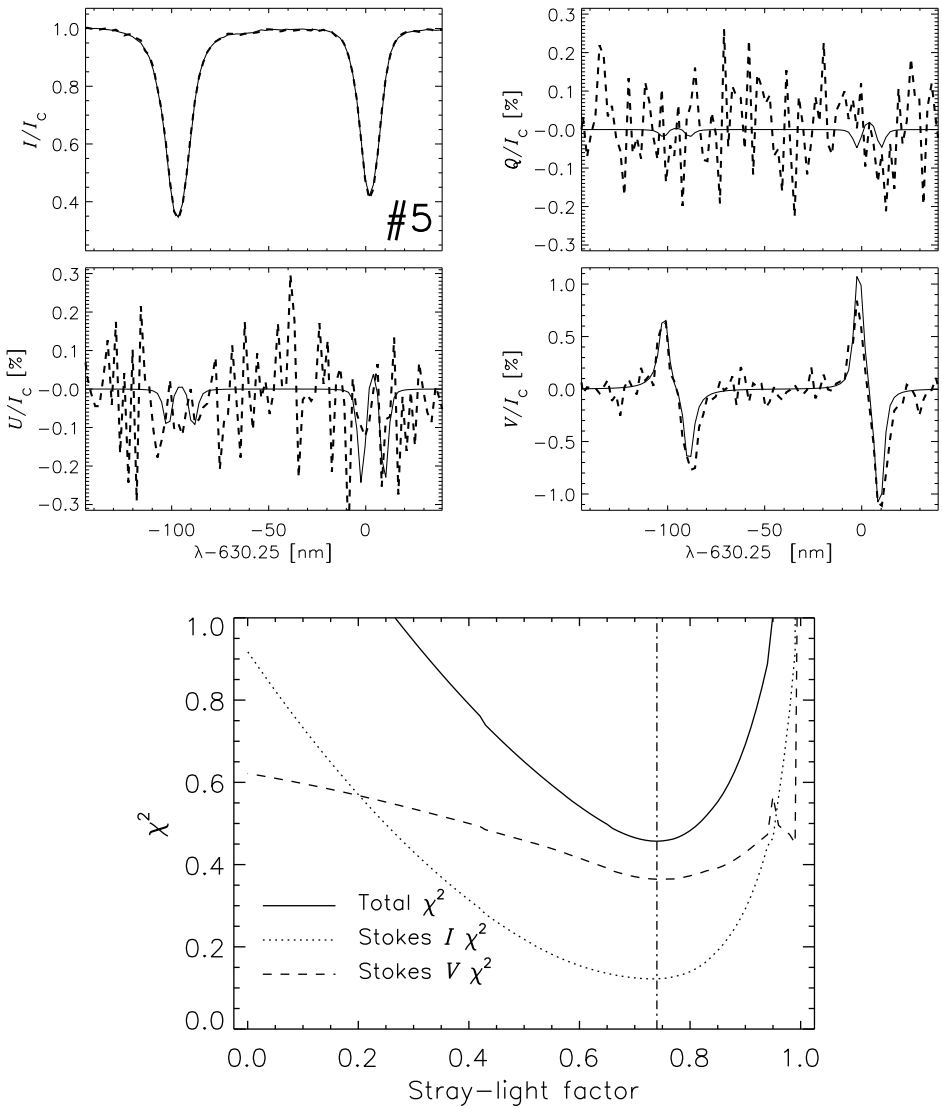

FIGURE 7.29:— Top: Observed (dashed) and best-fit (solid) Stokes profiles emerging from network pixel #5. The field strength, inclination and the stray-light factor retrieved from the inversion are 185 G, 126°, and 73%, respectively. Bottom: χ^2 values of the fits resulting from the inversion of the profile with fixed, erroneous stray-light factors. The solid, dotted and dashed lines stand for the total, Stokes I, and V χ^2, respectively. The vertical line represents the "true" stray-light factor.

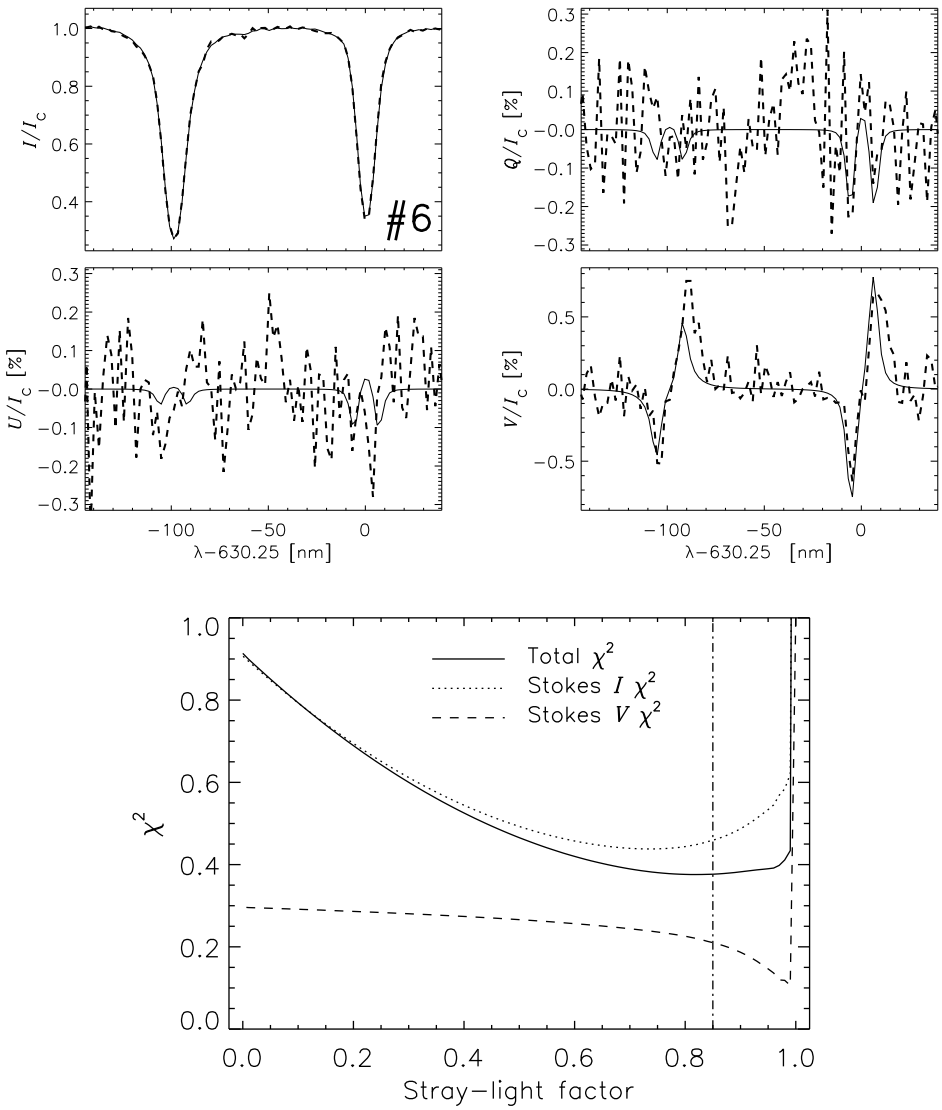

FIGURE 7.30:— Top: Same as 7.29 but for pixel #6. The field strengths, inclinations and the stray-light factors retrieved from the inversion are 219 G, 105°, and 84%, respectively. Bottom: χ^2 values of the fits. The solid,dotted and dashed lines stand for the total, Stokes I and V χ^2, respectively. The vertical line represents the "true" stray-light factors.

I or V. In our case we have weighted both profiles equally, therefore the best fit finds an α value that is somewhere between 0.7 and 1.

The analysis of the remaining 9 pixels leads to similar results as for the first case explained in this section. These tests have also been carried out varying the initialization of the magnetic field strength (100, 800, and 1500 G). In all cases, the results turn out to be the same.

In addition, there are a number of arguments supporting our claim that ME inversions successfully separate the stray-light factor from the field strength when applied to high angular resolution observations, even in the weak field regime:

(i) We obtain weak fields from the measurements, much in the same way as we got them from the MHD simulations with average unsigned flux density of 10 Mx cm^{-2} (see Chapter 6).

(ii) The inversions do not depend on the initial guess adopted for the magnetic field strength. If the code were unable to disentangle the stray-light factor and the magnetic field strength, the histograms of Figs. 7.25 and 7.26 would certainly be worse.

(iii) Our results are in agreement with those of Lites et al. (2007a, 2008a), using the same data.

Finally we want to point out that these tests have been carried out with pixels belonging to the normal map. As the high S/N map provides polarization signals that are less affected by photon noise, we find it unnecessary to repeat them given that the normal map represents the worst-case scenario in terms of noise.

7.11 Discussion

Up to now, the analysis of IN fields has been controversial. Visible lines seemed to deliver mostly kG fields while IR lines yielded hG fields. To explain these conflicting results, it has been argued that visible and IR lines sample different magnetic structures in the resolution element (Socas-Navarro 2003 & Sánchez Almeida & Socas Navarro). Also, Bellot Rubio & Collados (2003) suggested that noise may be responsible for the different magnetic field distributions resulting from visible and infrared lines, and highly recommended to improve the S/N of the measurements. Even more recently, Martínez González, Collados, & Ruiz Cobo (2006) have shown that the Fe I 630.2 nm lines do not contain sufficient information to obtain reliable field strengths from IN regions at $1''$ spatial

resolution. Given these concerns, other authors have explored new ways to derive IN fields (e.g., Trujillo Bueno et al. 2004; Asensio Ramos et al. 2006; López Ariste et al. 2006).

The polarimetric sensitivity provided by the *Hinode*/SP is almost 10 times larger than that by ground-based instruments at 1″. The results presented here suggest that, most probably, previous analyses were strongly biased by the spatial resolution and the atmospheric seeing. Our tests demonstrate that the results from the ME inversion of *Hinode*/SP data are biased neither by the initialization nor by the intrinsic noise of the observations.

Thus, the *Hinode*/SP measurements indicate that most IN fields are weak. This is in agreement with the picture derived from the more magnetically sensitive Fe I lines at 1565 nm (Lin 1995; Lin & Rimele 1999; Collados 2001; Khomenko et al. 2003; Martínez González et al. 2008; Domínguez Cerdeña et al. 2006). It is also in agreement with the simultaneous inversion of visible Fe I lines at 630 nm and infrared Fe I lines at 1565 nm (Martínez González et al. 2008). Rezaei et al. (2007) also found weak fields in the IN using the Fe I 630 nm lines, at a slightly worse resolution of 1″.

Our results confirm the findings of López Ariste et al. (2006), whose analysis of the Mn I 553 nm line indicate that that the IN is dominated by fields below 600 G. They also partially agree with the analysis of the near-infrared Mn I 1526.2 nm line (Asensio Ramos et al. 2007). They found a Gaussian-shaped field strength distribution centered at around 250-350 G. The manganese lines are important because the hyperfine effects they show make it possible to derive the strength of the field directly from the profiles, without interferences from the stray-light factor or the magnetic filling factor.

The slope of the field strength distribution in the IN is similar to that obtained from magnetoconvection simulations of $\langle B \rangle$=10 Mx cm^{-2}. The observed field inclinations, however, turn out to be significantly larger than those predicted by current simulations. The agreement with MHD simulations may improve with the implementation of new boundary conditions and/or increased grid resolution.

The distribution of field inclinations shows that there is a large occurrence of horizontal fields in the IN. The fields tend to be more horizontal in granules than in intergranular lanes. The scenario of an IN filled by nearly horizontal hG fields is compatible with the large trasverse magnetic fluxes found by Lites et al. (2007a, 2008a) and Martínez González et al. (2007). This clear dominance of horizontal magnetic fields may be generated by the action of a near-surface turbulent dynamo (Abbett 2007; Schüssler & Vögler 2008). It may also be due to the emergence of horizontal fields from the upper convection zone, under the action of granular motions (Steiner et al. 2008).

The distribution of magnetic fields show as that there are also magnetic fields in granules. These fields are weaker than those found in intergranular lanes and tend to be horizontally oriented. However, vertical fields do also exist in granules. We also find that the polarization signals are equally distributed between upflows and downflows.

We find flux densities of 7–25 Mx cm^{-2} in the IN. These values are of the same order of magnitude as previous estimates at lower spatial resolutions (e.g., Martin 1987; Wang 1995). However, we find magnetic filling factors of $\sim 50\%$. The transverse flux in the IN is a factor 3-3.5 times larger than the longitudinal flux density, not in agreement with the results of Lites et al. (2007a, 2008a).

Measurements based on the Hanle effect (Trujillo Bueno, Shchukina, & Asensio Ramos 2004) suggest that the IN is filled by nearly horizontal fields with an average field strength of ~ 130 G. This value is surprisingly close to the average field strength of about 125 G and to the peak of the distribution of field strengths we have found in the IN using the high S/N observations (see Table 7.2). The results support the idea of an IN filled by turbulent fields which appear and disappear following the granular motions.

7.12 Conclusions

In this Chapter we have used the Milne-Eddington inversion strategy described in Chapter 6 to infer the magnetic field vector from high spatial resolution spectropolarimetric measurements of the quiet Sun performed by *Hinode*.

The inversion strategy has been applied to a quiet Sun raster scan and to a time sequence of ~ 2 hours with very high S/N, both taken with the *Hinode*/SP. We have demonstrated that noise does not significantly affect the results of ME inversions, provided a sufficiently large polarization threshold is used to invert the Stokes profiles. A threshold around 4.5 times the noise level seems to yield correct inferences. In addition, we have shown that the results do not depend on the initial magnetic field strength of the model, because the information contained in the Stokes profiles observed at the resolution of *Hinode* is sufficent to disentangle the various model parameters.

The inferred field strength distributions indicate that internetwork regions are mainly formed by hG field concentrations, contrary to what is obtained from the same lines at $1''$. Together with Rezaei et al. (2007), this is the first time that Fe I 630 nm observations confirm the weak IN fields indicated by near-infrared measurements, which seems to definitely close the discrepancy between the results derived from both spectral regions. Our analysis shows that quiet Sun internetwork regions consist mainly of weak fields with magnetic filling

factors of about 45% at a resolution of 0.″3 (after correcting the dilution of the polarization signals due to telescope diffraction). These results confirm the picture of weak internetwork fields derived from ground-based measurements in the near infrared (see, e.g., Collados 2001).

We still do not know the origin of the ubiquitous horizontal IN fields or the granular fields detected bu *Hinode*. In the next Chapter we analyze time series of *Hinode*/SP measurements in an attempt to identify the physical mechanisms responsible for the observed distributions of IN magnetic fields.

8

Magnetic field emergence in the quiet Sun

The previous Chapter was dedicated to the analysis of quiet Sun's magnetic fields. To that end we used high spatial resolution spectropolarimetric data recorded with the *Hinode* satellite. In this chapter we explore the benefits of high-cadence time series of spectropolarimetric measurements taken with the same instrument. More specifically, we investigate the process of emergence of magnetic fields into the solar surface, in an attempt to understand the origin of the horizontal IN fields. As the result, we discover a new form of flux emergence above granules, which seems to involve vertical magnetic fields.

8.1 Introduction

The analysis of spectropolarimetric measurements taken with the spectropolarimeter aboard *Hinode* indicates that the internetwork harbors a substantial amount of magnetic flux, being the intrinsic magnetic fields predominantly *weak* and tending to be horizontally oriented. We now have a good understanding of the properties of such fields, but their origin remains largely unknown.

There have been different theoretical approaches to the origin of quiet Sun photospheric magnetic fields. Cattaneo (1999) suggested that the action of a local dynamo at the solar surface may generate considerable amounts of magnetic flux. But the questions of how these fields appear on the solar photosphere and whether or not a local dynamo operates are still open.

A way to seek for the origin of the fields is to perform spectropolarimetric observations at high cadence. This would allow the evolution of individual magnetic features to be observed, therefore gaining additional information about their dynamics.

At present, the *Hinode* spectropolarimeter is the most suitable instrument to perform high-cadence time series of spectropolarimetric measurements in the quiet Sun. It provides very high spatial resolution data in the absence of atmospheric seeing. The absence of the Earth's atmosphere permits recording long time series under very stable conditions. This allows rapid processes to be studied in detail although at the cost of smaller fields of view and/or larger noise levels in the polarization spectra.

There have been attempts to characterize the quiet Sun magnetic fields by analyzing high-cadence time series. Lites et al. (1996) employed the Advanced Stokes Polarimeter (ASP) to record time sequences of maps in quiet Sun regions with spatial resolutions of $\sim 1''$. They reported on the existence of small-scale ($1''$-$2''$), predominantly horizontal magnetic features typically lasting $\sim$5 minutes. Their findings have been confirmed by Martínez González et al. (2007) using time series taken with the Tenerife Infrared Polarimeter (Collados 1999) installed at the Vacuum Tower Telescope of Teide Observatory in Tenerife. They presented convincing evidence of low-lying loops that connect opposite-polarity flux concentrations in the solar internetwork. Figure 8.1 shows a pictorical view of such loops linking different magnetic patches on the solar surface (courtesy of M. J. Martínez González).

Analysis of magnetograph data have significantly contributed to this topic as well. De Pontieu (2002) used the Swedish Vacuum Solar Telescope to record high-spatial resolution longitudinal magnetograms of the quiet Sun. His observations show flux concentrations emerging in the internetwork and disappearing in about 10-15 minutes, with no evidence for flux cancellation, i.e., he did not find opposite-polarity magnetic fields at the emergence sites. The observations were taken away from disk center, so there is a possible connection with the small-scale magnetic loops discovered by Lites et al. (1996) and confirmed by Martínez González et al. (2007). More recently, Lamb et al. (2008) have employed MDI longitudinal magnetograms with a spatial resolution of $1\farcs2$, to analyze the emergence of small-scale magnetic features that seem to be apparently of unipolar flux.

As previously mentioned, improvements in the spatial resolution of spectropolarimetric measurements and the ability of taking high-cadence maps should provide new insights into the emergence, evolution and disappearance of small-scale magnetic flux concentrations over quiet Sun regions. Indeed, Centeno et al. (2007) and Ishikawa et al. (2007) have made use of the *Hinode*/SP

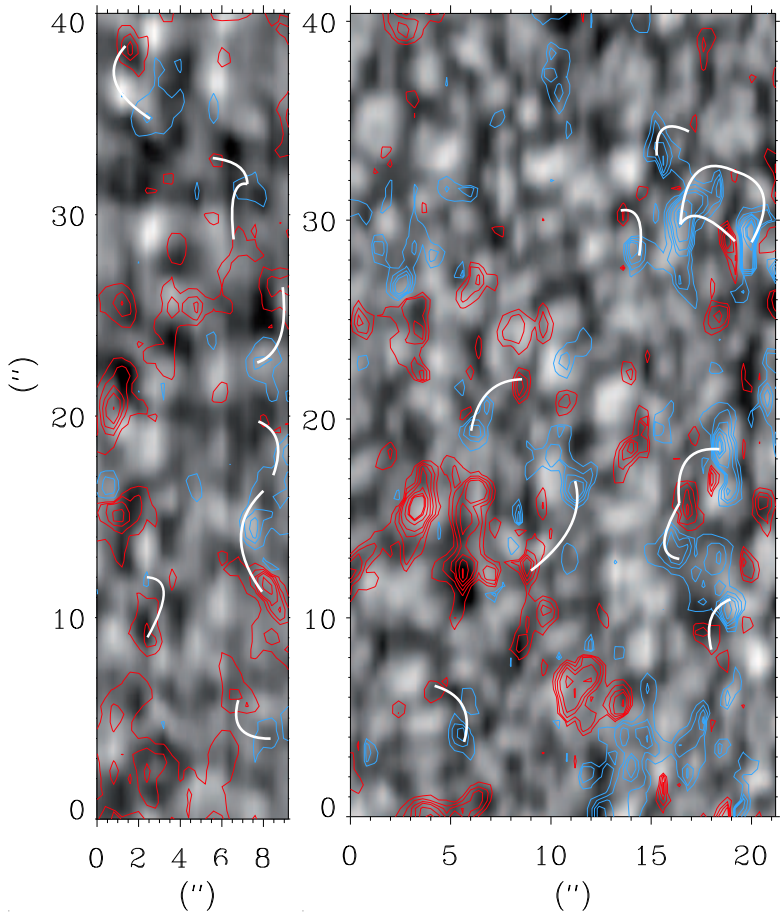

FIGURE 8.1:— Pictorial view of low-lying magnetic loops in quiet Sun regions. Red and blue contours represent fields of opposite sign. The loops are indicated with white lines. The background represents continuum intensity maps as recorded with the TIP instrument at the VTT (see text for details). Cortesy of M. J. Martínez González.

capabilities to confirm the existence of very small-scale magnetic loops in quiet Sun areas and plage regions, respectively. Current radiative MHD simulations are able to model the emergence of magnetic flux tubes from the near-surface layers of the solar convection zone into the photosphere (e.g., Cheung et al. 2007)

In this Chapter we concentrate on the analysis of long time series of raster scan maps taken by *Hinode*/SP over quiet Sun regions. The idea is to analyze the evolution of emerging flux in the quiet solar photosphere. The Chapter is structured as follows: we first describe the observations and perform a quali-

tative analysis of typical emergence events. Then, we evaluate line parameters from the observed Stokes profiles. At the end we discuss the possible origin of the emergence phenomena and present different physical scenarios that might explain the observations.

8.2 Observations

The data under analysis consist of three sequences of narrow raster scans performed with the spectropolarimeter aboard *Hinode* at disk center. As described in Chapter 7, the SP measures the Stokes profiles of the two Fe I lines at 630.2 nm. The advantage of the *Hinode*/SP over current magnetographs is that, although it cannot achieve their very high cadences, we get the four Stokes profiles of the two lines with a spectral sampling of 2.15 pm pixel^{-1}. This, together with a spatial sampling of about $0\farcs16$ and high polarimetric sensitivities, makes the SP data ideal to analyze the evolution of photospheric emergence events.

The parameters of each of the observing runs can be found in Table 8.1. Two of them scanned a narrow internetwork area with a cadence of about 2 minutes and signal-to-noise ratios of about 1000. A third one was obtained by scanning a smaller quiet sun area with shorter integration times, to increase the temporal resolution but at the expense of lower signal-to-noise ratios. In addition, to monitor the conditions of the chromosphere, filtergrams in the Ca II H line core were acquired with the *Hinode* Broadband Filter Imager (BFI; Tsuneta et al. 2008). Only for one of the data sets we have Dopplergrams and magnetograms taken with the Narrowband Filter Imager (NFI) in the chromospheric Mg b I line at 517.2 nm. Dopplergrams are determined from the ratio of the difference of blue and red wing intensities divided by their sum. The blue/red images are taken at a distance of ± 11.2 pm from line center. The Stokes V images from which the magnetograms are constructed were taken at the same wavelength positions. To first order, the magnetograms are not affected by flow velocities. This observing run belongs to the *Hinode* Operation Plan (HOP) 14, entitled "Canary Islands Campaign".

Figure 8.2 shows G band and Ca II H images corresponding to the data set #1. In the same figure, the area scanned by the spectropolarimeter is outlined by the red box. The slit is parallel to the Y-axis and the SP scans from left to right. The zero position along the slit is on the bottom left corner. The green box indicates the position of event A at $\Delta t = 8$ min (see next section). The Ca II H filtergram shows that the SP slit is placed in an internetwork region, far from network areas (brighter regions near the top and bottom of the FOV).

TABLE 8.1:— Basic parameters for the three observing runs. The first three columns specify the data set and the initial date and time (UT). The fourth column stands for the total duration of the run. The fifth and sixth columns are the number of slit positions in a scan and the corresponding slit integration time. The second row block stands for the estimated noise levels for V, Q, and U in units of $10^{-3}\,I_c$, the field-of-view (FOV), and the cadence. The three last columns indicate the available filtergram (FG) data with their temporal resolutions and pixel sizes.

DATA SET	DATE (2007)	TIME	DURATION	SLITS	EXP. TIME
1.....	Feb. 11	11:07:08	4:33h	25	4.8s
2.....	Mar. 10	00:17:03	5:30h	25	4.8s
3.....	Oct. 6	08:01:07	1:59h	18	1.6s
NOISE V - Q/U	FOV	CAD.[a]	FG DATA	CAD.	PIXEL SIZE
1.1 - 1.2	$4'' \times 81\farcs9$	∼123s	Ca II H	64s	$0\farcs054$
1.1 - 1.2	$4'' \times 81\farcs9$	∼123s	Ca II H	35.5s	$0\farcs108$
1.7 - 1.8	$2\farcs9 \times 41\farcs0$	∼34s	Ca II H/Mg I	32/35s	$0\farcs054/0\farcs08$

[a]Notice that the temporal cadence does not coincide with the number of slit scans × the exposure time. There is an extra time needed to move the slit back from the last scan to the position of the first one.

Only the top of the slit observed part of the photospheric network. We focus our analysis only on IN areas.

The average response height of the *Hinode* Ca II H line filtergrams corresponds to $z = 247$ km (see Carlsson et al. 2007 who evaluated the temperature response function of the Ca II H line, taking into account the *Hinode* filters). The Mg I line is formed within the chromosphere, closer to the photosphere (on average) than the Ca II H line core, accordingly to Lites et al. 1999. However, the average height at which this line is more sensitive to temperature is still a matter of debate.

The Mg I magnetograms and Dopplergrams will allow us to analyze this kind of event in the lower chromosphere. Also, given that magnetic fields outside the photospheric network are not associated with enhanced Ca II K or H emission (Lites et al. 1999; Rezaei et al. 2007), the detection of transient Ca II H brightenings at or near the position of emerging flux would indicate that the emergence process is able to transfer a certain amount of energy to the (low) chromosphere.

The SP data have been corrected for dark current, flat-field, and instrumental cross-talk using standard routines included in the SolarSoft package. The absolute wavelength scale for the observed Stokes spectra has been determined by comparing the line core positions of Fe I 630.1 and 630.2 nm, averaged over quiet Sun areas, with the Fourier Transform Spectrometer atlas. This is done

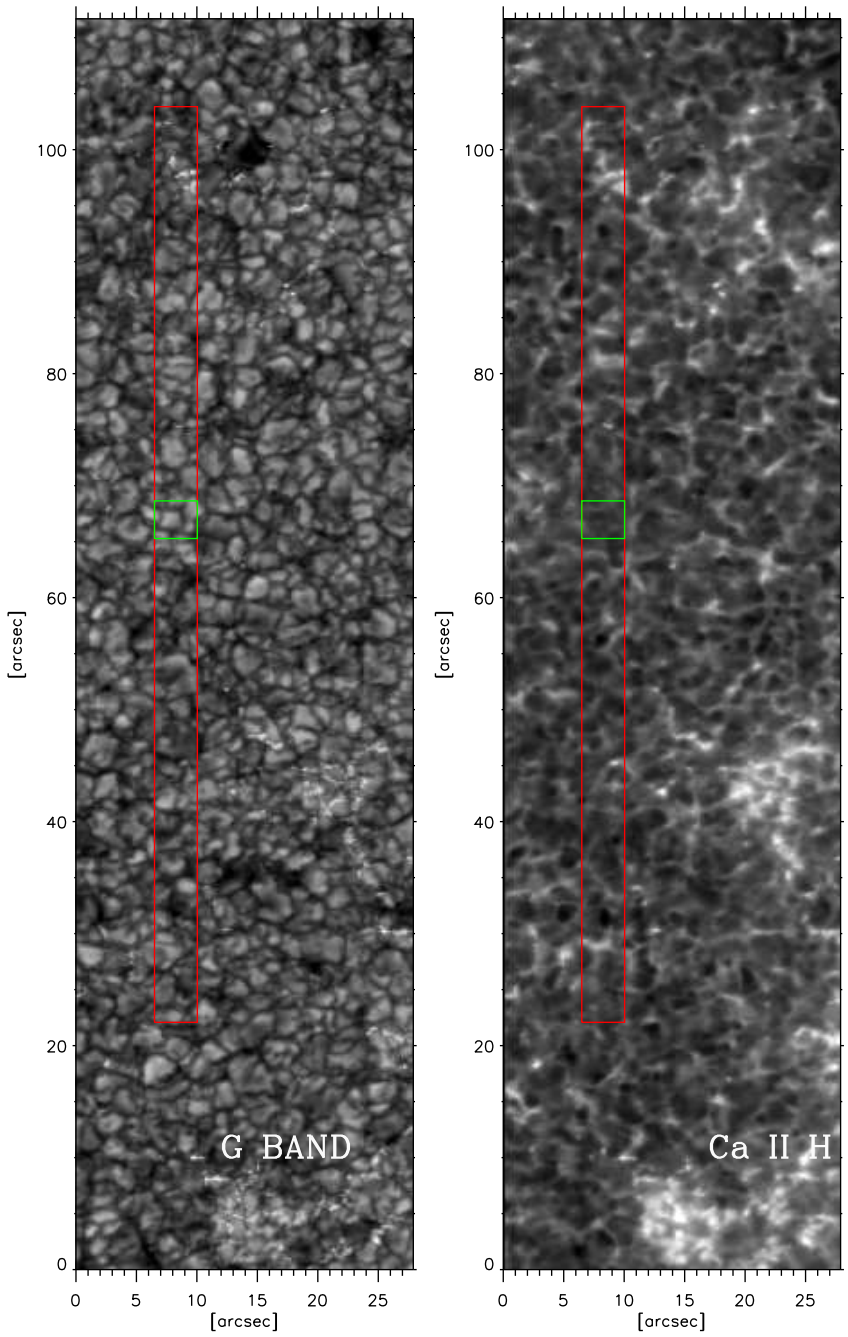

FIGURE 8.2:— Left: *G*-band image of the center of the solar disk on February 11, 2007. Right: Ca II H image of the same area. The red box shows the area scanned with the SP (data set #1). The green box shows the position of emergence event A (see text for details). The FOV is $93\farcs5 \times 28\farcs1$. North is up and West to the right.

for each of the observing runs. To remove the gravitational redshift we simply subtract the corresponding wavelength shift of 615 m s^{-1}. For further details see Sect. 7.2. The calibration algorithm applied to the filtergrams removed cosmic rays, hot pixels, and dark current.

The SP maps, BFI filtergrams, and NFI magnetograms have been aligned as follows: to align the Ca II H filtergrams with the SP data we have compared the G-band images recorded with the BFI and the continuum intensity maps constructed from the SP raster scans. The corresponding X and Y offsets of the images have been calculated through Fourier cross-correlation techniques with sub-pixel accuracy. To remove the additional image shift between the G-band and the Ca II H images, a correction to the computed offsets was applied. The offsets between the G-band and Ca II H images can be found in Shimizu et al. (2007). The Mg I magnetograms have been aligned with the SP by comparing them with a photospheric magnetogram constructed from SP Stokes V profiles.

8.3 Emergence processes in the quiet Sun

By visual inspection of the continuum intensity maps together with the circular and linear polarization maps (Figs. 8.3 and 8.4), we have found several emergence events in which the appearance and disappearance of magnetic flux is clear. These events can be classified in two groups:

1.– the emergence of small-scale magnetic loops

2.– the emergence and disappearance of what seem to be a new form of small-scale magnetic fields in the quiet Sun, in which unipolar flux patches appear above granular cells with apparently vertical orientation.

Lets us give an example of each of the two types. Figure 8.3 shows the first of them, i.e., the emergence of a small magnetic loop. Displayed are the continuum intensity and circular and linear polarization signals (from top to bottom, respectively). The Y-axis represents the image of the Sun through the slit, while the X-axis is the scan direction and hence represents both time and space.

The emergence of magnetic loops into the photosphere is observed as horizontal fields above granules and footpoints of opposite polarity rooted in the adjacent intergranular lanes. In this example, the loop starts to be visible from the beginning of the sequence and rises with time (the linear polarization signal patch grows accordingly, as indicated by the blue contours). The footpoints of the loop, each of different polarity (red contours), appear at t=0.5 min and separate as the flux emerges. The linear polarization patch starts to become

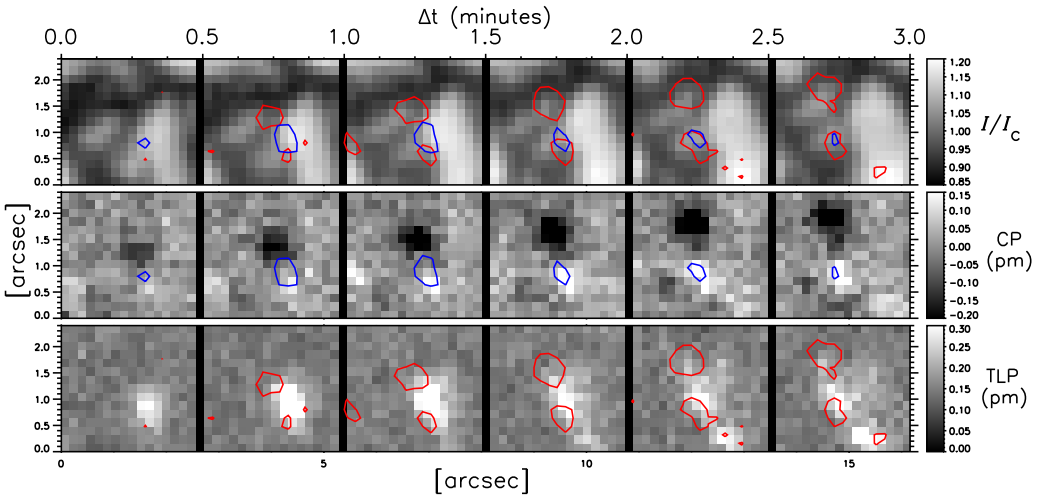

FIGURE 8.3:— Time evolution of the emergence of a magnetic loop observed on September 25, 2007. The cadence was ∼30 s and the maps covered a FOV of 2.″56 × 2.″4. From top to bottom: normalized continuum intensity, and circular (CP) and linear (TLP) polarization signals. The red/blue contours enclose areas with CP/TLP signals larger than 0.12 pm. $\Delta t = 0$ min corresponds to 15:15:33 UT.

smaller 1.5 minutes later. This indicates that the apex of the loop continues rising, leaving the photospheric layers where the two Fe I lines are formed.

This emergence event is nothing but the observational evidence of the rise of small magnetic loops from deep photospheric layers towards the chromosphere. The loop shown in Fig. 8.3 is similar to those reported by Ishikawa et al. (2007) in plage regions and Centeno et al. (2007) in quiet Sun areas, using similar *Hinode*/SP time series. The frequency of appearance of these loops seems to be much higher than ever thought (Martínez González & Bellot Rubio, in preparation).

Figure 8.4 shows an example of the second type of emergence events. The observations clearly show circular polarization signals that appear above granular convection cells and disappear soon afterwards.

These photospheric events differ from the emergence of magnetic loops in that there is no linear polarization signal associated with the magnetic features. Contrary to the behavior exhibited by the magnetic loops, it is the circular polarization signal which appears above the granular cells. We identify these events as the emergence of vertical field lines in granules. Therefore, they are different phenomena. The appearance of unipolar flux concentrations in the quiet Sun has been reported by de Pontieu (2002) and Lamb et al. (2008) at much lower spatial resolutions. It is thus very difficult to establish as association

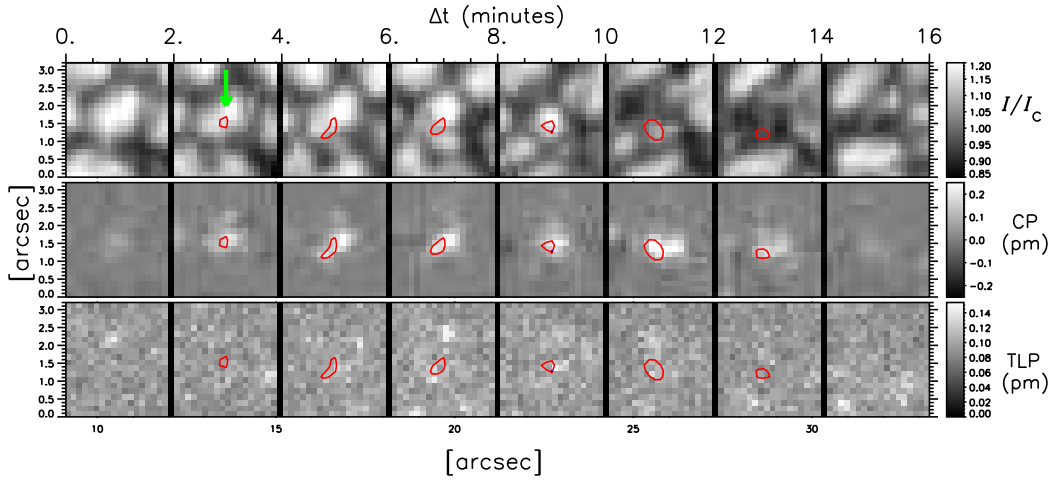

FIGURE 8.4:— Time evolution of the emergence of a magnetic patch observed on March 10, 2007. The cadence was ∼60 s and the maps covered a FOV of $3\farcs5 \times 3\farcs5$. From top to bottom: normalized continuum intensity, and circular (CP) and linear (TLP) polarization signals. The red/blue contours enclose areas with CP/TLP signals larger than 0.15 pm. $\Delta t = 0$ min corresponds to 00:54 UT.

between their results and ours. To our knowledge this is the first time that vertical magnetic fields are observed to appear in granules. From now on, we will concentrate on the analysis of these vertical-field emergence events.

8.4 Statistical analysis of the emergence processes

We have detected a total of 9 emergence events on a surface area of 655 arcsec^2 in about 5 hours, and another 4 events on a surface area of 118 arcsec^2 in ∼2 hours (Table 8.1). Thus, the frequency of appearance is not large compared with the many cases of small-scale magnetic loop emergences that are observed in the same data sets. In this section we analyze several properties of these emergence events. We will pay special attention to five representative examples that will be referred to as events A, B, C, D, and E.

To carry out a qualitative analysis of these events we have evaluated the following properties: the spatial position of the emergence along the slit; the initial and final time of the event as well as its total duration; the maximum size of the flux concentration in arcsec^2; the maximum spatially averaged unsigned longitudinal magnetic flux density; the maximum magnetic flux; and the maximum blue shifted zero-crossing velocity. In addition, we have evaluated several Stokes profile parameters to analyze their temporal evolution: the

circular polarization signal, the total linear polarization signal, and the LOS velocity.

The LOS velocity is derived from the Stokes V zero-crossing wavelengths for pixels whose Stokes V amplitude exceeds 4 times the corresponding noise levels. The circular polarization (CP) maps have been calculated by integrating the blue lobe of the Fe I line at 630.25 nm, i.e.,

$$\mathrm{CP} = \int_{\lambda'-\lambda_a}^{\lambda'-\lambda_b} \frac{V(\lambda)}{I_\mathrm{c}} d\lambda, \tag{8.1}$$

where λ' is the wavelength position of the blue peak of Stokes V. λ_a and λ_b are the limits for the wavelength integration range, ($\lambda_b - \lambda_a = 23.6$ pm). In the same way, the total linear polarization signal (TLP) is computed as

$$\mathrm{TLP} = \int_{\lambda_0-\lambda_a}^{\lambda_0-\lambda_b} \frac{[Q^2(\lambda) + U^2(\lambda)]^{1/2}}{I_\mathrm{c}} \mathrm{d}\lambda, \tag{8.2}$$

where λ_0 is the central wavelength of the Fe I 630.25 nm line and λ_a and λ_b are wavelength integration limits with $\lambda_b - \lambda_a = 62.4$ pm. The integration ranges for the CP and the TLP are as narrow as possible to minimize the contribution of noise. The CP and the TLP are measured in pm.

To calculate the longitudinal magnetic flux for each individual pixel we use the standard magnetograph formula (see, e.g. Landi Degl'Innocenti 1992) based on the weak-field approximation[1]

$$V(\lambda) = -\phi\, C \frac{dI(\lambda)}{d\lambda}, \tag{8.3}$$

where $\phi = fB\cos\gamma$ is the longitudinal magnetic flux density; $C = k\lambda_0^2\bar{g}$ is a calibration constant, $\bar{g}$ is the effective Landé factor, λ_0 the central wavelength of the line, and $k = 4.67\times10^{-13}$ [Å^{-1} G^{-1}]. ϕ is measured in units of Mx cm^{-2}.

To determine ϕ we need the Stokes I and V profiles. In particular we use all the wavelength samples along the spectral line. Therefore, Eq. (8.3) can be solved analytically using linear least squares. The solution is (Domínguez Cerdeña et al. 2003)

$$\phi = \frac{\sum_i V(\lambda_i) \left(\frac{dI(\lambda)}{d\lambda}\right)_i}{C \sum_i \left(\frac{dI(\lambda)}{d\lambda}\right)_i^2} \tag{8.4}$$

[1]This approach provides correct field strengths since the internetwork is mainly formed by hG field concentrations.

where $i = 1 \ldots n$ refers to the different wavelength samples. The derivative of Stokes I is evaluated numerically. The SP provides more wavelength samples than classical magnetographs. Using the whole line profile we substantially reduce the effect of noise in the determination of the flux density.

The magnetic flux is measured in Mx, and is given by $\Phi = \phi\, A$, where $A \approx 116^2$ km^2 stands for the area sampled by a single pixel on the solar surface. The spatially averaged unsigned flux density is given by $\overline{\phi} = \sum_i |\phi_i|/N$, where N is the number of pixels, i. Finally, the total unsigned flux is $\Phi_{\rm T} = NA \sum_i |\phi_i|$.

Table 8.2 summarizes the different properties for the emergence events. Unless otherwise indicated, the various quantities are calculated for pixels whose CP$>$ 0.15 pm, which is approximately 6 times the noise level.

The size of the patches varies from 1.6 to 6.72 arcsec^2, although it depends on the CP threshold used to define the extent of the flux concentrations. They are smaller than the hosting convection cells. The average lifetime of the magnetic flux patches is about 13 min. The mean magnetic flux density is $\sim$30 Mx cm^{-2}, and the flux do not surpass $1.5{\times}10^{18}$ Mx, with a mean flux of $\sim 5{\times}10^{17}$ Mx.

For comparison, the emerging unipolar flux concentrations found by de Pontieu (2002) show magnetic fluxes of about $5{\times}10^{17}$ Mx and flux densities of $\sim$200 Mx cm^{-2}. The sizes of the emerging patches are about 1.5 arcsec^2, smaller than those presented in Table 8.2. Note that it is difficult to perform a direct comparison of the fluxes since the instrumental sensitivities as well as the angular resolution and the method of analysis are different.

The flux values shown in Table 8.2 are close to the average of $\sim 10^{16} - 10^{17}$ Mx found in internetwork areas (e.g., Socas-Navarro and Sánchez Almeida 2002), but far from typical network values of $\sim 10^{19}$ (e.g., Schrijver et al. 1997b). The mean magnetic flux density of $\sim$30 Mx cm^{-2} is, approximately, equivalent to field strengths of $\sim$ 70 G, assuming a "effective" filling factor of $\sim$ 45% for typical internetwork field concentrations (see Chapter 7). In any case, we caution that these field strengths are rough estimates only. To derive reliable values for the field strengths associated with these emergence processes, an analysis based on inversion techniques is mandatory.

8.5 Qualitative analysis

The events marked with capital letters in Table 8.2 are studied in more detail in this Section. Figures 8.5 through 8.10 show the corresponding time sequences. Each of the figures is structured as follows: the first row gives the continuum intensity at 630 nm normalized to the average continuum intensity of the cor-

TABLE 8.2:— Phenomenological properties of flux emergence events occurring in granular cells. The first column identifies the event. The next column shows the corresponding data set from table 8.1. The Y-position of the emergence event (along the slit), the initial and final time of the emergence in UT, as well as the total duration are shown in next four columns. The subsequent ones provide with the maxima of: the size of the emergence, the average unsigned flux density, the total unsigned flux, and the blue-shifted zero-crossing velocity, respectively. The initial time corresponds to the first slit position of the map showing CP larger than 0.15 pm.

EVENT (ID)	DATA SET	SLIT [pixel]	t_i	t_f	ΔT [m]	SIZE [$''^2$]	$\overline{\phi}$ [Mx/cm^2]	Φ_T [10^{17}Mx]	v_{LOS} [km/s]
1 (A)	1	280	11:09:23	11:33:04	23.7	6.72	52.9	13.1	2.7
2 (C)	1	127	15:00:59	15:09:38	8.4	5.12	39.7	5.7	4.0
3 (D1)	1	260	11:07:08	11:35:15	28.1	6.72	28.2	7.3	3.0
(D2)	1	266	11:13:35	11:30:55	17.3	2.88	29.5	5.0	$\sim$2.5
4[a]	1	122	11:11:25	11:24:25	13.0	4.16	23.5	3.4	$\sim$1.9
5	1	360	12:07:43	12:20:43	13.0	4.16	33.2	6.5	$\sim$3.5
6	1	85	13:14:51	13:25:41	10.8	3.52	26.5	4.4	2.1
7 (B)	2	82	00:56:01	01:09:00	13.0	5.12	27.6	4.7	2.1
8	2	195	03:21:04	03:27:34	6.5	2.56	27.0	3.6	1.5
9	2	251	01:09:00	01:22:00	13.0	4.16	31.5	4.1	2.4
10 (E1)	3[b]	148	08:53:37	09:08:32	14.9	4.48	34.0	7.6	2.4
11 (E2)	3[b]	144	08:48:50	08:56:00	7.2	1.60	24.7	1.9	3.4
12	3[b]	191	09:40:46	09:43:46	3.0	1.60	18.0	1.3	1.9
13	3[b]	189	09:43:46	09:51:31	7.8	6.08	26.8	7.9	2.7
MEAN	-	-	-	-	13.1	4.21	30.2	5.5	-

a:– The various physical quantities have been evaluated for pixels whose CP exceeds 0.08.
b:– Same as *a* but for pixels with CP$>$ 0.12.

responding raster scans. Maps of the circular polarization signal (CP) and of the total linear polarization signal (TLP) are displayed in the second and third rows, respectively. The fourth row shows Ca II filtergrams, and the last row depicts LOS velocities evaluated from the Stokes V zero-crossing wavelengths. In addition, Mg I magnetograms are shown in the sixth row only for event E. As in Fig. 8.3, the Y-axis represents the image of the Sun through the slit and the X-axis the scan direction and time.

To track magnetic flux emergences we have overplotted contour lines enclosing areas where the CP and TLP signals are larger than 0.15 pm (red and blue respectively). In case of event E the contours corresponds to 0.12 pm. White areas in the velocity maps represent pixels which Stokes V amplitude is smaller than 0.4 I_c.

We note that the cadence of the Ca II H filtergrams and Mg I magnetograms is larger than that of the SP maps. Therefore only a few of them are displayed.

In particular, we show the ones whose observation time is closer to that corresponding to the central slit position of each map. Hence, only half of the total number of maps is available. The maps not shown have been visually inspected to look for transient brightenings (Ca II H) and polarization signals (Mg b I), though. Also, to increase the S/N, the chromospheric filtergrams have been spatially rebined to match the SP pixel size of 0.″16.

8.5.1 Event A

For this event (Fig. 8.5) the circular polarization maps show a unipolar flux concentration (white patch) barely visible at $\Delta t = 0$ min. It grows both in size and in strength, reaching the maximum size and circular polarization signals 8 min later. At that point, the flux concentration looks roundish and occupies an area of $\sim 4 \times 4$ pixels (some 200 000 km^2; red contours), which corresponds approximately to one third of the granular cell surface. The granule is defined to be the region where the continuum intensity is at least 1.05 times brighter than the average quiet Sun. At $\Delta t = 16$ min the signal starts to fade away. At $\Delta t = 24$ min (not shown), the circular polarization signal has vanished completely. No clear negative polarity signals are detected in the area of interest during the whole sequence. The continuum intensity maps demonstrate that the magnetic flux appears in an existing granule and persists there for 20 min while the granule evolves. Interestingly, the flux concentration does not seem to be disturbed by the granular flows: it remains co-spatial with the brightest part of the granule until $\Delta t = 16$ min, and never gets advected to the adjacent intergranular lanes.

There is no detectable linear polarization signal associated with this event. Only the last two maps show traces of linear polarization when the circular polarization signal is almost absent. The observed linear polarization patch lies close to the flux concentration (less than 1″ up and right), but we believe it is not related to its disappearance.

The emergence is characterized by blueshifted velocities already from the initial stages. At $\Delta t = 10$ min we observe the strongest upflows of about -2.5 km s^{-1}. From $\Delta t = 10$ to 22 min a greenish patch can be seen in the velocity. The shape of the patch resembles that of the granular cell. A careful look at the data reveals that the area occupied by the granule shows Stokes V signals that slightly exceed the noise limit. These signals may represent a background magnetic field component.

We do not detect any Ca II H brightness enhancement associated with the emergence event: the brightenings observed at $\Delta t = 2$ and 20 min seem to be too far from the magnetic feature.

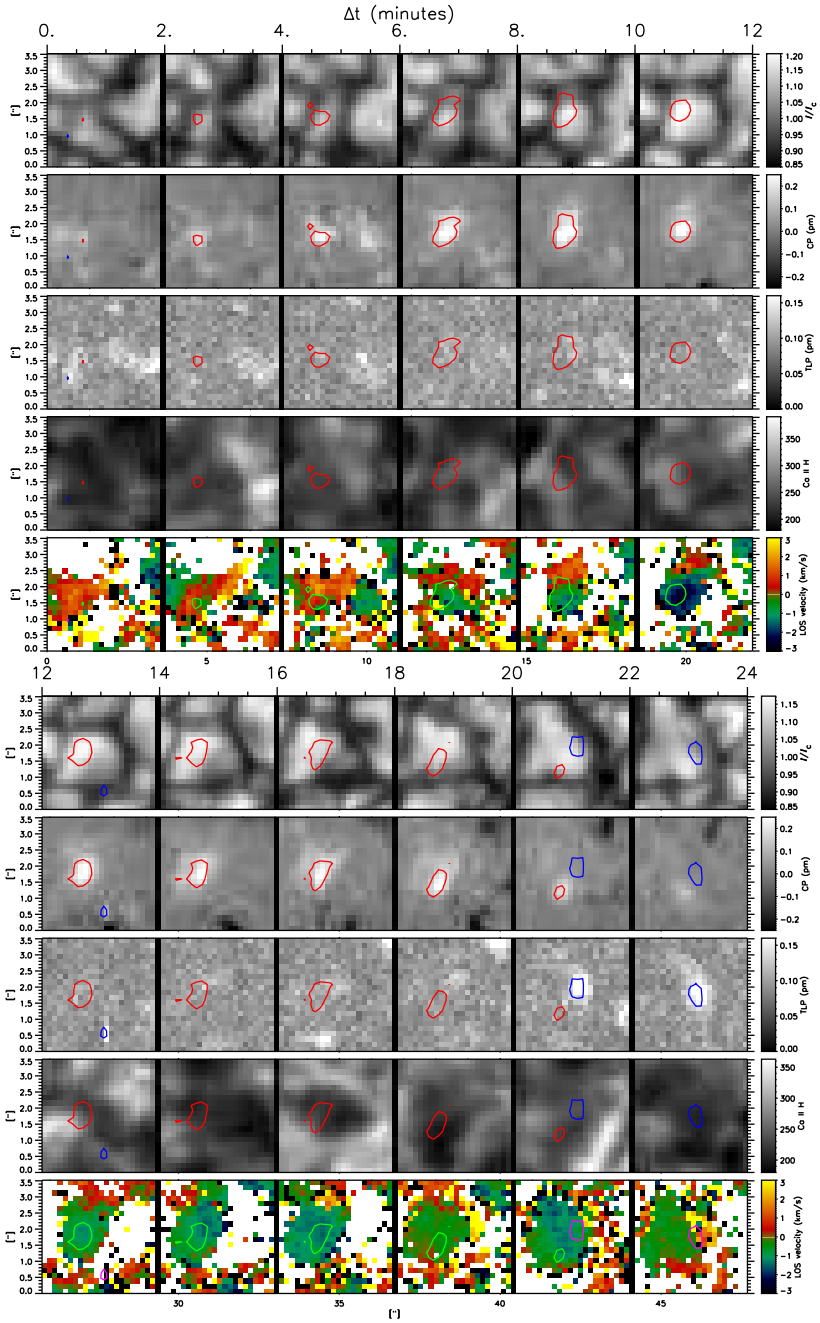

FIGURE 8.5:— Evolution of a flux emergence process (event A) observed on February 11, 2007. The cadence is 123 s and the maps cover a FOV of $3\farcs5 \times 3\farcs5$. From top to bottom: continuum intensity, circular and total linear polarization signals, Ca II H line core intensity, and LOS velocity. Negative velocities indicate blueshifts. $\Delta t = 0$ min corresponds to 11:09:23 UT.

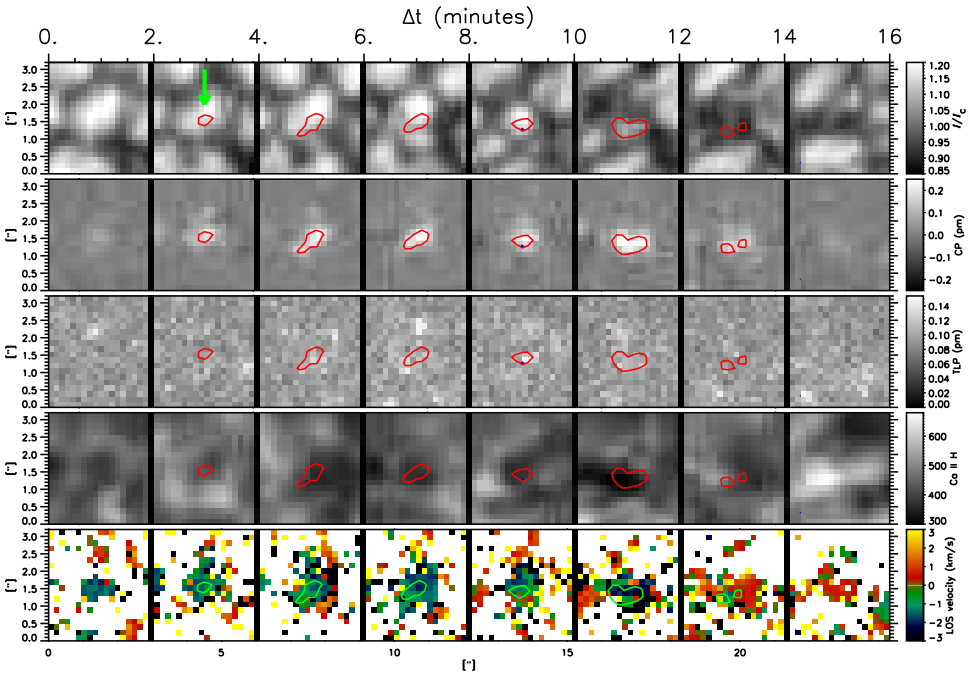

FIGURE 8.6:— Emergence process (event B) observed on March 10, 2007. The panels show the same quantities as in Fig. 8.5. The green arrow marks the emergence site. $\Delta t = 0$ corresponds to 00:54 UT.

8.5.2 Event B

This second event (Fig. 8.6) differs slightly from the previous one. It starts at $\Delta t = 2$ min and has a shorter duration. The maximum spatial size of the magnetic patch is similar to that of event A. However, it occupies about half of the granule at $\Delta t = 6$ min, and almost the whole granule 4 min later. The circular polarization signal reaches a maximum at $\Delta t = 14$ min. As before, there is no evidence for horizontal magnetic fields since no linear polarization is detected.

The emerging flux interacts differently with the plasma: as shown by the continuum intensity maps, the granule starts to diminish in size at $\Delta t = 10$ min, disappearing completely four minutes later, while the flux concentration still persists. Thus, the observations suggest that the magnetic field somehow contributed to the granular disruption. Throughout the sequence, the flux concentration appears to be decoupled from the advection flow (e.g., it moves towards the center of the granule between $\Delta t = 6$ min and $\Delta t = 10$ min).

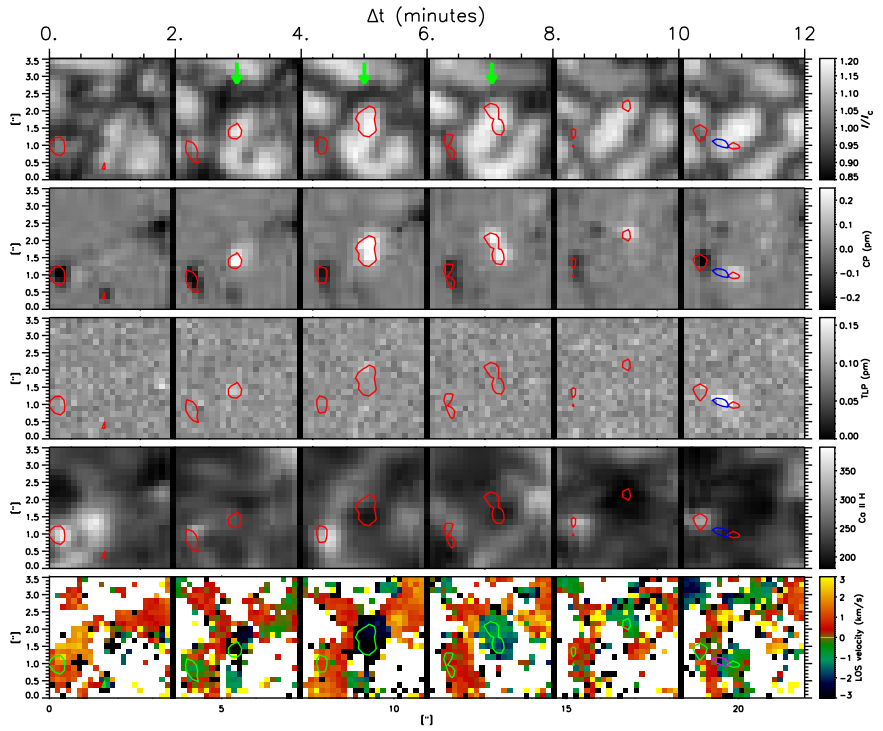

FIGURE 8.7:— Emergence process (event C) observed on February 11, 2007. The panels show the same quantities as in Fig. 8.5. $\Delta t = 0$ corresponds to 14:58 UT. Green arrows indicate the position of the emergence event in order not to mislead it with the neighboring magnetic signals.

Similarly to the first case, blueshifts are observed right from the beginning of the process. From $\Delta t = 16$ min on, weak downflows are detected instead, corresponding to the granule disappearance. The largest upflows of -2.2 km s^{-1} are comparable with those of event A. The Ca II H filtergrams show no significant brightenings associated with the process.

8.5.3 Event C

In Fig. 8.7 we show the third emergence process. In this case the magnetic feature becomes visible at $\Delta t = 2$ min and disappears at $\Delta t = 10$ min. In contrast with events A and B, the magnetic patch elongates at $\Delta t = 6$ min, just after it reaches its maximum spatial size. Two minutes later the magnetic patch becomes significantly smaller. In this event, the granule in which the flux emerges modifies its shape with time. Except for the fact that the magnetic patch drifts towards the North together with the edge of the granule, there is

no evidence of interaction between the granule and the magnetic patch.

The circular polarization signal is maximum at $\Delta t = 4$ min. Notice that there are no detectable linear polarization signals until $\Delta t = 10$ min. The signal pertains to a small magnetic loop which appears in the same granular cell when the flux emergence C is over. At both ends of the magnetic patch there exist opposite-polarity magnetic features corresponding to the footpoints of the magnetic loop. They are rooted in intergranular lanes (cf. Fig. 8.3).

This emergence event shows the strongest blueshift at $\Delta t = 4$ min, reaching $-4\ \mathrm{km\,s^{-1}}$, and it is the shortest in time. In the rest of the frames weak upflows are detected. Again, no significant brightenings in the Ca II H line are associated with the process. Other magnetic patches within the FOV do show enhanced Ca II H brightenings, though. This demonstrates the quality of the alignment.

8.5.4 Event D

This emergence event (Fig. 8.8) is the longest in duration we have found. It differs from the others in that two magnetic features of opposite polarity appear at different times in the same granule. They are identify as events D1 and D2 in Table 8.2. There is no evidence of connection between the two magnetic patches.

The positive-polarity patch (white) becomes visible in the circular polarization map at $\Delta t = 0$ min. It changes its spatial size with time, reaching the maximum size and circular polarization signal at $\Delta t = 8$ min. A second patch, smaller in size and of opposite polarity, emerges within the same granule at a distance of $1''$ $\Delta t = 6$ min. The white patch fades progressively from $\Delta t = 8$ to 24 min. At $\Delta t = 26$ min it is no longer seen. The black patch preserves its size and polarization strength. At $\Delta t = 16$ min it starts to fade as well, disappearing 4 min earlier that the white one. The distance between the two magnetic patches does not change.

At $\Delta t = 6$ min the size of the magnetic patches occupy a small fraction of the hosting granule. The granule evolves and changes it shape during the process. At $\Delta t = 12$ it clearly splits in two. Between $\Delta t = 16$ and 20 min the granule seems to be distorted, perhaps as a consequence of the action of the magnetic features. It finally disappears at $\Delta t = 22$. As can be seen in the continuum intensity maps, the white magnetic patch appears at the granular edge ($\Delta t = 0$ min) and moves towards the granular center with time. Also, note that the white patch ended in an intergralular lane at $\Delta t = 24$ min.

There exist some linear polarization signals from $\Delta t = 0$ to 14 min. They are not located between the opposite-polarity patches. At $\Delta t = 4$ and 12 min we find the largest linear polarization patches. They coincide with the emergence

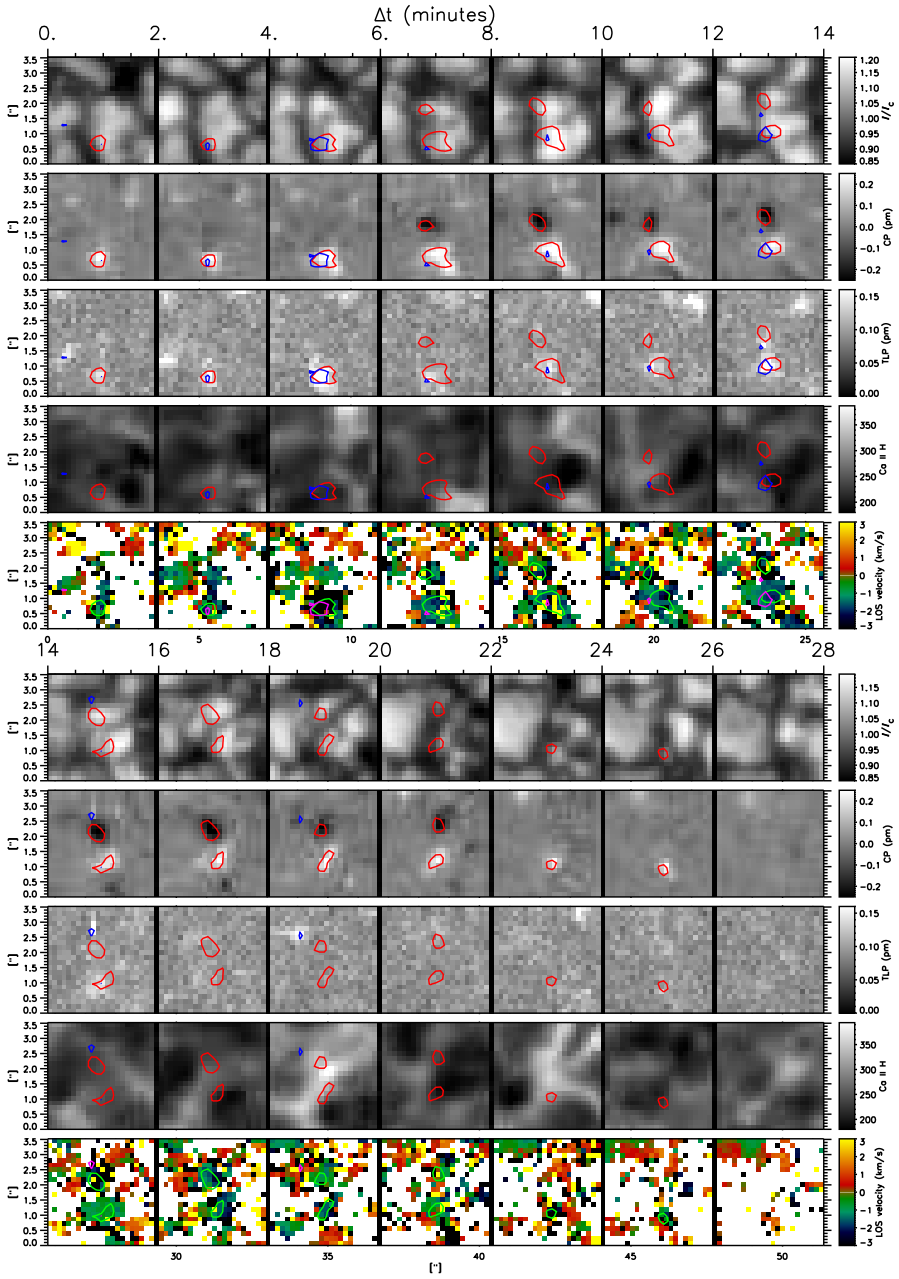

FIGURE 8.8:— Emergence process (event D) observed on February 11, 2007. The panels show the same quantities as those of Fig. 8.5. $\Delta t = 0$ corresponds to 11:07 UT. In this particular case we have an emergence process with opposite polarities. Note the linear polarization signal appearing at $\Delta t = 4$ min and $\Delta t = 12$ min.

of positive-polarity flux (white). The white patch seems not to change with the appearance of the linear polarization signals. Therefore, the existence of non-negligible linear polarization signals may indicate that the field lines are occasionally bent.

The emergence event shows the strongest blueshift at $\Delta t = 4$ min, reaching -3 km s^{-1}. Given the large asymmetries of the Stokes profiles in this case (see Sect. 8.6), the velocities are less reliable. We do not know what happens in the early stages of the emergence due to a lack of data. Finally, the Ca II H line shows no clear brightenings associated with the emerging flux.

8.5.5 Event E

Figures 8.9 and 8.10 show the time evolution of an emergence event (E1) with a cadence of ∼30 s from data set #3. It occurs close to an existing strong magnetic signal, located in an intergranular lane. The faster cadence achieved by these observations allows us to carry out a deeper analysis of the emergence process although at the expense of lower signal-to-noise ratios. The process starts above a granular cell at $\Delta t = 5$ min, with circular polarization signals larger than 0.12 pm (red contours). From $\Delta t = 0$ to 4.5 min, there is diffuse weak circular polarization (at the level of noise) over the granule[2] At $\Delta t =$ 12.5 min later, the magnetic signal weakens and starts to diminish. From $\Delta t = 13.5$ to 14.5 min the granule center shows sparse polarization signal until it fades below the noise level.

No opposite-polarity signals or linear polarization signals are associated with the emerging flux during the whole sequence. From $\Delta t = 4$ to 6 min we find a non-negligible amount of linear polarization signal (blue contours). It appears at the edge of the granular cell, relatively close to the emerging flux patch, but not related to it. The circular polarization signal occupies a significant area of the granular cell surface and appears at its very center. The granular cell evolves normally with time, without being distorted by the magnetic flux.

In line with the previous cases, the emerging flux shows blueshifts already from the initial stages, with maximum velocities of ~ -2.4 km s^{-1} at $t = 8$ min. With a cadence of ∼30 s, the photospheric 5-min oscillations are clearly seen in the velocity maps.

In the same time sequence we detect another magnetic flux emergence (E2). It is smaller in spatial size than the previous one and persists for a shorter time.

[2] In order not to misidentify the emergence with the adjacent magnetic patches the position of the starting point of the emergence as well as the point where it emerges at $\Delta t = 5$ min are indicated with green arrows in the circular polarization maps.

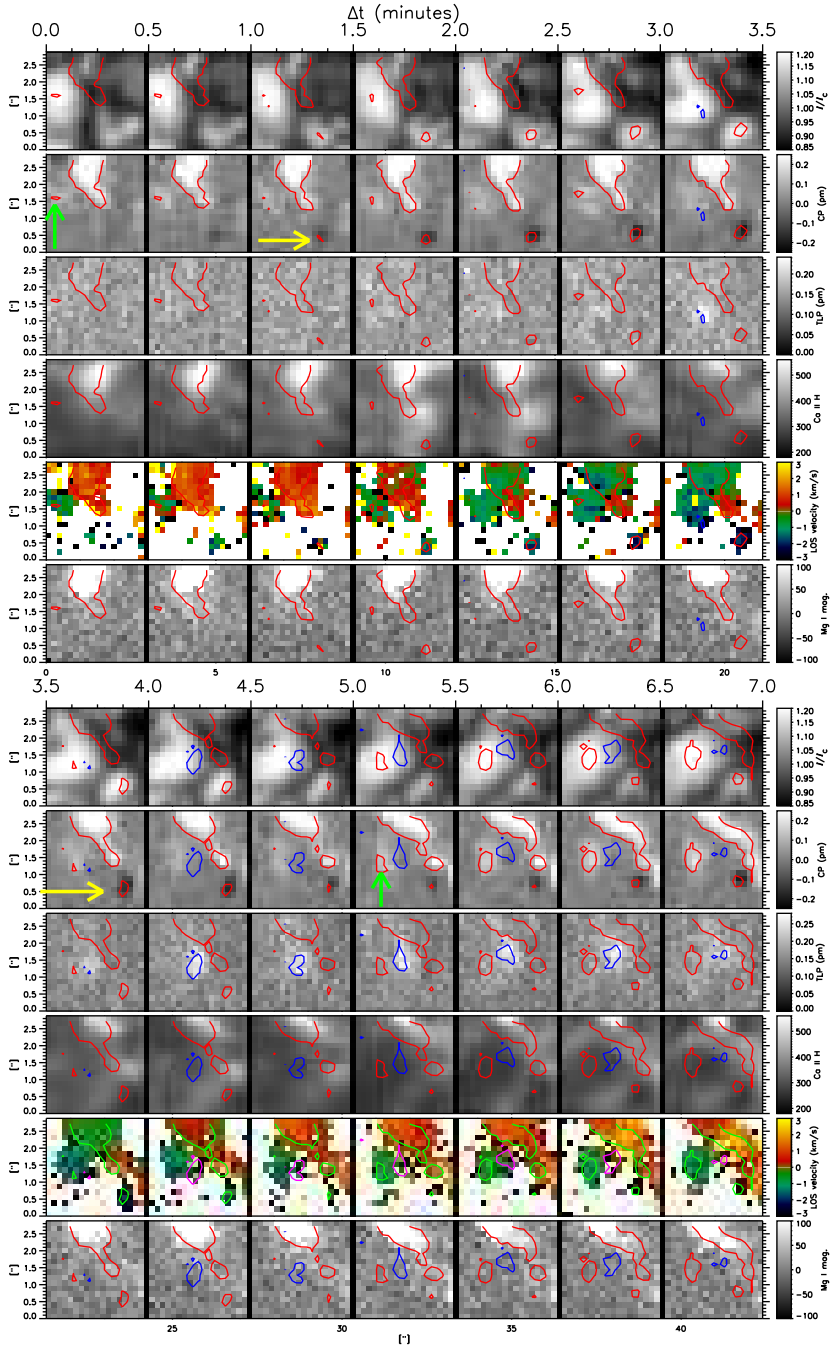

FIGURE 8.9:— Emergence process (event E) observed on October 6, 2007. This plot represents the first half of the event. The cadence of the SP maps is 34 s and cover a FOV of $4\farcs0 \times 2\farcs88$. The five first rows show the same quantities as Fig. 8.5. The last row shows a magnetogram taken in the Mg I 517.2 nm line. $\Delta t = 0$ corresponds to 8:47:38 UT.

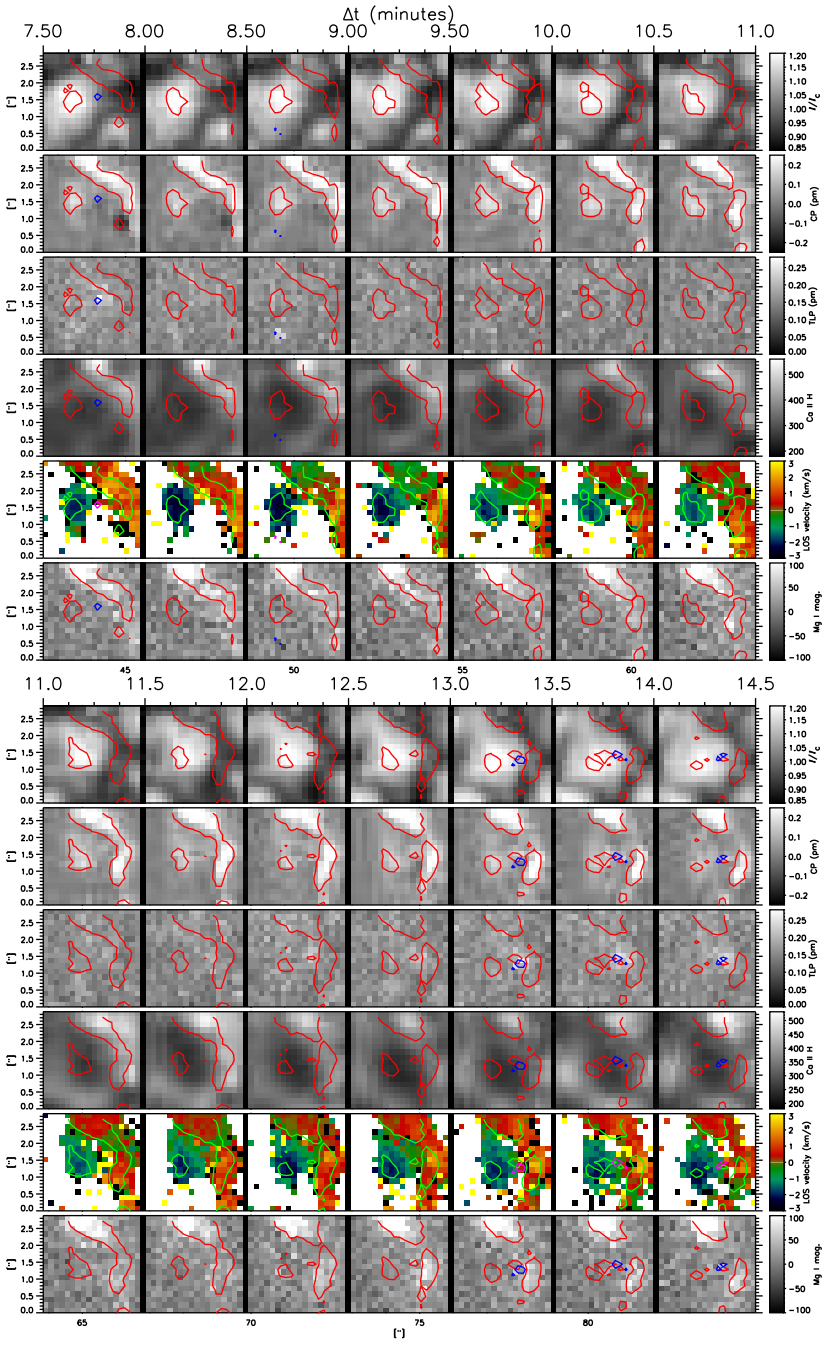

FIGURE 8.10:— Continuation of the emergence process (event E) of Fig. 8.9

The emerging flux is observed for the first time at $\Delta t = 1$ min (see yellow arrow) and disappears at $\Delta t = 7$ min. There is no relationship between events E1 and E2.

8.5.6 Relation with the chromosphere

Data set #3 (Table 8.1) has a higher cadence than the other two. In addition, the chromosphere can be better examined because Mg I b magnetograms are available, besides the Ca II H filter images. Here we look for any chromospheric change that may be related to the emergence events E1 and E2 using the Mg I b magnetograms.

As for the other four events, no chromospheric brightening is detected in the Ca II H filtergrams. This suggests that there is no energy transfer from the photosphere to higher layers. But more surprising is the fact that no magnetic signal is visible in the Mg I magnetograms at the emergence sites. The qualitative analysis of the emergence suggests that the field lines are vertically oriented and occur above granules. Therefore, the absence of signal in the Mg I magnetograms indicates that there is no connection between the emergence events and the chromosphere. As a result, the field lines that emerge vertically through the granule have to bend or to open at some point. We do not observe the ensuing change in the polarity of the field lines.

In contrast to these emergence events, the rise of magnetic loops from deep photospheric layers is clearly visible in the Mg I magnetograms. In particular, some time after the emergence of the loop in the photosphere, its two footpoints, which have opposite magnetic signals, are seen as two magnetic patches in the chromosphere. Also, they separate with time (Martínez González & Bellot Rubio, in prep.). This finding indicates that the loop reaches the chromosphere. However, we do not find any evidence that the vertical magnetic flux emerging in granules reaches the chromosphere. This makes these events to be *essentially photospheric*.

In summary, all five events show the same behavior: a magnetic flux concentration that *appears* just at the center of a granule and some minutes later vanishes, interacting or not with the plasma flow. All of the examples examined do not show linear polarization signals at the locations of the emergence, which points in a very preliminary way to a vertical configuration of the field lines. The chromospheric observables at our disposal indicate that these fields do not reach the chromosphere or are not concentrared enough to be detected.

8.6 Properties of the Stokes I and V profiles

In this section we examine the Stokes profiles in order to provide constraints to the physical mechanism behind the emergence of vertical magnetic flux through convective cells. As we have shown, there is no linear polarization signals associated with these events. Hence, we focus on the Stokes I and V profiles pertaining to each of the emergence processes, paying special attention to their shapes and any intrinsic peculiarity. We also analyze the temporal evolution of the emergence process by means of changes in the Stokes I and V shapes.

8.6.1 Profile shapes and spatial distribution

The visual inspection of the Stokes V profiles associated with the emerging flux reveals distinct properties that lead us to classify them in four classes. Most of them are far from *normal*. By *normal* we mean profiles showing two lobes of opposite sign, an anti-symmetric shape, and a well defined zero-crossing point.

In Fig 8.11 we show four example profiles representing each of the classes, from I to IV. The profiles have been taken from event A at $\Delta t = 10$ min and are of positive polarity (as the emerging flux). Similar Stokes profiles are found in all the events analyzed in this Chapter.

Class I profiles are characterized by their asymmetric shape. These profiles occur all around the emerging magnetic patch, although they are more frequent towards the center. They have positive area and amplitude asymmetries ($\delta A > 0$, $\delta a > 0$), independently of the polarity of the flux. Class II stands for one-lobed profiles, i.e., profiles whose asymmetry is strong enough to suppress one of the lobes of a regular Stokes V profile. Profiles belonging to this class possess δA and δa close to one. Class I and II profiles are found in all emergence events presented in Sect. 8.4.

Class III contains V profiles showing three lobes, e.g., two positive and one negative (bottom left panel). Class IV comprises profiles with two lobes of the same sign. These two classes of profiles are less frequent and occur in the vicinity of the emerging patch, closer to the granular edges. Classes II and IV may be understood as extreme cases of classes I and III, in which the profiles have lost one of their lobes.

These unusual shapes provide additional information about the vertical stratification of the atmospheric parameters, although their analysis and interpretation is not straightforward. They cannot be the result of atmospheric seeing (space-borne observations) or instrumental effects (e.g., telescope diffraction which mixes the signals from nearby pixels). The strong asymmetries of classes I and II require large gradients of the atmospheric parameters, at least

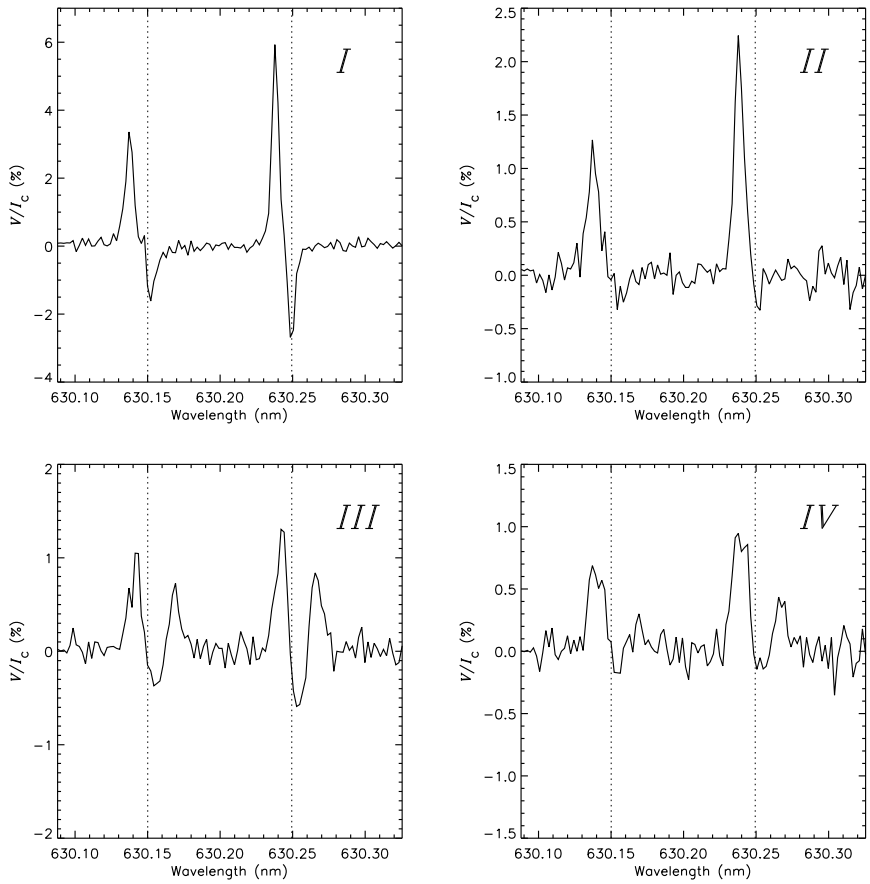

FIGURE 8.11:— Different classes of Stokes V profiles that are found in the emergence event A. They exemplify the kind of profiles associated with magnetic flux patches emerging in granular cells. The vertical lines represent the reference wavelengths of the 630.15 and 630.25 nm spectral lines.

in the velocity (Illing et al. 1975; Auer & Heasley 1978). These gradients should be more prominent for class II profiles. Several mechanisms may cause such strong gradients. For instance, the presence of canopy or magnetopause-like environments, i.e, at least two different media are present along the line of sight, each of them showing different magnetic and/or dynamic properties (e.g., a magnetic atmosphere and a field-free one). Such a configuration introduces strong discontinuities along the LOS, and produces asymmetries on the Stokes profiles.

Class I and II profiles have been detected earlier in ground-based observa-

tions of quiet solar regions at $1''$ (e.g., Sigwarth et al. 1999). Attempts to find the physical mechanisms responsible for such strong asymmetries have been made by Grossmann-Doerth et al. (2000) and Ploner et al. (2001).

The superposition of two Stokes V profiles, with positive area asymmetry and of opposite polarity, emerging from two distinct atmospheres within the same pixel, may explain classes III and IV. In Fig 8.11 we have indicated the central wavelength of each spectral line with vertical lines. Notice that, for classes III and IV, there seems to be a strong, red-shifted component of opposite polarity. The very existence of classes III and IV indicates that magnetic fields of opposite polarity coexist within the same pixel either horizontally *or* vertically. These kind of profiles can be also generated with specific magnetic field configurations (Steiner 2000). In particular, they can be generated by a single magnetic component where the field inclination and velocity changes dramatically with height. We will discuss a number of possible physical scenarios behind these profiles in Sect. 8.7.

To show how the Stokes V profiles are spatially distributed, in Fig. 8.12 we display a set of 5×5 ($0\farcs8 \times 0\farcs8$) profiles corresponding to event B at $\Delta t = 10$ min. The central profile corresponds to the spatial location where the magnetic flux is maximum. Note that it does not coincide with the position of maximum continuum intensity.

As previously mentioned, class I and II profiles are seen at the center and at the edges of the granule, whereas class III and IV profiles occur only at the edges. The amplitude of the Stokes V profiles is larger at the granule center and diminishes as the edges are approached. We have found that about 20% of the Stokes V profiles belongs to classes III and IV, for event D. The percentage is smaller for events A, C and D. We did not find such profiles in emergence event E.

It is interesting to note how the Stokes V profiles change from class I to III as we move diagonally from the center of the emergence toward the bottom, rightmost profile. Suppose that these three-lobed profiles originate from two distinct magnetic atmospheres, each harboring magnetic fields of opposite polarity. One possible physical scenario that may favor the formation of class III profiles at the edge of the granule can be the following. The profiles at the center of the magnetic patch exhibit a well-defined polarity. Also, there is a clear absence of linear polarization signals. This indicates that the field at the center of the patch is vertically oriented. If the field lines become more horizontal as one moves toward the granule edge and, moreover, some of these field lines change their orientation, i.e., the field becomes of opposite polarity, then a strong discontinuity in the inclination of the field lines may be observed along the line of sight. This discontinuity would be capable of producing anomalous Stokes

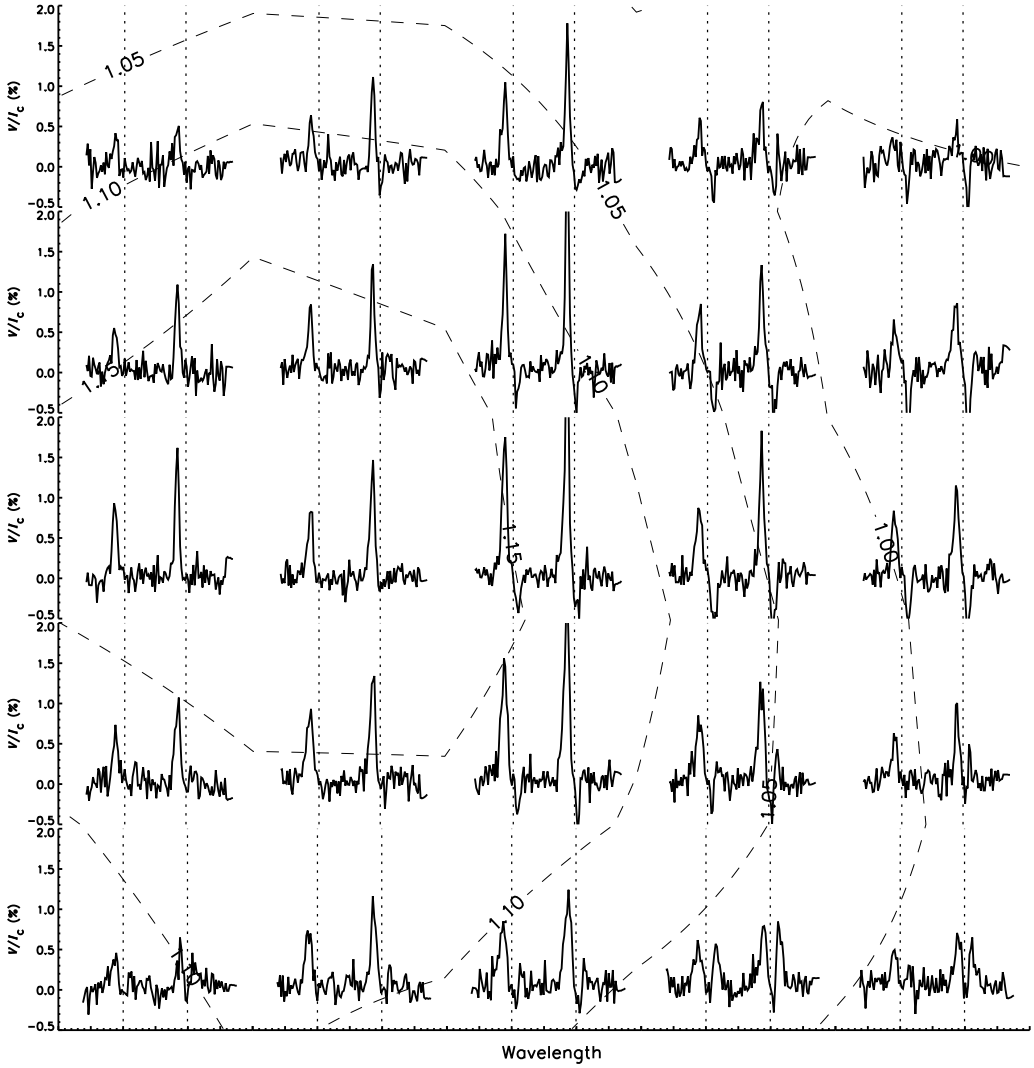

FIGURE 8.12:— Set of Fe I 630.15 and 630.25 nm Stokes V profiles observed at the center of the flux concentration of event B at $\Delta t = 10$ min. The central profile corresponds to the pixel showing the largest circular polarization signal. The vertical lines represent the central wavelengths of the two lines. Overplotted are contour lines of the continuum intensity (dashed lines). The four classes of profiles described on the text are clearly distinguishable (cf. Fig. 8.11).

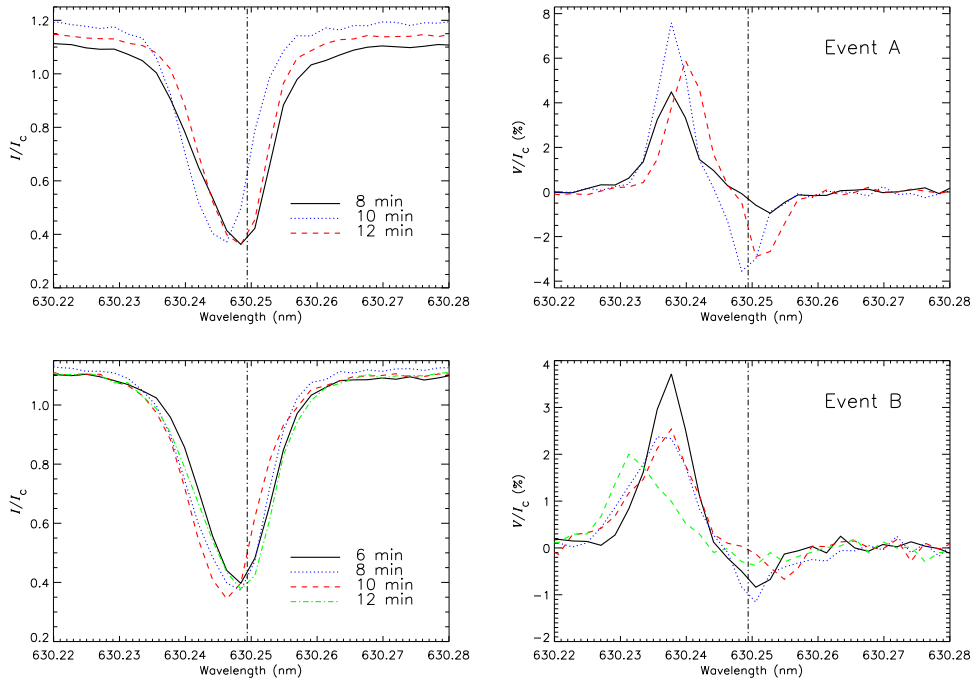

FIGURE 8.13:— Stokes I (left) and V (right) profiles of Fe I 630.25 nm observed at the center of the flux concentration A (top) and B (bottom). Different line shapes stand for different times through the evolution of the emergence. The vertical lines mark the zero point of the velocity scale.

V profiles (cf. the crossover effect in sunspots, e.g., Grigorjev and Katz 1972).

There is a total absence of linear polarization signals and we cannot confirm this scenario on the basis of a visual inspection of the observations alone. Therefore, inversions are of fundamental importance to obtain information about the inclination of the field from the observed Stokes I and V spectra.

8.6.2 Dynamic and magnetic properties

Figure 8.13 displays the temporal evolution of the Stokes I and V profiles for emergence events A and B. The changes in the profile shapes provide indications of the rise of magnetic flux from deep photospheric layers.

We start with the Stokes spectra corresponding to event A (Fig 8.13, top panels). The profiles have been taken from the center of the magnetic flux concentration, where the magnetic flux is maximum. We represent only the observations corresponding to $\Delta t = 8$, 10 and 12 minutes (solid, dotted, and

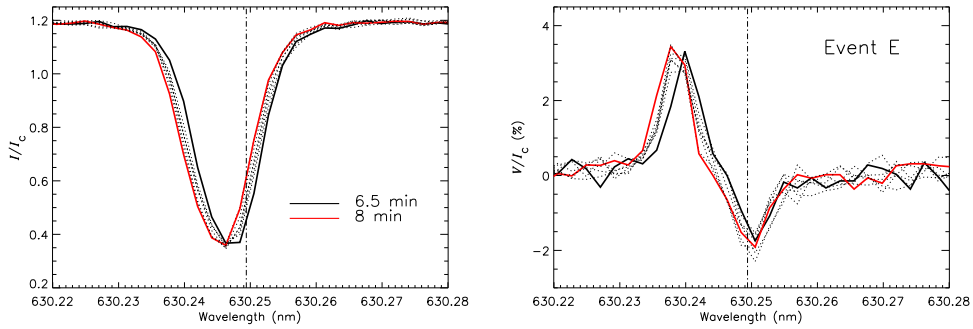

FIGURE 8.14:— Stokes I (left) and V (right) profiles of Fe I 630.25 nm observed at the center of the flux concentration E. Dotted lines stand for different times through the evolution of the emergence. The vertical lines mark the zero point of the velocity scale.

dashed lines, respectively). Both Stokes I and V exhibit strong asymmetries at $\Delta t = 8$ min. Notice that the blue wing of Stokes I is significantly blueshifted while the line core remains almost at rest. This suggest the existence of strong upflows in deep atmospheric layers and smaller velocities higher up. The signature of large gradients of atmospheric parameters is even more conspicuous in Stokes V. The asymmetry of Stokes V is extreme in this case, with the red lobe being almost absent. It belongs to class II. Such a degree of asymmetry can only be produced by large velocity *and* magnetic field gradients. At $\Delta t = 10$ min, the whole line is affected by a strong blueshift, but the velocity gradient seems to have decreased significantly since the profiles look more symmetric. At $\Delta t = 12$ min, the gradients are still small and the global velocity shift is reduced. Altogether, this qualitative interpretation of the Stokes I and V profiles suggests that we are witnessing the rise of magnetic fields through the granule, from the bottom of the photosphere to higher layers. Apparently, the field is vertical because we do not detect linear polarization signals.

The time evolution of the Stokes I and V profiles pertaining to event B (bottom panels from Fig. 8.13) shows the same tendencies. In this case, the changes in the profile shapes are smaller, showing weaker blueshifts and polarization signals. However, the asymmetries are more pronounced, indicating stronger gradients of the physical quantities. As for event A, the Stokes I profile stays almost at rest at $\Delta t = 6$. Two minutes later the blue wing is slightly blueshifted due to plasma upflows. The flux reaches higher layers at $\Delta t = 10$ min (red lines). After the magnetic flux has risen Stokes I recovers its initial shape. Stokes V follows the same behavior, although the strong asymmetries make it difficult to compare the profiles. Finally, we do not find any conspicu-

ous property in the profile shapes providing hints as to why the magnetic flux contributes to the disappearance of the granule in the case of event B.

The analysis of the Stokes V profiles of events C and D leads to the same conclusion. However, event E shows a different behavior. Figure 8.14 displays a set of Stokes I and V profiles corresponding to emergence event E from $\Delta t = 6.5$ to 10 min (black and red lines, respectively). Dotted profiles represent intermediate steps. We have taken this time range because there is a strong blue-shift in the zero-crossing velocity as can be seen in Figs. 8.9 and 8.10. The largest blue-shift corresponds to $\Delta t = 8$ min (red profile). The Stokes V profiles are less asymmetric than in events A to D and they show no clear indications of the rise of magnetic flux from deep photospheric layers upwards, in spite of the higher temporal cadence. We remark that, although the amplitude of the Stokes V profiles does not vary with time (within the time period covered by Fig. 8.14), the wavelength location of the blue peak is blue-shifted while that for the red peak is not. Also, the zero-crossing wavelengths seem to be bluer than the wavelength position of the minimum intensity.

Consequently, event E does not show the same physical properties as the other events. This might indicate that event E is a different physical phenomenon, which could also explain why the origin and end of this emergence is not clear. However, it is important to remark that the observations suggest a magnetic configuration in which the field lines are oriented vertically in the granular cell. So there might be different mechanisms able to produce circular polarization signals in granules.

8.7 Discussion

Throughout this Chapter we have presented clear proofs of vertical magnetic flux rising at the center of granular cells. The Stokes I and V profiles of four out of five analyzed events exhibit strong asymmetries at different times. The significant blueshifts of the Stokes I blue wings while the line cores remain at rest suggest strong upflows in deep atmospheric layers and smaller velocities higher up. The signature of large gradients of atmospheric parameters is very conspicuous in Stokes V. Large velocity *and* magnetic field gradients cause profile asymmetries that can be rather extreme, i.e., class II Stokes V profiles. We find indications of smooth gradients later on: the whole Stokes I profiles are blueshifted and they look more regular. Finally, the velocity shift is reduced and the gradients are decreased. Altogether points to the rise of magnetic flux in granules. The magnetic flux comes from lower layers. The field lines are vertically oriented as suggested by the absence of linear polarization signals.

To the best of our knowledge, this form of small-scale magnetic flux emergence has not been described in the literature. It differs significantly from the emergence processes in granular convection studied by Centeno et al. (2007) and Ishikawa et al. (2007), since we do not detect linear polarization signals or opposite-polarity foot-points surrounding them. Clearly, the geometry of the fields is not that of small magnetic loops. Lamb et al. (2008) have described examples of the emergence of unipolar flux, but at a poorer resolution of $1\farcs2$. No association of the flux with granules or intergranules was made in their paper. They suggested that the origin of the unipolar flux appearance is coalescence of pre-existing field lines with the same polarity, which were below the detection limit imposed by the intrinsic noise and the spatial resolution of their observations. While it is not possible for us to rule out the scenario of field-line coalescence, we do not find evidence for diffuse magnetic fields in the emergence sites prior to the events (except for event E), at the much higher spatial resolution and sensitivity of *Hinode*.

Current magnetoconvection simulations do not seem to explain our observations either. The simulations of Vögler et al. (2005) do show magnetic fields in granules, but they are much weaker than the ones reported here, and do not undergo emergence processes. Those granular fields may be the result of recycling of flux initially placed in intergranular lanes, or an effect of enhanced magnetic diffusivities. Cheung et al. (2007), on the other hand, have studied the rise of magnetic flux tubes from the convection zone to the photosphere. Depending on the magnetic flux stored in the tubes, the arrival of magnetic fields at the solar surface has very different observable consequences. For the stronger tubes, a darkening and distortion of the granular convection is expected (and actually observed), while weaker tubes do not modify the brightness of surface granules. In both cases, magnetic fields tend to emerge at the center of granular cells, showing large inclinations to the vertical. The fields are then advected by the horizontal flow towards the intergranular lanes, where they become more vertical and form opposite-polarity patches. Our events do not share these properties.

A hypothetical scenario for the emergence of unipolar vertical magnetic fields would be that granular upflows drag horizontal field lines initially placed in the upper convection zone, carrying them to the photosphere where they would emerge in the granules. However, it is not clear how the horizontal fields may turn into vertical fields. Also, at some point one should observe opposite polarities where the field lines return to the solar surface, but we do not detect them, perhaps as a consequence of still insufficient sensitivity or because they occur outside of the FOV. What is clear is that the scenario of vertical fields emerging in granules faces important conceptual problems.

A radically different interpretation is that these events we do not involve the emergence of new flux, but the "excitation" of already existing, mixed, quasi-isotropic fields (López Ariste et al. 2008). Such fields would be largely decoupled from convective motions and hence not affected by them. If the degree of mixing is sufficiently high, the absence of linear polarization cannot be taken as a proof that the field is vertical. This scenario should be investigated more thoroughly, both to demonstrate the existence of tangled fields in the solar photosphere and to assess whether they are indeed compatible with the observations presented here.

8.8 Conclusions

In this Chapter we have described different cases of the emergence of apparently unipolar, vertical fields in granular cells. A total of 13 such events have been detected during the ∼10 hours covered by the *Hinode* observations. Their lifetimes are of the order of ∼ 15 minutes. They bring magnetic fluxes of ∼ 30 Mx cm^{-2} comparable to typical IN magnetic concentrations.

At this stage we cannot offer a clear explanation of the events observed with *Hinode*, but we hope that the report of such processes will stimulate further observational and theoretical work.

The characterization of emergence processes at the smallest scales is important to understand the energy balance and origin of quiet Sun magnetic fields. In particular, they may hold the key to determine whether a local dynamo operates in the solar photosphere, as has been suggested on theoretical grounds (Cattaneo 1999). Also, a good knowledge of the ways magnetic fields emerge through the surface may help refine numerical simulations of magneto convection such as those performed by Vögler et al. (2005), Schaffenberger et al. (2006), Stein & Nordlund (2006), and Abbett (2007). If some form of flux emergence is not observed in the simulations, additional ingredients might need to be implemented in current codes.

We plan to perform detailed inversions of the observed profiles in an attempt to derive a consistent picture of the physics behind these processes. To this end we will apply the SIR inversion code to the Stokes profiles. In particular, we will employ a modified version of the SIR code (SIRJUMP) which can deal with sharp discontinuities of the physical quantities along the LOS, in an effective manner. The results of these *preliminary* inversions indicate that weak vertical fields of about 250 G are present in the lower photosphere, together with strong upflows of some -2.5 km s^{-1}. The field strength is negligible above $\log \tau_5 \sim -1$ originating a sharp discontinuity which moves to higher layers with time until

it leaves the line-forming region. The scenario coming out from the inversions is compatible with the qualitative suggestions made from the shapes of the profiles: in the first stages of the emergence we could be seeing the ascent of magnetic fields that do not fill the line-forming region completely. Once the fields reach the upper photosphere, the gradients of atmospheric parameters decrease significantly and, as a consequence, the Stokes profiles become less asymmetric.

Finally, the results presented here are neatly different that the horizontal fields found in IN regions (Chapter 7). Also, the *Hinode*/SP is still unable to resolve the different components that may form these magnetic events, provided they are not generated by strong discontinuities on the magnetic field stratification. Therefore, to better understand the nature of the vertical fields above granules, higher spatial resolution as well as better temporal cadences are needed. To this end new instrumentation is being built in order to achieve spatial resolutions of the order of $0\farcs1$, three times larger than current spectropolarimetric data.

9

On the inference of magnetic field vectors from IMaX measurements

To make progress in the understanding of the quiet-Sun magnetism, spectropolarimetric measurements at spatial resolutions better than $\sim 0\farcs3$ are necessary. To date, the only planned instruments capable of delivering such high spatial resolutions are vector magnetographs. Unlike spectropolarimeters, these instruments observe spectral lines at only few wavelength positions. Also, their resolving power is limited due to the spectral widths of the tunable filters they employ. Both introduce additional difficulties to obtain accurate determinations of the magnetic field vector. One of these instruments is IMaX[1], a vector-polarimeter that will provide near diffraction-limited measurements of the solar photosphere at resolutions of $\sim 0\farcs1$ ($\sim$ 80 km), with high cadence and polarimetric sensitivity. In this Chapter, we analyze how the limited angular resolution and wavelength sampling affect the magnetic field strengths, inclinations, azimuths, and LOS velocities derived from Milne-Eddington inversions of IMaX measurements. The results show that IMaX will provide satisfactory values for the magnetic field strength, and LOS velocity when only four wavelength samples along the spectral line plus one point in the continuum are observed. We also show that the Fe I line at 525.02 nm is better suited for magnetic field vector determinations.

[1] A description of the instrument can be found in Chapter 2

9.1 Introduction

The analysis of *Hinode*/SP measurements has shown us that the internetwork consist of weak magnetic flux concentrations with magnetic filling factors of the order of $\sim 45\%$. However, there is still a unknown fraction of flux that remain undetectable using current spectropolarimeters. The way to measure the hidden polarization signals using observations of Zeeman sensitive lines is to increase the spatial resolution. Spectropolarimetric measurements at $0\farcs1$ can be expected to imply larger polarization signals, by a factor of 9 in comparison with current observations at $0\farcs3$.

To date, there is no instrument capable of full spectropolarimetry at resolutions better than $0\farcs3$[2]. However, filter-based instruments are being designed and built to observe the solar photosphere with very high spatial resolution and polarimetric accuracy. These instruments have drawbacks when compared with spectropolarimeters, i.e., the smaller angular resolution and wavelength sampling. These disadvantages can imply poorer inferences of the physical quantities from the polarization signals.

One of those instruments is IMaX. It will achieve spatial resolutions of $0\farcs1$ on the solar surface. The resolution will be ensured because it is aboard the *Sunrise* mission, a stratospheric balloon that will get rid of most of the Earth's atmosphere and that includes a one-meter telescope. Will it be possible to infer the full vector magnetic field from IMaX measurements using appropriate inversion techniques?

To assess the accuracy to which the magnetic field strength, inclination, azimuth, and LOS velocity can be obtained, we simulate an IMaX observation with the help of MHD models to synthesize the Stokes profiles of the photospheric Fe I 525.02 and 525.06 nm lines. The profiles are degraded by telescope diffraction and detector pixel size to a spatial resolution of 80 km on the solar surface. Then, we determine the magnetic field vector and velocity using ME inversions and compare them with the MHD models to estimate the ME model parameters uncertainties. We carry out additional inversions to:

- evaluate the errors in the inferences introduced by the limited resolving power of the instrument,

- study the effects of the limited wavelength sampling and the different position of wavelength samples on the inferred model parameters,

[2]At the time this thesis was written the CRisp Imaging SpectroPolarimeter (CRISP) was installed and ready for observations at the Swedish 1-meter Solar Telescope on La Palma, Tenerife. CRISP provides polarimetric images near the diffraction limit of a 1 meter telescope.

Table 9.1:— Basic parameters of *Sunrise* and IMaX.

Aperture	100 cm	
Working wavelength	525.02 nm	
Spatial resolution	$\sim 0\farcs1$	~ 80 km
Central obscuration	35.2%	
CCD pixel size	$0\farcs05\times0\farcs05$	
Smearing filter width	~ 60 mÅ	

- and investigate the drawbacks of the noise for vector magnetographs.

9.2 Methodology

To simulate an IMaX observation we first take model atmospheres from radiative MHD simulations of Vögler et al. (2005) with a mean flux $\langle B\rangle = 140$ G. These atmospheres are necessary to generate the observations by synthesizing the Stokes I, Q, U, and V profiles. The 525 nm spectral region is synthesized in a wavelength range that extends 1 nm, including the Fe I 525.02 and 525.06 nm spectral lines. The sampling interval was 1 pm. Next, the monochromatic images are degraded considering telescope diffraction and detector pixel size. We also convolve the Stokes profiles with a Gaussian to account for the limited resolving power of the tunable filter. At the end we add noise and select four wavelength samples across the line plus a wavelength point in the nearby continuum. The inference of the physical quantities from the simulated profiles is done using the MILOS code. A detailed description of the synthesis and degradation processes can be found in Sect. 5.3 and in Sect. 6.3, respectively. We perform different tests in order to examine how the uncertainties are amplified when applying ME inversions to simulated observations with minimal wavelength sampling and limited resolving power.

For the analysis, we consider the results of ME inversions of the Stokes profiles degraded by telescope diffraction and with no noise, a PSF equal to a Dirac delta, and 61 wavelength samples as *the reference* solution. By comparing this reference with the outcome of ME inversions of the same Stokes profiles affected by noise, limited spectral resolution, and wavelength sampling, we quantify the loss of information induced by the measuring process, leaving aside errors due to the ME assumption and to telescope diffraction. In Appendix C we analyze the reliability of ME inversions when analyzing synthetic ME profiles affected by different instrumental widths and sampled at only few wavelength samples and with different sample point positions. The errors are significantly

smaller than those associated to the ME approximation to describe real profiles.

This Chapter is structured as follows: Sect. 9.3 describes the degradation of the data and discusses the effects of tunable filters on the simulated Stokes profiles. In that Section we also analyze the effects of noise and the drawbacks of selecting only a few wavelength positions across the line. Section 9.4 deals with the results of ME inversions. We estimate the errors that can be assigned to the model parameters derived from ME inversion of IMaX vector-magnetograph data and analyze the effects of the instrumental profile and the limited wavelength sampling over the inferences. In Sect. 9.5 we summarize the main conclusions.

9.3 Simulating IMaX observations

9.3.1 Spatial degradation

In Chapter 6 (Sect. 6.3.4) we already carried out a spatial degradation by telescope diffraction of a real object. In that particular case we simulated the spectropolarimeter attached to the *Hinode*/SOT. Here, the telescope aboard the *Sunrise* stratospheric balloon has a diameter twice as large as that of the *Hinode* spacecraft. Therefore the spatial resolution is greater and the effects of diffraction on the polarization signals are expected to be smaller. The parameters describing the telescope and the detector are given in Table 9.1. Notice that polarimetric measurements in the absence of atmospheric seeing and with an effective spatial resolution of $\sim 0\farcs1$ has never been attained.

Figure 9.1 shows maps of the continuum intensity for the original data and for the spatially degraded data corresponding to the simulations with $\langle B \rangle = 140$ G. The contrast due to diffraction and CCD pixel size has decreased by only 4%. The pixel size of the detector is twice the grid resolution of the original MHD model, thus the binning in the degraded image is not readily noticeable. Figure 9.2 shows the MTFs of *Sunrise*/IMaX.

We do not discuss all the effects caused by telescope diffraction but outline the two most important ones: first, diffraction blurs the data mixing the light from nearby pixels and diminishing the amplitude of the polarization signals; second, diffraction smoothes out profile asymmetries. Photon noise becomes more important because of the smaller polarization signals.

Figure 9.3 displays monochromatic images of Stokes Q, U and V taken at +7.7 pm from the central wavelength of the Fe I 525.02 nm spectral line and corresponding to $\langle B \rangle = 140$ G. (A) stands for the original images and (B) for the images spatially degraded by telescope diffraction and CCD pixel size. To emphasize details we represent a small area of the snapshot. The effects of

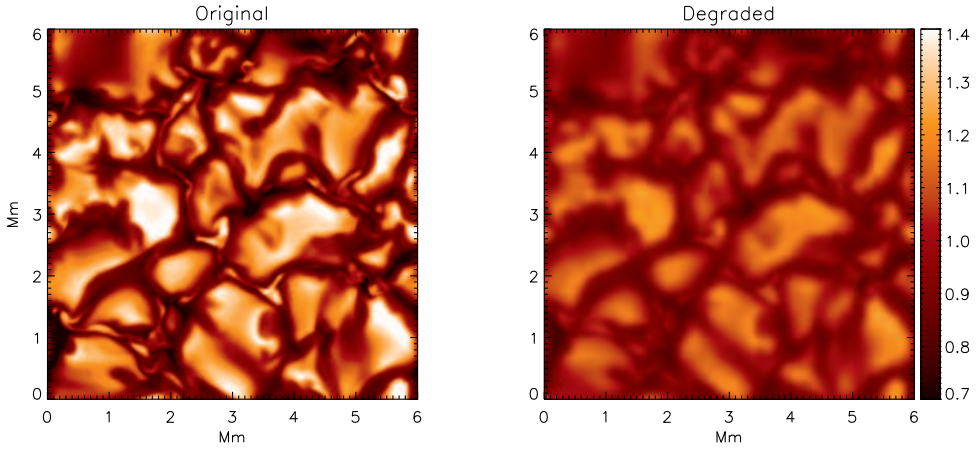

FIGURE 9.1:— Continuum intensity for the non-degraded data (left) and for the spatially degraded data (right) considering telescope diffraction and detector pixel size.

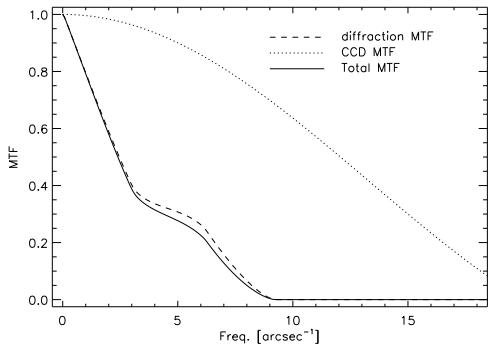

FIGURE 9.2— Dotted line: MTF of the CCD (pixelation effect); dashed line: diffraction limited MTF; and solid line: total MTF.

diffraction are clearly seen on the different maps. Notice that weak magnetic structures disappear due to diffraction. We have added noise at the level of $10^{-3} I_c$ in order to see how the noise affects the weakest signals.

9.3.2 Effects of the smearing filter

In IMaX, the selection of wavelength samples is done with an étalon in double-pass (smearing filter). The FWHM of the étalon corresponds to ~ 6 pm which limits the resolving power of the instrument. For simplicity, we approximate its shape by a Gaussian function. The finite width of the étalon affects the Stokes profiles by diminishing their amplitudes and by smoothing out the profile shapes.

Figure 9.3 show monochromatic Stokes Q, U and V images taken at +7.7 pm

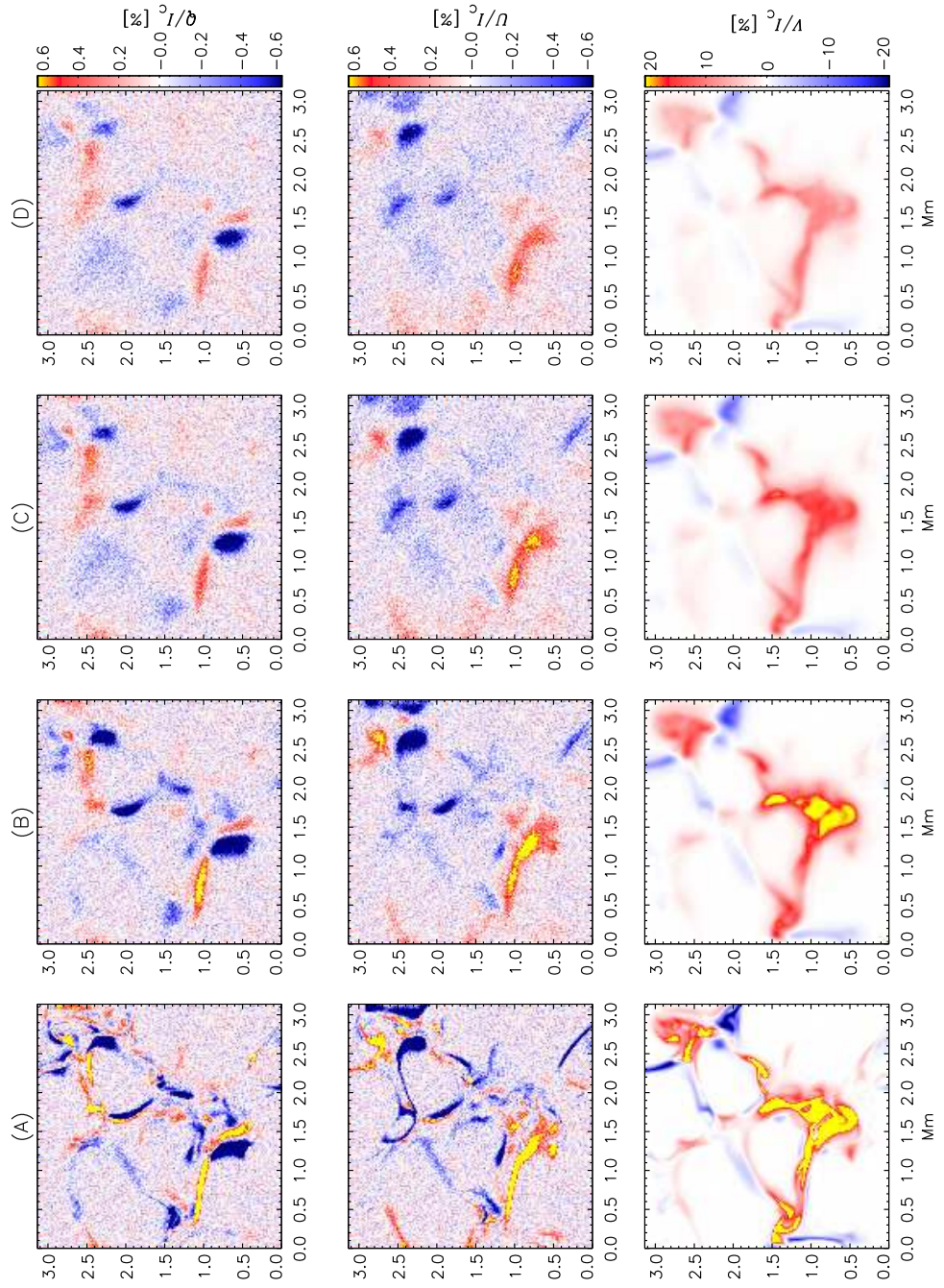

FIGURE 9.3:— Monochromatic images taken at +7.7 pm of the central wavelength of the Fe I 525.02 nm line. From bottom to top: the original data (A), the spatially degraded data (B), and the data taken into account filter widths of 6 (C) and 10 pm (D). Only a region of 150×150 pixels is displayed.

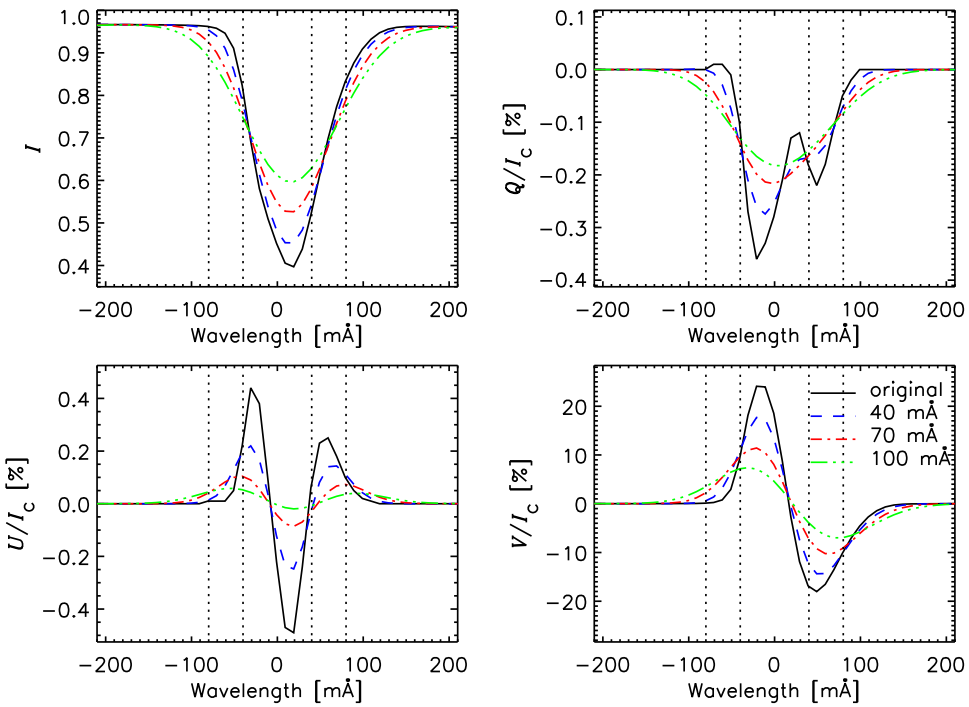

FIGURE 9.4:— Stokes I, Q, U and V profiles of the Fe I 525.02 nm line corresponding to pixel $(x, y) = (94, 214)$ from the degraded image by telescope diffraction only (black) and the same profiles convoluted with three different smearing filter widths, 4, 7 and 10 pm (color coded lines). The pixel corresponds to an intergranular lane. The vertical lines indicate wavelength samples at [±8,±4] pm from the central wavelength of the line.

considering smearing filter widths of 6 and 10 pm, columns (C) and (D) respectively. It can be seen how the smearing filter smoothes out the polarization maps. The weakest signals disappear and the amplitudes diminish. As a consequence, the effective spatial resolving power of the telescope decreases: the larger the smearing filter width the poorer the spatial resolution. Therefore, the information content on the images is reduced.

These effects are more pronounced for the Stokes Q and U maps, than for the Stokes V map. The reason is that Stokes Q and U exhibit smaller amplitudes than Stokes V. Notice how noise is more appreciable in Stokes Q and U for larger filter widths.

Figure 9.4 shows the spatially degraded Stokes profiles by diffraction of the Fe I 525.02 nm line corresponding to the pixel $(x, y) = (94, 214)$ and convoluted with smearing filters of widths 4, 7 and 10 pm (color coded lines). The vertical

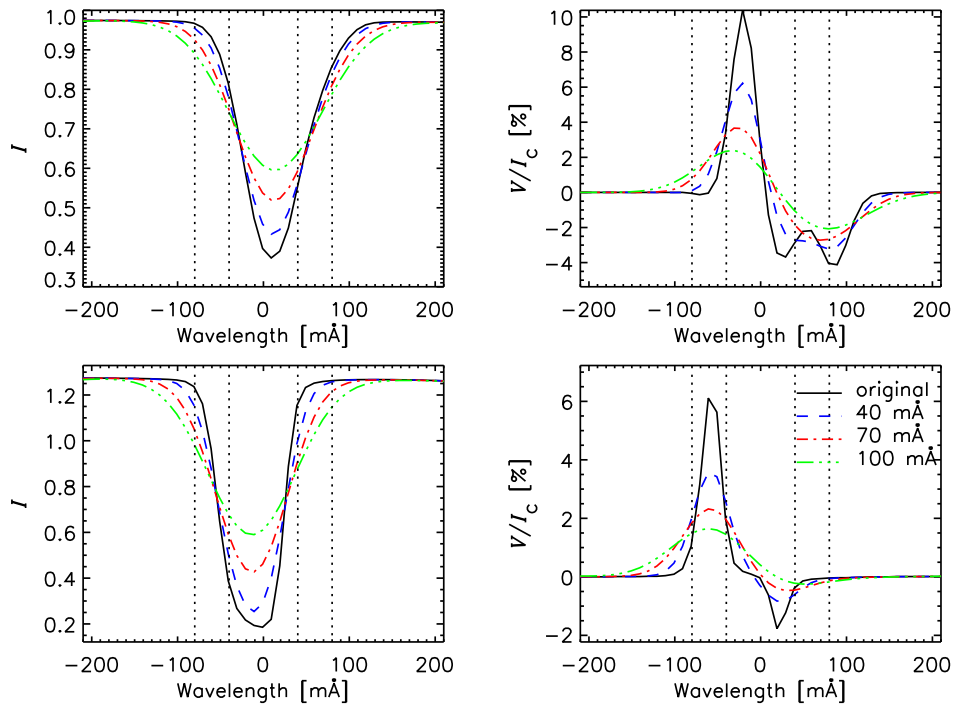

FIGURE 9.5:— Same as Fig. 9.4 but for Stokes I and V corresponding to pixels $(x, y) = (85, 200)$ and $(193, 121)$.

lines indicate wavelength samples at [-8,-4,4,8] pm from the central wavelength of the line. The effects of the smearing filter are quite apparent. First, the asymmetries of the profiles are smoothed out. Notice that an instrumental filter of 10 pm width can modify the shape of the Stokes profiles such that they are seen as profiles with a well-defined symmetry.

Second, the amplitude of the polarization signals are lowered. Notice that for filter widths larger than 7 pm, the amplitude of the profiles is decreased by more than half of their original size. In this example, the linear polarization profiles would be detectable above the noise levels of $10^{-3} I_c$ provided there is no smearing filter; they are buried by noise for filter widths of 10 pm.

These two effects reduce the information content on the profiles. The sensitivity to flow velocities decreases because the smearing filter broadens the profiles and make them shallower (Cabrera Solana, Bellot Rubio, & del Toro Iniesta 2005). The sensitivity to other model parameters also decreases with the smearing filter (see Chapter 4).

Two additional examples are shown in Fig. 9.5, one exhibiting a three lobed

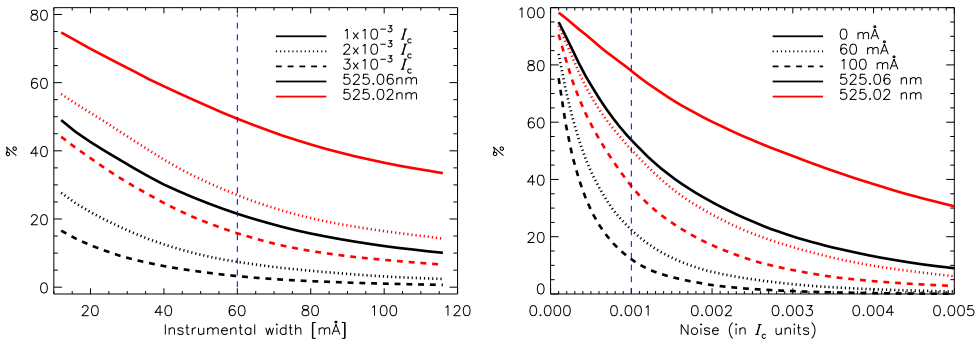

FIGURE 9.6:— Variation of the number of pixels whose Stokes Q or U amplitudes exceed specified noise levels, in percent, as a function of the instrumental filter width and of the noise for various filter widths (left and right, respectively). Vertical lines indicate the IMaX parameters.

Stokes V profile and another with a large asymmetry (top and bottom panels respectively). In both cases a smearing filter width of 10 pm almost transforms Stokes V in regular (i.e., with a given parity) profiles.

9.3.3 The effect of noise

As we have shown, the smearing profile reduces the amplitude of the polarization signals. Consequently, they are more affected by photon noise. In this section we quantify the influence of photon noise on the measurements. To this end, Fig. 9.6 (left panel) shows, as a function of the smearing filter width, the percentage of pixels whose Stokes Q or U amplitudes exceed specified noise levels (see insert in the figure). The Fe I 525.02 and 525.06 nm spectral lines are represented in red and black, respectively. Note that the amount of pixels showing signals above the noise decrease monotonically with the filter width. The figure shows that the ability to detect linear polarization signals depends on the instrumental profile.

In the right panel of Fig. 9.6, we represent the percentage of pixels with detectable linear polarization signal above noise against the noise level of the profiles with fixed filter widths of 0, 6 and 10 pm. Notice that the amount of polarization signal decreases quite rapidly with noise.

Let us assume that the noise level corresponds to $10^{-3}I_{\rm c}$ and that the width of the smearing profile is 6 pm. This values are indicated with vertical lines in Fig. 9.6. For the Fe I 525.02 nm spectral line we obtain that $\sim 50\%$ of the pixels show linear polarization signals above the noise. For the 525.06 nm line this

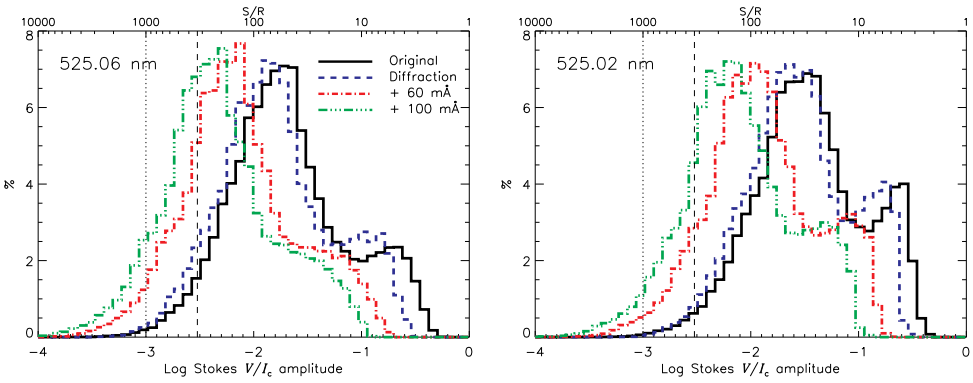

FIGURE 9.7:— Distribution of the Stokes V/I_c amplitudes in the original, spatially degraded and spatially and spectrally degraded images with two different smearing filters. The Stokes profiles have been taken from the simulation run having $\langle B \rangle = 140$ G. Vertical lines represent two different S/N ratios.

percentage decreases to $\sim 20\%$. The figure shows clear differences between the two lines. The one having larger effective Landé factor, i.e., Fe I 525.02 nm with $g_{\rm eff} = 3$, shows Stokes Q and U profiles with larger amplitudes. This makes it easy to detect linear polarization signals with this spectral line in quiet-Sun regions. Interestingly, the percentage of pixels showing linear polarization signals above the noise for the Fe I 525.02 nm line and smearing filter of 6 pm coincides with that percentage calculated with the 525.06 nm line without a smearing filter.

Of interest is that $\sim 30\%$ of the pixels are no longer detectable in linear polarization when we apply a filter width of 6 pm. This loss of sensitivity can be compensated by lowering the noise level. For instance, if we are to recover the previous loss of $\sim 30\%$ of the pixels, the S/N has to be increased from 1000 to 2800. This translates into about a factor 9 in exposure time, which may have some unwanted consequences on high spatial resolution observations.

Figure 9.7 shows the distributions of Stokes V amplitudes in the original, spatially degraded maps and the degraded maps taking into account two different smearing filter widths for the Fe I 525.02 and 525.06 nm spectral lines (right and left, respectively). The histograms show an asymmetric distribution of amplitudes. The effects of diffraction are weak and similar to those explained in Chapter 6. It is very noticeable the effects of the smearing filter against those caused by diffraction. The smearing filter shifts the distribution as a whole toward smaller amplitude values. It also modifies the shape of the histogram.

There is a secondary maximum at larger amplitude values for the original

and degraded images. These maximum smoothes out for the 525.06 nm line when applying the smearing filter. The origin of these peaks is in the Zeeman saturation of the lines (Stenflo 1973). In the weak field approximation, the Stokes V amplitude increases linearly with the magnetic field strength until the field reaches a saturation limit. At that point the relation between the amplitude of Stokes V and the magnetic field is no longer linear. This saturation limit occurs when the Zeeman splitting of the line, $\Delta\lambda_{\rm B} \propto \lambda^2 g_{\rm eff} B$, is larger than its Doppler with. From this relationship the Fe I line at 525.02 and 525.06 nm lines saturate at $\sim$ 650 and $\sim$ 1500 G, respectively assuming $\Delta\lambda_{\rm D} = 30$ mÅ. This partially explains why the ratio of the amplitude between the main and secondary peaks is different for the two spectral lines.

A comparison of the histograms for both lines show that the distribution of 525.02 nm Stokes V amplitudes is located at larger values, mainly due to its larger sensitivity to the magnetic field. The effects of the smearing filter is similar for both lines. As a consequence, the smearing profile affects more to the 525.06 nm line. In Fig. 9.7 we have represented two different noise levels, at 1 and 3 times $10^{-3} I_{\rm c}$, dotted and dashed, vertical lines respectively. Below these noise levels the Stokes V signal would not be detectable. Notice that the peak of the histograms for the 525.06 nm line is closer to these limits than the peak for its neighbor line.

To analyze the effects of the spatial degradation and smearing filter on the linear and circular polarization signals we have taken the Stokes profiles sampled at 61 wavelength points. IMaX will observe only four wavelength points plus one in the continuum. Therefore, a smaller percentage of pixels showing polarimetric signals above the noise levels is to be expected. Figs. 9.4 and 9.5 show vertical lines indicating four wavelength points. Notice that the wavelengths do not coincide with the locations at which the Stokes profiles have their extrema. Therefore, limited wavelength sampling translates into a decrease on the fraction of polarization signals detectable above the noise level.

9.3.4 Effects of the secondary peaks of the Fabry-Pérot

Another important effect that we have to take into account is due to the secondary peaks of the étalon. The effect is a spectral information corruption due to light from the secondary peaks of the étalon.

In Fig. 2.2 we represent FTS spectral atlas (black) around the 525.0 nm spectral region and overplotted is the IMaX transmission filter. The secondary peaks of the étalon are represented by the blue line. The contribution of these secondary peaks is reduced by introducing a pre-filter in the optical path.

Figure 9.8 shows the FTS for the Fe I lines at 525 nm before and after the

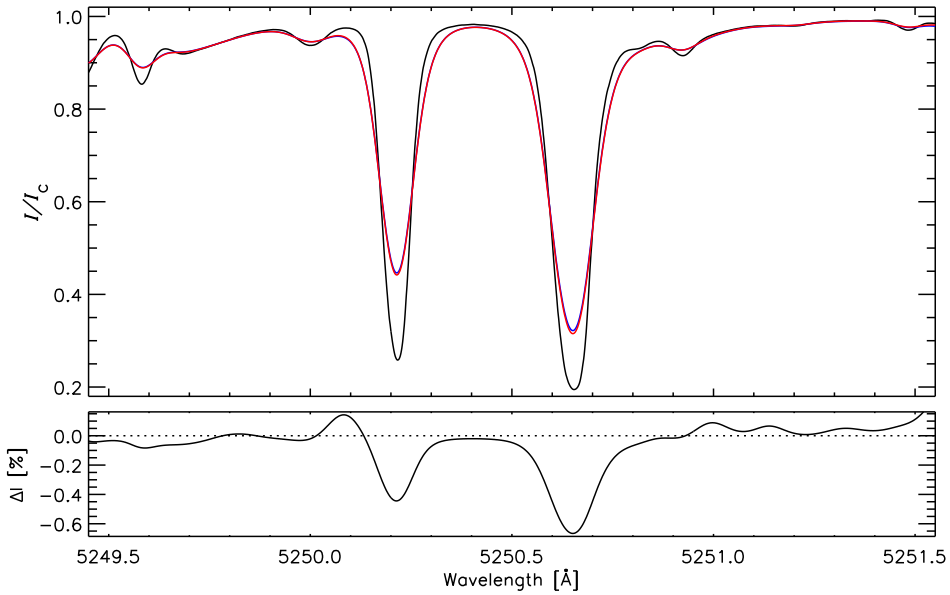

FIGURE 9.8:— FTS atlas after (red) and before (black) being convolved by the instrumental profile (see Fig. 2.2). Bottom panel: difference between the FTS convolved with the instrumental profile taking into account its secondary peaks and the same but neglecting the contribution of the secondary peaks.

convolution with the transmission filter in black and red lines respectively. We can see how the lines are broader and the residual intensity decreases. In the same plot we represent the difference of the FTS convolved with the transmission filter taking into account the secondary peaks of the étalon and without taking them into account. The differences are below 0.6%. This percentage is above typical noise levels.

9.4 Inversion of the Stokes profiles

As we have shown, the smearing filter has a strong impact on the Stokes profiles. In addition, IMaX will observe only four wavelength samples across the line plus a point in the nearby continuum. Both things will diminish the sensitivity of the spectral line to the atmospheric quantities. Therefore, we expect large uncertainties in the inferred ME parameters. To quantify these errors, we invert the simulated profiles under the following conditions:

1. The Stokes profiles degraded by telescope diffraction and CCD pixel size

with no noise, a Dirac delta PSF, and 61 wavelength samples. This will provide us with a *reference*.

2. The profiles as before but with noise added at the level of 10^{-3} I_c and with a smearing filter of width 6 pm, represented by a Gaussian function.

3. The spatially and spectrally degraded profiles with noise, sampled at only four wavelengths plus a point in the continuum.

The comparison of the ME inferences with the reference model will allow estimation of the uncertainties due to the limited angular resolution and spectral sampling. The analysis is done for the two Fe I lines at 525.02 and 525.06 nm, separately. This permits the quantitative comparison of the diagnostic capabilities for vector magnetic field measurements between the two lines.

In the inversion, we assume a single one-component model atmosphere. Remarkably, we have assumed no stray-light contamination to correct for the effects of diffraction. In other words, we assume that the effects of diffraction in the polarization profiles are negligible. The initialization of the magnetic field vector is, for all tests: $B = 200$ G, $\gamma = 20°$, and $\chi = 20°$.

9.4.1 Reference model

In Chapter 5 we determined the errors associated to the ME approximation by analyzing real observations in the case in which the instrument measures the Stokes profiles with no noise, very high spectral resolution, and optimum wavelength sampling. The analysis was done with the help of the same MHD models used in this Chapter. The conclusion was that ME inversions provide satisfactory results that turn out to be averages over the real stratifications. We also showed that errors due to the ME assumption dominate against those associated to photon noise. This analysis where carried out for the pair of Fe I lines at 630 nm. These uncertainties have to be again evaluated since we use a different spectral region containing the Fe I lines at 525.02 and 525.06 nm, for both lines separately.

In this section we do not resume the central discussion of Chapter 5, about the suitability of ME inversions to analyze high-spatial resolution observations. We just show the rms errors of the magnetic field strength, inclination, azimuth, and LOS velocity taken from the FWHM of the histograms of the differences between the inferred ME parameters and the real ones at $\log \tau = -1.5$[3] (see Table 9.2).

[3]This optical depth layer is the one that provides smaller rms errors for the inferred model quantities.

TABLE 9.2:— Rms errors associated to the ME approximation for the two spectral lines candidates to be observed with the IMaX vector magnetograph. The errors have been calculated from the difference between the model parameters from the ME inversion of the Stokes profiles with no noise and no instrumental effects and optimum wavelength sampling, and the real stratifications at $\log\tau = -1.5$.

Spectral line	B [G]	γ [°]	χ [°]	$v_{\rm LOS}$ [m/s]
525.02 nm	80	13	18	295
525.06 nm	71	14	21	320

Notice that the rms for the magnetic field strength are slightly larger for the Fe I line at 525.02 nm despite its larger sensitivity to the magnetic field than the 525.06 nm line. The rms for the inclination and for the LOS velocity are of the same order of magnitude for both lines, while the azimuth rms is smaller for the 525.02 nm line.

Figure 9.9 shows scatter plots of the magnetic field strength, inclination, azimuth and LOS velocity from the simulations at $\log\tau = -1.5$ vs the ME model parameters inferred from the inversion of the Stokes vector degraded by telescope diffraction and CCD pixel size and with no noise added. The results corresponds to the Fe I line at 525.02 nm. The green lines represent one-to-one correspondences. The rms shows the expected uncertainties for the ME inversion of IMaX observations with no noise, no smearing filter and optimum wavelength sampling (red line). In the figure we represents all pixels corresponding to one of the snapshots of the $\langle B\rangle = 140$ G simulation run. Because of an IMaX pixel contains 4 pixels in the MHD maps, we compare each inverted pixel with the mean of the corresponding 4 pixels in the simulations. The results from this inversion represent the reference model.

In the figure we can see that the rms are small for the field strength and for the LOS velocity. They do not increase significantly in comparison with those values reported in Table 9.2 despite the effects of telescope diffraction. This demonstrates the suitability of ME inversions for diffraction-limited spectropolarimetric observations at $0''.1$.

9.4.2 Test results

To get an insight into the uncertainties of the magnetic field vector and LOS velocity due to the smearing filter and limited wavelength sampling, Fig. 9.10 shows maps for the magnetic field strength, inclination and azimuth, and LOS velocity as retrieved from the ME inversion of the Fe I at 525.02 nm profiles from $\langle B\rangle = 140$ G simulation run. The first column shows the inversion results

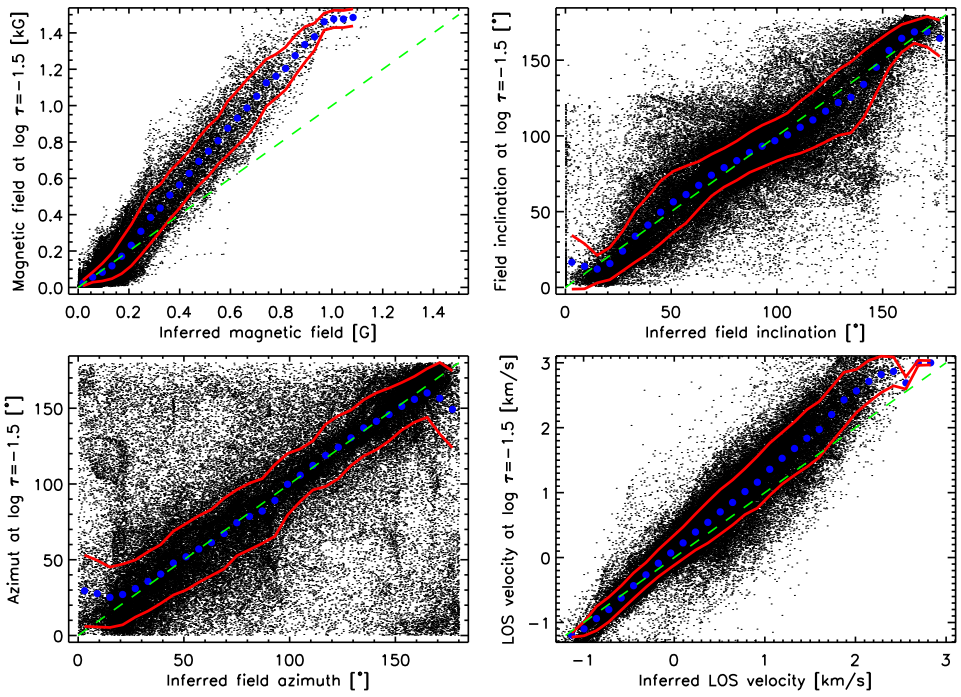

FIGURE 9.9:— Magnetic field strength, inclination, azimuth and LOS velocity at $\log \tau = -1.5$ form the MHD simulations vs the ME parameters inferred from the fit of the Stokes vector degraded by telescope diffraction and detector pixel size, and with no noise added, corresponding to the Fe I line at 525.02 nm. The green lines represent one-to-one correspondences. The blue dots represents the average mean values over very small, evenly-spaced intervals along the X-axis. The red line represents the rms fluctuations of the ME parameters.

of the degraded profiles by telescope diffraction and CCD pixel and no noise (referred to as the reference). The second column stands for the results of inverting the profiles convolved with a smearing filter of 6 pm FWHM. The third column, illustrates the same as before but with the spectral line sampled at four wavelength points located at [-8,-4,4,8] pm form line center, plus the continuum. For the last two column maps the S/N is 1000. Only a region corresponding to 150×150 pixels is displayed (same region than that represented in Fig. 9.3).

The qualitative comparison of the inversion results taking into account the smearing filter and that considering limited wavelength sampling in addition to the smearing with the reference shows that the field strength and the LOS velocity are well recovered. Only slight differences between the reference and inferred maps are seen. The inferred magnetic field strength maps show that the uncertainties are larger when the field strength is weak (below 100 G).

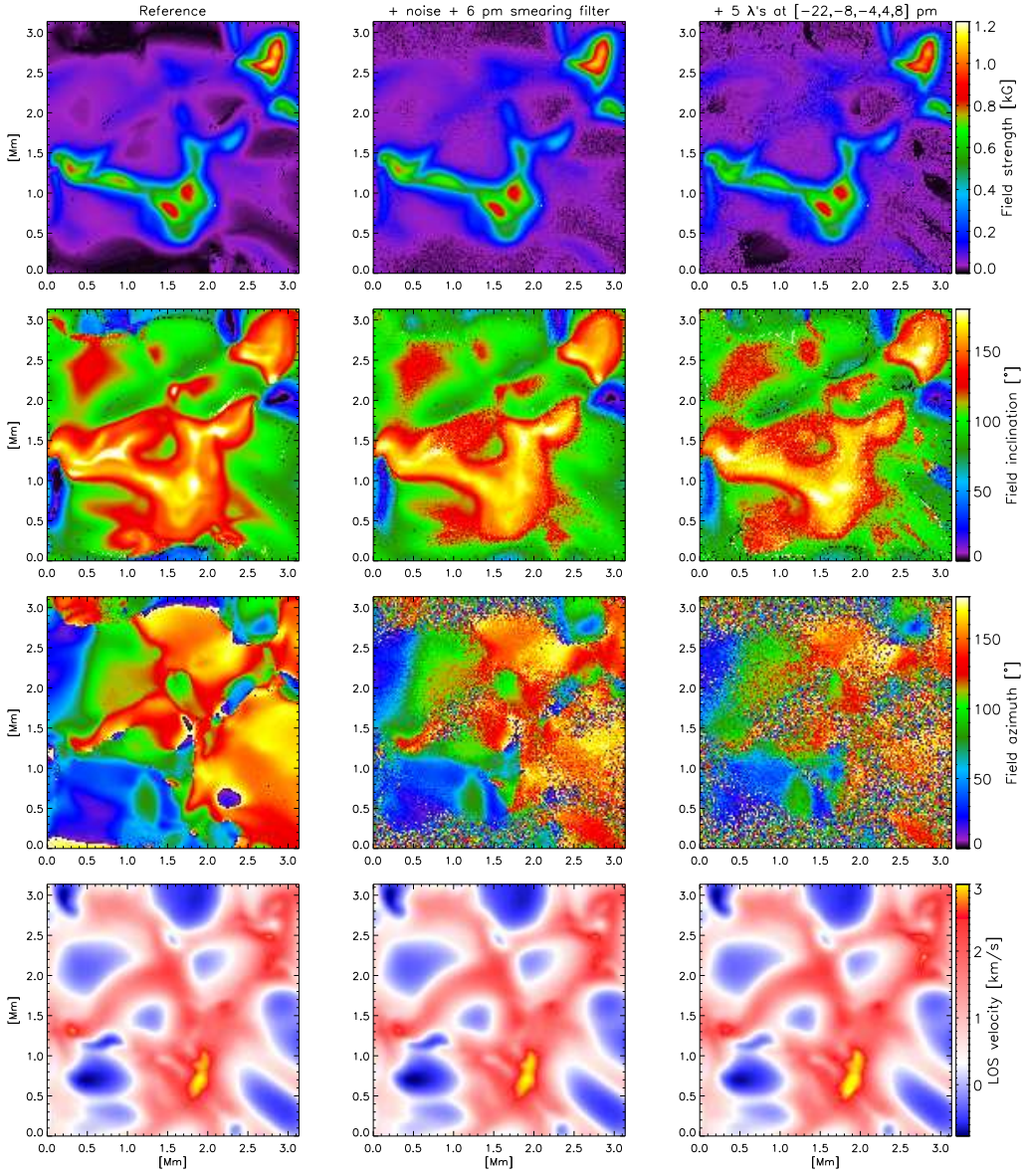

FIGURE 9.10:— From top to bottom: magnetic field strength, inclination and azimuth, and LOS velocity. Left represents the result of the ME inversion of the Fe I at 525.02 nm profiles from $\langle B \rangle = 140$ G simulation run degraded by telescope diffraction. Middle shows the maps retrieved from the ME inversion of the degraded profiles convolved with a 6 pm filter. Right the same but with the spectral line sampled at four wavelength points at [-8,-4,4,8] pm form the line center, plus a continuum point. Except for the reference, in all maps S/N=1000.

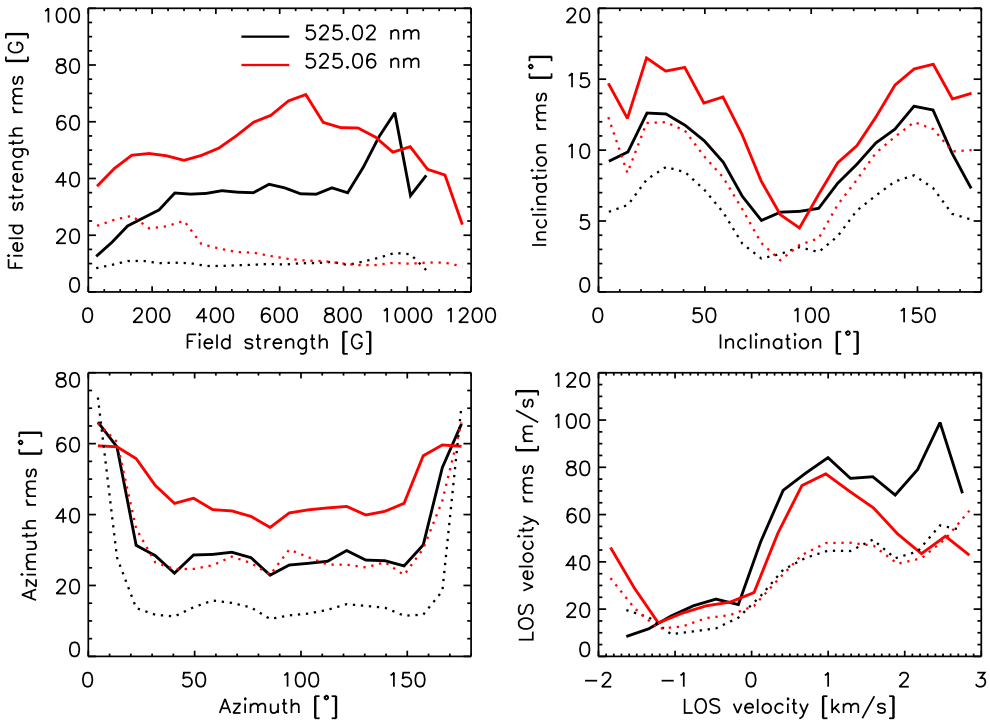

FIGURE 9.11:— Rms differences between the inferred ME parameters and the reference model. Black and red lines stand for the Fe I lines at 525.02 nm and Fe I at 525.06 nm, respectively. Dotted represents the rms of the inversion of the profiles with a smearing filter of 6 pm. Solid lines indicate the rms of the same profiles sampled at only four wavelength points at [-8,-4,4,8] pm form the line center, plus a continuum point.

The uncertainties are larger in the inclination and azimuth maps because the smearing together with the noise and the limited sampling reduces dramatically Stokes Q and U amplitudes. The noisier areas on the recovered maps for the inversion with 4 wavelength samples along the line correspond to pixels where the magnetic field is weak and therefore, the linear polarization signal is buried in noise.

These results indicate that it is possible to infer the magnetic field strength and the LOS velocity from IMaX measurements with reasonable precision. For instance, the inversion recovers fields as weak as hundred Gauss. On the contrary, the inclination and azimuth maps illustrate that these parameters are inferred with less reliability.

Figure 9.11 displays the rms of the difference between the inferred ME parameters and the reference. The rms values have been calculated by taking bins in the X-axis of size 100 G, 6°, and 300 $\mathrm{m\,s^{-1}}$. Black and red lines refer to

the pair of Fe I lines at 525.02 nm and at 525.06 nm, respectively. The solid line stands for the inversion results of the data with a smearing filter of 6 pm and the profiles sampled at [-8,-4,4,8] pm from line center, plus a continuum point. In the same Figure we show the results from the inversion of the same data only affected by a smearing filter of 6 pm (dotted line). To calculate the rms, only pixels whose Stokes Q, U or V amplitudes of the Fe I line at 525.06 nm exceed three times the noise level have been considered, except for the LOS velocity in which case we included all pixels.

The results show that the errors for the magnetic field strength are of the order of 50 G, for the Fe I line at 525.02 nm. The magnetic field rms is slightly smaller for this line than for the one at 525.06 nm. Also, the Fe I line at 525.02 nm shows smaller field inclination and azimuth rms values. The maximum inclination and azimuth error values are $\sim 10^\circ$ and $\sim 25^\circ$, respectively. This results show the larger sensitivity to the magnetic field vector of the Fe I line at 525.02 nm against Fe I at 525.06 nm. The fluctuations of the rms in the magnetic field vector are associated with the field vector distribution in the simulations. Finally, the averaged LOS velocity rms (of 120 $\mathrm{m\,s^{-1}}$) do not exceed 30 $\mathrm{m\,s^{-1}}$for both lines.

In summary, the results show that both lines are suitable for magnetic field strength and velocity inferences by means of ME inversions. Among the two, Fe I at 525.02 nm is more appropriate to determine the magnetic field vector. The expected errors for the inclination and azimuth are somehow large.

9.5 Summary and conclusions

We have analyzed and simulated IMaX observations to study the performance of the instrument and to select the most suitable line to be observed. To this end, Stokes profiles of the Fe I lines at 525.02 and 525.06 have been calculated using MHD simulations and then spatially degraded by telescope diffraction and detector pixel size to match the IMaX resolution. Then, we have carried out numerical experiments to analyze the effects of the limited resolving power and wavelength sampling of IMaX on the inferred quantities be means of ME inversions.

The degradation of the profiles due to smearing has two main effects: first, it reduces the amplitude of Stokes Q, U and V; secondly, it smoothes out profile asymmetries. A consequence is that different magnetic structures that are seen in the polarization maps disappear due to the combined effect of the smearing filter and the photon noise. Therefore, we detect less amount of polarization. This effects are more pronounced on the linear polarization maps. In this

sense, it is important to achieve high S/N to minimize the effects of the limited angular resolution.

The limited wavelength sampling do also affects to the amount of polarization signal that can be detected above the noise because we might not sample the wavelength locations at with the maximum are placed. The effects of limited wavelength sampling are less strong that those originated by the smearing filter, though.

From the inversion of the simulated IMaX observations we conclude that it is possible to satisfactorily determine the magnetic field strength and LOS velocity from IMaX measurements, with a smearing filter of 6 pm and with 4 wavelength samples across the line plus a point in the nearby continuum.

The Fe I line at 525.02 nm is better suited for magnetic field determinations because its larger effective Landé factor than the Fe I line at 525.06 nm. A consequence is that this line detect more magnetic structures above the noise level, allowing the detection of weaker fields. This also helps to determine the field strengths with better accuracy when the field is weak. As a drawback, this line is more sensitive to temperature changes, originating on large profile shape asymmetries.

10

Summary and conclusions

We have introduced the concept of Response Functions (RFs) in Milne-Eddington (ME) atmospheres and written them in an analytical form. These RFs have allowed the analysis of Stokes profiles formation physics under ME conditions. We have targeted the Fe I line at 525.06 nm to construct a ME model representative of the quiet-Sun that we have used to discuss the properties of the response functions. The RFs permitted us to investigate the sensitivity of spectral lines to model parameters. Also, RFs showed which Stokes profiles and wavelength samples were more sensitive to these parameters. For instance, it turned out that Stokes V was more sensitive to weak fields than to strong fields. And that the wavelength samples with maximum sensitivities did not coincide with the extrema of the profiles. In addition, the RFs to thermodynamic parameters were very similar, which explained the trade-off often found among them in ME inversion codes.

We have proposed a method for the selection of wavelength samples for given measurements that consisted in a suitable combination of RFs. This provide us with a method to optimize the selection of wavelength samples and number of wavelength points of spectral lines, maximizing the physical information contained in the spectra.

We have analytically evaluated the minimum variation of the model parameters that can be detected above the noise level. This can provide an useful method to select spectral lines, and number and position of wavelength samples, to be observed by vector magnetographs. As a practical example we have calculated the minimum affordable errors for IMaX and PHI.

We have reviewed inversion method techniques that are most frequently

applied to spectropolarimetric data and have developed MILOS: an inversion code for the radiative transfer equation. MILOS fits Stokes profiles under the Milne-Eddington approximation to infer the model parameters that characterize the solar atmosphere. It uses an iterative schema based on the Levenberg-Marquardt algorithm.

We have examined whether ME inversions are adequate to analyze high spatial resolution observations of the quiet Sun. To this end we have employed realistic model atmospheres from radiative magnetohydrodynamic (MHD) simulations to synthesize the Fe I lines at 630.15 and 630.25 nm. The MHD simulations describe quite satisfactorily the physical conditions of the solar photosphere as was inferred from the comparison between the average intensity profile of the simulated spectra and the FTS quiet-Sun atlas. Then, we have evaluated the uncertainties that MILOS commits when interpreting real measurements, inverting the simulated Fe I spectral lines at 630 nm simultaneously. The comparison between the inferred model parameters and the MHD models, have provided the required uncertainties. In the inversion we have considered that the spectra are photon-noise free, there are no instrumental effects, and the spectral resolution is equal to a Dirac delta. The conclusions obtained are the following:

- ME inferences cannot be assigned to single atmospheric layers.
- ME inversions provide model parameters that are fair estimations of the physical quantities at $\log\tau = -1$. The rms differences are 30 G, 6°, 20° and 500 $\mathrm{m\,s^{-1}}$, for the magnetic field strength, inclination, azimuth, and velocity, respectively.
- Individual differences may be rather large, even when the best-fit profile reproduce satisfactorily the Stokes vector. This limits the interpretation of ME inversions, making them more adequate for statistical analyses of set of profiles rather than for individual pixel analyses.
- Errors due to the ME approximation dominate those due to photon noise.

We have satisfactorily simulated high-spatial resolution observations taken with the spectropolarimeter attached to the Solar Optical Telescope aboard *Hinode*. To this end we have employed MHD simulations to generate the Stokes profiles and have then degraded the "observations" to account for telescope diffraction and CCD pixilation, so that the *Hinode*/SP resolution of $0\farcs32$ was matched. The effects of diffraction on the polarization signals have been investigated and we have drawn the following conclusions:

- Diffraction reduces the general image contrast.
- It mixes polarization signals from different pixels to nearby ones, thus reducing the amount of circular and linear polarization signals in $\sim 80\%$ of the pixels.
- Diffraction leads to a decrease of the amount of polarization signals detectable above noise.
- Profiles asymmetries are smoothed out due to the action of the telescope.

The main conclusion we highlight is the dilution of the polarization signals due to diffraction.

We have proposed a new strategy for the analysis of high-spatial resolution data. It consists in ME inversions with a simple one-component model atmosphere filling the resolution element and a stray-light contamination factor. The stray-light is calculated locally in order to model the effects of telescope diffraction. To examine the reliability of the new inversion strategy, we have applied it to the simulated *Hinode*/SP observations.

The comparison between the inferred ME model parameters and the real stratifications has led to the conclusion that ME inversions perform quite satisfactorily and that the dilution of the polarization signals due to diffraction are well modeled using a local stray-light. This has proved the use of the Fe I lines at 630 nm for quiet-Sun magnetometry, when fields are stronger than 100 G and ME inversions are used. The errors in the field strengths are below 150 G for fields weaker than 1 kG. The errors in the field inclination do not surpass 20° for fields stronger than 200 G. We also find average stray-light factors of 55%. If one does not account for the dilution of the polarization signals, the field strengths are certainly underestimated.

We have analyzed *Hinode* first-light spectropolarimetric observations of quiet-Sun regions. In particular, we have studied a raster scan map and a time series of ~ 2 hours with high S/N. We have satisfactorily applied the proposed ME inversion strategy to correct the effects of telescope diffraction. From the distribution of IN field strengths and inclinations we conclude:

- The internetwork mostly consists in weak field concentrations. The average field strength results $\sim$ 41–124 G. The distribution of fields show a clear peak at 90 G.
- The IN magnetic fields tend to be horizontally oriented.
- A large fraction of granules host magnetic fields.

- The fraction of granules and intergranular lanes hosting magnetic fields is very similar, being about 25%, respectively.

- The magnetic fields in granules are more horizontal that those fields found in intergranular lanes, although we have also *found vertical fields in granules*.

- Strong fields are much abundant in downdrafts than in convective upflows.

- The magnetic filling factor in the internetwork averages 45%.

- The average longitudinal and transverse flux densities span 7–25 Mx cm^{-2} and 23–85 Mx cm^{-2}, respectively, depending on the S/N of the measurements. These fluxes are consistent with the large occurrence of horizontal fields.

Finally, to give consistence to the results we have demonstrated that the ME inferences of IN Stokes profiles are trustworthy because they do not depend on the magnetic field initialization used in the inversion and ME inversions retrieve properly both the stray-light and the field strength with the help of the full Stokes vector. This validates the ME inversion results.

From the analysis of high-cadence time series of *Hinode* spectropolarimetric measurements we have discovered a new form of flux emergence in granular cells. This emergence seems to carry vertical magnetic fields from subsurface layers to the photosphere, as shown by the qualitative analysis of the Stokes profiles from 5 emergence events out of 13 events occurring during $\sim$ 10 hours of *Hinode* observations. These emergence events are different from the emergence of magnetic loops in the IN and constitute a new magnetic phenomenon. They are characterized by weak flux-density values ($\sim$ 30 G) and durations of $\sim$ 15 minutes. Unfortunately, the analysis did not provide enough binding information to clarify the underlying physical scenario.

We have investigated how well we are able to infer the vector magnetic field and the velocity from IMaX measurements. To this end we have first simulated IMaX observations using MHD models of the solar photosphere. The analysis encompass three steps: the synthesis of the Stokes profiles emerging from the simulations, the degradation of the spectra by telescope diffraction, and the interpretation of the profiles using ME inversion techniques. The main conclusions are:

- Fabry-Pérot interferometers smoothes the asymmetries of Stokes profiles out,

- the limited resolving power of the IMaX Fabry-Pérots in addition to the limited number of wavelength samples, reduces the amount of detectable polarization signals above the noise,
- it is important to achieve high S/N in the measurements to minimize the lost of polarization signals
- IMaX will benefit from the use of the Fe I 525.02 nm line because its sensitivity to the magnetic field, which translates into larger polarization signals,
- the Fe I 525.02 nm line is better suited for the determination of vector magnetic fields,
- it is possible to determine the magnetic field strength and plasma velocity from the IMaX spectral line sampled at five wavelength samples located at $[\pm 40, \pm 80]$ mÅ from the central wavelength of the line, plus a wavelength point in the nearby continuum. The predicted rms errors are: $\sigma_B \leq$ 200 G, $\sigma_\gamma \leq 30^{\rm o}$, $\sigma_v \leq 600$ m/s.

A

Explicit formulae for the analytical Response Functions

In Chapter 2.3 (Eq. 2.15) we presented the RTE for polarized light in a plane-parallel atmosphere. We also shown that in a Milne-Eddington (ME) model atmosphere, an analytical solution is found for the RTE (see, e.g. Unno 1956; Rachkovsky 1962, 1967; Landolfi & Landi Degl'Innocenti 1982).

The evaluation of RFs in a ME model atmosphere reduces to the derivatives of the Stokes vector, $\mathbf{I} = (I, Q, U, V)$, with respect to the nine parameters, $(B_0, B_1, \eta_0, B, \gamma, \chi, \Delta\lambda_{\rm D}, v_{\rm LOS}, a)$. In order to easily show such derivatives suppose a generic parameter x. Then,

$$
\begin{aligned}
\frac{\partial I}{\partial x} &= B_1\mu\left(T_1\frac{\partial \eta_I}{\partial x} + \eta_I\frac{\partial T_1}{\partial x} - \Delta^{-1}\eta_I T_1\frac{\partial \Delta}{\partial x}\right)\Delta^{-1}, \qquad \text{(A.1)}\\
\frac{\partial Q}{\partial x} &= -B_1\mu\left(\frac{\partial T_2}{\partial x} + \frac{\partial \rho_Q}{\partial x}\Pi + \rho_Q\frac{\partial \Pi}{\partial x} - \Delta^{-1}\frac{\partial \Delta}{\partial x}[T_2 + \rho_Q\Pi]\right)\Delta^{-1},\\
\frac{\partial U}{\partial x} &= -B_1\mu\left(\frac{\partial T_3}{\partial x} + \frac{\partial \rho_U}{\partial x}\Pi + \rho_U\frac{\partial \Pi}{\partial x} - \Delta^{-1}\frac{\partial \Delta}{\partial x}[T_3 + \rho_U\Pi]\right)\Delta^{-1},\\
\frac{\partial V}{\partial x} &= -B_1\mu\left(\frac{\partial T_4}{\partial x} + \frac{\partial \rho_V}{\partial x}\Pi + \rho_V\frac{\partial \Pi}{\partial x} - \Delta^{-1}\frac{\partial \Delta}{\partial x}[T_4 + \rho_V\Pi]\right)\Delta^{-1},
\end{aligned}
$$

where for simplicity

$$\begin{aligned} T_1 &= \eta_I^2 + \rho_Q^2 + \rho_U^2 + \rho_V^2, \\ T_2 &= \eta_I^2\eta_Q + \eta_I(\eta_V\rho_U - \eta_U\rho_V), \\ T_3 &= \eta_I^2\eta_U + \eta_I(\eta_Q\rho_V - \eta_V\rho_Q), \\ T_4 &= \eta_I^2\eta_V + \eta_I(\eta_U\rho_Q - \eta_Q\rho_U), \\ T_5 &= \eta_I^2 - \eta_Q^2 - \eta_U^2 - \eta_V^2 + \rho_Q^2 + \rho_U^2 + \rho_V^2. \end{aligned} \tag{A.2}$$

Δ and Π are defined in Eqs. (4) and (5), respectively. Their derivatives are thus given by

$$\begin{aligned} \frac{\partial\Delta}{\partial x} &= 2\eta_I\frac{\partial\eta_I}{\partial x}T_5 + \eta_I^2\frac{\partial T_5}{\partial x} - 2\Pi\frac{\partial\Pi}{\partial x}, \\ \frac{\partial\Pi}{\partial x} &= \eta_Q\frac{\partial\rho_Q}{\partial x} + \frac{\partial\eta_Q}{\partial x}\rho_Q + \eta_U\frac{\partial\rho_U}{\partial x} + \frac{\partial\eta_U}{\partial a}\rho_U + \eta_V\frac{\partial\rho_V}{\partial x} + \frac{\partial\eta_V}{\partial x}\rho_V. \end{aligned} \tag{A.3}$$

The derivatives of $T_1, ..., T_5$ are given by

$$\begin{aligned} \frac{\partial T_1}{\partial x} &= 2\left(\eta_I\frac{\partial\eta_I}{\partial x} + \rho_Q\frac{\partial\rho_Q}{\partial x} + \rho_U\frac{\partial\rho_U}{\partial x} + \rho_V\frac{\partial\rho_V}{\partial x}\right), \\ \frac{\partial T_2}{\partial x} &= 2\eta_I\frac{\partial\eta_I}{\partial x}\eta_Q + \eta_I^2\frac{\partial\eta_Q}{\partial x} + \frac{\partial\eta_I}{\partial x}(\eta_V\rho_U - \eta_U\rho_V) + \\ &\quad \eta_I\left(\frac{\partial\eta_V}{\partial x}\rho_U + \eta_V\frac{\partial\rho_U}{\partial x} - \frac{\partial\eta_U}{\partial x}\rho_V - \eta_U\frac{\partial\rho_V}{\partial x}\right), \\ \frac{\partial T_3}{\partial x} &= 2\eta_I\frac{\partial\eta_I}{\partial x}\eta_U + \eta_I^2\frac{\partial\eta_U}{\partial x} + \frac{\partial\eta_I}{\partial x}(\eta_Q\rho_V - \eta_V\rho_Q) + \\ &\quad \eta_I\left(\frac{\partial\eta_Q}{\partial x}\rho_V + \eta_Q\frac{\partial\rho_V}{\partial x} - \frac{\partial\eta_V}{\partial x}\rho_Q - \eta_V\frac{\partial\rho_Q}{\partial x}\right), \\ \frac{\partial T_4}{\partial x} &= 2\eta_I\frac{\partial\eta_I}{\partial x}\eta_V + \eta_I^2\frac{\partial\eta_V}{\partial x} + \frac{\partial\eta_I}{\partial x}(\eta_U\rho_Q - \eta_Q\rho_U) + \\ &\quad \eta_I\left(\frac{\partial\eta_U}{\partial x}\rho_Q + \eta_U\frac{\partial\rho_Q}{\partial x} - \frac{\partial\eta_Q}{\partial x}\rho_U - \eta_Q\frac{\partial\rho_U}{\partial x}\right), \\ \frac{\partial T_5}{\partial x} &= 2\left(\eta_I\frac{\partial\eta_I}{\partial x} - \eta_Q\frac{\partial\eta_Q}{\partial x} - \eta_U\frac{\partial\eta_U}{\partial x} - \eta_V\frac{\partial\eta_V}{\partial x} + \rho_Q\frac{\partial\rho_Q}{\partial x} + \right. \\ &\quad \left.\rho_U\frac{\partial\rho_U}{\partial x} + \rho_V\frac{\partial\rho_V}{\partial x}\right). \end{aligned} \tag{A.4}$$

The derivatives with respect to η_0 can be easily calculated from Eq. (A.2.)

$$\begin{aligned}
\frac{\partial \eta_I}{\partial \eta_0} &= \frac{(\eta_I - 1)}{\eta_0}, \\
\frac{\partial \eta_{Q,U,V}}{\partial \eta_0} &= \frac{\eta_{Q,U,V}}{\eta_0}, \\
\frac{\partial \rho_{Q,U,V}}{\partial \eta_0} &= \frac{\rho_{Q,U,V}}{\eta_0}.
\end{aligned} \tag{A.5}$$

The derivatives with respect to γ and ψ are

$$\begin{aligned}
\frac{\partial \eta_I}{\partial \chi} &= 0, \quad \frac{\partial \eta_V}{\partial \chi} = 0, \quad \frac{\partial \rho_V}{\partial \chi} = 0, \\
\frac{\partial \eta_Q}{\partial \chi} &= -2\eta_Q \tan 2\chi, \\
\frac{\partial \eta_U}{\partial \chi} &= 2\eta_U \cot 2\chi, \\
\frac{\partial \rho_Q}{\partial \chi} &= -2\rho_Q \tan 2\chi, \\
\frac{\partial \rho_U}{\partial \chi} &= 2\rho_U \cot 2\chi, \\
\frac{\partial \eta_I}{\partial \gamma} &= \frac{\eta_0}{2}\left[\phi_p - \frac{\phi_b + \phi_r}{2}\right] \sin 2\gamma, \\
\frac{\partial \eta_Q}{\partial \gamma} &= \frac{\eta_0}{2}\left[\phi_p - \frac{\phi_b + \phi_r}{2}\right] \sin 2\gamma \cos 2\chi, \\
\frac{\partial \eta_U}{\partial \gamma} &= \frac{\eta_0}{2}\left[\phi_p - \frac{\phi_b + \phi_r}{2}\right] \sin 2\gamma \sin 2\chi, \\
\frac{\partial \eta_V}{\partial \gamma} &= -\eta_V \tan \gamma, \\
\frac{\partial \rho_Q}{\partial \gamma} &= \frac{\eta_0}{2}\left[\psi_p - \frac{\psi_b + \psi_r}{2}\right] \sin 2\gamma \cos 2\chi, \\
\frac{\partial \rho_U}{\partial \gamma} &= \frac{\eta_0}{2}\left[\psi_p - \frac{\psi_b + \psi_r}{2}\right] \sin 2\gamma \sin 2\chi, \\
\frac{\partial \rho_V}{\partial \gamma} &= -\rho_V \tan \gamma.
\end{aligned} \tag{A.6}$$

The derivatives with respect to the other parameters imply the derivatives of the absorption and dispersion profiles and these lead us to obtain the derivatives of the Voigt and Voigt-Faraday functions (as defined by Landi degl'Innocenti,

1976):

$$\begin{aligned}
\frac{\partial \phi_j}{\partial x} &= \sum_{M_l - M_u = j} S_{M_l M_u, j} \frac{\partial H(a,\upsilon)}{\partial x}, \\
\frac{\partial \psi_j}{\partial x} &= 2 \sum_{M_l - M_u = j} S_{M_l M_u, j} \frac{\partial F(a,\upsilon)}{\partial x}.
\end{aligned} \tag{A.7}$$

By using the chain rule and the derivatives of $H(a,\upsilon)$ and $F(a,\upsilon)$ with to respect a and υ,

$$\begin{aligned}
\frac{\partial H(a,\upsilon)}{\partial a} &= -2\frac{\partial F(a,\upsilon)}{\partial \upsilon}, \\
\frac{\partial F(a,\upsilon)}{\partial a} &= \frac{1}{2}\frac{\partial H(a,\upsilon)}{\partial \upsilon}, \\
\frac{\partial H(a,\upsilon)}{\partial \upsilon} &= 4aF(a,\upsilon) - 2\upsilon H(a,\upsilon), \\
\frac{\partial F(a,\upsilon)}{\partial \upsilon} &= \frac{1}{\sqrt{\pi}} - aH(a,\upsilon) - 2\upsilon F(a,\upsilon),
\end{aligned} \tag{A.8}$$

we find

$$\begin{aligned}
\frac{\partial H(a,\upsilon), F(a,\upsilon)}{\partial B} &= \frac{\partial H(a,\upsilon), F(a,\upsilon)}{\partial \upsilon} \frac{\Delta\lambda_{i_j}}{\Delta\lambda_\mathrm{D}} \frac{1}{B}, \\
\frac{\partial H(a,\upsilon), F(a,\upsilon)}{\partial v_\mathrm{LOS}} &= \frac{\partial H(a,\upsilon), F(a,\upsilon)}{\partial \upsilon} \frac{-\lambda_0}{c\Delta\lambda_\mathrm{D}}, \\
\frac{\partial H(a,\upsilon), F(a,\upsilon)}{\partial \Delta\lambda_\mathrm{D}} &= \frac{\partial H(a,\upsilon), F(a,\upsilon)}{\partial \upsilon} \frac{-\upsilon}{\Delta\lambda_\mathrm{D}}.
\end{aligned} \tag{A.9}$$

B

Inversion result for high S/N maps

This appendix shows the resulting maps from the inversion of the high S/N map (data set #2) discussed in Chapter 7. The Figures display the magnetic field strengths, inclinations, azimuths, stray-light factors and LOS velocities, respectively.

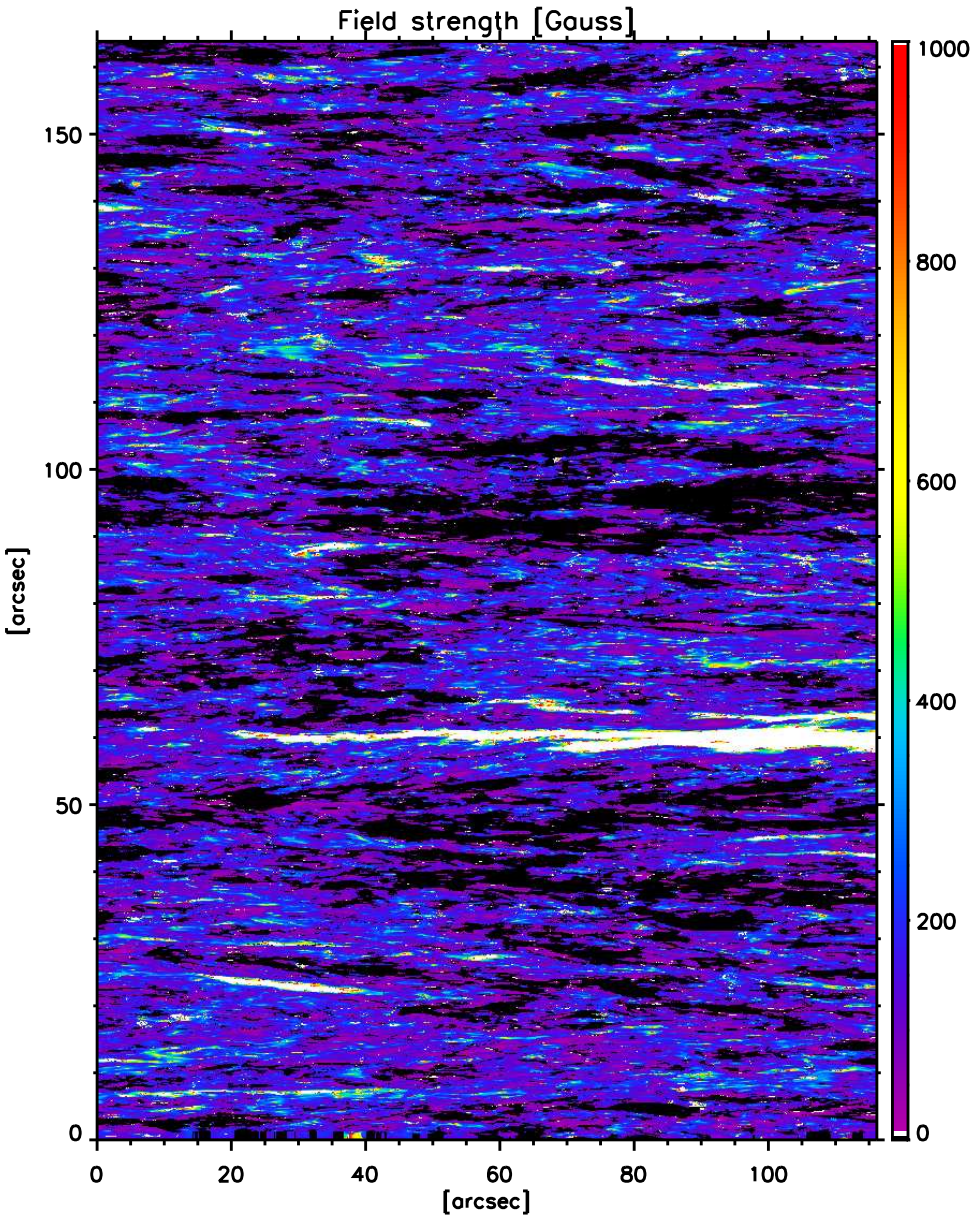
Field strength [Gauss]
1000
800
600
400
200
0
150
100
50
0
[arcsec]
0
20
40
60
80
100
[arcsec]

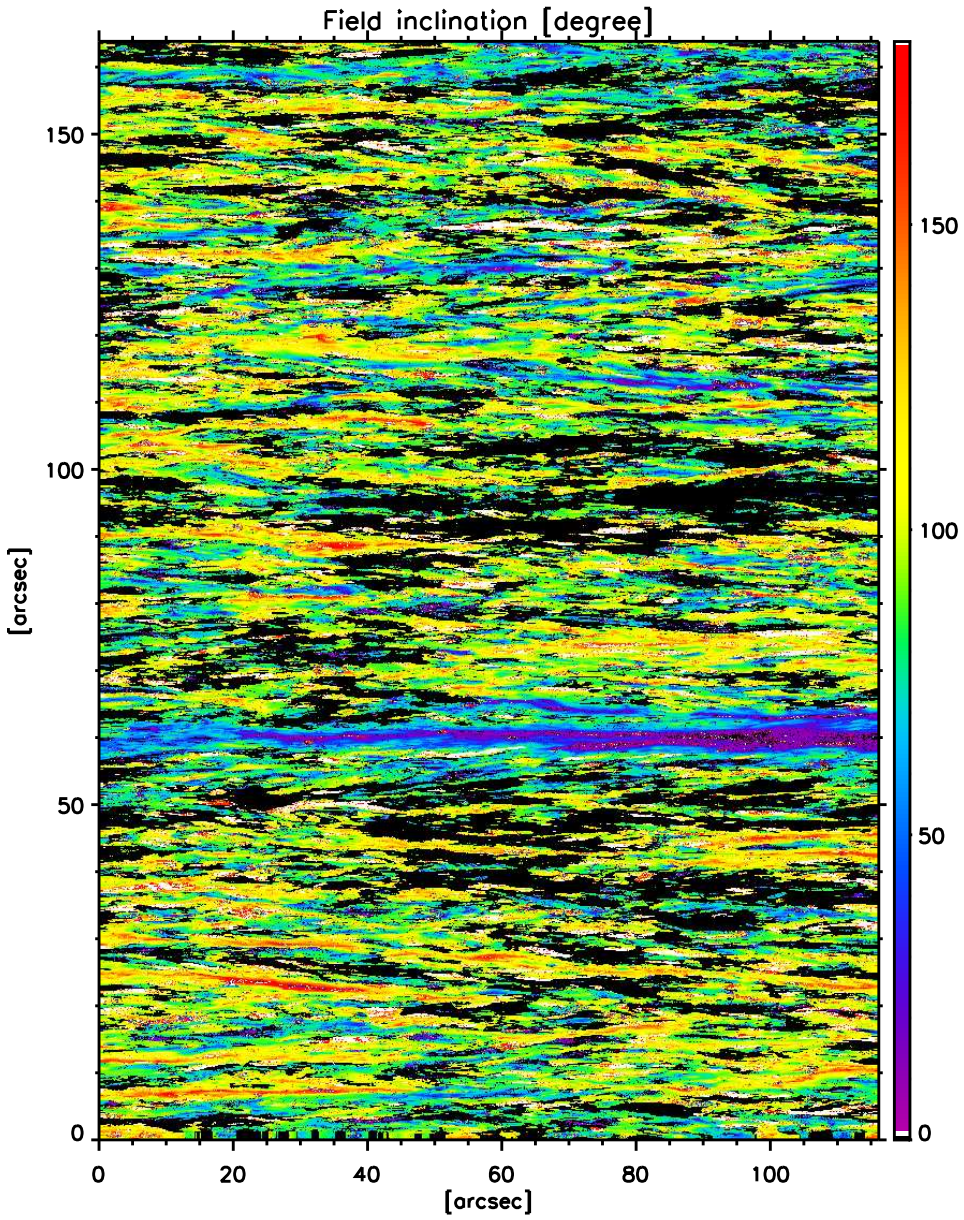
Field inclination [degree]
150
100
50
0
[arcsec]
0
20
40
60
80
100
[arcsec]
150
100
50
0

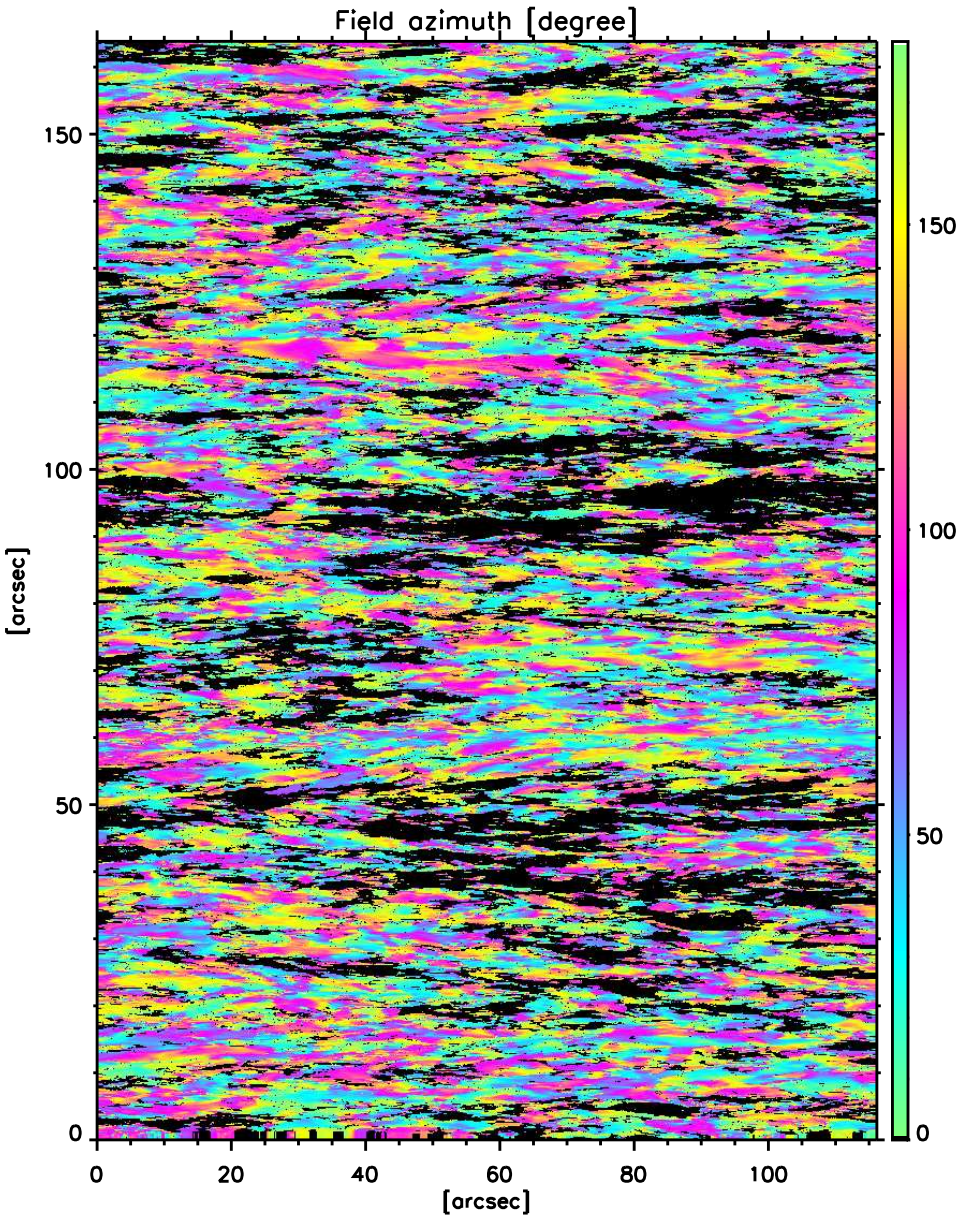
Field azimuth [degree]
150
100
50
0
[arcsec]
0
20
40
60
80
100
[arcsec]
150
100
50
0

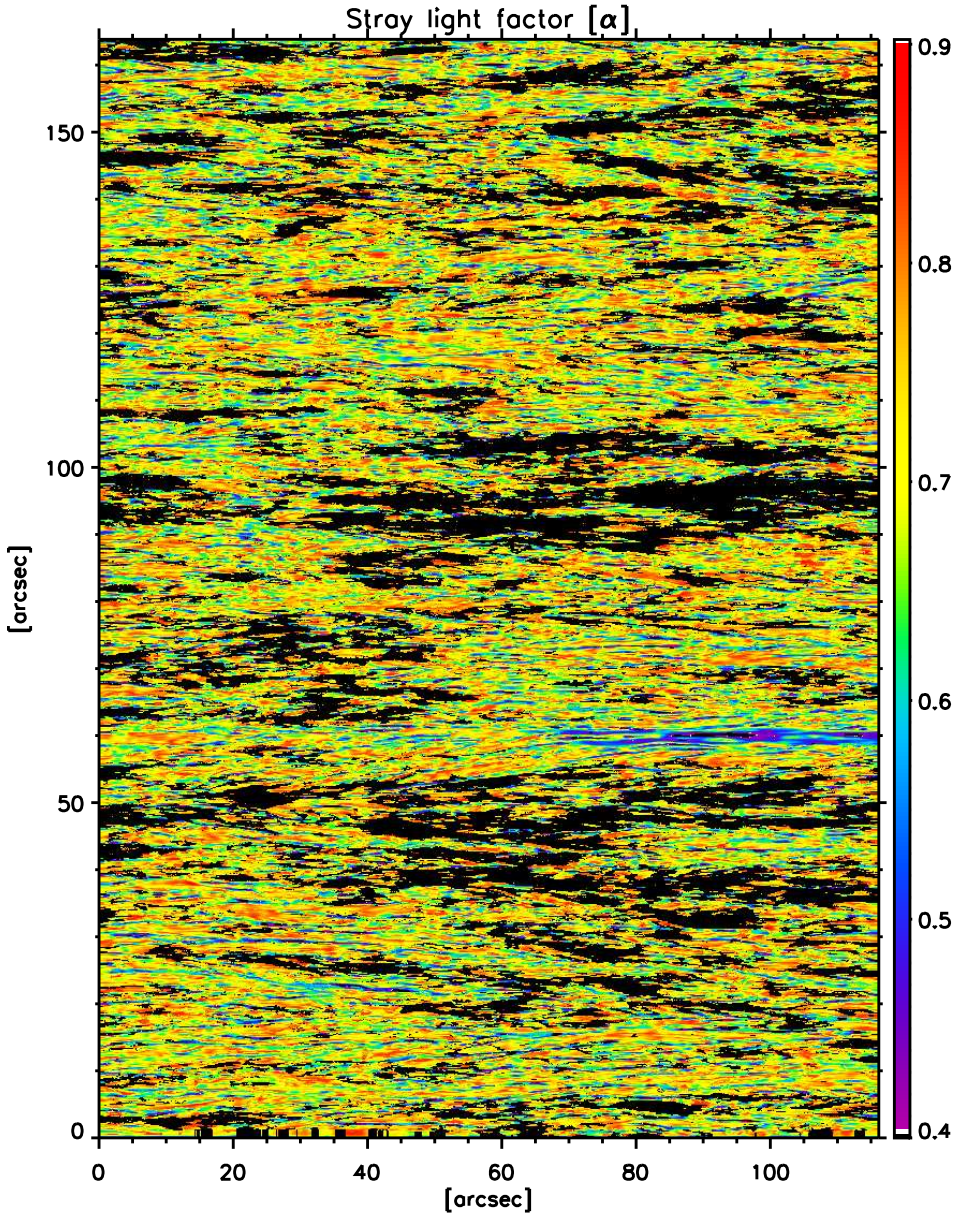
Stray light factor [α]
150
100
50
0
[arcsec]
0
20
40
60
80
100
[arcsec]
0.9
0.8
0.7
0.6
0.5
0.4

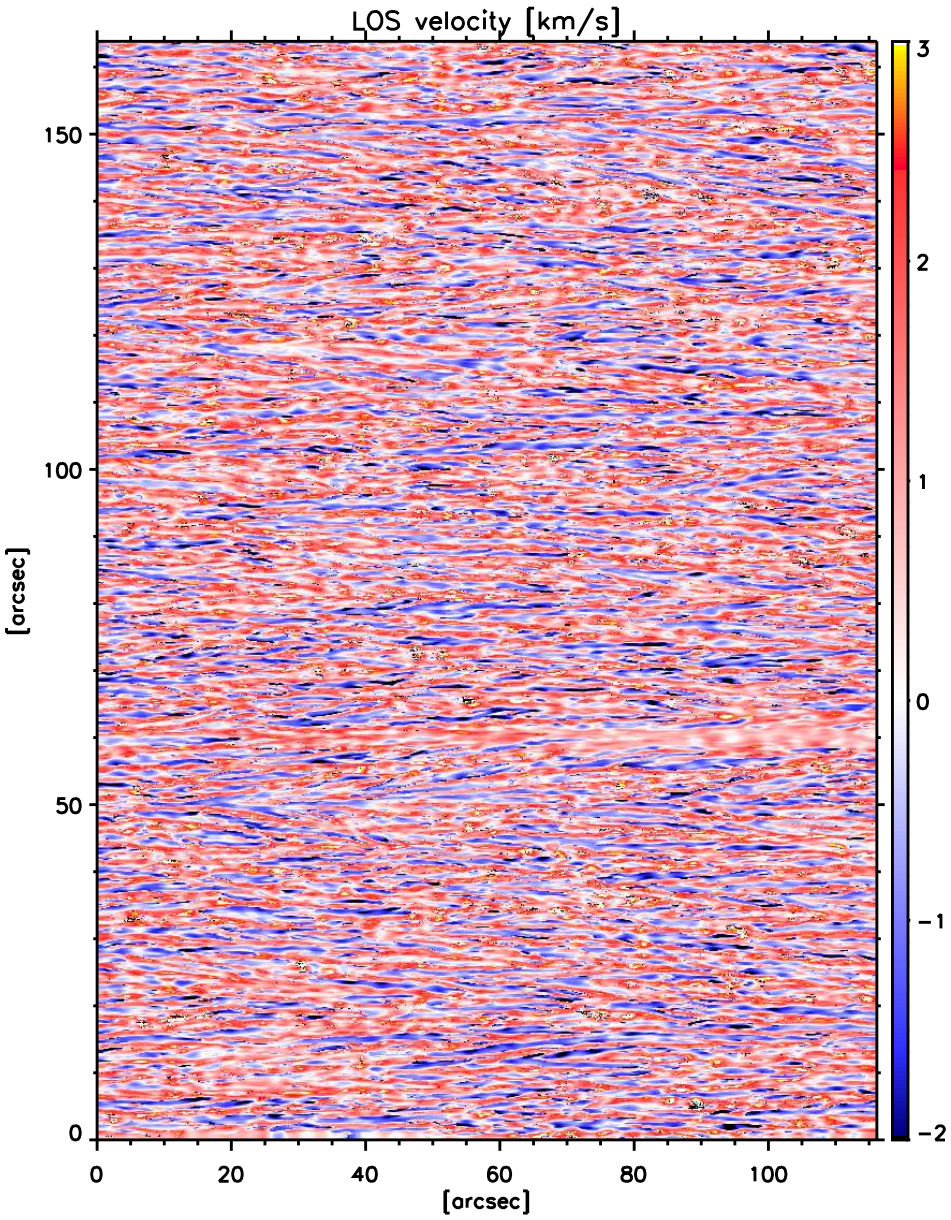
LOS velocity [km/s]
3
2
1
0
−1
−2
150
100
50
0
[arcsec]
0
20
40
60
80
100
[arcsec]

C

Numerical tests

In this Appendix we carry out numerical tests to check the accuracy of the MILOS code to infer the magnetic field vector and the LOS velocity from the Stokes profiles observed by vector magnetographs. In particular we analyze the uncertainties of ME inversions applied to ME profiles with limited spectral resolution and wavelength sampling. We also evaluate the uncertainties of the ME model parameters when the spectral line samples are placed at different wavelength positions.

We focus our attention in the Fe I spectral lines at 525.02 and 525.06 nm. These two lines show different sensitivities to the magnetic field, being 1.5 and 3 the Landé factors.

C.0.1 Reference profiles and initialization of the code

We use the MELANIE[1] code to synthesize the Stokes profiles emerging from 10 000 ME model atmospheres with a uniform random distribution of vector magnetic fields (B from 0 to 2500 G, inclination and azimuth from 0 to 180°) and LOS velocities (between -4 and 4 km s^{-1}). The remaining model parameters have been taken from a fit to the FTS atlas. The wavelength sampling has been 0.1 pm, with a total of 100 samples across the spectral line.

All inversions have been carried out under with the following initialization: $\lambda_0 = 10$, maximum number of iterations $k = 300$ (with ϵ_1 small enough to allow the 300 iterations), $S_0 = 0.2$, $S_1 = 0.8$, $\eta_0 = 6.5$, $B = 200$ G, $\gamma = 20°$, $\chi = 20°$, $\Delta\lambda_D = 30$ mÅ, $v_{LOS} = 0.25$ km s^{-1} and $a = 0.03$. Noise of the order

[1] code developed by Héctor Socas Navarro at the High Altitude Observatory (HAO).

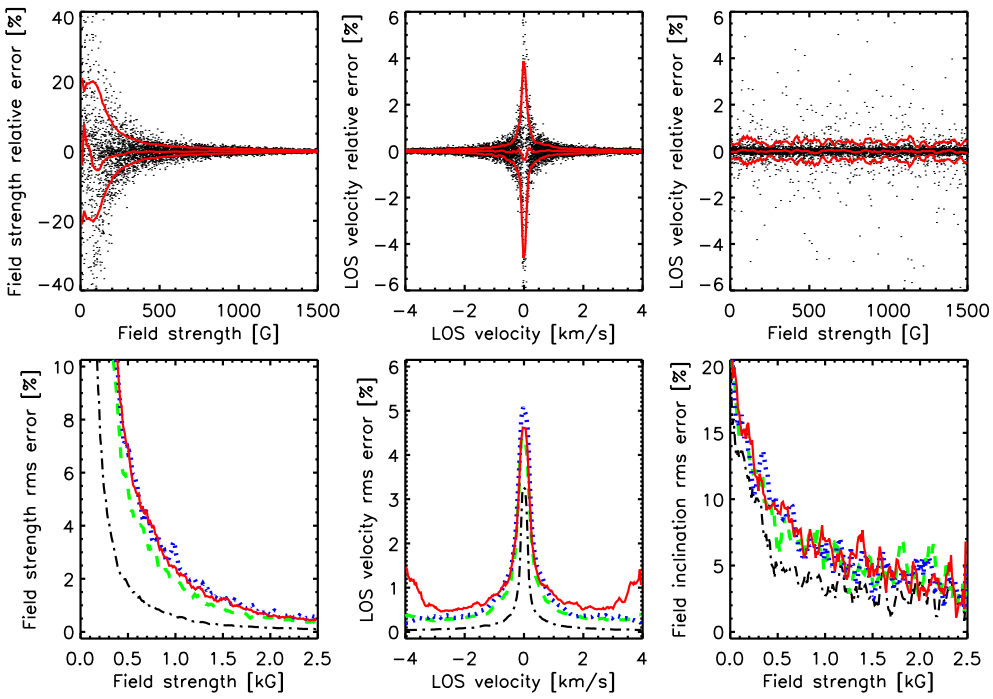

FIGURE C.1:— *Top*: Relative errors for the magnetic field strength, field inclination and LOS velocity from the inversion of five wavelength samples ($[\pm 40, \pm 80]$ mÅ plus a wavelength point in the continuum). The solid lines stand for the corresponding mean and rms values. *Bottom*: rms errors for different parameters. The dash-dotted line corresponds to the full profile inversion, dashed to $[\pm 80, \pm 40, 0]$ mÅ, solid to $[\pm 60, \pm 30]$ mÅ, and dotted to $[\pm 100, \pm 40]$ mÅ.

of 10^{-3} at the level of Stokes I have been added to the simulated profiles used throughout this Appendix. In what follows we describe in detail each of the tests that have been carried out.

C.0.2 Dependence with the wavelength sampling

Here we evaluate the ME uncertainties when inferring physical parameters from the Fe I 525.06 nm spectral line sampled at only few wavelength points and when these samples are taken at different wavelength positions. To this end we have performed three set of inversions: one with the spectral line sampled at five wavelength positions plus a wavelength point in the nearby continuum, and two inversions of the same spectral line sampled at only four wavelength positions plus the continuum. For all inversions the noise was $10^{-3} I_c$. An instrumental filter of 6 pm FWHM has been considered.

The upper panels of Fig. C.1 show the relative errors of the parameters inferred from the inversion of five wavelength samples ($[\pm 40, \pm 80]$ mÅ plus a wavelength point in the continuum) versus the real values. The panels show the individual uncertainties of each of the 10 000 ME inversions. Overploted is the corresponding rms values (red line). The bottom panels show the rms values of the relative errors but for the magnetic field strength, its inclination and the LOS velocity from the inversion of the spectral line by taking into account: the full profile (100 wavelength samples), five wavelength samples, $[\pm 80, \pm 40, 0]$, plus a wavelength point in the continuum (green) and two sets of four wavelength sampling (plus continuum) at $[\pm 60, \pm 30]$ and $[\pm 100, \pm 40]$ mÅ (red and blue lines, respectively)

The retrieved errors when considering the full profile are almost negligible, being for the magnetic field strength smaller than 2% for fields larger than $\sim$500 G, or smaller than 0.1% for the LOS velocity. These results are solely due to photon noise and slightly augmented by the 6 pm FWHM filter. The results for the inclination are noisier.

In general, the uncertainties are larger when limiting the number of wavelength samples. The errors in the inferred field strengths are smaller than $\sim$3% for strong fields, $B > 1000$ G. They become larger for weak fields mainly due to the noise, i.e., the weaker the magnetic field strength, the smaller amplitude size of the polarimetric signals (for fields on the weak field regimen and fixed orientation), therefore the Stokes profiles are more affected by noise. For the field inclination (bottom right panel) rms errors of $\sim$5% are to be expected for fields stronger than 1000 G. Note that the inclination is more uncertain for weak fields. The relative errors in the velocity are less than 1% except for velocities close to zero (upper middle panel). Interestingly, the errors in the inferred velocities do not depend on the field strength, as demonstrated by the upper right panel of Fig. C.1. When the velocity is mainly determined by the Stokes I profile, i.e., in the absence of a magnetic field, it is determined from all Stokes parameters likewise, when a magnetic field is present.

Figure C.1 also illustrates the dependence of the errors on the number of wavelength samples and sample points (bottom panels). First, notice the larger errors when decreasing the number of wavelength samples. Secondly, and more interestingly, note that the use of one more wavelength point decreases the rms error of the field strength by less than 1% only, with no clear improvement in the field inclination and LOS velocity. Moreover, there are no significant differences on the field strength and inclination by using different wavelength positions. The error in the LOS velocity, however, increases at high velocity values when the points are less distant (red curve). In this case, the wavelength points sample only one wing of the line because of the large velocities, hence

providing lower sensitivity (see Fig. 3.3). Notice that in this case, the spectral shift corresponding to 3 km s^{-1} would be 5.1 pm, large enough to misplace one of the selected wavelength samples, consequently the Stokes profile is poorer sampled, yielding large uncertainties.

In all tests, the thermodynamic parameters are not well recovered because of crosstalk problems (Chapt. 3.2.2). This, however, does not imply a poor determination of the magnetic field vector and LOS velocity as our results show. The mean values for the thermodynamic parameters and averaged for all the 10 000 ME inversions were, for the 525.06 nm spectral line and for the tests discussed in this section: $\eta_0 = 7.4 \pm 0.9$, $\Delta\lambda_D = 0.0300 \pm 0.0007$, $a = 0.30 \pm 0.03$, $S_0 = 0.02 \pm 0.02$ and $S_1 = 1.00 \pm 0.02$.

C.0.3 Dependence with the instrumental profile

Here we determine the variation of the uncertainties of the different model parameters with respect to the width of the instrumental profile. To this end, the Stokes profiles of the basis are convolved with instrumental profiles of different widths ranging from 4 to 12 pm. The filter profiles are described by a Gaussian function. To amplify the effects of the instrumental profile we have only taken 4 wavelength samples within the spectral line ($[\pm 40, \pm 80]$ mÅ) plus a point in the nearby continuum. The line used for this test is Fe I at 525.02 nm. The inversion procedure is the same as described before.

Figure C.2 displays the variation of the relative rms errors of the magnetic field strength and LOS velocity as a function of the real field strength and velocity values (left panels) and filter width (right panels). The relative errors are small even for widths of 120 mÅ. The rms values for the field strength and LOS velocity slightly increase with increasing filter width. This variation seems not to depend on the magnetic field range (top right panel).

The relative rms errors for the magnetic field inclination and its azimuth are in Fig. C.3. The errors for the field inclination are larger for weaker fields and for vertically oriented fields. In both cases, the error increases because of the linear polarization signals are smaller in amplitude, therefore more affected by noise. The variation of the rms errors with the filter width for different ranges of inclination angles is small. Also, the rms for the field azimuth do not vary much for increasing filter widths. In both cases, the relative uncertainties are smaller than 10%.

In summary, the rms of the inferences do not vary significantly with broader filter widths. This indicates that, the uncertainties due to the limited wavelength sampling and noise dominate. We caution that the ME profiles are symmetric ones, therefore the instrumental filter only diminishes the amplitude of

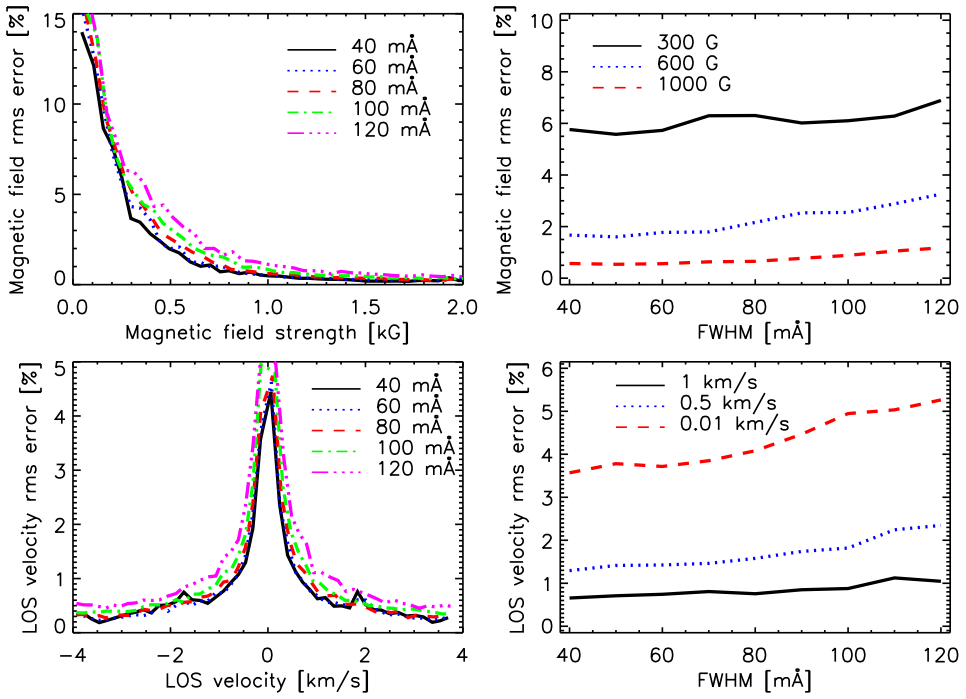

FIGURE C.2:— *Left:* Relative rms errors for the magnetic field strength (top) and for the LOS velocity (bottom) and for different instrumental widths. *Right:* relative rms errors as a function of the FWHM and for pixels having the indicated values of B and $v_{\rm LOS}$. The results correspond to the Fe I at 525.02 nm spectral line sampled at five wavelength,$[\pm 80, \pm 40]$ mÅ, plus a point in the nearby continuum.

the polarization Stokes profiles and smooths out the shape of the Stokes vector. The situation may be much unfavorable when dealing with real profiles, which exhibit asymmetries.

C.0.4 Influence of the stray light

In the previous tests, we have assumed that the magnetic field occupies the whole resolution element, i.e., we have considered magnetic filling factor equal one. However, current measurements of the magnetic field vector on the solar surface indicate that the magnetic field occupies only a fraction of the pixel. The filling factor depends on the spatial resolution and the observed solar feature. Besides, solar instrumentation is not free from scattered light contamination.

Then, suppose that a magnetic atmosphere occupies a fraction f of the res-

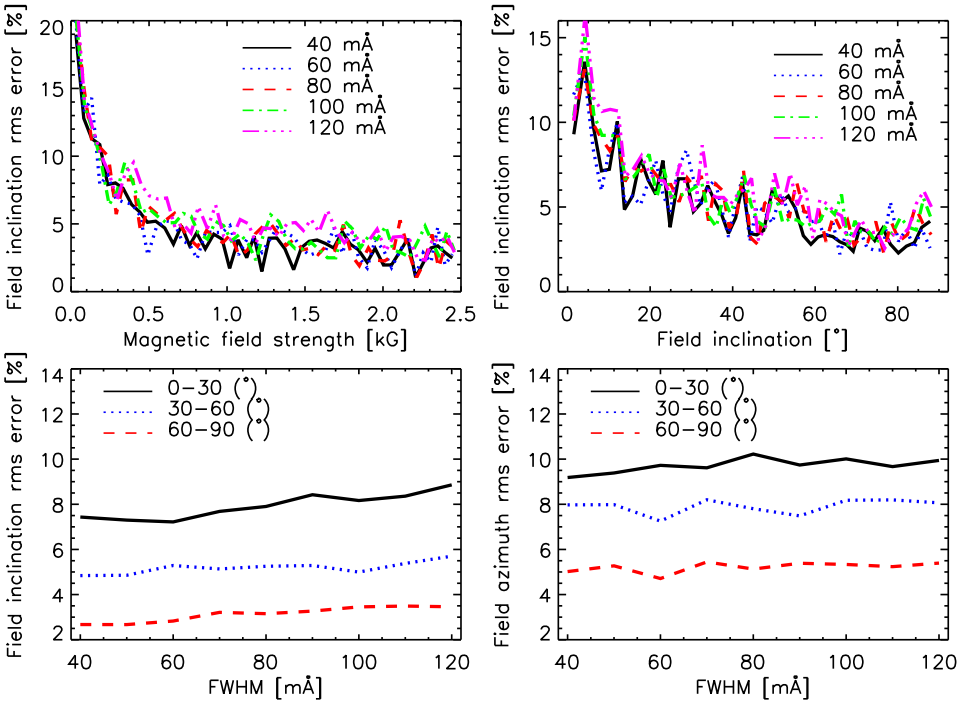

FIGURE C.3:— *Top panels*: Magnetic field inclination relative rms error with respect to the magnetic field strength and inclination for different instrumental profile widths. *Bottom panels:* Magnetic field inclination and azimuth errors with respect to the FWHM of the filter and for pixels having the indicated values of field inclination. As in Fig. C.2 the results correspond to the Fe I at 525.02 nm spectral line sampled at five wavelength,[±80, ±40] mÅ, plus a point in the nearby continuum.

olution element and another one and non-magnetized occupies the rest of the resolution element. Then, if $\mathbf{I}_{\rm m}$ stands for the magnetic component and $\mathbf{I}_{\rm nm}$ is that emerging from the non-magnetized atmosphere, the observed Stokes profile is $\mathbf{I} = (1-f)\mathbf{I}_{\rm m} + f\mathbf{I}_{\rm nm}$. This relation shows that the amplitude of the polarization signals decreases with increasing filling factor. The non-magnetized atmosphere can be considered as a stray-light contamination which may be known a priory. This section is then aimed at determining the effect of a stray-light contamination on the various parameter inferences.

To analyze the influence of stray light we have generated a second reference basis of Stokes profiles (magnetic component) contaminated by a stray-light profile (non-magnetic component). The stray light has been modeled using the same thermodynamic parameters than those used to generate the Stokes profiles. To make it different from the profiles of the basis we have broadened

the stray light profile by using a macroturbulent velocity of 1 km s^{-1}. We have also fixed the Doppler shift. These two things, together with the presence of a magnetic field vector, are the only differences between the non-magnetic component and the magnetic component. There is no recipe to simulate an ideal stray-light profile. In real observations it is usually evaluated by averaging the Stokes I profiles in the surrounding, non-magnetized areas. Therefore, it seems reasonable to consider the stray light as a broader Stokes I profile with fixed Doppler shift. The reference basis have been generated as described in Sect. C.0.1. The filing factor f has been generated with a uniform random distribution varying from $f = 0$ to 0.5.

The inversion procedure is the same as for the previous test. In addition we have the magnetic filling factor f as a free parameter. Initially, f have been set to 0.2 for all inversions. Besides, to worsen the situation, we have convolved the Stokes profiles with a Gaussian of 6 pm width simulating a smearing profile and taken only 5 wavelength samples at $[\pm 40, \pm 80]$ mÅ and the continuum. The spectral line used for this test is the Fe I line 525.06 nm. This situation clearly represents the worst case scenario.

The results are shown in Fig. C.4. The stray-light contamination has strong impact on the inferences. The scatter of the individual errors have increased for the magnetic field as well as for the field inclination as compared to the previous tests. The larger scatter is due to the reduced sensitivity of the spectral line by a second component, which worsens the determination of the filling factor. In addition, the polarization Stokes profiles are of smaller amplitude, depending on the f value.

Notice that we are using only 5 wavelength samples along the spectral line. This leaves a total of 20 observables. The ME code has to determine 10 free parameters. Also, the spectral line has mid sensitivity to the field strength. However, we obtain that the mean rms errors for the stray-light factor ranges from less that 5% for strong fields to ∼20% for weaker fields (bottom right panel). The errors on the magnetic field do not exceed ∼20% for weak fields. For the field inclination, the rms errors are smaller than ∼10%. Interestingly, the rms errors of the magnetic flux density (bottom left panel) are small: *the magnetic flux is always determined with high accuracy.* Note the fluctuation on the rms errors (red solid lines). This indicates worse convergence of the ME code for individual pixels. Finally, the accumulations of points at the bottom right corner for the field inclination panel is due to that the inclination can be neither smaller than 0° nor larger than 180°.

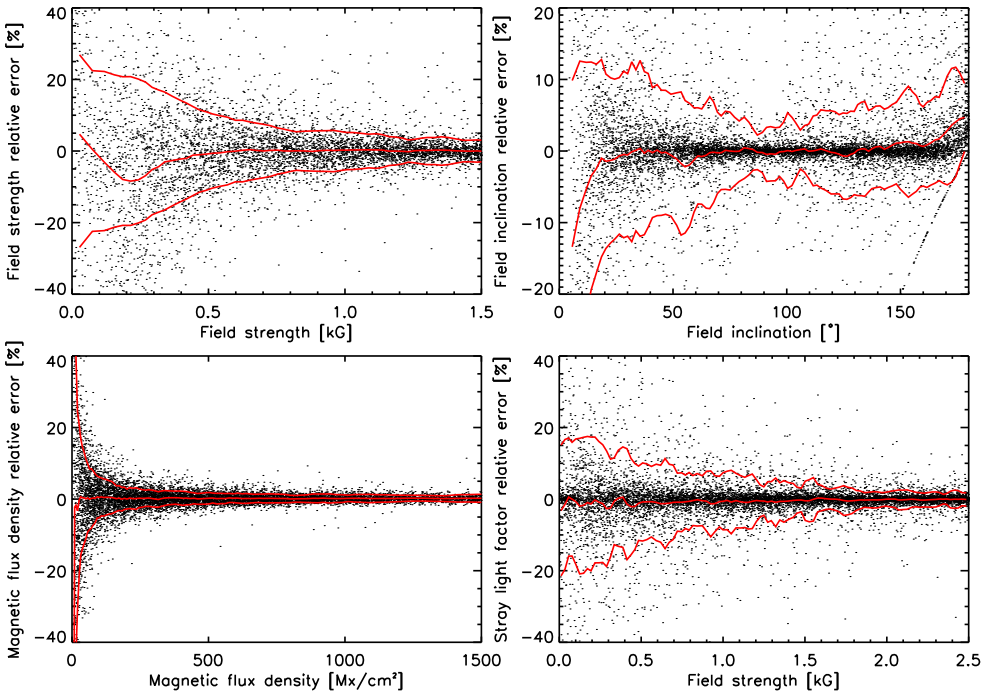

FIGURE C.4:— Individual relative errors for the magnetic field strength, field inclinations, magnetic flux density (absolute valued) and stray light factor, for the Fe I at 525.06 nm spectral line sampled at five wavelength,$[\pm 80, \pm 40]$ mÅ, plus a point in the nearby continuum. The red solid lines stand for the corresponding rms errors.

C.1 Conclusions

The accuracy of the physical parameters retrieved from ME inversions depends on the observed spectral line, the number of wavelength samples and position of the wavelength points. It also depends on the signal to noise ratio and on the FWHM of the smearing profile. The field strength vector inferences are more affected by these factors than the that for the LOS velocity. For weak fields, the errors are larger.

Four wavelength samples plus the continuum are sufficient to recover the magnetic field vector and LOS velocity with high accuracy ($\sim$1%) when dealing with ME Stokes profiles. The quality of the inferences does not increase much when using 5 wavelength samples. The differences on inclination are not detectable, being the same for all cases. The results slightly depend on the target spectral line.

These results are in agreement with those reported by Graham et al. (2002).

In our tests we also take into account the effect of different wavelength points selection. The accuracy of the results is better or at least of the order of those presented for different instruments, i.e, compared to the rms noise of 20 ms^{-1} on the velocity for MDI (Scherrer et al. 1995) or to the 13 ms^{-1} and 10 G on velocity and field strength for HMI (Scherrer & SDO/HMI Team 2002). Also compare with those from Martínez Pillet (2007) for the PHI instrument aboard the Solar Orbiter. The accuracy reported in this case is of 8 m s^{-1} and 7 G on the velocity and longitudinal field strength.

These results are valid and constrained to *symmetric ME Stokes profiles* and high spatial resolution measurements, where the magnetic field fills the whole resolution elements. The extrapolation of these results to real solar data seems not to be straightforward. We have modeled the effect of the stray-light contamination and the results worsen.

D

Application to PHI

The goal of the Polarimetric and Helioseismic Imager (PHI; Marsch et al. 2005) is to obtain high resolution maps of the vector magnetic field and the line-of-sight (LOS) velocity in the solar photosphere. PHI consists of two telescopes: the High Resolution Telescope (PHI-HRT) and the Full Disk Telescope (PHI-FDT). Spectropolarimetry is carried out using a double Fabry-Pérot interferometer, conceptually based on $LiNbO_3$ etalons, which performs the wavelength selection within the spectral line, and two polarization modulation packages, based on liquid crystal retarders, to modulate the polarization of the incident light. The photospheric line to be observed is Fe I 617.3 nm.

In this Section we investigate how well we are able to infer atmospheric parameters from PHI-HRT data, providing feedback to optimize its design. In many respects, PHI-HRT is very similar to the IMaX. Therefore, we carry out similar tests as those presented in the previous section, i.e., we study the influence of spectral resolution and wavelength sampling on the accuracy of the atmospheric parameters derived from PHI-HRT measurements.

D.0.1 Methodology

To simulate the observational process of PHI we follow the same strategy as for IMaX, i.e., we first synthesize the Stokes profiles, we then degrade them to the PHI-HRT resolution and finally the "observations" are analyzed by means of ME inversions. In this case the telescope diameter is equivalent to a 0.73m telescope at 1 AU and the pixel size is $0\farcs11$, which limits the spatial resolution to 162 km ($\sim 0\farcs22$) on the solar surface. We use the same MHD models but a

different spectral line which is, in this case, Fe I at 617.3 nm.

As for IMaX we consider the results of ME inversions of the spatially degraded Stokes profiles with no noise, no spectral PSF, and 61 wavelength samples as *the reference* solution. In the next two sections we study the influence of spectral resolving power, noise, and limited wavelength sampling on the vector magnetic fields and line-of-sight velocities derived from ME inversions of the simulated measurements.

D.0.2 Effects of the finite spectral resolution

PHI uses a Fabry-Pérot interferometer to perform the wavelength selection within the line. The finite spectral resolution of the instrument reduces the amount of information carried by the line, and therefore is a source of uncertainties in the determination of atmospheric parameters. The spectral PSF of PHI can be described as a Gaussian function whose FWHM lies somewhere between 75 mÅ and 120 mÅ.

We estimate the effect of limited spectral resolution as follows. The synthetic Stokes profiles are convolved with PSFs of different widths. Specifically, we vary the FWHM from zero to 200 mÅ in steps of 10 mÅ. We then add noise at the level of 10^{-3}, apply a ME inversion to the profiles sampled at 61 wavelength positions, and compare the inferred maps with our *reference*. In the ME inversion we consider no contribution of stray light.

Figure D.1 shows the variation of the mean and rms errors (defined as the difference between the inferred and the *reference* parameters) with the FWHM, for the LOS velocity (upper panel) and the magnetic field strength and inclination (middle and bottom panels). In the last two panels we have considered only pixels whose Stokes Q, U *or* V amplitudes exceed three times the noise level. Different conclusions can be drawn from this figure. First, we note that the rms errors for filter widths of 0 mÅ are $\sigma_{\rm v} \sim 4$ m/s in velocity, $\sigma_{\rm B} \leq 30$ G in field strength, and $\sigma_\gamma \leq 8^{\rm o}$ in field inclination. These errors are solely due to the photon noise of 10^{-3} added to the observables (which was zero in the reference profiles). Therefore, *they represent the minimum uncertainties that PHI would produce* even if the spectral line is critically sampled at 61 wavelength positions.

The mean and rms errors of the velocity increase with filter width, although the variation is weak. We estimate rms errors of about 30 m/s and 50 m/s for 60 mÅ and 120 mÅ filter widths, respectively. The errors in the magnetic field strength also vary smoothly with the FWHM. For filters narrower than 120 mÅ, the rms errors are always smaller than ~ 30 G. Interestingly, the mean errors increase with increasing field strength: in the range 150–750 G they are roughly

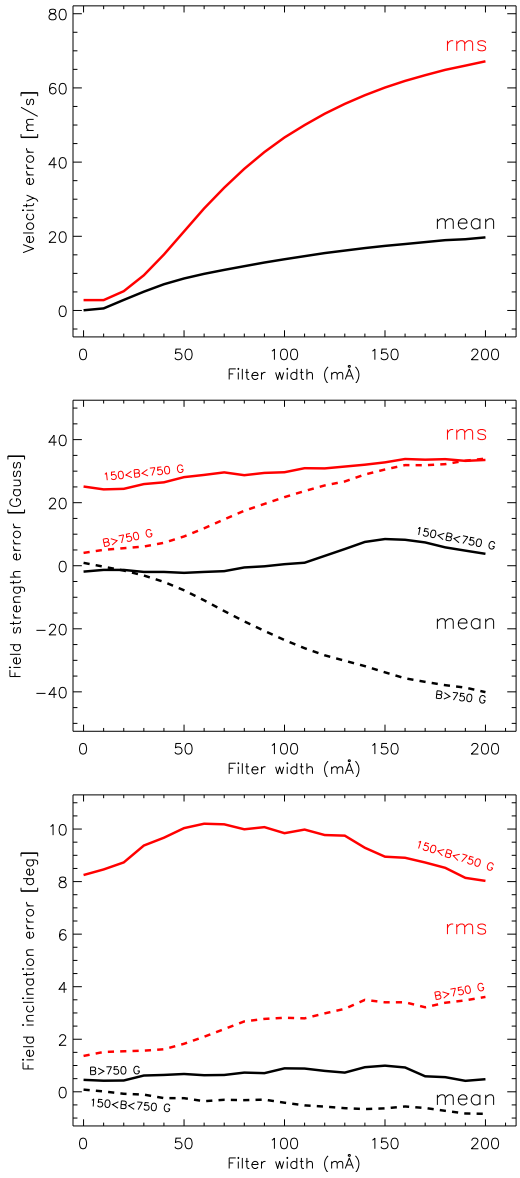

FIGURE D.1:— Variation of the mean (black) and rms (red) values of the error with the FWHM of the instrumental PSF. Top: LOS velocity. Middle: magnetic field strength. Bottom: magnetic field inclination. The dashed curve in the central and bottom panels represents pixels with field strengths larger than 750 G (in the reference map) and the solid curve field strengths ranging from 150 to 750 G.

constant, which is not the case for fields stronger than 750 G. The fact that the mean errors of field strength and velocity vary with the FWHM is related to the asymmetries of the profiles. Stokes profiles formed in real atmospheres exhibit asymmetries induced by vertical gradients of the atmospheric parameters. The Stokes profiles coming from ME atmospheres are *symmetric*, however. While the spectral PSF smears out the asymmetries, it also allows better fits to the observations. Consequently, the mean errors vary with filter width, and the variation is larger for stronger fields.

From this analysis we conclude that instrumental profiles of up to 120 mÅ FWHM provide accurate results. It is important to keep in mind, however, that the spectral PSF also affects the Stokes profiles in two different ways: first it reduces their amplitudes, and second it smoothes the asymmetries out. A detailed description of such effects can be found in Sect. 9.3.

D.0.3 Effects of number of wavelength samples

PHI-HRT will achieve a spatial resolution of about 160 km in the solar photosphere. At this resolution the smallest dynamical structures accessible evolve on time scales of 10–50 seconds (assuming a scale height of 100 km). Thus, the scanning of the spectral line should not take longer. This fact limits PHI to sample only a few wavelength positions within the line. Currently, scans of five wavelength positions plus one in the nearby continuum are being considered. The limited wavelength sampling introduces additional uncertainties in the inference process. To determine these errors we carry out ME inversions of the Stokes profiles sampled with different numbers of wavelength points, from 2 to 8, plus the continuum. First, the profiles have been convolved with a 120 mÅ FWHM filter and have been added noise at the level of $10^{-3} I_{\rm c}$. Again, we compare the inferred maps with the *reference* solution.

Figure D.2 shows the variation of the normalized errors with the number of wavelength samples, for the LOS velocity and field strength and inclination. Only pixels whose Stokes Q, U or V amplitudes are larger than three times the noise level have been considered for the magnetic parameters. The selection of the particular samples were: [±140,0]; [±140,±70]; [±140,±70,0] (PHI baseline); [±140,±80,±40]; [±140,±80,±40,0]mÅ plus a wavelength point in the continuum for the three- through seven-sample case, respectively. The errors do not change much with the number of samples, provided it is larger than 5. The reason for such a behavior is the strong smearing of the Stokes profiles after the instrument action. It is important to remark, however, that the sampling will further reduce the number of detectable profiles since in general the observed wavelength positions will not coincide with the maximum Stokes Q

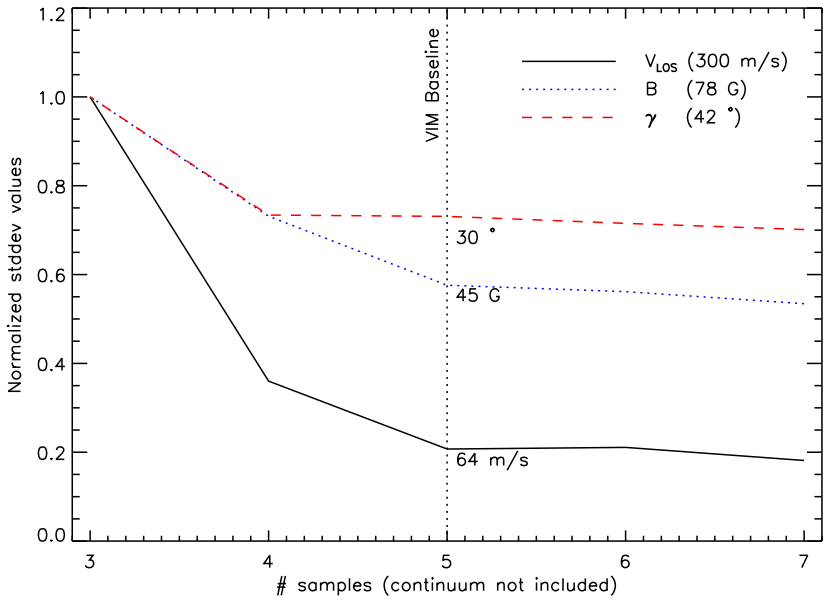

FIGURE D.2:— Standard deviations for the differences between the reference and the PHI results varying the number of wavelength samples. Values are normalized to their maxima.

or U signals.

In summary, we find that the five samples within the line plus one in the continuum are an optimum choice, since a small increase in the number of samples does not produce significant improvements, while a decrease produce worse results. The errors are of about 45 G, 30°, and 64 $\mathrm{m\,s^{-1}}$, for the field strength, inclination, and LOS velocity respectively.

Bibliography

Abbett, W. P. 2007, ApJ, 665, 1469

Auer, L. H., & Heasley, J. N. 1978, A&A, 64, 67

Auer, L. H., House, L. L., & Heasley, J. N. 1977, Sol. Phys., 55, 47

Anstee, S. D., & O'Mara, B. J. 1995, MNRAS, 276, 859

Asensio Ramos, A., Trujillo Bueno, J., & Landi Degl'Innocenti, E. 2008, ApJ, in press (arXiv:0804.2695v1)

Asensio Ramos, A., Martínez González, M. J., & Rubiño-Martín, J. A. 2007a, A&A, 476, 959

Asensio Ramos, A., Martínez González, M. J., López Ariste, A., Trujillo Bueno, J., & Collados, M. 2007b, ApJ, 659, 829

Asplund, M., Nordlund, Å., Trampedach, R., Allende Prieto, C., & Stein, R. F. 2000, A&A, 359, 729

Barklem, P. S., Anstee, S. D., & O'Mara, B. J. 1998, Publications of the Astronomical Society of Australia, 15, 336

Barklem, P. S., Piskunov, N., & O'Mara, B. J. 2000, A&A Supp.Ser., 142, 467

Bellot Rubio, L. R. 2006, Astronomical Society of the Pacific Conference Series, 358, 107

Bellot Rubio, L. R., & Collados, M. 2003, A&A, 406, 357

Born, M., & Wolf, E. 1980, Principles of optics: Electromagnetic Theory of Propagation of Light (Oxford: Pergamon Press)

Borrero et al. 2008, Sol. Phys., in press

Brault J., Neckel H., 1987, Spectral atlas of solar absolute disk-averaged and disk-center intensity from 3290 to 12510Å, ftp.hs.uni-hamburg.de/pub/outgoing/FTS-atlas

Cabrera Solana, D., Bellot Rubio, L. R., & del Toro Iniesta, J. C. 2005, A&A, 439, 687

Cameron, R., Schüssler, M., Vögler, A., & Zakharov, V. 2007, A&A, 474, 261

Carroll, T. A., & Kopf, M. 2008, A&A, 481, L37

Carroll, T. A., & Staude, J. 2001, A&A, 378, 316

Carlsson, M., et al. 2007, PASJ, 59, 663

Cattaneo, F. 1999, ApJ, 515, L39

Cattaneo, F., Emonet, T., & Weiss, N. 2003, ApJ, 588, 1183

Centeno, R., et al. 2007, ApJ, 666, L137

Charbonneau, P. 1995, ApJS, 101, 309

Cheung, M. C. M. 2006, PhD Thesis, University of Göttingen, Germany, http://webdoc.sub.gwdg.de/diss/2006/cheung/

Cheung, M. C. M., Schüssler, M., & Moreno-Insertis, F. 2007, A&A, 467, 703

Collados, M. 1999, in Third Advances in Solar Physics Euroconference, ed. B. Schmieder, A. Hofmann, & J. Staude, ASP Conf., 184, 3

Collados, M. 2001, Advanced Solar Polarimetry – Theory, Observation, and Instrumentation, 236, 255

Danilovic, S., Gandorfer, A., Lagg, A., Schüssler, M., Solanki, S. K., Vögler, A., Katsukawa, Y., & Tsuneta, S. 2008, A&A, 484, L17

Domínguez Cerdeña, I., Sánchez Almeida, J., & Kneer, F. 2006, ApJ, 646, 1421

Domínguez Cerdeña, I., Kneer, F., & Sánchez Almeida, J. 2003, ApJ, 582, L55

Emonet, T., & Cattaneo, F. 2001, ApJ, 560, L197

Faurobert-Scholl, M. 1993, A&A, 268, 765

Faurobert, M., Arnaud, J., Vigneau, J., & Frisch, H. 2001, A&A, 378, 627

Foukal, P. 1990, New York, Wiley-Interscience, 492

Frutiger, C. 2000, PhD thesis, ETH Zürich, Switzerland, Diss ETH No. 13896

Gandorfer, A. M., Solanki, S. K., Barthol, P., Lites, B. W., Martínez Pillet, V., Schmidt, W., Soltau, D., & Title, A. M. 2006, Proc. SPIE, 6267

Gingerich, O., & de Jager, C. 1968, Sol. Phys., 3, 5

Gingerich, O., Noyes, R. W., Kalkofen, W., & Cuny, Y. 1971, Sol. Phys., 18, 347

Graham, J. D., López Ariste, A., Socas-Navarro, H., & Tomczyk, S. 2002, Sol. Phys., 208, 211

Gray, D. F. 1992, The Observation and Analysis of Stellar Photospheres, Cambridge, UK: Cambridge University Press

Grigorjev, V. M., & Katz, J. M. 1972, Sol. Phys., 22, 119

Grossmann-Doerth, U. 1994, A&A, 285, 1012

Grossmann-Doerth, U., Schüssler, M., Sigwarth, M., & Steiner, O. 2000, A&A, 357, 351

Holweger, H. 1970, A&A, 4, 11

Holweger, H., & Mueller, E. A. 1974, Sol. Phys., 39, 19

Howard, R., & Stenflo, J. O. 1972, Sol. Phys., 22, 402

Ichimoto, K., et al. 2008, Sol. Phys., 249, 233

Illing, R. M. E., Landman, D. A., & Mickey, D. L. 1975, A&A, 41, 183

Ishikawa, R., et al. 2008, A&A, 481, L25

Jefferies, J. T., & Mickey, D. L. 1991, ApJ, 372, 694

Jones, D. R., Perttunen, C. D., & Stuckman, B. E., 1993, Journal of Optimization Theory and Applications, 79, 157

Keller, C. U., Aebersold, F., Egger, U., Povel, H. P., Steiner, P., & Stenflo, J. O. 1992, Lest Fundation. Technical Report NO. 53

Keller, C. U., Deubner, F.-L., Egger, U., Fleck, B., & Povel, H. P. 1994, A&A, 286, 626

Keller, C. U., Schüssler, M., Vögler, A., & Zakharov, V. 2004, ApJ, 607, L59

Kentischer, T. J., Schmidt, W., Sigwarth, M., & Uexkuell, M. V. 1998, A&A, 340, 569

Khomenko, E.V., Collados, M., Solanki, S.K., Lagg, A., & Trujillo Bueno, J. 2003,A&A, 408, 1115

Khomenko, E., & Collados, M. 2007a, ApJ, 659, 1726

Khomenko, E., & Collados, M. 2007b, Memorie della Societa Astronomica Italiana, 78, 166

Khomenko, E. V., Shelyag, S., Solanki, S. K., Vögler, A. 2005a, A&A, 442, 1059

Khomenko, E. V., Martínez González, M. J., Collados, M., Vögler, A., Solanki, S. K., Ruiz Cobo, B., & Beck, C. 2005b, A&A, 436, L27

Khomenko, E. 2006, Solar MHD Theory and Observations: A High Spatial Resolution Perspective, 354, 63

Kosugi, T., et al. 2007, Sol. Phys., 243, 3

Kurucz, R. L., Furenlid, I., & Brault, J. T. L. 1984, National Solar Observatory Atlas, Sunspot, New Mexico: National Solar Observatory

Lagg, A., Woch, J., Krupp, N., & Solanki, S. K. 2004, A&A, 414, 1109

Lamb, D. A., DeForest, C. E., Hagenaar, H. J., Parnell, C. E., & Welsch, B. T. 2008, ApJ, 674, 520

Landi Degl'Innocenti, E. 1976, A&AS, 25, 379

Landi Degl'Iinnocenti, E., & Landi Degl'Iinnocenti, M. 1977, A&A, 56, 111

Landi Degl'Innocenti, E. 1992, in Solar Observations: Techniques and Interpretation, ed. F. Sanchez, M. Collados, & M. Vázquez, Cambridge: Cambridge University Press, 73

Landolfi, M., & Degl'Innocenti, E. L. 1982, Sol. Phys., 78, 355

Levenberg, K. 1944, Quart. Appl. Math, 2, 164-168

Leighton, R. B., Noyes, R. W., & Simon, G. W. 1962, ApJ, 135, 474

Lites, B. W. 2002, ApJ, 573, 431

Lites, B. W., Casini, R., Garcia, J., & Socas-Navarro, H. 2007b, Memorie della Societa Astronomica Italiana, 78, 148

Lites, B. W., Elmore, D. F., & Streander, K. V. 2001, Advanced Solar Polarimetry – Theory, Observation, and Instrumentation, 236, 33

Lites, B. W., Leka, K. D., Skumanich, A., Martinez Pillet, V., & Shimizu, T. 1996, ApJ, 460, 1019

Lites, B. W., Rutten, R. J., & Berger, T. E. 1999, ApJ, 517, 1013

Lites, B. W., & Skumanich, A. 1990, ApJ, 348, 747

Lites, B. W., Skumanich, A., Rees, D. E., & Murphy, G. A. 1988, ApJ, 330, 493

Lites, B. W., & Socas-Navarro, H. 2004, ApJ, 613, 600

Lites, B. W., et al. 2007a, PASJ, 59, 571

Lites, B. W., et al. 2008a, ApJ, 672, 1237

Lites, B. W., et al. 2008b, in prep.

Lin, H. 1995, ApJ, 446, 421

Lin, H., & Rimmele, T. 1999, ApJ, 514, 448

Livingston, W., & Harvey, J. 1971, Solar Magnetic Fields, 43, 51

Livingston, W. C., & Harvey, J. 1975, BAAS, 7, 346

López Ariste, A., & Casini, R. 2002, ApJ, 575, 529

López Ariste, A., Tomczyk, S., & Casini, R. 2002, ApJ, 580, 519

López Ariste, A., Tomczyk, S., & Casini, R. 2006, A&A, 454, 663

Marquardt, D. 1963, J. Soc. Indust. Appl. Math. 11, 431-441

Marsch, E., Marsden, R., Harrison, R., Wimmer-Schweingruber, R., & Fleck, B. 2005, Advances in Space Research, 36, 1360

Martin, S. F. 1984, In Keil S. L. (Ed.) Small-Scale Dynamical Processes in Quiet Stellar Atmospheres, New Mexico, 30

Martínez González, M. J. 2007, Memorie della Societa Astronomica Italiana, 78, 59

Martínez González, M.J., Collados, M., & Ruiz Cobo, B. 2006,A&A, 456, 1159

Martínez González, M. J., Collados, M., Ruiz Cobo, B., & Beck, C. 2008, A&A, 477, 953

Martínez González, M. J., Collados, M., Ruiz Cobo, B., & Solanki, S. K. 2007, A&A, 469, L39

Martínez Pillet, V., Lites, B. W., & Skumanich, A. 1997, ApJ, 474, 810

Martínez Pillet, V., Bonet, J. A., Collados, M., Jochum, L., Mathew, S., Medina Trujillo, J. L., Ruiz Cobo, B., del Toro Iniesta, J. C., Lopez Jimenez, A. C., Castillo Lorenzo, J., and 17 coauthors. 2004, Proc. SPIE, 5487, 1152

Mein, P. 1971, Sol. Phys., 20, 3

Mihalas, D. 1978, in Stellar Atmospheres, Vol. 455

Neckel H., 1999, Solar Physics 184, 421

Orozco Suárez, D., Bellot Rubio, L. R., & del Toro Iniesta, J. C. 2007, ApJ, 662, L31

Orozco Suárez, D., & del Toro Iniesta, J. C. 2007, A&A, 462, 1137

Orozco Suárez, D., et al. 2007a, ApJ, 670, L61

Orozco Suárez, D., et al. 2007b, PASJ, 59, 837

Orozco Suárez, D., Bellot Rubio, L. R., del Toro Iniesta, J. C., & Tsuneta, S. 2008, A&A, 481, L33

Piskunov, N. E., Kupka, F., Ryabchikova, T. A., Weiss, W. W., & Jeffery, C. S. 1995, A&A Supp.Ser., 112, 525

Ploner, S. R. O., Schussler, M., Solanki, S. K., Sheminova, V. A., Gadun, A. S., & Frutiger, C. 2001, Advanced Solar Polarimetry – Theory, Observation, and Instrumentation, 236, 371

De Pontieu, B. 2002, ApJ, 569, 474

Press, W. H., Teukolsky, S. A., Vetterling, W. T., & Flannery, B. P. 1992, Numerical Recipes - The Art of Scientific Computing. Cambridge: Cambridge University Press

Rachkovsky, D. N. 1962, Izv. KrymskoiAstrofiz. Obs., 27, 148

Rachkovsky, D. N. 1967, Izv. KrymskoiAstrofiz. Obs., 37, 56

Rees, D. E., López Ariste, A., Thatcher, J., & Semel, M. 2000, A&A, 355, 759

Rezaei, R., Schlichenmaier, R., Beck, C. A. R., Bruls, J. H. M. J., & Schmidt, W. 2007, A&A, 466, 1131

Ruiz Cobo, B., & del Toro Iniesta, J. C. 1992, ApJ, 398, 375

Ruiz Cobo, B., & del Toro Iniesta, J. C. 1994, A&A, 283, 129

Sánchez Almeida, J. 2003, A&A, 411, 615

Sánchez Almeida, J., & Lites, B.W. 2000, ApJ, 532, 1215

Sánchez Almeida, J., & Martínez Pillet, V. 1994, ApJ, 424, 1014

Sánchez Almeida, J., Ruiz Cobo, B., & del Toro Iniesta, J. C. 1996, A&A, 314, 295

Schaffenberger, W., Wedemeyer-Böhm, S., Steiner, O., & Freytag, B. 2006, Solar MHD Theory and Observations: A High Spatial Resolution Perspective , 354, 345

Shchukina, N., & Trujillo Bueno, J. 2003, Astronomical Society of the Pacific Conference Series, 307, 336

Shelyag, S., Schüssler, M., Solanki, S. K., Berdyugina, S. V., Vögler, A. 2004, A&A, 427, 335

Shelyag, S., Schüssler, M., Solanki, S. K., Vögler, A. 2007, A&A, 469, 731

Scherrer, P. H., et al. 1995, Sol. Phys., 162, 129

Scherrer, P. H., & SDO/HMI Team 2002, Bulletin of the American Astronomical Society, 34, 735

Schrijver, C. J., Title, A. M., Hagenaar, H. J., & Shine, R. A. 1997a, Sol. Phys., 175, 329

Schrijver, C. J., Title, A. M., van Ballegooijen, A. A., Hagenaar, H. J., & Shine, R. A. 1997b, ApJ, 487, 424

Schüssler, M. 2001, Advanced Solar Polarimetry – Theory, Observation, and Instrumentation, 236, 343

Schüssler, M. 2003, Astronomical Society of the Pacific Conference Series, 307, 601

Schüssler,M., Shelyag, S., Berdyugina, S., Vögler, A., & Solanki, S.K. 2003,ApJ, 597, L173

Schüssler, M., Vögler, A. 2006, ApJ, 641, L73

Schüssler, M., Vögler, A. 2008, A&A, 481, L5

Semel, M. 1967, Annales d'Astrophysique, 30, 513

Shimizu, T. 2004, The Solar-B Mission and the Forefront of Solar Physics, 325, 3

Shimizu, T., et al. 2007, PASJ, 59, 845

Shimizu, T., et al. 2008, Sol. Phys., 249, 221

Sigwarth, M., Balasubramaniam, K. S., Knölker, M., & Schmidt, W. 1999, A&A, 349, 941

Skumanich, A., & Lites, B. W. 1987, ApJ, 322, 473

Smithson, R. C. 1975, BAAS, 7, 346

Socas-Navarro, H. 2003, Neural Networks, 16, 355

Socas-Navarro, H. 2005, ApJ, 621, 545

Socas-Navarro, H., & Sánchez Almeida, J. 2002, ApJ, 565, 1323

Socas-Navarro, H., & Sánchez Almeida, J. 2003, ApJ, 593, 581

Socas-Navarro,H., & Lites, B. W. 2004, ApJ, 616, 587

Socas-Navarro, H., López Ariste, A., & Lites, B. W. 2001, ApJ, 553, 949

Solanki, S. K. 1993, Space Science Reviews, 63, 1

Spruit, H. C., Title, A. M., & van Ballegooijen, A. A. 1987, Sol. Phys., 110, 115

Stein, R. F., & Nordlund, Å. 2006, ApJ, 642, 1246

Steiner, O. 2000, Sol. Phys., 196, 245

Steiner, O. 2003, A&A, 406, 1083

Steiner, O., Rezaei, R., Schaffenberger, W., & Wedemeyer-Böhm, S. 2008, ApJ, 680, L85

Stenflo, J. O. 1973, Sol. Phys., 32, 41

Stenflo, J. O. 1982, Sol. Phys., 80, 209

Stenflo, J. O. 1993, IAU Colloq. 141: The Magnetic and Velocity Fields of Solar Active Regions, 46, 205

Stenflo, J. O., Solanki, S., Harvey, J. W., & Brault, J. W. 1984, A&A, 131, 333

Stix, M. 2004, The sun: an introduction, 2nd ed., Astronomy and astrophysics library, Berlin: Springer

Suematsu, Y., et al. 2008, Sol. Phys., 249, 197

Thevenin, F. 1989, A&A Supp.Ser., 77, 137

Title, A. M., & Schrijver, C. J. 1998, Cool Stars, Stellar Systems, and the Sun, 154, 345

Tsuneta, S., et al. 2008, Sol. Phys., 249, 167

del Toro Iniesta, J. C. 2003, Introduction to Spectropolarimetry. Cambridge, UK: Cambridge UniversityPress

del Toro Iniesta, J. C., & Collados, M. 2000, Appl. Opt., 39, 1637

del Toro Iniesta, J. C., Collados, M., Sanchez Almeida, J., & Semel, M. 1990, A&A, 227, 591

del Toro Iniesta, J. C., & Ruiz Cobo, B. 1996, Sol. Phys., 164, 169

Trujillo Bueno, J., Shchukina, N., & Asensio Ramos, A. 2004, Nature, 430, 326

Uitenbroek, H., Tritschler, A., & Rimmele, T. 2007, ApJ, 668, 586

Unno, W. 1956, PASJ, 8, 108

Vögler, A. 2003, PhD Thesis, University of Göttingen, Germany, http://webdoc.sub.gwdg.de/diss/2004/voegler/

Vögler, A., & Schüssler, M. 2007, A&A, 465, L43

Vögler, A., Shelyag, S., Schüssler, M., Cattaneo, F., Emonet, T., & Linde, T. 2005, A&A, 429, 335

Wang, J., Wang, H., Tang, F., Lee, J. W., & Zirin, H. 1995, Sol. Phys., 160, 277

Wedemeyer-Böhm, S. 2008, A&A, 487, 399

Westendorp Plaza, C., del Toro Iniesta, J. C., Ruiz Cobo, B., Martínez Pillet, V., Lites, B. W., & Skumanich, A. 1998, ApJ, 494, 453

Zirin, H. 1985, Australian Journal of Physics, 38, 961

Zirin, H. 1995, Sol. Phys., 159, 203